NEXT-GENERATION ELECTROCHEMICAL ENERGY STORAGE DEVICES

EDITED BY: Yuxin Tang, Oleksandr Malyi, Wenping Sun and Jianqing Zhao
PUBLISHED IN: Frontiers in Chemistry

frontiers Research Topics

ISSN 1664-8714
ISBN 978-2-88963-569-6
DOI 10.3389/978-2-88963-569-6

About Frontiers

Frontiers is more than just an open-access publisher of scholarly articles: it is a pioneering approach to the world of academia, radically improving the way scholarly research is managed. The grand vision of Frontiers is a world where all people have an equal opportunity to seek, share and generate knowledge. Frontiers provides immediate and permanent online open access to all its publications, but this alone is not enough to realize our grand goals.

Frontiers Journal Series

The Frontiers Journal Series is a multi-tier and interdisciplinary set of open-access, online journals, promising a paradigm shift from the current review, selection and dissemination processes in academic publishing. All Frontiers journals are driven by researchers for researchers; therefore, they constitute a service to the scholarly community. At the same time, the Frontiers Journal Series operates on a revolutionary invention, the tiered publishing system, initially addressing specific communities of scholars, and gradually climbing up to broader public understanding, thus serving the interests of the lay society, too.

Dedication to Quality

Each Frontiers article is a landmark of the highest quality, thanks to genuinely collaborative interactions between authors and review editors, who include some of the world's best academicians. Research must be certified by peers before entering a stream of knowledge that may eventually reach the public - and shape society; therefore, Frontiers only applies the most rigorous and unbiased reviews.
Frontiers revolutionizes research publishing by freely delivering the most outstanding research, evaluated with no bias from both the academic and social point of view. By applying the most advanced information technologies, Frontiers is catapulting scholarly publishing into a new generation.

What are Frontiers Research Topics?

Frontiers Research Topics are very popular trademarks of the Frontiers Journals Series: they are collections of at least ten articles, all centered on a particular subject. With their unique mix of varied contributions from Original Research to Review Articles, Frontiers Research Topics unify the most influential researchers, the latest key findings and historical advances in a hot research area! Find out more on how to host your own Frontiers Research Topic or contribute to one as an author by contacting the Frontiers Editorial Office: researchtopics@frontiersin.org

NEXT-GENERATION ELECTROCHEMICAL ENERGY STORAGE DEVICES

Topic Editors:
Yuxin Tang, University of Macau, China
Oleksandr Malyi, University of Oslo, Norway
Wenping Sun, Zhejiang University, China
Jianqing Zhao, Soochow University, China

Citation: Tang, Y., Malyi, O., Sun, W., Zhao, J., eds. (2020). Next-generation Electrochemical Energy Storage Devices. Lausanne: Frontiers Media SA.
doi: 10.3389/978-2-88963-569-6

Table of Contents

frontiers in Chemistry

ORIGINAL RESEARCH
published: 04 March 2019
doi: 10.3389/fchem.2019.00107

Enhanced Cycling Stability of Cation Disordered Rock-Salt $Li_{1.2}Ti_{0.4}Mn_{0.4}O_2$ Material by Surface Modification With Al_2O_3

Baojun Huang, Rui Wang, Yansheng Gong, Beibei He* and Huanwen Wang*

Faculty of Materials Science and Chemistry, China University of Geosciences, Wuhan, China

Cation disordered rock-salt lithium-excess oxides are promising candidate cathode materials for next-generation electric vehicles due to their extra high capacities. However, one major issue for these materials is the distinct decline of discharge capacities during charge/discharge cycles. In this study, Al_2O_3 layers were coated on cation disordered $Li_{1.2}Ti_{0.4}Mn_{0.4}O_2$ (LTMO) using atomic layer deposition (ALD) method to optimize its electrochemical performance. The discharge capacity after 15 cycles increased from 228.1 to 266.7 mAh g^{-1} for LTMO after coated with Al_2O_3 for 24 ALD cycles, and the corresponding capacity retention enhanced from 79.7 to 90.9%. The improved cycling stability of the coated sample was ascribed to the alleviation of oxygen release and the inhibition on the undesirable side reactions. Our work has provided a new possible solution to address some of the capacity fading issues related to the cation disordered rock-salt cathode materials.

Keywords: lithium-ion batteries, cathode, cation disorder, rock-salt, Li-excess

OPEN ACCESS

Edited by:
Yuxin Tang,
Nanyang Technological University, Singapore

Reviewed by:
Xianhong Rui,
Guangdong University of Technology, China
Jianqing Zhao,
Soochow University, China
Renheng Wang,
Shenzhen University, China

****Correspondence:***
Rui Wang
wangrui@cug.edu.cn
Beibei He
babyfly@mail.ustc.edu.cn

Specialty section:
This article was submitted to Electrochemistry, a section of the journal Frontiers in Chemistry

Received: *25 December 2018*
Accepted: *11 February 2019*
Published: *04 March 2019*

Citation:
Huang B, Wang R, Gong Y, He B and Wang H (2019) Enhanced Cycling Stability of Cation Disordered Rock-Salt $Li_{1.2}Ti_{0.4}Mn_{0.4}O_2$ Material by Surface Modification With Al_2O_3. Front. Chem. 7:107. doi: 10.3389/fchem.2019.00107

INTRODUCTION

Cathode materials with high energy densities are crucial for next generation of lithium-ion batteries, especially when used in hybrid and electric vehicles (Zu and Li, 2011; Goodenough and Park, 2013; Rui et al., 2015; Wang et al., 2017; Lv et al., 2018; Tan et al., 2018; Zhang et al., 2019). For this reason, Layer-structured Li-excess materials, which could deliver capacities as high as 300 mAh g^{-1}, have been researched for more than 10 years (Lu et al., 2002; Wang et al., 2013; Yu et al., 2014; Hu et al., 2018). But these materials undergo irreversible O loss in the first cycle, which may cause structure densification and voltage degradation in subsequent cycles (Xu et al., 2011). Recently, cation disordered rock-salt Li-excess materials, sharing similar chemical compositions with layered Li-excess materials, have also attracted lots of attentions because of their high capacities (Yabuuchi et al., 2011, 2015, 2016a,b; Lee et al., 2014, 2015, 2017, 2018; Twu et al., 2015; Freire et al., 2016, 2017; Cambaz et al., 2018; Kitchaev et al., 2018; Zhao et al., 2019). Besides, it is reported that the O redox may undergo reversible reactions in the first cycle in this material (Wang et al., 2015), which provides the possibility to achieve reversible changes during the lengthy electrochemical cycles. However, many of these materials have problems in their cycling performances. Wang et al. prepared a cation disordered $Li_{1.23}Ni_{0.155}Ru_{0.615}O_2$ material, and the capacity drops from 295.3 to 250 mAh g^{-1} only after 5 charge-discharge cycles (Wang et al., 2017). Okada's group prepared another cation disordered $Li_{1.2}Mn_{0.4}Ti_{0.4}O_2$ material, but its capacity drops from 226 to about 200 mAh g^{-1} just after 6 cycles (Kitajou et al., 2016).

Similar problems happened to layered Li-excess materials, and some literatures have reported that atomic layer deposition (ALD) method may be an effective method to alleviate the problem. ALD is a powerful technique to precisely render a uniform and conformal layer at Å level on arbitrary substrate surfaces due to its pulsing and controllable reaction. Belharouak's team coated $Li_{1.2}Ni_{0.13}Mn_{0.54}Co_{0.13}O_2$ porous powder with ultrathin Al_2O_3 film using ALD technique, and the coated material shows higher first cycle coulombic efficiency and improved cycling performance (Zhang et al., 2013). Xiao et al. reported that the $AlPO_4$ coating layer by ALD can effectively protect the $Li_{1.2}Mn_{0.54}Co_{0.13}Ni_{0.13}O_2$ against the attack from the electrolyte, and can significantly improve its initial coulombic efficiency and thermal stability (Xiao et al., 2017a). Meanwhile, Oxide-based coatings at the surface of different cathode materials via ALD method have been demonstrated to be very conformal and uniform as reported in the literatures (Zhao and Wang, 2012; Zhao et al., 2012; Zhao and Wang, 2013a,b), thus they can effectively prevent from the electrolyte attack for enhanced cycling stability of the coated cathode.

In this study, we coated a cation disordered rock-salt $Li_{1.2}Ti_{0.4}Mn_{0.4}O_2$ material with different thicknesses of Al_2O_3 layers by ALD technique and studied their effects on the cycling stabilities. $Li_{1.2}Ti_{0.4}Mn_{0.4}O_2$ is a typical cation disordered rock-salt material but with poor cycling performances (Kitajou et al., 2016; Yabuuchi et al., 2016a). In our previous study, we found that the valence of Mn in disordered materials may be lower than 3+ after the first cycle (Wang et al., 2015), and this low valence may cause Mn dissolution into the electrolyte (Nicolau et al., 2018). In this case, we infer that Al_2O_3 coating may be an effective method to increase the reversibility and cycling performances of this cation disordered material.

EXPERIMENTAL

$Li_{1.2}Ti_{0.4}Mn_{0.4}O_2$ was synthesized by the traditional solid-state reaction using the precursors of Li_2CO_3 (99%, Alfa Aesar), Mn_2O_3 (98%, Alfa Aesar), and TiO_2 (99%, Sigma-Aldrich). Stoichiometric amounts of precursors were ball-milled for 4 h and then pressed into a pellet. The pellet was calcinated at 900°C for 12 h in Ar, then pulverized and ball-milled at 300 rpm for 4 h. The obtained material was denoted as LTMO.

Coating was achieved by the Atomic Layer deposition (ALD) method using an Ensure Nanotech ALD system (LabNano-9100). During the ALD process, as-prepared LTMO sample was first placed in a home-made sample holder and heated to 200°C in the reaction chamber under ca. 1.0 mbar. Nitrogen with a flow rate of 20 sccm was used as the carrying and purge gas. The $Al(CH_3)_3$ and water were employed as aluminum and oxygen precursors, respectively. In each cycle, pulse time of $Al(CH_3)_3$ was controlled at 0.02 s, and exposure time water precursor was 0.02 s. 8 s nitrogen purge steps were used after $Al(CH_3)_3$ and water exposures. The LTMO sample was coated with Al_2O_3 layers for 16, 24, 40 ALD cycles. The coated samples were denoted as LTMO/nAl_2O_3, where n stands for the number of ALD cycles.

Morphologies and crystal structures of LTMO with or without Al_2O_3 layers were analyzed by scanning electron microscope (SEM, SU 8010) and powder X-ray diffractometer (XRD, Bruker D8 Advance), respectively. High Resolution Transmission Electron Microscope (HRTEM, TF 20) was used to record detailed crystalline structures of the samples. X-ray photoelectron spectroscopy (XPS, ESCALab 250Xi) with monochromatic Al K-α radiation was carried out to investigate the valences of the species in the samples.

To fabricate the cathode electrode, different Al_2O_3-coated LTMO samples were firstly ball-milled with Ketjen black at 150 rpm for 4 h, then manually mixed with polytetrafluoroethylene (PTFE) binder. The mixture was rolled into a thin film, in which the weight ratios of LTMO/nAl_2O_3, Ketjen black, and PTFE are 70: 20: 10. The surface mass density of each electrode film is about 4.4 mg cm^{-2}. Cells were assembled according to our previous study (Wang et al., 2015). Typically, a two electrode swagelok cell was fabricated using the Al_2O_3-coated LTMO thin film and lithium foil as the working electrode and the counter electrode, respectively. Borosilicate glass fiber membrane (Whatman) was used as the separator, and 1 M solution of $LiPF_6$ dissolved in ethylene carbonate/dimethyl carbonate (1:1 by volume) was used as the electrolyte. All cells were cycled on an LANHE CT2001A system (Wuhan LAND Electronics Co.) between 4.8 and 1.5 V with a current density of 10 mA g^{-1} at room temperature. The electrochemical impedance spectroscopy (EIS) data were recorded using a Gamry Reference 3,000 equipment. Cyclic voltammetry (CV) was measured on a CHI760E electrochemical workstation with the scanning rate of 0.5 mV s^{-1} and the potential range of 4.8–1.5 V.

RESULTS AND DISCUSSION

X-ray diffraction (XRD) patterns of the samples are shown in **Figure 1a**, and all the results correspond well to the disordered rock-salt structure. According to previous studies, cations are randomly placed on the 4b position (1/2, 1/2, 1/2), and the O atom is placed on the 4a position (0, 0, 0) (Wang et al., 2015). In cation disordered rock-salt materials, Li excess could build the 0-TM channels, through which Li ions could move out and back into the cathode material (Lee et al., 2015). According to the XRD patterns, no signal of Al_2O_3 is detected, and the reason may be that the amount of coated Al_2O_3 is too small or the coated Al_2O_3 is amorphous. The morphologies of LTMO before and after Al_2O_3 coating are shown in **Figures 1b,c**. No obvious differences are observed, indicating the coated Al_2O_3 particle may be too small to be surveyed in SEM. Energy Dispersive Spectrometers of the two samples are shown in **Figure 2a**. The characteristic peak of Al element could clearly be observed in the LTMO/24Al_2O_3 sample, while didn't show up in the LTMO sample. The LTMO/24Al_2O_3 sample was further examined by the elemental mapping experiments. and the results are shown in **Figures 2b-f**. Results show that Ti, Mn, O and Al elements distribute uniformly in the sample, which infer the Al_2O_3 layer exists uniformly in the sample.

In order to directly observe the coating Al_2O_3 layers on the surface of LTMO particles, we investigate bare LTMO and LTMO/24Al_2O_3 samples using high resolution transmission

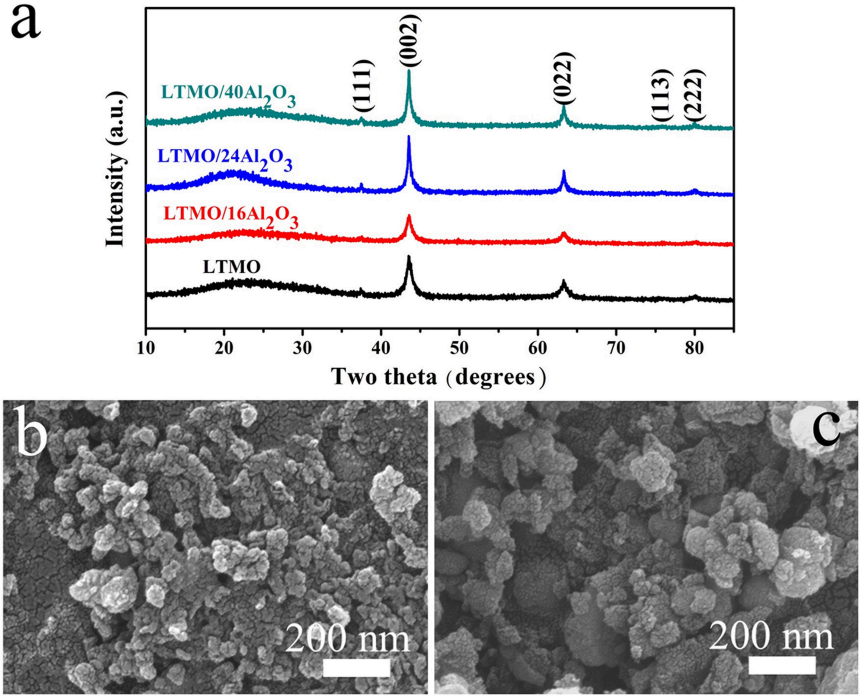

FIGURE 1 | (a) XRD pattern of the bare LTMO and different Al_2O_3-coated LTMO; SEM image of **(b)** LTMO and **(c)** LTMO/24Al_2O_3.

electron microscopy (HR-TEM). **Figure 3a** is the HR-TEM image of bare LTMO particles, showing well-defined lattice fringes in the surface region as well as those in the bulk region. In contrast, an obvious coating film in the surface region is clearly observed for LTMO/24Al_2O_3 sample (**Figure 3b**). It is different from the inner areas, and we infer it may be the Al_2O_3 coating layer. The thickness of the coating layer is around 3–5 nm.

In order to confirm Al_2O_3 layer exists on the sample surfaces, XPS was used to probe the surface compositions of the LTMO and LTMO/24Al_2O_3. All spectra were calibrated with the C 1s peak at 284.6 eV. **Figure 4A** presents the elemental XPS spectra of LTMO and LTMO/24Al_2O_3 samples, showing both samples contain the characteristic peaks of Ti, Mn, O, and C. From the partial enlarged figure (inset of the **Figure 4A**), the elemental peak of Al is only observed in the LTMO/24Al_2O_3 spectrum. The core level binding energies of Ti are aligned at 457.9 eV ($2p_{3/2}$) and 463.6 eV ($2p_{1/2}$) (**Figure 4B**), which is in good agreement with Ti^{4+} ions in other titanium-based compounds (Kim et al., 2017). The Mn 2p XPS spectra of LTMO and LTMO/24Al_2O_3 reveal peaks at 641.6 eV and 653.2 eV (**Figure 4C**), which are characteristic peaks of Mn^{3+} $2p_{3/2}$ and $2p_{1/2}$ (Das et al., 2011, 2013). This result confirms the valences of Mn in both samples are 3+. The Al $2p_{3/2}$ core level XPS spectrum displays a binding energy of 74.7 eV for the LTMO/24Al_2O_3 (**Figure 4D**), affirming that the chemical composition of the surface coating is Al_2O_3 for the LTMO/24Al_2O_3 sample.

The charge and discharge profiles of uncoated and coated LTMO samples for the first cycle are shown in **Figure 5A**, showing all the samples have the identical profiles except for the voltage platform and capacity. It is obviously seen that all the coated LTMO samples have higher first discharge plateau and coulombic efficiency, and we think this may be the effect of Al_2O_3 layer. Though the O reaction in LTMO may happen in the form of O redox, there might still be little amount of oxygen release in the first cycle. We infer the Al_2O_3 layer may alleviate this oxygen release and improve the O reaction reversibility, thus improve the discharge plateau and coulombic efficiency. The charge and discharge profiles for the 10th cycle are shown in **Figure 5B**, and the LTMO/24Al_2O_3 sample presents the largest discharge capacity. **Figure 5C** shows the cycling stability of the pristine and ALD coated samples. Bare LTMO shows an initial discharge capacity of 286.3 mAh g^{-1} (818.6 Wh kg^{-1}) and the capacity drops rapidly to 228.1 mAh g^{-1} (587.7 Wh kg^{-1}) after 15 cycles, which is only 79.7% for its initial discharge capacity. After coated with Al_2O_3 for 16 ALD cycles, an initial discharge of 289.1 mAh g^{-1} (856.6 Wh kg^{-1}) is observed and the capacity retention reaches 85.2%. It is worth noting that the LTMO/24Al_2O_3 sample could deliver a capacity of 293.4 mAh g^{-1} and energy density of 884.5 Wh kg^{-1} in the first cycle. After 15 cycles, the capacity and energy density could still maintain 266.7 mAh g^{-1} and 709.5 Wh kg^{-1}, respectively. And the capacity retention after 15 cycles is 90.9%, which is 11.2% higher than that of the pristine LTMO. Besides, the coulombic efficiencies also increased from 91.5 to 93.0% after the 24 cycles ALD coating. However, further increasing the ALD cycle numbers of coated Al_2O_3, the inferior performance for LTMO/40Al_2O_3 is obtained, and the capacity retention decreases to 84.6%. The reason should

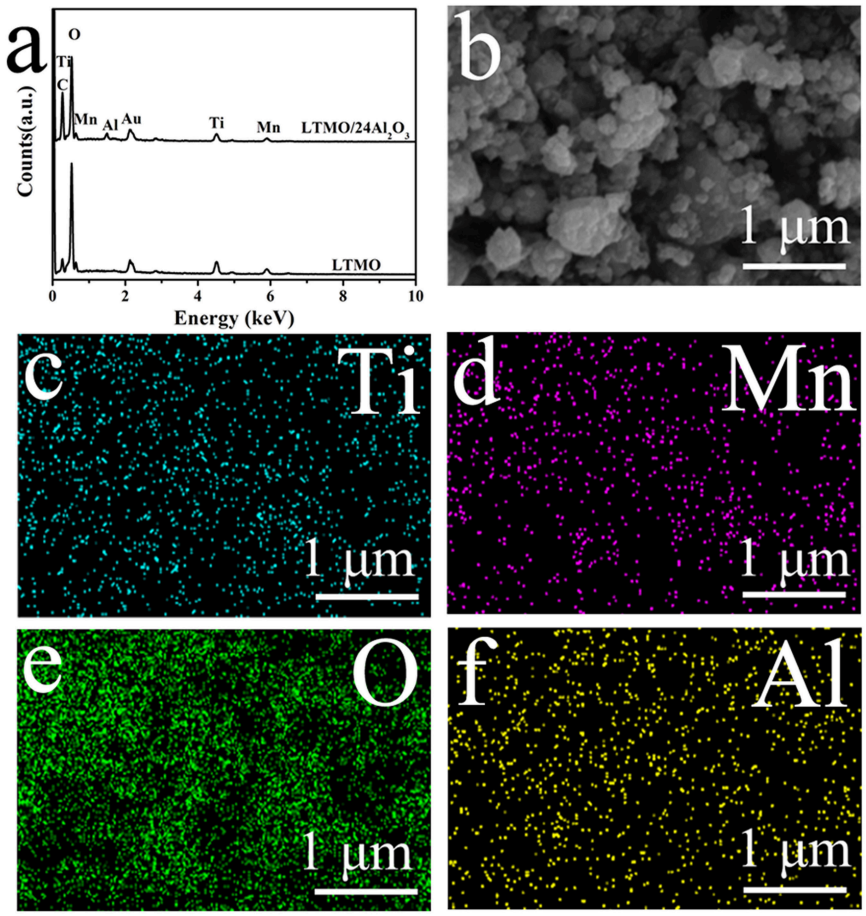

FIGURE 2 | (a) EDS element analysis LTMO and LTMO/24Al_2O_3; **(b–f)** element mapping of LTMO/24Al_2O_3.

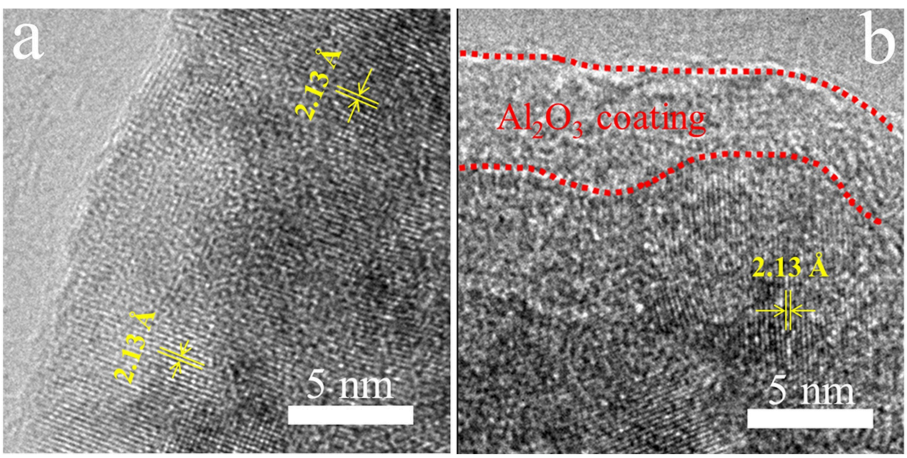

FIGURE 3 | HR-TEM images of **(a)** LTMO and **(b)** LTMO/24Al_2O_3.

be the thick insulated Al_2O_3 layer may inhibit the electric and ionic transportation (Jung et al., 2010). Based on above results, it can be concluded that proper thickness of Al_2O_3 layer can greatly improve the cycling stability of LTMO electrodes, while the over-thick Al_2O_3 layer leads to the reverse effect on the electrode.

Figure 6 show the cyclic voltammetric (CV) curves of LTMO and LTMO/24Al_2O_3 samples in the first three cycles at a

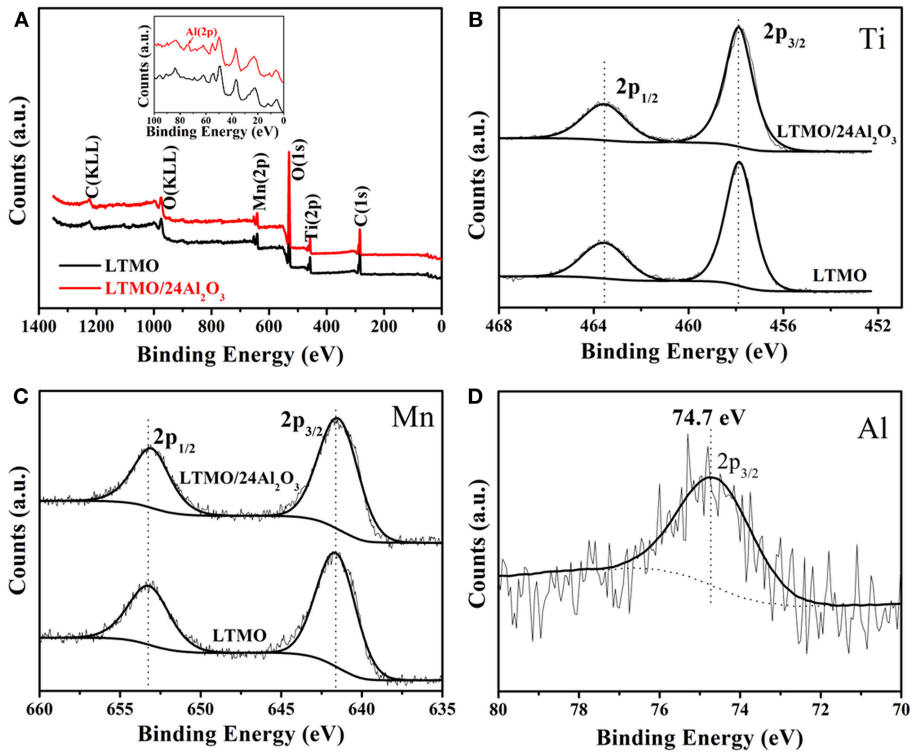

FIGURE 4 | (A) XPS survey spectrum and core level spectra of transition metals of LTMO and LTMO/24Al_2O_3: **(B)** Ti 2p; **(C)** Mn 2p; **(D)** Al 2p.

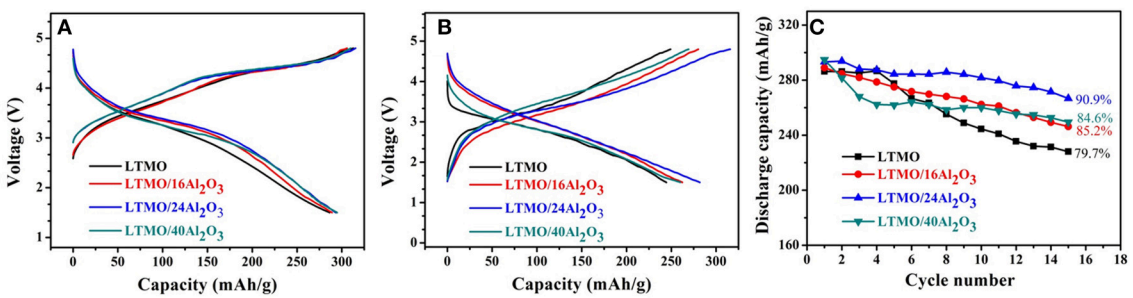

FIGURE 5 | (A) Initial charge-discharge curves; **(B)** 10th charge-discharge curves; **(C)** cyclic performance of the pristine LTMO and Al_2O_3-coated LTMO electrodes.

scanning rate of 0.5 mV s^{-1}. For the LTMO electrode (shown in the **Figure 6A**), the anodic peaks located at about 3.95 V corresponds to the oxidation of Mn^{3+} to Mn^{4+} (Xiao et al., 2017b) during the initial charge process. Another anodic peaks at around 4.63 V may be attributed to the oxygen loss from the crystal structure and formation of O_2^{2-} or O_2 from O^{2-}, which is usually observed on the Mn-based Li-excess cathode materials (Ma et al., 2016). While this peak disappears in the subsequent cycles, showing the irreversibility of the oxidation of O^{2-} in the LTMO electrode. In the following cathodic process, the peak at around 2.89 V corresponds to the reduction of Mn^{4+} to Mn^{3+} (Kong et al., 2017). It can be clearly seen that this peak moves to lower voltage range in the following cycles, indicating the decreasing of the valence of Mn. As to LTMO/24Al_2O_3 (shown in **Figure 6B**), two differences can be observed. First, the anodic peak at around 4.63 V still can be observed in the second and third cycles. Second, the cathodic peak located at around 3.17 V doesn't move during the cycles. These results infer the oxygen loss from the crystal structure in LTMO/24Al_2O_3 is milder than in LTMO. As a result, the Mn redox reaction in LTMO/24Al_2O_3 happens between Mn4+ and Mn3+. While Mn in pristine LTMO reduces to lower than 3+ because of the O loss and related densification in the first cycle.

In order to investigate the intrinsic factor of the improvement in the electrochemical performance of the LTMO/24Al_2O_3

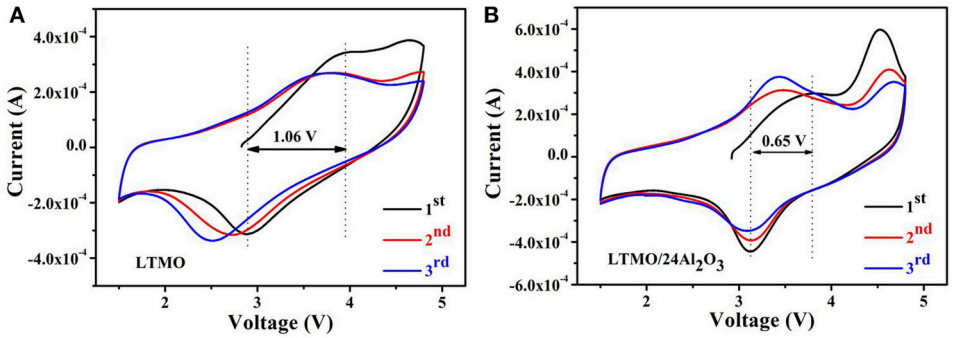

FIGURE 6 | Cyclic voltammetry of **(A)** LTMO and **(B)** LTMO/24Al_2O_3.

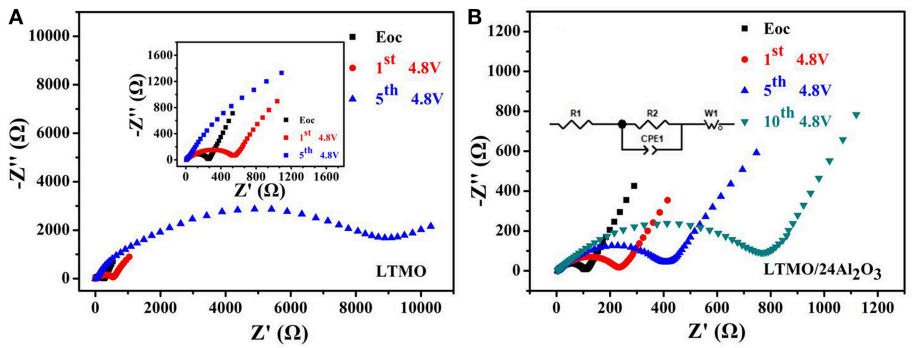

FIGURE 7 | EIS profiles of **(A)** LTMO and **(B)** LTMO/24Al_2O_3 at the charge state of 4.8 V in the different cycles; inset: an equivalent-circuit simulation model.

sample, electrochemical impedance spectra (EIS) were collected on the bare LTMO and the LTMO/24Al_2O_3 after charging to 4.8 V and resting for 4 h at the different cycles, shown in **Figures 7A,B**, respectively. All the Nyquist plots comprised a depressed semicircle from high to middle frequencies and an inclined line at low frequency. The simulated equivalent circuit is presented as an inset. The R_1 represents the Ohmic resistance coming from the separator, electrolyte and other components. The semicircle shows the charge transfer reaction composed of a charge transfer resistor (R_2) and a constant phase element (CPE_1), the inclined line stands for the Warburg diffusion impedance (ZW). The LTMO/24Al_2O_3 electrode shows the smaller R_2 of 101.6 Ω before cycling and remains at 228.4 Ω, 433.8 Ω and 851.3 Ω after 1st, 5, and 10th cycling, respectively. Nevertheless, the much larger R_2 values of the LTMO electrode are seen (i.e., 255.8 Ω before cycling and changed to 557.7 Ω after 1st cycling, even to 10,207 Ω for the 5th cycling, respectively), which infer complex side reactions may happen on the electrode surface and these reaction products may have blocked the ionic transfer process and result in worse cycling performance. Thus, it can be concluded that an appropriate thickness of Al_2O_3 layer guarantees the stable charge transfer and structural integrity of the cathode electrodes, which led to good cycling performance.

CONCLUSION

ALD technique was successfully used to deposit ultrathin Al_2O_3 coating layer onto the surface of the LTMO particles. Comparing with the uncoated LTMO, ALD process can reduce the polarization, restrain the undesirable side reactions, and suppress the increasing charge transfer resistance during cycling, which results in the significantly improved electrochemical performance of Al_2O_3-coated LTMO (LTMO/24Al_2O_3). The controllable ALD technology provides a promising guideline for the surface modification of disordered rock-salt cathode materials with high electrochemical performance.

AUTHOR CONTRIBUTIONS

RW conceived and designed the research. BaH carried out the experiments. YG and HW contributed to the discussion. RW wrote the manuscript with the help of BeH. All authors reviewed the manuscript.

ACKNOWLEDGMENTS

This work was supported by the National Natural Science Foundation of China (51702294 and 51702295).

REFERENCES

Cambaz, M. A., Vinayan, B. P., Euchner, H., Johnsen, R. E., Guda, A. A., Mazilkin, A., et al. (2018). Design of nickel-based cation-disordered rock-salt oxides: the effect of transition Metal (M = V, Ti, Zr) Substitution in $LiNi_{0.5}M_{0.5}O_2$ binary systems. *ACS Appl. Mater. Interfaces* 10, 21957–21964. doi: 10.1021/acsami.8b02266

Das, R., Jaiswal, A., Adyanthaya, S., and Poddar, P. (2011). Effect of particle size and annealing on spin and phonon behavior in $TbMnO_3$. *J. Appl. Phys.*109:064309. doi: 10.1063/1.3563571

Das, R., Jaiswal, A., and Poddar, P. (2013). Static and dynamic magnetic properties and interplay of Dy^{3+}, Gd^{3+} and Mn^{3+} spins in orthorhombic $DyMnO_3$ and $GdMnO_3$ nanoparticles. *J. Phys. D.* 46:045301. doi: 10.1088/0022-3727/46/4/045301

Freire, M., Kosova, N. V., Jordy, C., Chateigner, D., Lebedev, O. I., Maignan, A., et al. (2016). A new active Li-Mn-O compound for high energy density Li-ion batteries. *Nat. Mater.*15, 173–177. doi: 10.1038/nmat4479

Freire, M., Lebedev, O. I., Maignan, A., Jordy, C., and Pralong, V. (2017). Nanostructured Li_2MnO_3: a disordered rock salt type structure for high energy density Li ion batteries. *J. Mater. Chem. A.* 5, 21898–21902. doi: 10.1039/c7ta07476j

Goodenough, J. B., and Park, K. S. (2013). The Li-ion rechargeable battery: a perspective. *J. Am. Chem. Soc.* 135, 1167–1176. doi: 10.1021/ja3091438

Hu, E., Yu, X., Lin, R., Bi, X., Lu, J., Bak, S., et al. (2018). Evolution of redox couples in Li- and Mn-rich cathode materials and mitigation of voltage fade by reducing oxygen release. *Nat. Energy* 3, 690–698. doi: 10.1038/s41560-018-0207-z

Jung, Y. S., Cavanagh, A. S., Dillon, A. C., Groner, M. D., George, S. M., and Lee, S.-H. (2010). Enhanced stability of $LiCoO_2$ cathodes in lithium-ion batteries using surface modification by atomic layer deposition. *J. Electrochem. Soc.* 157, A75–A81. doi: 10.1149/1.3258274

Kim, D., Quang, N. D., Hien, T. T., Chinh, N. D., Kim, C., and Kim, D. (2017). 3D inverse-opal structured $Li_4Ti_5O_{12}$ Anode for fast Li-Ion storage capabilities. *Electr. Mater. Lett.* 13, 505–511. doi: 10.1007/s13391-017-7101-x

Kitajou, A., Tanaka, K., Miki, H., Koga, H., Okajima, T., and Okada, S. (2016). Improvement of cathode properties by lithium excess in disordered rocksalt $Li_{2+2x}Mn_{1-x}Ti_{1-x}O_4$. *Electrochemistry* 84, 597–600. doi: 10.5796/electrochemistry.84.597

Kitchaev, D. A., Lun, Z., Richards, W. D., Ji, H., Clément, R. J., Balasubramanian, M., et al. (2018). Design principles for high transition metal capacity in disordered rocksalt Li-ion cathodes. *Energy Environ. Sci.* 11, 2159–2171. doi: 10.1039/c8ee00816g

Kong, J.-Z., Zhai, H.-F., Qian, X., Wang, M., Wang, Q.-Z., Li, A.-D., et al. (2017). Improved electrochemical performance of $Li_{1.2}Mn_{0.54}Ni_{0.13}Co_{0.13}O_2$ cathode material coated with ultrathin ZnO. *J. Alloys Compd.* 694, 848–856. doi: 10.1016/j.jallcom.2016.10.045

Lee, J., Kitchaev, D. A., Kwon, D.-H., Lee, C. W., Papp, J. K., Liu, Y. S., et al. (2018). Reversible Mn^{2+}/Mn^{4+} double redox in lithium-excess cathode materials. *Nature* 556, 185–190. doi: 10.1038/s41586-018-0015-4

Lee, J., Papp, J. K., Clement, R. J., Sallis, S., Kwon, D. H., Shi, T., et al. (2017). Mitigating oxygen loss to improve the cycling performance of high capacity cation-disordered cathode materials. *Nat. Commun.* 8:981. doi: 10.1038/s41467-017-01115-0

Lee, J., Seo, D.-H., Balasubramanian, M., Twu, N., Li, X., and Ceder, G. (2015). A new class of high capacity cation-disordered oxides for rechargeable lithium batteries: Li–Ni–Ti–Mo oxides. *Energy Environ. Sci.* 8, 3255–3265. doi: 10.1039/c5ee02329g

Lee, J., Urban, A., Li, X., Su, D., Hautier, G., and Ceder, G. (2014). Unlocking the potential -disordered oxides for rechargeable lithium batteries. *Science* 343, 519–522. doi: 10.1126/science.1246432

Lu, Z., Beaulieu, L. Y., Donaberger, R. A., Thomas, C. L., and Dahn, J. R. (2002). Synthesis, Structure, and Electrochemical Behavior of $Li[Ni_xLi_{1/3-2x/3}Mn_{2/3-x/3}]O_2$. *J. Electrochem. Soc.* 149, A778–A791. doi: 10.1149/1.1471541

Lv, Z., Luo, Y., Tang, Y., Wei, J., Zhu, Z., Zhou, X., et al. (2018). Editable Supercapacitors with Customizable stretchability based on mechanically strengthened ultralong MnO_2 nanowire composite. *Adv. Mater.* 30:1704531. doi: 10.1002/adma.201704531

Ma, Q., Li, R., Zheng, R., Liu, Y., Huo, H., and Dai, C. (2016). Improving rate capability and decelerating voltage decay of Li-rich layered oxide cathodes via selenium doping to stabilize oxygen. *J. Power Sources* 331, 112–121. doi: 10.1016/j.jpowsour.2016.08.137

Nicolau, B. G., Petronico, A., Letchworth-Weaver, K., Ghadar, Y., Haasch, R. T., Soares, J. A. N. T., et al. (2018). Controlling interfacial properties of lithium-ion battery cathodes with alkylphosphonate self-assembled monolayers. *Adv. Mater. Interfaces* 5:1701292. doi: 10.1002/admi.201701292

Rui, X., Sun, W., Wu, C., Yu, Y., and Yan, Q. (2015). An advanced sodium-ion battery composed of carbon coated $Na_3V_2(PO_4)_3$ in a porous graphene network. *Adv. Mater.* 27, 6670–6676. doi: 10.1002/adma.201502864

Tan, H., Xu, L., Geng, H., Rui, X., Li, C., and Huang, S. (2018). Nanostructured $Li_3V_2(PO_4)_3$ Cathodes, *Small* 14:1800567. doi: 10.1002/smll.201800567

Twu, N., Li, X., Urban, A., Balasubramanian, M., Lee, J., and Liu, L. (2015). Designing new lithium-excess cathode materials from percolation theory: nanohighways in $Li_xNi_{2-4x/3}Sb_{x/3}O_2$. *Nano Lett.* 15, 596–602. doi: 10.1021/nl5040754

Wang, R., He, X., He, L., Wang, F., Xiao, R., Gu, L., et al. (2013). Atomic structure of Li_2MnO_3 after partial delithiation and re-lithiation. *Adv. Energy Mater.* 3, 1358–1367. doi: 10.1002/aenm.201200842

Wang, R., Li, X., Liu, L., Lee, J., Seo, D.-H., Bo, S.-H., et al. (2015). A disordered rock-salt Li-excess cathode material with high capacity and substantial oxygen redox activity: $Li_{1.25}Nb_{0.25}Mn_{0.5}O_2$. *Electrochem. Commun.* 60, 70–73. doi: 10.1016/j.elecom. 2015. 08.003

Wang, R., Li, X., Wang, Z., and Zhang, H. (2017). Electrochemical analysis graphite/electrolyte interface in lithium-ion batteries: p-Toluenesulfonyl isocyanate as electrolyte additive. *Nano Energy* 34, 131–140. doi: 10.1016/j.nanoen.2017.02.037

Wang, X., Huang, W., Tao, S., Xie, H., Wu, C., Yu, Z., et al. (2017). Attainable high capacity in Li-excess Li-Ni-Ru-O rock-salt cathode for lithium ion battery. *J. Power Sources* 359, 270–276. doi: 10.1016/j.jpowsour.2017.05.070

Xiao, B., Liu, H., Liu, J., Sun, Q., Wang, B., Kaliyappan, K., et al. (2017a). Nanoscale manipulation of spinel lithium nickel manganese oxide surface by multisite Ti occupation as high-performance cathode. *Adv. Mater.* 29:1703764. doi: 10.1002/adma.201703764

Xiao, B., Wang, B., Liu, J., Kaliyappan, K., Sun, Q., Liu, Y., et al. (2017b). Highly stable $Li_{1.2}Mn_{0.54}Co_{0.13}Ni_{0.13}O_2$ enabled by novel atomic layer deposited $AlPO_4$ coating. *Nano Energy* 34, 120–130. doi: 10.1016/j.nanoen.2017.02.015

Xu, B., Fell, C. R., Chi, M., and Meng, Y. S. (2011). Identifying surface structural changes in layered Li-excess nickel manganese oxides in high voltage lithium ion batteries: A joint experimental and theoretical study. *Energy Environ. Sci.* 4, 2223–2233. doi: 10.1039/c1ee01131f

Yabuuchi, N., Nakayama, M., Takeuchi, M., Komaba, S., Hashimoto, Y., Mukai, T., et al. (2016a). Origin of stabilization and destabilization in solid-state redox reaction of oxide ions for lithium-ion batteries. *Nat. Commun.* 7:13814. doi: 10.1038/ncomms13814

Yabuuchi, N., Takeuchi, M., Komaba, S., Ichikawa, S., Ozaki, T., and Inamasu, T. (2016b). Synthesis and electrochemical properties of $Li_{1.3}Nb_{0.3}V_{0.4}O_2$ as a positive electrode material for rechargeable lithium batteries. *Chem. Commun.* 52, 2051–2054. doi: 10.1039/c5cc08034g

Yabuuchi, N., Takeuchi, M., Nakayama, M., Shiiba, H., Ogawa, M., Nakayama, K., et al. (2015). High-capacity electrode materials for rechargeable lithium batteries: Li_3NbO_4-based system with cation-disordered rocksalt structure. *PNAS* 112, 7650–7655. doi: 10.1073/pnas.1504901112

Yabuuchi, N., Yoshii, K., Myung, S. T., Nakai, I., and Komaba, S. (2011). Detailed studies of a high-capacity electrode material for rechargeable batteries, Li_2MnO_3-$LiCo_{1/3}Ni_{1/3}Mn_{1/3}O_2$. *J. Am. Chem. Soc.* 133, 4404–4419. doi: 10.1021/ja108588y

Yu, X., Lyu, Y., Gu, L., Wu, H., Bak, S.-M., Zhou, Y., et al. (2014). Understanding the rate capability of high-energy-density li-rich layered $Li_{1.2}Ni_{0.15}Co_{0.1}Mn_{0.55}O_2$ cathode materials. *Adv. Energy Mater.* 4:1300950. doi: 10.1002/aenm.201300950

Zhang, X., Belharouak, I., Li, L., Lei, Y., Elam, J. W., Nie, A., et al. (2013). Structural and Electrochemical Study of Al_2O_3 and TiO_2 Coated $Li_{1.2}Ni_{0.13}Mn_{0.54}Co_{0.13}O_2$ Cathode Material Using ALD. *Adv. Energy Mater.* 3, 1299–1307. doi: 10.1002/aenm.201300269

Zhang, X., Rui, X., Chen, D., Tan, H., Yang, D., Huang, S., et al. (2019). $Na_3V_2(PO_4)_3$: an advanced cathode for sodium-ion batteries, *Nanoscale* 11, 2556–2576. doi: 10.1039/C8NR09391A

Zhao, E., He, L., Wang, B., Li, X., Zhang, J., Wu, Y., et al. (2019). Structural and mechanistic revelations on high capacity cation-disordered Li-rich oxides for rechargeable Li-ion batteries. *Energy Storage Mater.* 16, 354–363. doi: 10.1016/j.ensm.2018.06.016

Zhao, J., Qu, G., Flake, J. C., and Wang, Y. (2012). Low temperature preparation of crystalline ZrO_2 coatings for improved elevated-temperature performances of Li-ion battery cathodes. *Chem. Commun.* 48, 8108–8110. doi: 10.1039/c2cc33522k

Zhao, J., and Wang, Y. (2012). Ultrathin surface coatings for improved electrochemical performance of lithium ion battery electrodes at elevated temperature. *J. Phys. Chem. C.* 116, 11867–11876. doi: 10.1021/jp3010629

Zhao, J., and Wang, Y. (2013a). Atomic layer deposition of epitaxial ZrO_2 coating on $LiMn_2O_4$ nanoparticles for high-rate lithium ion batteries at elevated temperature. *Nano Energy* 2, 882–889. doi: 10.1016/j.nanoen.2013.03.005

Zhao, J., and Wang, Y. (2013b). Surface modifications of Li-ion battery electrodes with various ultrathin amphoteric oxide coatings for enhanced cycleability. *J. Solid State Electrochem.* 17, 1049–1058. doi: 10.1007/s10008-012-1962-6

Zu, C.-X., and Li, H. (2011). Thermodynamic analysis on energy densities of batteries. *Energy Environ. Sci.* 4, 2614–2624. doi: 10.1039/c0ee00777c

Conflict of Interest Statement: The authors declare that the research was conducted in the absence of any commercial or financial relationships that could be construed as a potential conflict of interest.

frontiers in Chemistry

ORIGINAL RESEARCH
published: 31 May 2019
doi: 10.3389/fchem.2019.00389

The Electrochemical Performances of n-Type Extended Lattice Spaced Si Negative Electrodes for Lithium-Ion Batteries

Moonsang Lee[1†], Dockyoung Yoon[2,3†], Uk Jae Lee[4], Nurzhan Umirov[3], Aliya Mukanova[5], Zhumabay Bakenov[5] and Sung-Soo Kim[3]*

[1] Korea Basic Science Institute, Daejeon, South Korea, [2] SK Innovation, Daejeon, South Korea, [3] Graduate School of Energy Science and Technology, Chungnam National University, Daejeon, South Korea, [4] School of Integrative Engineering, Chung-Ang University, Seoul, South Korea, [5] National Laboratory Astana, School of Engineering, Nazarbayev University, Institute of Batteries, Astana, Kazakhstan

The electrochemical performances of lithium-ion batteries with different lattice-spacing Si negative electrodes were investigated. To achieve a homogeneous distribution of impurities in the Si anodes, single crystalline Si wafers with As-dopant were ball-milled to form irregular and agglomerated micro-flakes with an average size of ~10 μm. The structural analysis proved that the As-doped Si negative materials retain the increased lattice constant, thus, keep the existence of the residual tensile stress of around 1.7 GPa compared with undoped Si anode. Electrochemical characterization showed that the As-doped Si anodes have lower discharge capacity, but Coulombic efficiency and capacity retention were improved in contrast with those of the undoped one. This improvement of electrochemical characteristics was attributed to the increased potential barrier on the side of Si anodes, inherited from the electronic and mechanical nature of Si materials doped with As. We believe that this study will guide us the way to optimize the electrochemical performances of LIBs with Si-based anodes.

Keywords: lithium-ion batteries, silicon, dopant, arsenic, discharge capacity, retention

OPEN ACCESS

Edited by:
Jianqing Zhao,
Soochow University, China

Reviewed by:
Yong Min Lee,
Daegu Gyeongbuk Institute of Science and Technology (DGIST), South Korea
Zhiqiang Xie,
University of Tennessee Space Institute (UTSI), United States

***Correspondence:**
Sung-Soo Kim
kimss@cnu.ac.kr

†These authors have contributed equally to this work

Specialty section:
This article was submitted to Electrochemistry, a section of the journal Frontiers in Chemistry

Received: *18 February 2019*
Accepted: *14 May 2019*
Published: *31 May 2019*

Citation:
Lee M, Yoon D, Lee UJ, Umirov N, Mukanova A, Bakenov Z and Kim S-S (2019) The Electrochemical Performances of n-Type Extended Lattice Spaced Si Negative Electrodes for Lithium-Ion Batteries. Front. Chem. 7:389. doi: 10.3389/fchem.2019.00389

INTRODUCTION

Lithium-ion batteries (LIBs) have been considered as an important energy storage device for modern portable electronics and electric vehicles (Goodenough and Park, 2013; Nitta et al., 2015; Kim et al., 2016). Until now, the graphite is typically used as anode material in commercial LIBs. However, its theoretical capacity (372 mAh g^{-1}) is not sufficient for the next-generation mobile applications requiring high energy density (Peng et al., 2010; Ma et al., 2014; Ko et al., 2015). To overcome the energy density problem of current LIBs, the use of Si as the anode in LIBs can be an alternative way due to its unique physical properties such as high theoretical capacity of 3,580 mAh g^{-1} ($Li_{15}Si_4$ state) and low discharge potential (<0.5 V vs. Li/Li^+) (Wang and Dahn, 2006; Liu et al., 2012; Shi et al., 2016). Even if the Si material has such good advantages for LIBs, the commercial success of LIBs with Si anodes has been impeded by fast capacity fading of Si anodes. This fading results from large volume change more than 300% of Si anodes during lithiation and delithiation, leading to their disintegration (Ryu et al., 2004; Kim et al., 2011). Furthermore, semiconductor characteristics of Si make it even more difficult to be utilized in the practical application of LIBs as

a negative electrode owing to the electrical losses due to large ohmic resistance (Wen and Tian, 2013; Wang et al., 2015).

Recently, various research groups have reported that the electrochemical performances of LIBs with Si anodes can be improved by using Si/Metal alloy electrode (Umirov et al., 2019a,b), the formation of nanostructured-anodes (Mukanova et al., 2018a,b), hollow and yolk-shell structured-composites (Yao et al., 2011; Wang et al., 2013), and doping of Si with impurities such as copper (Cu) (Wen and Tian, 2013), arsenic (As) (McSweeney et al., 2014), aluminum (Al) (Legrain and Manzhos, 2015), silver (Ag) (Talla et al., 2015), boron (B) (Long et al., 2011; Rousselot et al., 2012; Yi et al., 2013), nitrogen (N) (Han et al., 2016), and phosphorus (P) (Domi et al., 2016). Among other approaches, incorporating dopants into Si architectures has gained considerable attention as a suitable route for improving the rate capability, electrical conductivity, and capacity retention of the Si anodes (Mukanova et al., 2018b).

To date, many methods have been proposed for the Si powder preparation, including solution and solid-state based techniques, etc. Taking into account that the electronic/silicon-based semiconductor technologies have widely entered into society and industry, it is easy to imagine how much semiconductor class Si containing waste is produced every day. These silicon materials can be recycled for use in LIBs.

In this paper, we used the Si wafer in order to demonstrate the possibility of the Si electronic wastes to be reused in LIBs. As-modulated Si micro-flake anodes were investigated as an anode. To achieve a homogeneous distribution of As-impurity in the Si anodes, As-doped Si wafer was prepared by ball-milling and employed for the anode in a lithium cell. Moreover, this work covers the comparative analysis in the structural and electrochemical responses of As-doped and undoped Si microflake anodes to investigate the effects of the lattice spacing in Si anodes.

We believe that this paper will shed lights on the trends in the electrochemical performance [cycle retention, Coulombic efficiency (CE), and rate capability] of LIBs with the Si microflake anode with different lattice spacing.

EXPERIMENTAL

The commercial As-doped single crystalline (100) Si wafers with a doping concentration of 1×10^{19} cm^{-3} were provided by SK Hynix and used as the anode material for LIBs. The doping concentrations of Si wafer were confirmed by secondary ion mass spectrometry (SIMS) (not shown in this paper). Furthermore, the intrinsic (undoped) Si wafers were used as the control samples to compare the effects of As doping. To remove native oxide on Si surface, Si wafers were immersed in diluted 10% hydrofluoric acid solution for 3 min and followed by rinsing in deionized (DI) water of ultra-purity (resistance 18.2 MΩcm) for 5 min. Si wafers were mechanically grounded to achieve Si microflakes using zirconia balls for 2 h in paint shaker (KM-2000T, Nara Sci).

The undoped and As-doped Si based electrodes were fabricated via direct casting of slurry onto Cu foil using the Dr. Blade method. The slurry was prepared by thoroughly mixing of active material and PAI (Polyamide-Imide, Solvay Torlon 4000T) binder with the wt.% ratio of 9:1, respectively, in NMP (N-Methyl-2-pyrrolidone, Merck) solvent. After casting the electrodes were dried in convection oven at 110°C to remove NMP. The loading level of electrodes were adjusted to 5 mg/cm^2.

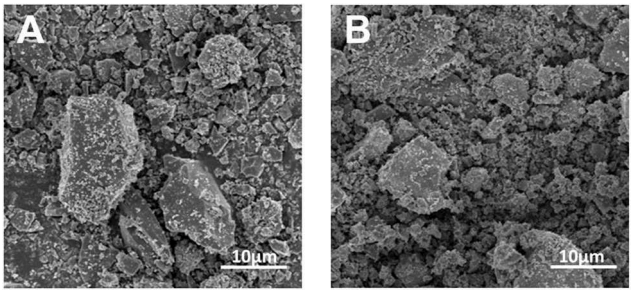

FIGURE 1 | Plan-view SEM image of **(A)** undoped and **(B)** As-doped Si powders after ball-milling.

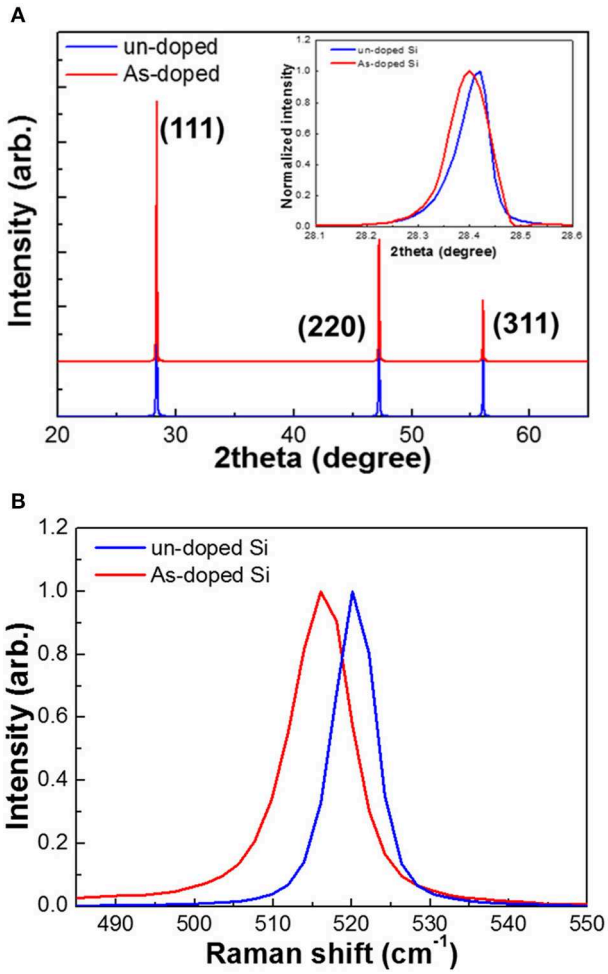

FIGURE 2 | (A) XRD patterns and **(B)** Raman spectra of undoped and As-doped Si anodes.

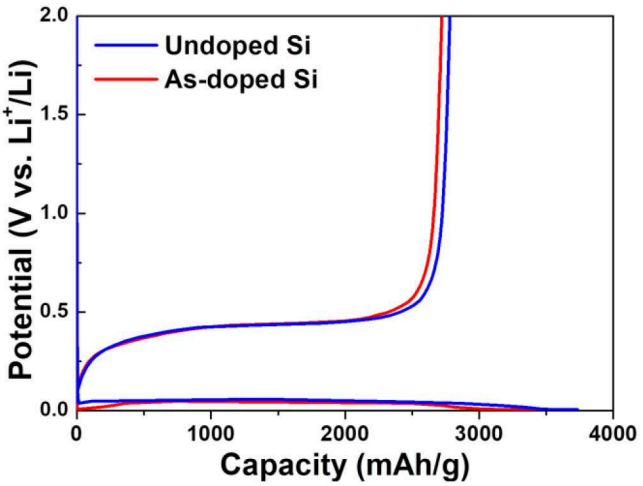

FIGURE 3 | Typical galvanostatic first charge-discharge curves of undoped and As-doped Si electrodes in the potential range from 0.005 to 2.000 V vs. Li/Li^+ at 1.0 A g^{-1}.

Electrochemical performances were studied using coin-type half configuration cells with Li metal as the counter electrodes, which were assembled in an Ar-filled glove box with <1 ppm of both oxygen and moisture. The electrolyte solution used was 1.3 M lithium hexafluoro phosphate ($LiPF_6$) dissolved in a solvent mixture of ethylene carbonate (EC) and diethyl carbonate (DEC) with a 3:7 volume ratio. Galvanostatic measurements were carried out to determine charge-discharge capacity and cycling retention in the potential range between 0.005 and 2.000 V vs. Li/Li^+ under a current density of 1.0 A g^{-1} (0.28 C) using a computer-controlled battery measurement system (TOSCAT 3000 U).

The surface morphologies of Si microflake anodes were evaluated by field emission scanning electron microscope (FE-SEM). The stress evolution, phase transition, and crystallinity of Si microflake anodes were investigated by micro Raman spectroscopy and X-ray diffraction (XRD).

RESULTS AND DISCUSSION

Figures 1A,B shows the plan-view SEM images of undoped and As-doped Si negative electrodes, respectively, after ball-milling for 2 h. The irregular and agglomerated particles were made up with the average size of 10 μm for both undoped and As-doped Si anodes. The particle size and distributions were measured by particle size analyzer (not shown in this paper). The similar morphology and size of micro particles of undoped and As-doped Si anodes were observed, indicating that As-dopants do not influence the morphology and particle size distribution of negative anodes.

Figure 2 exhibits XRD patterns and micro-Raman spectra of undoped and As-doped Si negative electrodes. The phase and crystallinity of Si anodes used in this work were investigated by XRD as shown in **Figure 2A**. It should be noted that all XRD peaks are sharp. This feature could be ascribed to the property of single crystalline Si. It is found that all the peak positions of XRD patterns can be indexed to those of cubic Si. It is interesting to note that the peak positions of As-doped Si anodes were shifted to the lower angles, which is attributed to the increased lattice

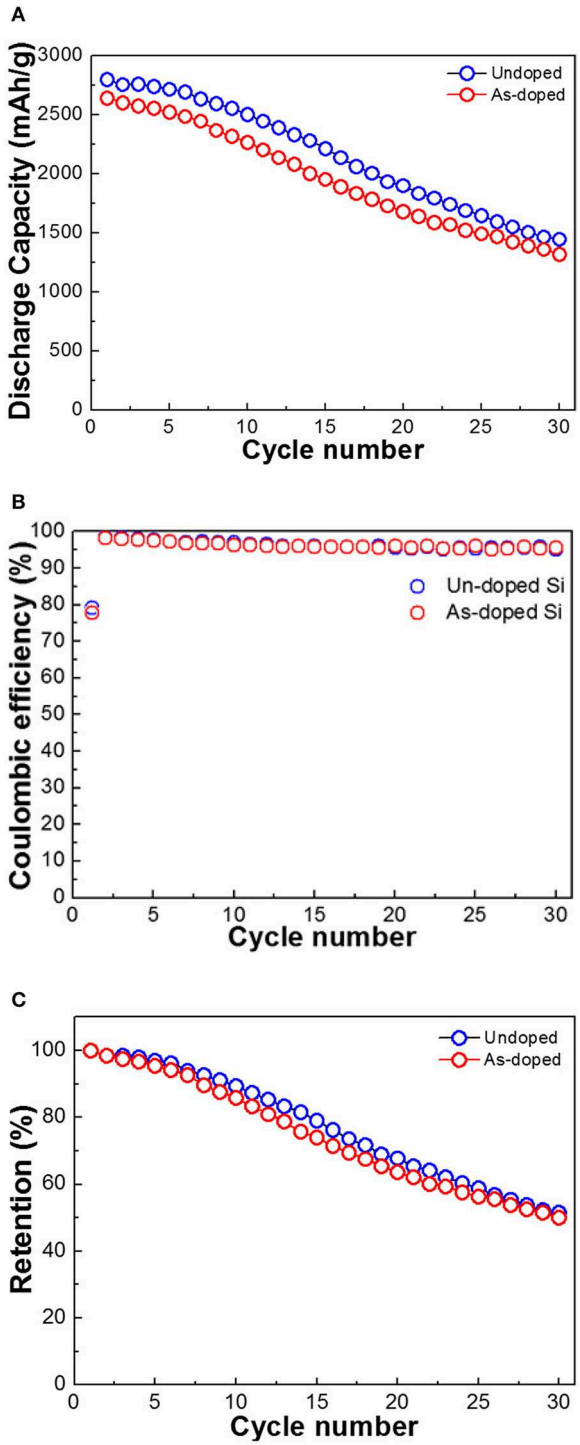

FIGURE 4 | Electrochemical performance of undoped and As-doped Si anodes: **(A)** cycle performance, **(B)** Coulombic efficiency, and **(C)** capacity retention of negative electrodes vs. Li/Li^+ at 1 A g^{-1}.

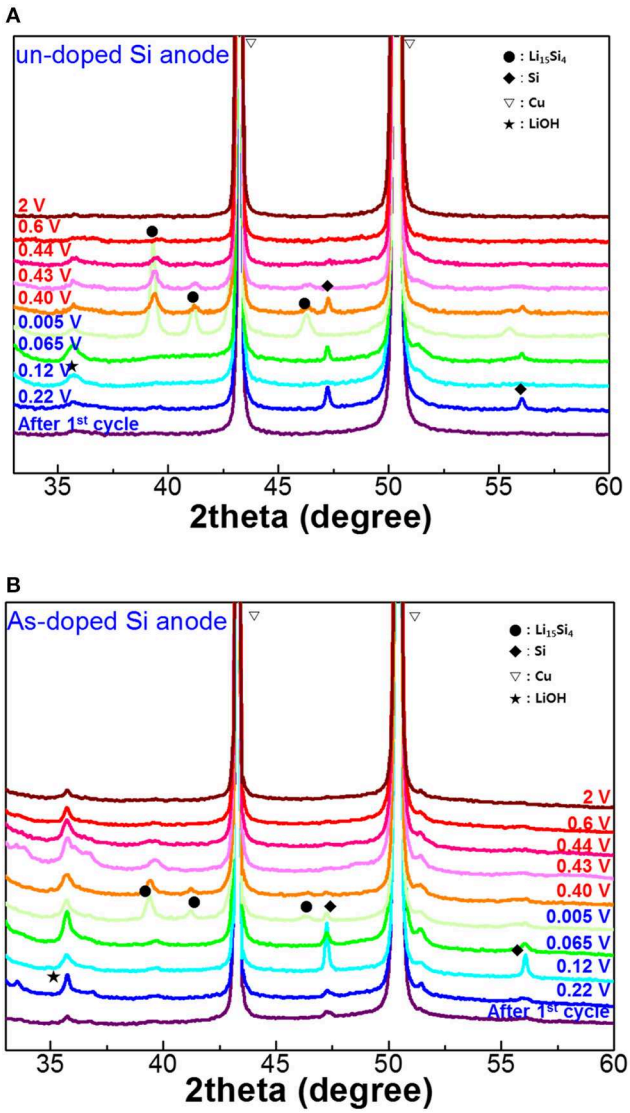

FIGURE 5 | XRD patterns of **(A)** undoped and **(B)** As-doped Si anodes after the first lithiation/delithiation as a function of discharge/charge cut-off voltages. The red letters represent discharge voltages, and the blue ones charge voltages.

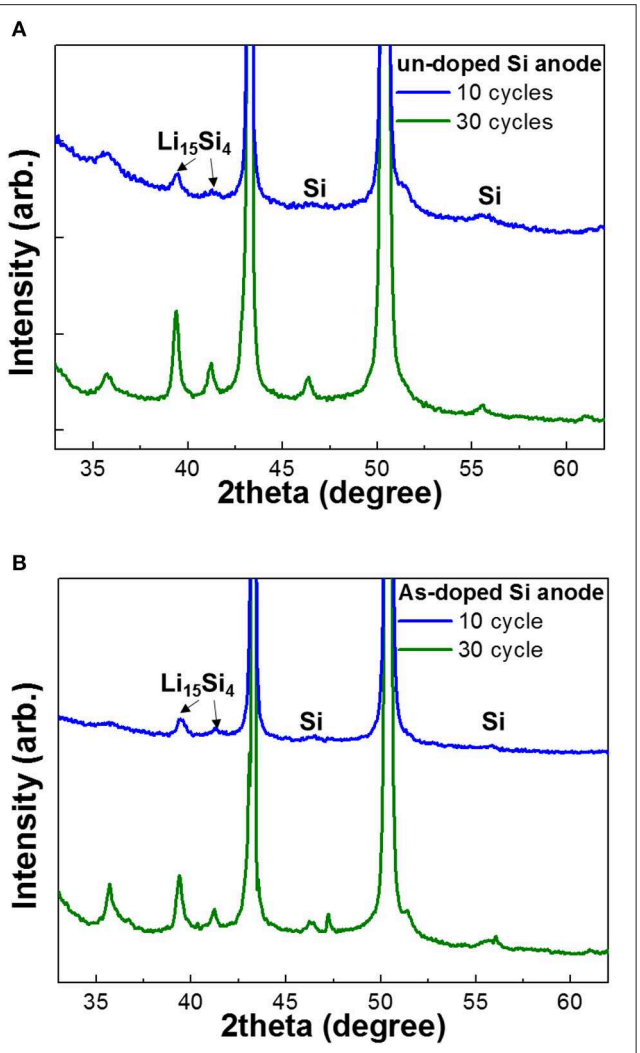

FIGURE 6 | XRD patterns of **(A)** undoped and **(B)** As-doped Si anodes vs. cycles.

constant by As-doping into Si structure as depicted in the inset of **Figure 2A**. Typical stress profiles of undoped and As-doped Si negative electrodes were studied by micro-Raman spectroscopy measurements at room temperature, as shown in **Figure 2B**. It is well-known that F_{2g}-phonon modes in crystalline Si can be identified with peaks at around 520 cm^{-1} (Shimizu et al., 2015). We can easily notice that the peak position for the As-doped Si anode has been red-shifted, indicating the residual tensile stress of approximately ∼1.7 GPa compared to the undoped one. The residual stress can be calculated using the following equation (Wu et al., 2007):

$$\sigma(\text{MPa}) = 434 \times \Delta\omega \quad (1)$$

where σ is the biaxial stress, Δω is the F_{2g} phonon peak shift. These data are in good agreement with the XRD results in **Figure 2A**.

In order to evaluate the electrochemical characteristics of Si negative electrodes with and without dopants, the various electrochemical examinations were performed. **Figure 3** illustrates the first charge and discharge behavior of undoped and As-doped Si thick film anodes. It is clearly seen that there are plateaus in the curves, which is attributed to lithiation and delithiation by the reactions of Si atoms with Li ions (Chevrier et al., 2010). The initial charge potential plateau is located near 0.1 V, which is in a good agreement with the formation of Li_xSi via lithiation of crystallized Si (Han et al., 2016). The first charge and discharge capacity for undoped and As-doped Si negative electrodes are 3,733, 2,782, 3,578, and 2,722 mAh g^{-1}, respectively. These values correspond to the initial CE of 74.5 and 76.1%, respectively.

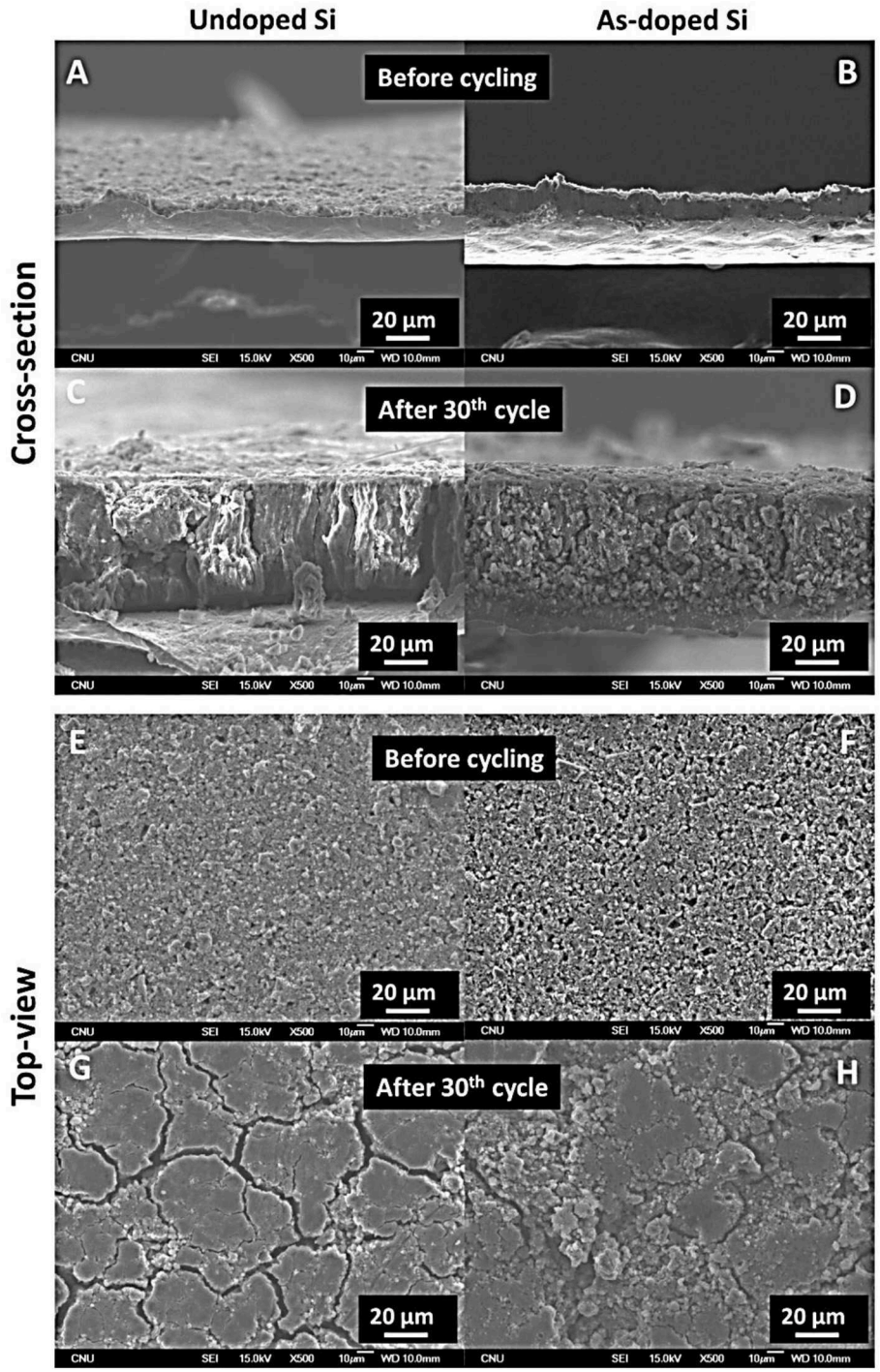

FIGURE 7 | Cross-section SEM micrographs of undoped and As-doped Si anodes **(A,B)** before and **(C,D)** after 30th cycle. Top-view SEM micrographs of undoped and As-doped Si anodes **(E,F)** before and **(G,H)** after 30th cycle.

Figure 4A illustrates the cycle performance of the cells with the undoped and As-doped Si negative electrodes. The discharge capacities of the LIBs with both types of the anodes were evaluated in a cut-off potential range of 0.005–2.000 V as seen in **Figure 3**. The discharge capacity of LIB with undoped Si negative electrode was higher than that of As-doped Si in all cycle ranges. One can easily observe that the discharge capacity fading of undoped Si anode is comparable with that of As-doped Si. Notably, a fading rate of discharge capacity with the undoped Si negative anode changed more sharply near 10 cycles. The

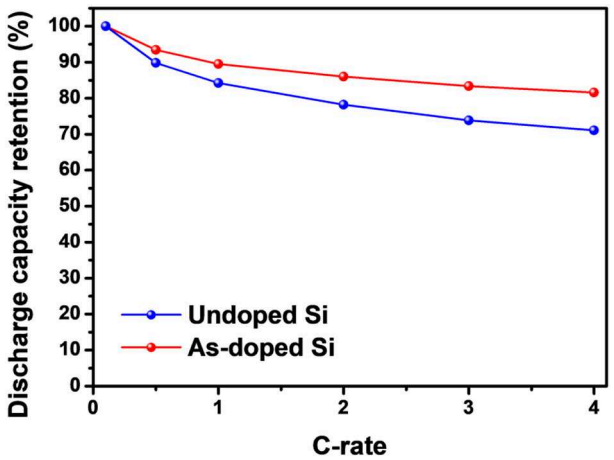

FIGURE 8 | Rate capability of undoped and As-doped Si electrodes from 0.1 to 4.0C (1C = 1.0 A/g).

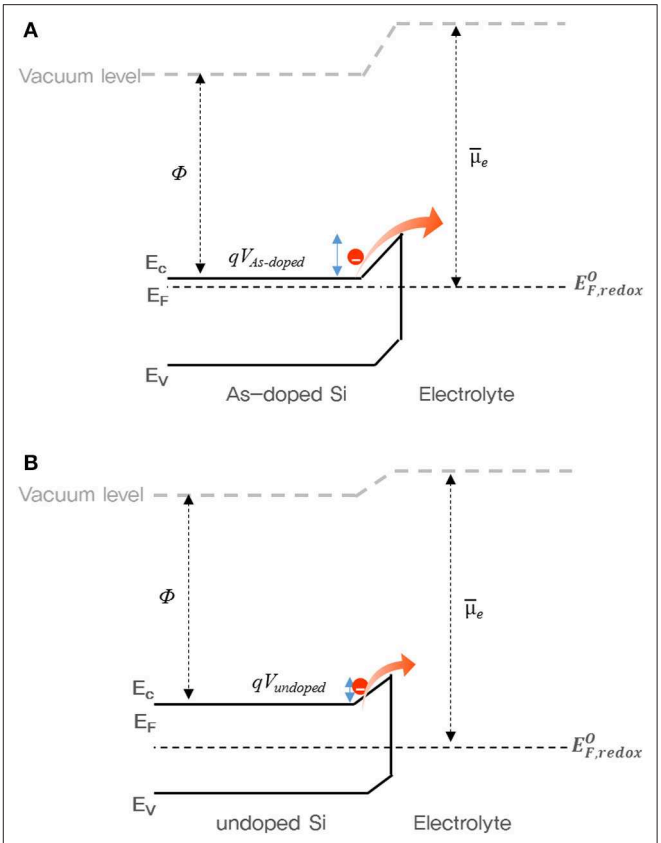

FIGURE 9 | Energy band diagram of cells with **(A)** As- and **(B)** undoped Si negative electrodes during charging state. E_C, E_V, E_F, $E_{F,redox}$, and u_e indicate the conduction band edge, valence band edge, Fermi level, redox fermi level of electrolyte, and electrochemical potential of the electrolyte.

initial discharge capacities of both anodes were decreased by approximately 50% after 30 cycles and their discharge capacities arrived at similar extent. **Figure 4B** shows the CE of both investigated materials. The subsequent cycle CE of cells with undoped and As-doped Si anodes start from 98.5 and 99.6% and further reaches over 95.0 and 95.8% after 30 cycles, respectively. In addition, the capacity retentions of both cells were measured as shown in **Figure 4C**. Despite the discharge capacity of undoped Si anode was higher than that with As-doped Si one, its capacity retention displays similar trends, corresponding to about 50% of retention. This phenomena can be explained by the fact that the As-doped Si anodes consumed more Li-ions for the generation of a solid-electrolyte interface (SEI) compared with the undoped Si anode and high energy barrier in energy band diagram, which will be mentioned later.

Figure 5 depicts 2theta X-ray rocking curves of the undoped and As-doped Si negative electrodes with various cut-off voltages (OCV) in charging/discharging states after the 1st cycle. After the formation process, there is no sign of the $Li_{15}Si_4$ phase presence in XRD curves for undoped and As-doped Si anodes. Besides, XRD patterns of both undoped and As-doped Si anodes discharged up to a potential of 0.005 V clearly revealed the presence of the peaks at 39° and 41°, indicating the formation of $Li_{15}Si_4$ silicate (Li and Dahn, 2007). It is essential to note that the intensity of XRD patterns of undoped Si negative electrodes was much higher than that of As-doped Si one. This implies that the phase transition of undoped Si anodes into $Li_{15}Si_4$ phase is easier to occur compared to the doped electrode. In the discharging states, the peak intensity of $Li_{15}Si_4$ reduced steadily with increasing the OCV, and finally disappeared at OCV of 2 V for undoped and As-doped Si anodes.

In order to estimate the phase transition of undoped and As-doped Si anodes, we performed XRD analysis as a function of cycle number as illustrated in **Figure 6**. No Li silicide peaks were found in the XRD spectra of the samples before cycling (not shown in this paper). The $Li_{15}Si_4$ phase peaks in XRD curves after 10 and 30 cycles were easily confirmed as seen in **Figures 6A,B**. Indeed, the XRD intensity of $Li_{15}Si_4$ phase in undoped Si anode is much higher than that in As-doped Si, which is consistent with the results obtained in **Figure 5**. In addition, the gradual increase of $Li_{15}Si_4$ phase upon 30 cycles is assigned to the activation process of Li-ion pathway in the electrode-electrolyte system, despite the fact that activation was accompanied by the fast capacity fading of both electrodes as observed in galvanostatic cycling.

Furthermore, we investigated the morphology of the electrodes at their cross-section and surface before and after 30 cycles using SEM imaging. Cross-sectional SEM images of undoped and As-doped Si (**Figures 7A,B**) showed that both electrodes have the thickness of approximately 20 μm before cycling, while after 30 cycles, thickness increased drastically (>200%) that can be observed in **Figures 7C,D**. Besides, both samples exhibited similar changes in volume expansion. From the top-view images of undoped Si vs. As-doped Si (**Figures 7E–H**), one can see that the morphology of electrodes looked the same before and after cycling. The extensive formation of cracks and partial pulverization of active electrode material after 30 cycles was observed in both cases shown in **Figures 7G,H**. Accordingly, SEM results

supported the capacity fading phenomena revealed by the galvanostatic tests earlier for the undoped and As-doped Si anodes.

Figure 8 compares the discharge capacity retentions of undoped and As-doped Si electrodes at various current densities from 0.1 to 4.0 C (1C = 1.0 A/g), respectively. Here, undoped Si exhibits considerable fading in discharge capacity at higher current densities compare with As-doped Si. More specifically, at the highest current density of 4.0 C, the undoped Si-based electrode shows 69% in capacity retention vs. 0.1 C. By contrast, the As-doped Si demonstrates better rate performance with ∼80% capacity retention. Obvious improvement in rate capability can be ascribed to the As-doping effect in Si structure and will be further discussed with the electronic energy band diagram.

To understand the charge/discharge characteristics of undoped and As-doped Si negative electrodes, we took the electronic energy band diagram of both Si anode-electrolyte interfaces into consideration as illustrated in **Figure 9**. It is well-known that when the semiconductor-electrolyte interface is formed, electrolyte and semiconductor reach electrochemical equilibrium by matching their electrochemical potentials. This occurs by charge transfer between both media (Prados et al., 2014). Considering this, each barrier heights of undoped and As-doped Si anodes are represented in **Figures 9A,B**, respectively. It is noteworthy to mention that the energy barrier height from As-doped Si anode side, $qV_{As-doped}$, was found to be higher than $qV_{undoped}$ of undoped Si anode after equilibrium state. Hence, the flux of electrons across the electrolyte in As-doped Si with the increased potential barrier height can be impeded, thus hindering charge flow in the cell. In previously published works, the addition of dopants such as B and P decreased the lattice spacing of Si anodes and led to the increase of the insertion energy of Li ions, thus suppressing the discharging and charging capacity in LIBs (Long et al., 2011; Domi et al., 2016). However, the charging/discharging capacities of As-doped Si anodes have a different aspect, apart from volume change. To understand the electrochemical behaviors of cells with As-doped Si anodes, the energy band diagrams were illustrated, as shownv in **Figure 9**. It was found that the potential barrier of cells with As-dopant is much higher than that of undoped Si anode. We can infer that the higher potential barrier on the anode side by highly n-type doping results in the reduced charging/discharging capacity of As-doped Si anodes, compared to that of undoped Si ones. This is in a fair agreement with the results of **Figures 5**, **6**. Moreover, we consider that slightly higher CE of As-doped Si negative electrode is related to the potential barrier. A lower charge/discharge capacity leads to the suppression of the phase transition from c-Si to a-Si, which may result in the improved CE, corresponding to the XRD results.

CONCLUSION

In summary, the electrochemical performance of the cells with As-doped Si negative electrodes was investigated. The ball-milling of single-crystalline Si wafers was used to fabricate the anodes, which particles were irregular and agglomerated micro-flakes. The XRD and Raman analysis revealed that As-doped Si anodes have larger lattice spacing compared to undoped Si samples, indicating the residual tensile stress of approximately ∼1.7 GPa. Despite the increased lattice spacing in As-doped Si anode, its charge/discharge capacity was lower compared with that of undoped Si anodes. The Coulombic efficiency and cyclic retention of As-doped Si negative electrodes, however, were comparable to those of the undoped Si anode. This effect was attributed to the increased potential barrier height on the side of As-doped Si, affecting the electrochemical performance of LIBs with the As-doped anode. We believe that this study will provide an effective approach to achieve the enhanced electrochemical performances of LIBs with Si-based anode derived from electronic waste materials.

DATA AVAILABILITY

The datasets generated for this study are available on request to the corresponding author.

AUTHOR CONTRIBUTIONS

ML and DY conceived design of the study and carried out the experiment; UL, ZB, and S-SK contributed to the interpretation of the results; NU, AM, ZB, and S-SK wrote sections of the manuscript. All authors contributed to manuscript revision, read and approved the submitted version.

ACKNOWLEDGMENTS

The authors acknowledge the financial support of the KETEP (Grant No.20164010201070) and the Nazarbayev University by the research grant No.110119FD4504 Development of 3D all solid-state thin film Li-ion microbatteries.

REFERENCES

Chevrier, V., Zwanziger, J., and Dahn, J. (2010). First principles study of Li–Si crystalline phases: charge transfer. Electronic structure, and lattice vibrations. *J. Alloys Compounds* 496, 25–36. doi: 10.1016/j.jallcom.2010.01.142

Domi, Y., Usui, H., Shimizu, M., Kakimoto, Y., and Sakaguchi, H. (2016). Effect of phosphorus-doping on electrochemical performance of silicon negative electrodes in lithium-ion batteries. *ACS Appl. Mater. Interfaces* 8, 7125–7132. doi: 10.1021/acsami.6b00386

Goodenough, J. B., and Park, K. -S. (2013). The Li-ion rechargeable battery: a perspective. *J. Am. Chem. Soc.* 135, 1167–1176. doi: 10.1021/ja3091438

Han, Y., Lin, N., Qian, Y., Zhou, J., Tian, J., Zhu, Y., et al. (2016). A scalable synthesis of N-doped Si nanoparticles for high-performance Li-ion batteries. *Chem. Commun.* 52, 3813–3816. doi: 10.1039/C6CC00253F

Kim, A., Park, E., Lee, H., and Kim, H. (2016). Highly reversible insertion of lithium into MoO2 as an anode material for lithium ion battery. *J. Alloys Compd.* 681, 301–306. doi: 10.1016/j.jallcom.2016.04.188

Kim, H., Chou, C.-Y., Ekerdt, J. G., and Hwang, G. S. (2011). Structure and properties of Li– Si alloys: a first-principles study. *J. Phys. Chem. C*. 115, 2514–2521. doi: 10.1021/jp1083899

Ko, M., Chae, S., and Cho, J. (2015). Challenges in accommodating volume change of Si anodes for Li-ion batteries. *Chem. Electro. Chem*. 2, 1645–1651. doi: 10.1002/celc.201500254

Legrain, F., and Manzhos, S. (2015). Aluminum doping improves the energetics of lithium. sodium, and magnesium storage in silicon: A first-principles study. *J. Power Sourc*. 274, 65–70. doi: 10.1016/j.jpowsour.2014.10.037

Li, J., and Dahn, J. (2007). An in situ X-ray diffraction study of the reaction of Li with crystalline Si. *J. Electrochem. Soc*. 154, A156–A161. doi: 10.1149/1.2409862

Liu, X. H., Zhong, L., Huang, S., Mao, S. X., Zhu, T., and Huang, J. Y. (2012). Size-dependent fracture of silicon nanoparticles during lithiation. *ACS Nano*. 6, 1522–1531. doi: 10.1021/nn204476h

Long, B. R., Chan, M. K., Greeley, J. P., and Gewirth, A. A. (2011). Dopant modulated Li insertion in Si for battery anodes: theory and experiment. *J Phys Chem C*. 115, 18916–18921. doi: 10.1021/jp2060602

Ma, D., Cao, Z., and Hu, A. (2014). Si-based anode materials for Li-ion batteries: a mini review. *Nano Micro Lett*. 6, 347–358. doi: 10.1007/s40820-014-0008-2

McSweeney, W., Lotty, O., Glynn, C., Geaney, H., Holmes, J. D., and O'Dwyer, C. (2014). The influence of carrier density and doping type on lithium insertion and extraction processes at silicon surfaces. *Electrochim. Acta* 135, 356–367. doi: 10.1016/j.electacta.2014.05.035

Mukanova, A., Jetybayeva, A., Myung, S. -T., Kim, S., and Bakenov, Z. (2018b). A mini-review on the development of Si-based thin film anodes for Li-ion batteries. *Mater Today Energy* 9, 49–66. doi: 10.1016/j.mtener.2018.05.004

Mukanova, A., Nurpeissova, A., Kim, S. -S., and Myronov, M., Bakenov, Z. (2018a). N-type doped silicon thin film on porous Cu current collector as a negative electrode for Li-ion batteries. *ChemistryOpen*. 7, 92–96 doi: 10.1002/open.201700162

Nitta, N., Wu, F., Lee, J. T., and Yushin, G. (2015). Li-ion battery materials: present and future. *Mater Today* 18, 252–264. doi: 10.1016/j.mattod.2014.10.040

Peng, B., Cheng, F., Tao, Z., and Chen, J. (2010). Lithium transport at silicon thin film: barrier for high-rate capability anode. *J. Chem. Phys.* 133:034701. doi: 10.1063/1.3462998

Prados, A., Ranchal, R., and Pérez, L. (2014). Blocking effect in the electrodeposition of Bi on n-GaAs in acidic electrolytes. *Electrochim. Acta* 143, 23–28. doi: 10.1016/j.electacta.2014.07.137

Rousselot, S., Gauthier, M., Mazouzi, D., Lestriez, B., Guyomard, D., and Roué, L. (2012). Synthesis of boron-doped Si particles by ball milling and application in Li-ion batteries. *J. Power Sources*. 202, 262–268. doi: 10.1016/j.jpowsour.2011.11.045

Ryu, J. H., Kim, J. W., and Sung, Y. -E., Oh, S. M. (2004). Failure modes of silicon powder negative electrode in lithium secondary batteries. *Electrochem Solid State Lett*. 7, A306–A309. doi: 10.1149/1.1792242

Shi, F., Song, Z., Ross, P. N., Somorjai, G. A., Ritchie, R. O., and Komvopoulos, K. (2016). Failure mechanisms of single-crystal silicon electrodes in lithium-ion batteries. *Nat. Commun.* 7:11886. doi: 10.1038/ncomms11886

Shimizu, M., Usui, H., Suzumura, T., and Sakaguchi, H. (2015). Analysis of the deterioration mechanism of Si electrode as a Li-ion battery anode using Raman microspectroscopy. *J. Phys. Chem. C*. 119, 2975–2982. doi: 10.1021/jp5121965

Talla, G., Guduru, R. K., Li, B. Q., and Mohanty, P. S. (2015). Doped-Si–Ag composite electrodes for Li-ion batteries. *Solid State Ionics* 269, 8–13. doi: 10.1016/j.ssi.2014.09.021

Umirov, N., Seo, D. H., Jung, K. N., Kim, H. Y., and Kim, S. S. (2019b). Ni added Si-Al Alloys with Enhanced Li^+ Storage Performance for Lithium-Ion Batteries. *J. Electrochem. Sci. Technol*. 10, 82–88. doi: 10.5229/JECST.2019.10.1.82

Umirov, N., Seo, D. H., Kim, T., Kim, H. Y., and Kim, S. S. (2019a). Microstructure and electrochemical properties of rapidly solidified Si–Ni alloys as anode for lithium-ion batteries. *J. Industr. Eng. Chem.* 71, 351–360. doi: 10.1016/j.jiec.2018.11.046

Wang, B., Li, X., Zhang, X., Luo, B., Zhang, Y., and Zhi, L. (2013). Contact-engineered and void-involved silicon/carbon nanohybrids as lithium-ion-battery anodes. *Adv Mater*. 25, 3560–3565. doi: 10.1002/adma.201300844

Wang, J., Meng, X., Fan, X., Zhang, W., Zhang, H., and Wang, C. (2015). Scalable synthesis of defect abundant Si nanorods for high-performance Li-ion battery anodes. *ACS nano*. 9, 6576–6586. doi: 10.1021/acsnano.5b02565

Wang, Y., and Dahn, J. (2006). Comparison of the reaction of Li x Si or Li0. 81C6 with 1 M LiPF6 EC: DEC electrolyte at high temperature. *Electrochem Solid State Lett.* 9:A340–3. doi: 10.1149/1.2200137

Wen, Z., and Tian, F. (2013). Cu-doped silicon film as anode for lithium ion batteries prepared by ion-beam sputtering. *Int. J. Electrochem. Sci*. 8, 10129–10137.

Wu, X., Yu, J., Ren, T., and Liu, L. (2007). Micro-Raman spectroscopy measurement of stress *in silicon*. *Microelectr. J.* 38, 87–90. doi: 10.1016/j.mejo.2006.09.007

Yao, Y., McDowell, M. T., Ryu, I., Wu, H., Liu, N., Hu, L., et al. (2011). Interconnected silicon hollow nanospheres for lithium-ion battery anodes with long cycle life. *Nano Lett.* 11, 2949–2954. doi: 10.1021/nl201470j

Yi, R., Zai, J., Dai, F., Gordin, M. L., and Wang, D. (2013). Improved rate capability of Si–C composite anodes by boron doping for lithium-ion batteries. *Electrochem. commun.* 36, 29–32. doi: 10.1016/j.elecom.2013.09.004

Conflict of Interest Statement: The authors declare that the research was conducted in the absence of any commercial or financial relationships that could be construed as a potential conflict of interest.

frontiers in Chemistry

ORIGINAL RESEARCH
published: 31 May 2019
doi: 10.3389/fchem.2019.00388

High-Performance Solid Composite Polymer Electrolyte for all Solid-State Lithium Battery Through Facile Microstructure Regulation

Jingjing Yang[1†], Xun Wang[1], Gai Zhang[1], Aijie Ma[1], Weixing Chen[1], Le Shao[2*†], Chao Shen[3] and Keyu Xie[3*]*

[1] School of Materials and Chemical Engineering, Xi'an Technological University, Xi'an, China, [2] Shaanxi Coal Chemical Industry Technology Research Institute Co. Ltd., Xi'an, China, [3] State Key Laboratory of Solidification Processing, School of Materials Science and Engineering, Center for Nano Energy Materials, Northwestern Polytechnical University and Shaanxi Joint Laboratory of Graphene (NPU), Xi'an, China

OPEN ACCESS

Edited by:
Jianqing Zhao,
Soochow University, China

Reviewed by:
Wangwang Xu,
Louisiana State University, United States
Xiaowei Wang,
National University of Singapore, Singapore

***Correspondence:**
Jingjing Yang
yangjingjing@xatu.edu.cn
Le Shao
shaole@sxccti.com
Keyu Xie
kyxie@nwpu.edu.cn

[†] These authors have contributed equally to this work

Specialty section:
This article was submitted to Electrochemistry, a section of the journal Frontiers in Chemistry

Received: 27 March 2019
Accepted: 14 May 2019
Published: 31 May 2019

Citation:
Yang J, Wang X, Zhang G, Ma A, Chen W, Shao L, Shen C and Xie K (2019) High-Performance Solid Composite Polymer Electrolyte for all Solid-State Lithium Battery Through Facile Microstructure Regulation. Front. Chem. 7:388. doi: 10.3389/fchem.2019.00388

Solid composite polymer electrolytes are the optimal candidate for all solid-state lithium batteries, because of their enhanced ionic conductivities, long-life cycle ability and compatibility to lithium anode. Herein, we reported a kind of solid composite polymer electrolyte comprised of poly(ethylene oxide), graphitic-like carbon nitride and lithium perchlorate, which was prepared by a facile solution blending method. Microstructure of the solid composite polymer electrolyte was regulated by thermal annealing and interaction among components and was characterized by XRD, DSC, FTIR-ATR, and ROM. The obtained solid composite polymer electrolyte achieved an ionic conductivity as high as 1.76 $\times 10^{-5}$ S cm^{-1} at 25°C. And the electrochemical stable window and the lithium ion transference number, t_+, were also obviously enhanced. $LiFePO_4$/Li solid-state batteries with the annealed PEO-$LiClO_4$-g-C_3N_4 solid polymer electrolyte presented a high initial discharge capacity of 161.2 mAh g^{-1} and superior cycle stability with a capacity retention ratio of 81% after 200 cycles at 1C at 80°C. The above results indicates that the thermal annealing treatment and g-C_3N_4 as a novel structure modifier is crucial for obtaining the high-performance solid composite polymer electrolytes used in the all solid-state lithium battery.

Keywords: all solid-state lithium battery, solid composite polymer electrolyte, microstructure, graphite-like carbonitride, electrochemical property

INTRODUCTION

During recent years, high-energy-density storage batteries are urgently needed to satisfy the increasing demand in electric vehicles, consumer electronics and grid energy storage (Manthiram et al., 2017; Fan et al., 2018). Lithium metal secondary batteries have been considered as the potential candidate for high-energy-density storage batteries, since lithium metal anode possessed the highest theoretical specific capacity (3,862 mAh g^{-1}) and the lowest reduction potential (−3.04V VS. standard hydrogen electrode) (Shen et al., 2018; Wu et al., 2018). Moreover, lithium metal used as the anode can even act as the lithium source in the battery with non-lithiated materials such as sulfur or oxygen as the cathode to achieve higher storage capacity compared to the current

commercial lithium-ion batteries (Pan et al., 2019). However, practical and large-scale development of lithium metal batteries with liquid electrolytes is limited by safety concerns and the rapid capacity attenuation and short cycling capability (Fan et al., 2018). During the charge-discharge process of lithium metal secondary batteries with organic liquid electrolytes, the propensity of faster lithium dendrites formation was resulted from the plating and stripping of Li ions on the anode, which would result in the capacity attenuation and poor cycling capability and short-circuit of cells.

In order to further develop the practical use of lithium metal as anode, scientists made great efforts to solve the lithium dendrites problems and achieved much progress on suppressing dendrite formation and growth (Li D. et al., 2018; Nie et al., 2018; Shen et al., 2018; Wu et al., 2018; Pan et al., 2019). Strategies such as electrolyte modification, multifunctional barriers, composite metallic lithium electrode, and 3D current collectors were proposed to suppress the formation of Lithium dendrites (Wu et al., 2018; Xiao et al., 2018). Replacement of current organic liquid electrolytes with the solid-state electrolytes is considered as the most promising way to realize excellent performance of lithium metal secondary batteries (Goodenough, 2018; Nie et al., 2018). Because the organic liquid electrolyte is flammable, toxic and environmental contamination, solid-state electrolytes are therefore of crucial importance because of their excellent safety and mechanical ability for dendritic growth inhibition (Ban et al., 2018). And all solid-state lithium metal batteries are widely regarded as promising candidates for next generation of energy storage devices with improved energy density and superior safety performances.

Solid-state electrolytes are generally divided into inorganic superionic conductors (or the solid ceramic electrolytes) and solid polymer electrolytes. Compared with the inorganic superionic conductors, solid polymer electrolytes, benefiting from shape versatility, flexibility, light weight and low processing costs, are being investigated as promising candidates to replace currently available organic liquid electrolytes in lithium metal batteries (Bae et al., 2018b), (Zhang X. et al., 2018). However, due to the inherent low ionic conductivity at RT and poor mechanical property of solid polymer electrolytes, polymer-based solid composite electrolytes taking advantage of the merits of both inorganic and polymeric materials have been attracting more and more attention in all solid-state lithium metal battery applications (Tan et al., 2018). And Poly(ethylene oxide) (PEO) based solid composite electrolytes were widely considered as promising candidates solid electrolytes for high energy density lithium metal batteries (Xue et al., 2015; Tan et al., 2018). Numerous fillers were added into the PEO-based composite solid electrolyte to improve the ionic conductivity and the interfacial properties in contact with the electrodes (Tan et al., 2018). And it was the simplest method to achieve the composite polymer electrolyte, whose physical properties can be easily controlled by compositional change (Tan et al., 2018; Xiao et al., 2018; Zhang J. et al., 2018). However, the particle agglomeration especially at high concentration of fillers would inhibit the further improvement of properties of the solid polymer electrolyte. New kind of effective filler or percolated nanofiller structure needs to be developed by researchers.

Graphitic-like carbon nitride (g-C_3N_4) is a stacked 2D structure, which was mainly composed of carbon, nitrogen and a few residual $-NH_2$ or –NH groups, and was metal-free and lightweight (Wang et al., 2012; Shi et al., 2014). And its intrinsic polarity and semiconductor property may be helpful to modulate the spatial and interface distribution of ionic charge carriers (Hu et al., 2017). These properties make g-C_3N_4 a potential candidate as polymer electrolyte filler for all-in-solid lithium batteries. Shi et al. proved that the introduction of 6.0 wt% g-C_3N_4 nanosheets in the sodium alginate (SA) nanocomposite films could greatly enhance the thermal stability and mechanical properties of SA biopolymer electrolyte nanocomposite films (Shi et al., 2014). Hu et al. reported about a kind of composite electrolyte with bis(triffuoromethanesulfonimide) lithium salt (LiTFSI), di(ethylene glycol) dimethyl ether (DGM) and g-C_3N_4, which was used to suppress lithium dendrite growth during cycling and improve the long-term cycling property of the composite electrolyte (Hu et al., 2017). But quantitative and even qualitative descriptions of the interactions between separate components of the state electrolyte system are still lacking. Understanding of the different interactions in the system and its influence on the microstructure and final electrochemical properties of the solid composite polymer electrolyte is crucial for achieving high performance solid polymer electrolyte.

In this article, we present for the very first time, to the best of our knowledge, the addition of g-C_3N_4 as fillers in PEO and its influence on the lithium ionic dissociation in lithium perchlorate ($LiClO_4$) and transport and the crystallization of PEO in solid composite polymer electrolytes. Thermal annealing treatment and the interactions regulation among components by addition of g-C_3N_4 were introduced to tailor the microstructure of the solid composite polymer electrolyte. And through controlling the microstructure of solid composite polymer electrolytes, excellent improvement of the desired physical and chemical properties and electrochemical properties was achieved. When the weight percent of g-C_3N_4 was 10%, the annealed solid composite polymer electrolyte gave the best performance in the all solid-state lithium battery with lithium metal as the anode and $LiFePO_4$ as the cathode.

EXPERIMENTAL SECTION

Materials

Poly(ethylene oxide) (Mw $= 6 \times 10^5$, Alfa Aesar), lithium perchlorate ($LiClO_4$, Aladdin, battery grade), poly(vinylidene fluoride) (PVDF, Solef® 5130, Solvay), and $LiFePO_4$ (DY-3, Shenzhen Dynanonic Co., Ltd) were commercially obtained and were dried before usage. Acetonitrile (ACN, Aladdin, AR), N-methly-2-pyrrolidone (NMP, AR), and urea (Aladdin, AR) were used as obtained. The Li metal used in our experiments was commercially obtained with a diameter of 15.8 and 0.6 mm of thickness.

Preparation of g-C_3N_4

The g-C_3N_4 filler was synthesized by thermal polymerization as we reported in the previous article (Wang et al., 2019). Twenty gram of urea was put into a crucible with a cover in the muffle furnace. And then the crucible was heated to 580°C to stay for 4 h, with a heating rate of 3°C/min. And the powder product was in light yellow color. The detailed characterization of pure g-C_3N_4 was displayed in **Figures S1**, **S3**.

Solid Composite Polymer Electrolyte Films Preparation

Firstly, the prepared g-C_3N_4 filler was ultrasonic dispersed in ACN. Then PEO and $LiClO_4$ (molar ratio of ethylene oxide (EO) to $LiClO_4$ is 15:1) were added into the solution under stirring, in order to obtain uniform mixture solution. The weight percentage of g-C_3N_4 compared to PEO was controlled as 0, 5, 10, 15, and 20%, respectively. The mixture solution was casted into a home-made Teflon mold and dried in the vacuum oven at 40°C for 48 h. And the above mentioned state polymer electrolytes films were firstly annealed at 120°C for 2 h and then quenched to RT before use. In contrast, the state polymer electrolyte films were also prepared without thermal annealing process. The thickness of obtained solid state polymer electrolyte films was regulated to about 100 μm. And the state polymer electrolytes films were cut into rounds with diameter of 19 mm before loaded into the glovebox.

Characterization

Bruker Vertex 70 FTIR spectrometer with Access ATR^{TM} attachment was used to characterize the composition of samples. The melting temperature of PEO in samples was collected by a differential scanning calorimeter (DSC, Mettler DSC823e) under nitrogen atmosphere. Samples with a mass of 5∼10 mg were sealed into aluminum crucible, and then heated at a rate of 10°C/min. X-ray powder diffraction (XRD) patterns were collected by a XRD-6000 (Shimazu, Japan) X-Ray diffractometer equipped with Cu K_α radiation in the range of 5∼50° at a scanning rate of 4°/min. The reflection optical microscopy (ROM) observations were performed with a Leica DM2500P optical microscope equipped with a C-5050ZOOM camera.

The ionic conductivity of SPEs was measured by electrochemical impedance spectroscopy (EIS) by using a Princeton PARSTAT 4000A (AMETEK) electrochemical workstation over frequency range from 1 to 10^5 Hz with an applied voltage of 10 mV. The measured SPEs were sandwiched between two stainless steel electrodes, which were assembled into CR2025 coin cells. And the temperature was controlled by an oven in the range of 25∼120°C. The electrochemical stability window was determined by linear sweep voltammetry (LSV) by a Princeton PARSTAT 4000A (AMETEK) electrochemical workstation. The cell was assembled by sandwiching SPEs between a stainless steel and lithium metal (SS/SPE/Li) as the counter and reference electrode, respectively. And the measurement was cycled from 2.0 to 6.0 V (VS. Li/Li^+) at a scan rate of 10 mV/S. The lithium transference number (t_+) was tested in a symmetric cell (Li/SPE/Li) by chronoamperometry combined with electrochemical impedance spectroscopy according to the method provided by Bruce et al. (Evans et al., 1987). In order to characterize the battery performances, the prepared state polymer electrolytes were fabricated as CR2025 coin-type cells with lithium metal anode and $LiFePO_4$ cathode. And $LiFePO_4$ was blended with carbon black (Super-P) and

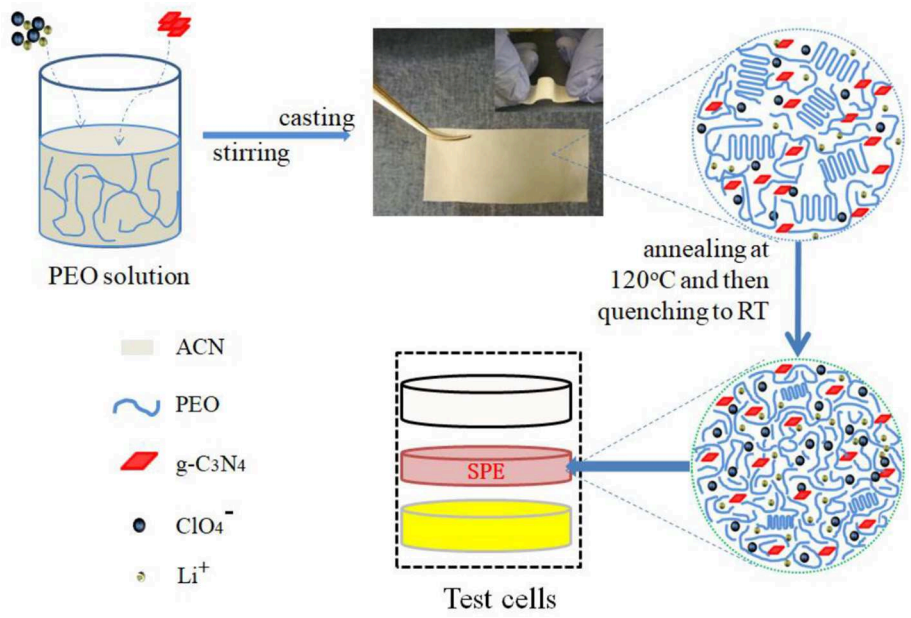

FIGURE 1 | The flowchart of the preparation of the PEO-$LiClO_4$-g-C_3N_4 solid composite polymer electrolyte film. Also the illustration of the microstructure was shown in the enlarged diagrams and the package method of test cells was shown.

poly(vinylidene fluoride) at a weight ratio of 8:1:1 with NMP as the solvent. The weight of cathode used in the test was controlled to about 2.40 mg. As a result, the weight of active material was about 1.92 mg. The battery performances of coin cells were examined at 80°C using a Battery Testing System (NEWARE CT-4008, Shenzhen, China), including cycle property and C-rate capability (0.1, 0.2, 0.5, 1, 2, and 5C). The cut-off voltages were chosen as 4.2 V (charge) and 2.5 V (discharge) during the charge-discharge cycle performance.

RESULTS AND DISCUSSION

Microstructure Regulation by Thermal Annealing and Interaction Among Components in Solid Composite Polymer Electrolytes

In order to avoid the effect of thermal history on the crystallization of PEO during the solid composite polymer electrolyte preparation process to an extreme, 120°C annealing and then quenching method was introduced, as shown in **Figure 1**. And we have reported on this preparation method in detail in a previous work (Wang et al., 2019). During the solid polymer electrolyte preparation process, samples were firstly dried at 40°C for 48 h, which would provide an isothermal crystallization condition for PEO. As a result, the crystallinity of PEO in the samples was high. However, when the sample was quenching from the amorphous state, the non-isothermal crystallization might happened, which gave a lower crystallinity of PEO in the sample. And this deduction was further proved by the following XRD and DSC results.

In order to clarify the influence of thermal annealing and the interaction among components of the solid composite polymer electrolyte on the microstructure of solid composite polymer electrolytes, XRD was used to characterize the crystallization of samples as shown in **Figure 2**. As shown in **Figure 2A**a, pure g-C_3N_4 gave a typical diffraction peak at 27.5°, which was the typical peak of (002) crystal plane of g-C_3N_4. Moreover, the interlamellar spacing of g-C_3N_4 was calculated as about 0.32 nm by Bragg equation. On the other hand, XRD patterns of the solid composite polymer electrolyte samples shown in **Figures 2A**b,c displayed three typical peaks at 19.3°, 23.4° and 27.5°, respectively. The two characteristic peaks at 19.3° and 23.4° were corresponded to (120) and (132)/(032)/(212)/(112) crystal planes of PEO, respectively (Wang et al., 2019). It was obvious that the intensity of typical diffraction peak of PEO at

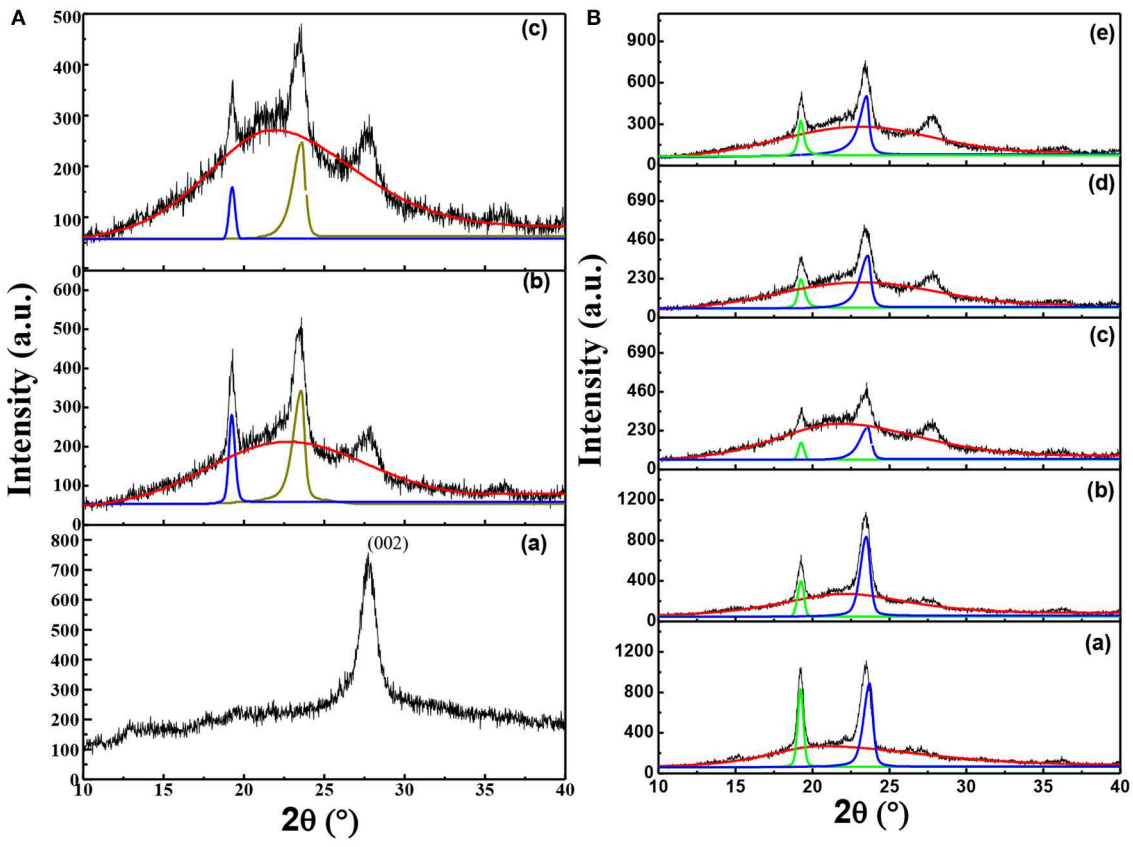

FIGURE 2 | (A) XRD patterns of g-C_3N_4(a), solid composite polymer electrolytes with 10% g-C_3N_4 prepared without thermal annealing at 120°C (b) and with thermal annealing (c); **(B)** XRD patterns of solid composite polymer electrolytes with different weight percent of g-C_3N_4 [(a) 0%; (b) 5%; (c) 10%; (d) 15%, and (e) 20%] at the same [EO]: [Li_+] ratio of 15:1.

19.3° and 23.4° greatly decreased after the sample annealing at 120°C and then quenching to RT, as shown in **Figures 2A**b,c.

Furthermore, the diffraction peaks of crystalline phase and amorphous phase in XRD patterns were fitted by the Jade 6.0 software. And the crystallization degree of PEO in samples was calculated by divided the summation of peak areas of crystallization phase and amorphous phase by the summation of peak areas of crystalline phase. Therefore, the crystallization degree of PEO was decreased from about 15.49% to about 8%, when the solid composite polymer electrolyte was thermal treated. This result demonstrated that the thermal annealing process could greatly suppress the crystallization of PEO.

As shown in **Figure 2B**, the intensity of diffraction peak observed at 27.5° increased with the content of g-C_3N_4 increasing. **Figures 2B**a–e showed that intensity of typical peaks of PEO crystals was firstly decreased and then increased due to the addition of g-C_3N_4, with a minimum value appeared in the solid composite polymer electrolyte with 10% g-C_3N_4. Moreover, when the content of g-C_3N_4 was chosen as 0, 5, 10, 15, and 20%, the crystallization degree of PEO was calculated as about 28, 25, 8, 19, and 20%, respectively. It was obvious that the introduction of g-C_3N_4 could significantly decrease the crystallinity of PEO. But the crystallization degree of PEO was firstly decreased and then increased as the content of g-C_3N_4 increased, with a minimum value in the solid composite polymer electrolyte with 10% g-C_3N_4. In the state polymer electrolyte, the porous microstructure of g-C_3N_4 sheets (as shown in **Figure S1**) might serve as the hard limitation and inhibit the ordered chain arrangement of PEO, while on the other hand also serve as the nucleation sites for PEO chains. As a result, the heterogeneous nucleation could be enhanced, when the content of g-C_3N_4 sheets was over 10%, which would improve the crystallization of PEO. Furthermore, the g-C_3N_4 nanosheets might change the priority growth of PEO crystal planes, as shown by the relative intensity of fitting peaks at 19.3° and 23.4° in **Figures 2B**a,e. It implied that the interaction between g-C_3N_4 and PEO could greatly influence the crystallization preference of crystal planes in PEO.

The effect of thermal annealing and the interaction among components of the solid composite polymer electrolyte on the crystallization of PEO was further proved by DSC. As shown in **Figures 3A**a,b the melting temperature of PEO was decreased from 52.4 to 48.7°C, when the state polymer electrolyte was annealed at 120°C and then quenched to RT. Also shoulder peak appeared at 46.0°C in **Figure 3A**a. It meant that PEO crystals in the sample undergone thermal annealing formed lamellae with thinner thickness and the thickness of lamellae gave a wider distribution. It implied that the thermal annealing process could regulate the crystallization of PEO.

Furthermore, the melting behavior of PEO in PEO homopolymer, PEO-$LiClO_4$ electrolyte and the solid composite polymer electrolytes with different content of g-C_3N_4 (5, 10, 15, and 20%), which were treated by the thermal annealing process, was displayed in **Figure 3B**. Due to the interaction between PEO chains and $LiClO_4$, the melting temperature of PEO crystals decreased from 66.7 to 53.3°C, as shown in **Figures 3B**a,b. Moreover, the addition of g-C_3N_4 further restrained the crystallization of PEO, as shown in **Figures 3B**c–f. The melting temperature of PEO crystals in the solid composite polymer electrolyte was 51.5, 48.7, 52.3, and 53.1°C, respectively, with the content of g-C_3N_4 increasing from 5 to 20%. The melting temperature of PEO firstly decreased and then increased, with a minimum value of 48.7°C in the sample with 10% g-C_3N_4. Also the crystallinity of PEO was calculated by dividing the melting enthalpy obtained from DSC curves in **Figure 3B** by the equilibrium enthalpy of PEO fusion (197 J/g). And the crystallinity of PEO in different samples shown in **Figure 3B** was about 54, 25, 22, 7, 18, and 20%, respectively. With the addition of $LiClO_4$, the coordination effect of EO unit and Li^+ would decrease the crystallization of PEO. Moreover, the introduction of g-C_3N_4 further decreased the crystallization of PEO. The residual $-NH_2$ or –NH groups presenting in g-C_3N_4 can act as active sites for hydrogen bonding with ether oxygen in PEO.

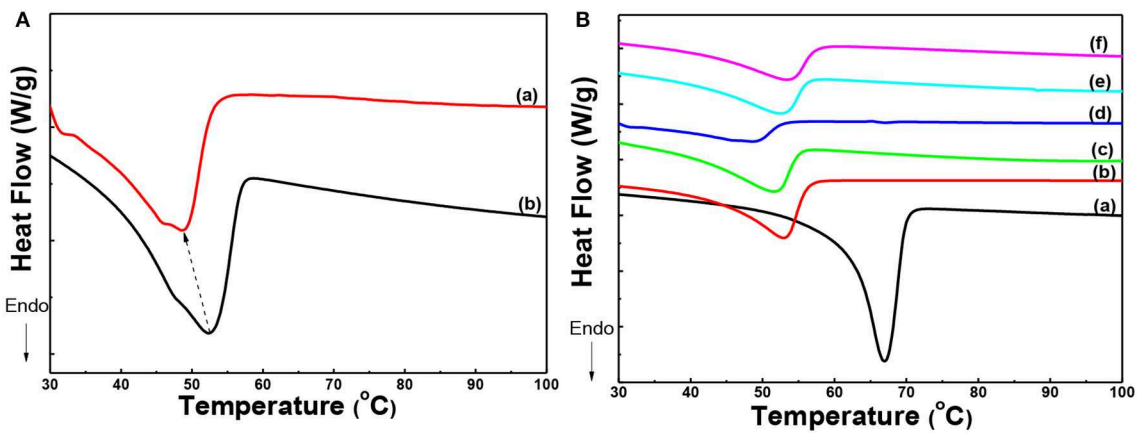

FIGURE 3 | (A) DSC curves of solid composite polymer electrolytes prepared with thermal annealing at 120°C (a) and without thermal annealing (b); **(B)** DSC curves of PEO (a) and solid composite polymer electrolytes with different weight percent of g-C_3N_4 annealed at 120°C [(b) 0%; (c) 5%; (d) 10%; (e) 15%, and (f) 20%] at the same [EO]: [Li^+] ratio of 15:1.

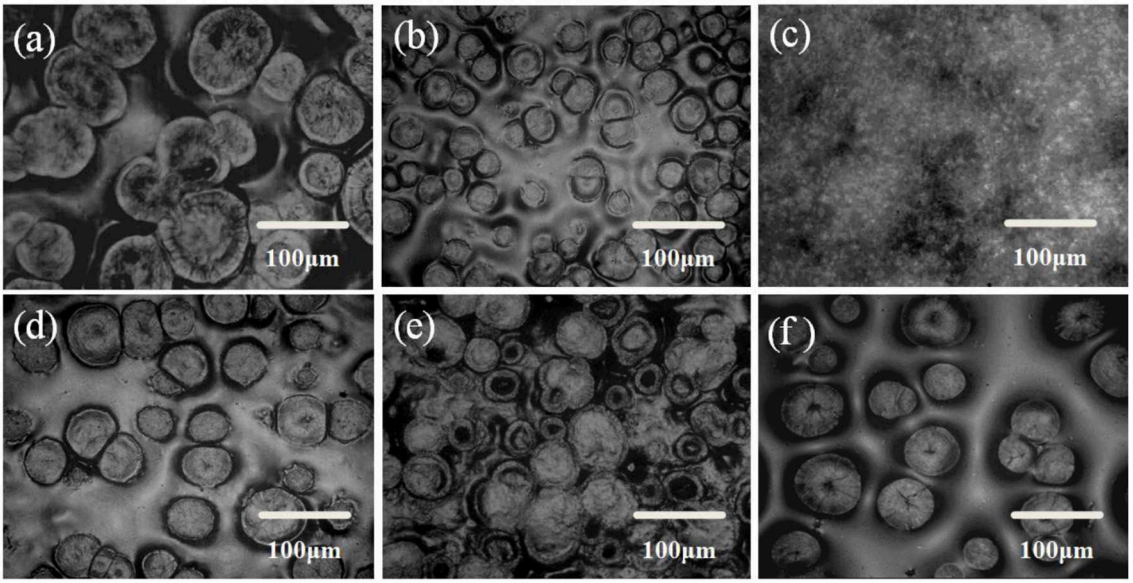

FIGURE 4 | ROM images of solid composite polymer electrolytes prepared with thermal annealing at 120°C [**(a)** PEO-$LiClO_4$; **(b)** PEO-$LiClO_4$-5% g-C_3N_4; **(c)** PEO-$LiClO_4$-10% g-C_3N_4; **(d)** PEO-$LiClO_4$-15% g-C_3N_4; **(e)** PEO-$LiClO_4$-20% g-C_3N_4] and without thermal annealing [**(f)** PEO-$LiClO_4$-10% g-C_3N_4].

And the hydrogen bonds formation restrained the chain folding of PEO, and then reduced the crystallinity of PEO in the solid composite polymer electrolytes. On the other hand, the existence of g-C_3N_4 also served as the heterogeneous nucleation sites for PEO crystallization. As a result, the crystallinity degree of PEO firstly decreased and then increased slightly in the solid composite electrolytes, with 10% as the optimum content. This result was in good accordance with the foregoing XRD results.

The influence of thermal annealing and the interaction among components of the solid composite polymer electrolyte on the microstructure morphology of solid composite polymer electrolyte was observed by ROM. Perfect spherulites with diameter of about 100 μm were formed in the solid PEO-$LiClO_4$ polymer electrolyte, as observed in **Figure 4a**. **Figures 4b–e** showed that the morphology perfection and the crystal's size and number of PEO obviously changed with the content of g-C_3N_4. PEO spherulites were firstly disappeared and then re-formed with the weight percent of g-C_3N_4 increasing, with 10% as a critical content. It was ascribed to the hydrogen bonding interaction between g-C_3N_4 and PEO that could inhibit the crystallization of PEO, while g-C_3N_4 could also serve as the heterogeneous nucleation sites for PEO. Therefore, when the content of g-C_3N_4 was over 10%, more and more spherulites were formed in the sample. It implied that the interaction between PEO and g-C_3N_4 could greatly affect the morphology of the solid composite polymer electrolyte.

Moreover, compared **Figure 4c** with **Figure 4f**, the thermal annealing treatment might greatly change the morphology of PEO crystals from spherulites to lamellae stack. It demonstrated that the thermal treatment also influenced the morphology of the solid composite polymer electrolyte. The morphology of the solid composite polymer electrolyte was tailored by the thermal treatment and the interactions among components in the sample. And the morphology would play an important role in the compatibility between solid electrolytes and electrodes. Uniformly distributed PEO crystals might control the nucleation of lithium, which would help to inhibit the lithium dendrite formation.

Effects of Interaction Among Components in Solid Composite Polymer Electrolytes on the Lithium Salt Dissociation

FTIR spectra of PEO, pure g-C_3N_4, the PEO-$LiClO_4$ solid polymer electrolyte and the PEO-$LiClO_4$-g-C_3N_4 solid composite polymer electrolyte were shown in **Figure S4**. And the typical band of $LiClO_4$ was identified at 624 cm^{-1}. In order to study the effect of g-C_3N_4 on the dissociation of $LiClO_4$ in the solid composite polymer electrolytes, FTIR-ATR spectra in the range of 610–650 cm^{-1} were carefully analyzed. It was reported that the peaks at ∼624 and ∼635 cm^{-1} were assigned to the dissociated free anion and the bonded ion pair in $LiClO_4$, respectively, Lin et al. (2016). As shown in **Figure 5**, the absorbance peak of dissociated free anion shifted from 624 to 623 cm^{-1}, as the weight percent of g-C_3N_4 increased to 15%. It demonstrated that the vibration energy level transition of free ClO_4^- was easier, due to the interaction of g-C_3N_4 and $LiClO_4$. It is because the residual $-NH_2$ and $-NH$ could coordinate with the lithium ion, which would accelerate the dissociation of $LiClO_4$. Moreover, the relative absorbance of peaks at ∼624 and ∼635 cm^{-1} (labeled as A_{624}/A_{635}) was obtained from curves in **Figure 5**. And A_{624}/A_{635} was 2.24, 3.01, 4.79, 4.34, and 4.41, respectively, with the weight percent of g-C_3N_4 increasing from 0 to 20%. It demonstrated that the introduction of g-C_3N_4 could enhance the dissociation of $LiClO_4$, with 10% as the optimum

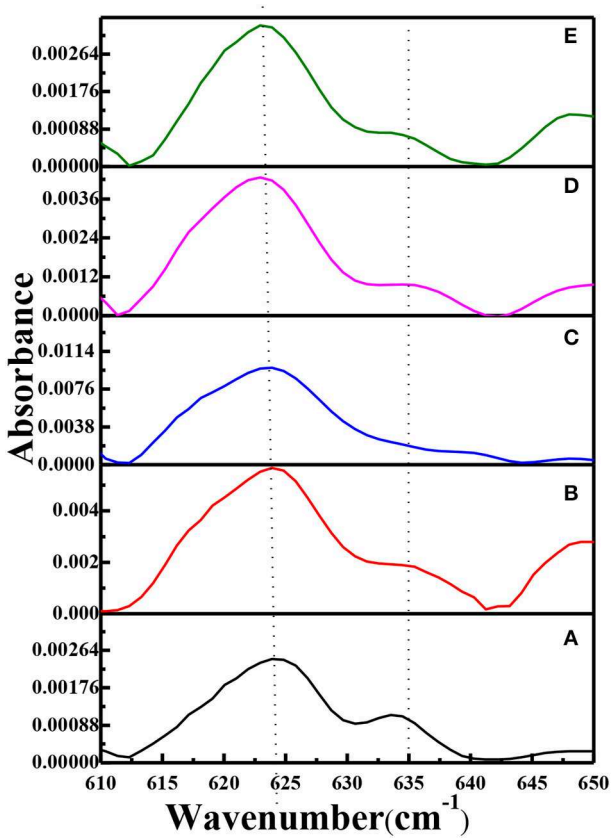

FIGURE 5 | FTIR-ATR spectra of solid composite polymer electrolytes prepared with thermal annealing at 120°C [(a) PEO-$LiClO_4$; (b) PEO-$LiClO_4$-5% g-C_3N_4; (c) PEO-$LiClO_4$-10% g-C_3N_4; (d) PEO-$LiClO_4$-15% g-C_3N_4; (e) PEO-$LiClO_4$-20% g-C_3N_4].

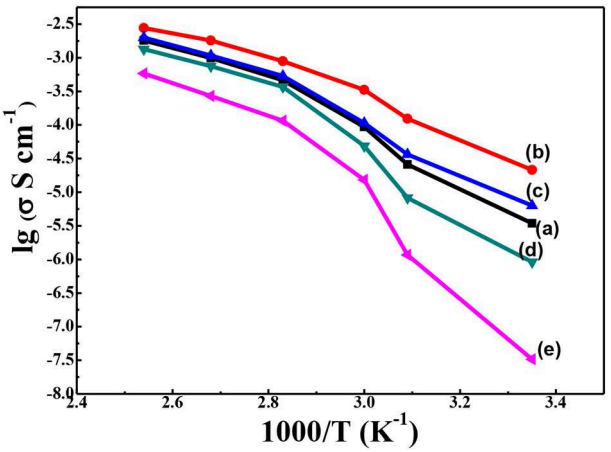

FIGURE 6 | Temperature-dependent ionic conductivity for the solid composite polymer electrolytes with different weight percent of g-C_3N_4 prepared with thermal annealing at 120°C [**(a)** 5%; **(b)** 10%; **(c)** 15%; and **(d)** 20%] and the PEO-$LiClO_4$ electrolyte **(e)** at the same [EO]: [Li^+] ratio of 15:1.

content. Also the residual $-NH_2$ and –NH groups in g-C_3N_4 could form hydrogen bonds with PEO, which would limit the ordered folding of PEO chains and helped to enhance the chain segment motion. As a result, the dissociation of $LiClO_4$ was accelerated, due to the coordination between Li^+ and the ether oxygen. The above factors contributed to the separation of Li^+ and ClO_4^- in the solid composite polymer electrolyte. And the dissociation of $LiClO_4$ in the solid composite polymer electrolyte is critical for the good ionic conductivity.

Ionic Conductivity and the Electrochemical Properties of the Solid Composite Polymer Electrolytes

In order to confirm our hypothesis of the increasing conductivity by thermal annealing treatment and the addition of g-C_3N_4, the ionic conductivity and electrochemistry properties of the solid composite polymer electrolytes were further studied. The ionic conductivity of the solid composite polymer electrolytes with different content of g-C_3N_4 was investigated by EIS. The Arrhenius plot of ionic conductivity with temperature from 25 to 120°C was displayed in **Figure 6**. Compared with that of PEO-$LiClO_4$ polymer electrolyte (**Figure 6**e), significant improvement of ionic conductivity was observed in the annealed solid composite polymer electrolyte. Moreover, the ionic conductivity was firstly increased and then decreased at each temperature with the content of g-C_3N_4 increasing from 5 to 20%, as shown in **Figures 6**a–d. The solid composite polymer electrolyte with 10% g-C_3N_4 exhibited the maximum ionic conductivity (1.76×10^{-5} S cm^{-1}) at 25°C, and the conductivity reached to about 1.08×10^{-3} S cm^{-1} at 100°C. And this ionic conductivity at room temperature was much higher than that of the recently reported PEO/g-C_3N_4/LiTFSI solid electrolytes (2.3×10^{-6} S cm^{-1}, at 30°C) (Sun et al., 2019). Also this ionic conductivity is nearly close to that (2.2×10^{-5} S cm^{-1} at 28°C) of the PEO based solid composite electrolyte, which needed LiTFSI as the lithium salt and 2D MXene as the filler (Pan et al., 2019). DSC and XRD results demonstrated that the crystallinity of PEO in the solid composite polymer electrolytes was greatly affected by the content of g-C_3N_4. And when the content of g-C_3N_4 was 10%, PEO gave the minimum crystallinity degree, which was preferred for the high ionic conductivity. Besides effects on the crystallinity of PEO, the residual $-NH_2$ or –NH groups exited on the 2D structure of g-C_3N_4 could coordinate with Li^+. Also the porous structure might provide a potential transport path for Li^+. When the content of g-C_3N_4 was 10%, continuous percolating pathways for Li^+ diffusion might be formed. Nonetheless, when the content of g-C_3N_4 was over 10%, the redundant inactive fillers would hinder lithium ionic conduction according to effective medium theory (EMT) (Li W. et al., 2018). Moreover, the modification of PEO-$LiClO_4$ using inorganic nanoparticles fillers were always enslaved to the aggregation of particles, which was also harmful for the ionic conducting (Bae et al., 2018a), Evans et al. (1987). As a result, it demonstrated that the thermal annealed PEO-$LiClO_4$-g-C_3N_4 solid composite polymer electrolyte using 10% g-C_3N_4 would give an easy way to achieve excellent ionic conductivity in the solid polymer electrolyte.

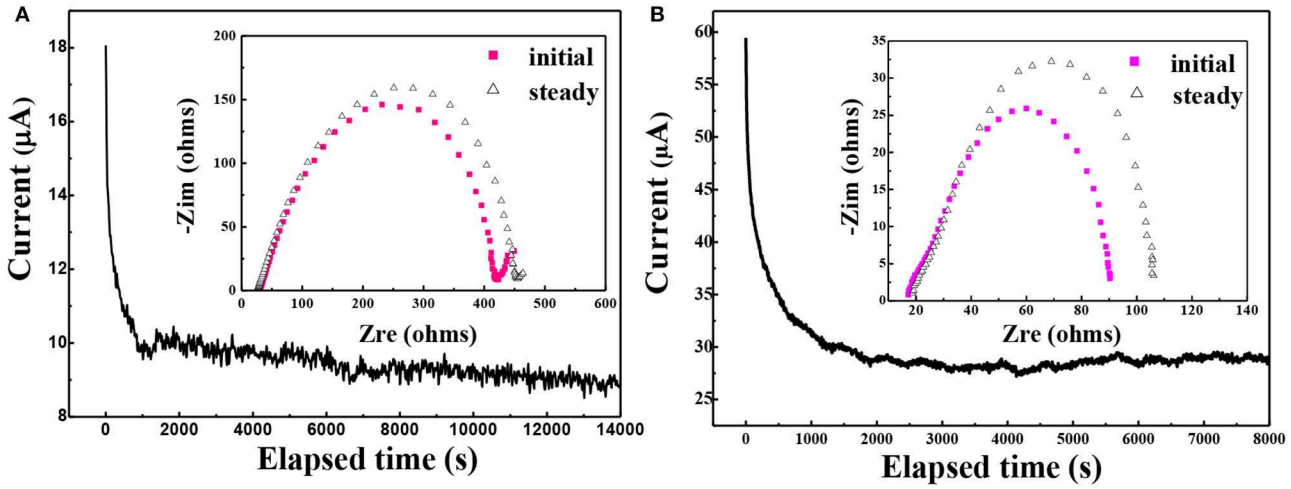

FIGURE 7 | Chronoamperometry of the Li/ PEO-$LiClO_4$/Li **(A)** and Li/ PEO-$LiClO_4$-10% g-C_3N_4/Li **(B)** cells at a potential of 10 mV at 80°C. Inset: the AC impedance spectra of the same battery before and after the polarization.

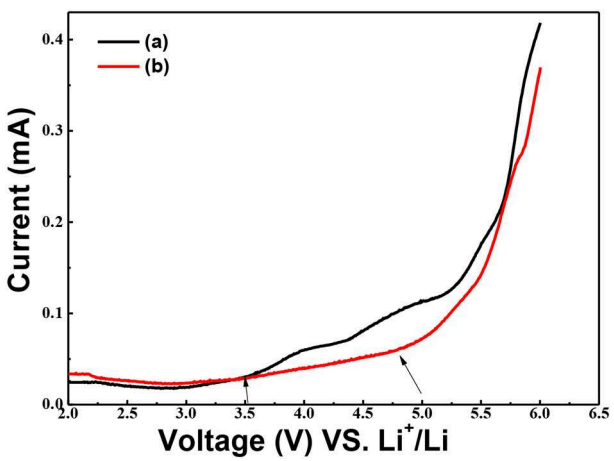

FIGURE 8 | Linear sweep voltammograms of the SS/ PEO-$LiClO_4$/Li (a) and SS/ PEO-$LiClO_4$-10% g-C_3N_4/Li (b) cells at 80°C. The electrolytes were swept in the potential range of 2.0∼6.0 V (*VS.* Li^+/Li) and the scan rate was set as10 mV S^{-1}.

Since the PEO-$LiClO_4$-10% g-C_3N_4 gave the best ionic conductivity, it was chosen for the following electrochemical studies. The lithium ion transportation in the solid composite polymer electrolytes was studied as well. And the lithium ion transference number, t_+, was analyzed according to the method provided by Bruce and coworkers (Evans et al., 1987). **Figure 7** showed the relation between time and current crossing a symmetric Li/PEO-$LiClO_4$/Li battery (A) and Li/PEO-$LiClO_4$-10% g-C_3N_4/Li (B) battery polarized by a small voltage of 10 mV at 80°C. The inset was the AC impedance spectra of the same battery before and after the polarization. And the t_+ can be calculated by the equation: $t_+ = \frac{I^s(\Delta V - I^0 R^0)}{I^0(\Delta V - I^s R^s)}$, where the I^0 and I^s are the initial current and the steady-state current, respectively; ΔV is the potential applied across the cell, and R^0 and R^s are the initial and steady-state interfacial resistances, respectively. Therefore, the t_+ of the PEO-$LiClO_4$ electrolyte was 0.241, while the t_+ of the annealed PEO-$LiClO_4$-g-C_3N_4 electrolyte was 0.37. It indicated that the thermal annealing treatment coupled with the addition of g-C_3N_4 would greatly enhance the mobility of Li^+. And this result was in good accordance with the FTIR-ATR results.

Effects of g-C_3N_4 on the electrochemical stability of the solid composite polymer electrolytes were characterized by the electrochemical window analysis. The electrochemical stability window of PEO-$LiClO_4$ electrolyte and annealed PEO-$LiClO_4$-g-C_3N_4 electrolyte at 80°C were measured by LSV, as shown in **Figure 8**. Detected current of PEO-$LiClO_4$ electrolyte increased sharply as the applying voltage exceeded 3.5 V, as seen from **Figure 8**a. But **Figure 8**b showed that the detected current of PEO-$LiClO_4$-g-C_3N_4 electrolyte was more stable and displayed a decomposition voltage at about 4.8 V. It implied that the annealed solid composite polymer electrolyte might guarantee a higher working voltage of electrode. And due to the interaction between g-C_3N_4 and PEO, the stability of the solid polymer electrolyte was greatly enhanced. It was reasonable to modify the properties of PEO electrolyte through physically thermal annealing treatment and using g-C_3N_4 as the filler.

The battery performance of all-solid-state lithium battery ($LiFePO_4$/Li) based on the solid polymer electrolyte was also performed. **Figure 9** showed the long-term cycling performance and coulombic efficiencies of $LiFePO_4$/Li batteries assembled using the annealed state polymer electrolyte with 10% g-C_3N_4 and PEO/$LiClO_4$ with a current density of 1 C at 80°C. As shown in **Figure 9A**, the cell based on PEO-$LiClO_4$ electrolyte gave an initial discharge capacity of only 133.3 mAh g^{-1}, and displayed a capacity retention ratio of 80% after 115 cycles. On the other hand, **Figure 9B** demonstrated that the cell based on the solid composite polymer electrolyte with a capacity retention ratio

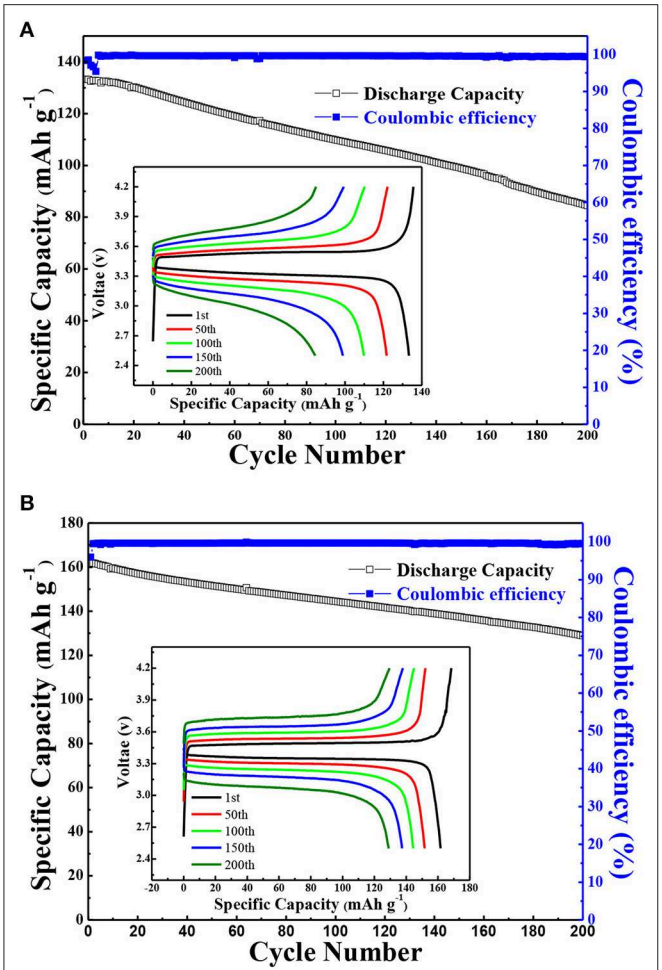

FIGURE 9 | The cycling performance and coulombic efficiencies of $LiFePO_4$/Li batteries assembled using PEO/$LiClO_4$ electrolyte **(A)** and using the annealed state polymer electrolyte with 10% g-C_3N_4 **(B)** at 80°C with a current density of 1 C. And the insert in **(A)** and **(B)** are typical potential VS. specific capacity profiles of the corresponding sample during the cycling performance.

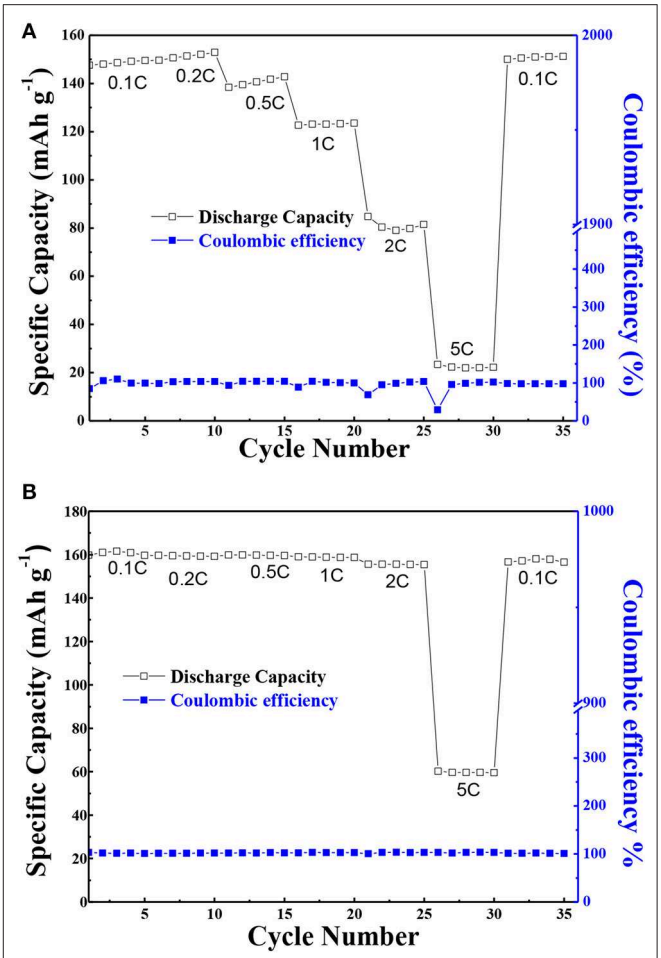

FIGURE 10 | The C-rate performance of $LiFePO_4$/Li coin cells at 80°C assembled using PEO/$LiClO_4$ electrolyte **(A)** and using annealed state polymer electrolyte with 10% g-C_3N_4 **(B)**. And every different C-rate was performed for 5 cycles with a charge current density of 0.1 C.

of 80% after 200 cycles possessed an initial discharge capacity of 161.2 mAh g^{-1}, which was very close to the theoretical capacity of $LiFePO_4$ (170 mAh g^{-1}). Moreover, this cycling performance was better than the reported $LiFePO_4$/Li solid-state batteries based on PEO-LiTFSI-g-C_3N_4 polymer electrolytes, which gave an initial discharge specific capacity of 161.3 mAh g^{-1} but cycled for 120 cycles at 60°C (Sun et al., 2019). The coulombic efficiency of batteries based on the solid composite polymer electrolyte during charge-discharge cycling test was as high as 99.7% in **Figure 9B**, which was higher than that of the battery based on the PEO-$LiClO_4$ electrolyte shown in **Figure 9A**. Moreover, the prevailing experiments using $LiFePO_4$ cathode in SPE based solid state lithium batteries were cycled within 3.8 V, in order to guarantee the cycle stability (Nie et al., 2018). In this article, the $LiFePO_4$/Li solid battery could operate in the range of 4.2∼2.5 V and gave excellent cycle stability. Furthermore, the charge-discharge voltage profiles of the corresponding $LiFePO_4$/Li solid battery during the cycling performance were displayed as the insert in **Figures 9A,B**. The voltage plateau at around 3.48 V was steady in **Figure 9B**, while a sloping voltage plateau was observed in **Figure 9A**. And the attenuation of specific capacity during charge-discharge cycling process was more clearly in the $LiFePO_4$/Li batteries with PEO/$LiClO_4$ electrolyte shown in **Figure 9A**, compared with that in the $LiFePO_4$/Li batteries with annealed PEO-$LiClO_4$-g-C_3N_4 electrolyte shown in **Figure 9B**. It implied that the addition of g-C_3N_4 enhanced the electrochemical stability of PEO-based solid polymer electrolytes.

Moreover, in order to ascertain the usefulness of the solid composite polymer electrolyte, the C-rate cycling property of PEO-$LiClO_4$ electrolyte and the annealed PEO-$LiClO_4$-g-C_3N_4 electrolyte at 80°C were characterized and results were shown in **Figure 10**. As shown in **Figure 10A**, the discharge specific capacity of the all solid-state battery based on the PEO-$LiClO_4$ electrolyte was 148.0, 150.6, 139.5, 123.1, 80.4, and 22.2 mAh g^{-1}, respectively, with the C-rate increasing from 0.1, 0.2, 0.5C, 1, 2 to 5C. And it was obvious that the discharge specific

capacity was gradually decreased at higher C-rates, which was reported as a typical characteristic of $LiFePO_4$ material (Brutti et al., 2012). The low discharge specific capacity at 5C-rate was attributed to the electrode polarization and solid electrolyte interface caused by the low electronic conductivity, limited diffusion of Li^+ into the $LiFePO_4$ structure (Kumar et al., 2014). On the other hand, **Figure 10B** showed the performance of the battery with PEO-$LiClO_4$-g-C_3N_4 electrolyte. It delivered an initial discharge specific capacity of 161.0 mAh g^{-1} at 0.1C-rate. And the discharge specific capacity was 159.5, 159.7, 158.8, and 155.6 mAh g^{-1}, respectively, at 0.2C-rate, 0.5C-rate, 1C-rate, and 2C-rate without any obvious attenuation. The battery was even able to deliver a specific capacity of 59.7 mAh g^{-1} even at 5C-rate, which was 168% higher than that of the battery based on the PEO-$LiClO_4$ solid polymer electrolyte. Moreover, when the rate returned to 0.1C, the average discharge capacity of the battery was still as high as 157.2 mAh g^{-1}. Also the coulombic efficiencies were close to 100%. This result implied that the PEO-$LiClO_4$-g-C_3N_4 solid polymer electrolyte could facilitate the cycling performance of $LiFePO_4$ cathode, due to its good compatibility with the cathode and good lithium ionic transport capability. Moreover, the solid state battery based on the solid composite polymer electrolyte was able to light up several LED lamps under a normal condition as shown in **Figure S5**. It demonstrated that the annealed PEO-$LiClO_4$-g-C_3N_4 electrolyte could be an outstanding candidate used in all solid-state lithium batteries.

CONCLUSIONS

To conclude, we reported a novel method to prepare the solid polymer electrolyte with high performance using facile thermal annealing treatment and by addition g-C_3N_4 as the modification filler. XRD and DSC results demonstrated that the crystallinity degree of PEO was greatly decreased by the thermal annealing treatment and by interaction between PEO chains and the g-C_3N_4 filler. Moreover, the dissociation of $LiClO_4$ was obviously enhanced as proved by the FTIR-ATR results. The final morphology of the obtained solid composite polymer electrolyte was even changed with the content of g-C_3N_4 increasing and changed by the thermal annealing treatment. When the weight percent of g-C_3N_4 was 10% in the annealed solid composite polymer electrolyte, spherulites morphology of PEO crystals was totally destroyed, which would facilitate the compatibility between the solid electrolyte and electrodes. And the crystallinity of PEO was only about 8%, which was helpful for the lithium ion transport in the solid composite polymer electrolyte.

As a result, the obtained solid composite polymer electrolyte with 10% g-C_3N_4 achieved an ionic conductivity as high as 1.76×10^{-5} S cm^{-1} at 25°C, due to the above microstructure regulation. The electrochemical stable window was increased to about 4.8 V. The lithium ion transference number, t_+, was changed from 0.24 to 0.37, and increased about 54.8%. Finally, the annealed PEO-$LiClO_4$-10% g-C_3N_4 electrolyte was also assembled into an all solid-state battery using $LiFePO_4$ as the cathode and lithium metal as the anode. And the battery demonstrated excellent performance, with a high initial discharge capacity of 161.2 mAh·g^{-1} and superior cycle stability with a capacity retention ratio of 81% after 200 cycles at 1C at 80°C. Furthermore, the C-rate cycling results also demonstrated that the stability of the assembled solid state battery was markedly improved by using PEO-$LiClO_4$-10% g-C_3N_4 electrolyte. The above results indicates that the thermal annealing treatment and g-C_3N_4 as a novel structure modifier provide an useful and facile way to prepare the state polymer electrolytes used in the all solid-state lithium battery.

DATA AVAILABILITY

The raw data supporting the conclusions of this manuscript will be made available by the authors, without undue reservation, to any qualified researcher.

AUTHOR CONTRIBUTIONS

LS and JY developed the concept and designed the experiment. They contributed equally to this work. XW and JY conducted the experiments. KX, GZ, and AM co-supervised the experiments. JY and LS wrote the manuscript. KX, CS, and WC helped to revise the work critically. All authors listed have made a substantial, crucial and direct contribution to the work, and approved it for publication.

FUNDING

This work was supported by the project sponsored by the Key R&D Program of Shaanxi (2017ZDCXL-GY-08-03), the National Natural Science Foundation of China (61604120, 51804259 and 21501139), Scientific Research Program Funded by Shaanxi Provincial Education Department (17JK0380 and 18JK0390), Natural Science Foundation of the province of Shaanxi (No.2018JQ2037), Innovation and entrepreneurship training program for college students (1070214082) and the Presidential Research Fund of Xi'an Technological University (No. XAGDXJJ18007).

SUPPLEMENTARY MATERIAL

The Supplementary Material for this article can be found online at: https://www.frontiersin.org/articles/10.3389/fchem.2019.00388/full#supplementary-material

REFERENCES

Bae, J., Li, Y., Zhao, F., Zhou, X., Ding, Y., and Yu, G. (2018b). Designing 3D nanostructured garnet frameworks for enhancing ionic conductivity and flexibility in composite polymer electrolytes for lithium batteries. *Energy Storage Mater.* 15, 46–52. doi: 10.1016/j.ensm.2018.03.016

Bae, J., Li, Y., Zhang, J., Zhou, X., Zhao, F., Shi, Y., et al. (2018a). A 3D nanostructured hydrogel framework-derived high-performance

composite polymer lithium-ion electrolyte. *Angew. Chem. Int. Ed.* 57, 1–6. doi: 10.1002/anie.201710841/

Ban, X., Zhang, W., Chen, N., and Sun, C. (2018). A high-performance and durable poly(ethylene oxide)-based composite solid electrolyte for all solid-state lithium battery. *J. Phys. Chem. C* 122, 9852–9858. doi: 10.1021/acs.jpcc.8b02556

Brutti, S., Hassoun, J., Scrosati, B., Lin, C. Y., Wu, H., and Hsieh, H. W. (2012). A high power Sn–C/C–$LiFePO_4$ lithium ion battery. *J. Power Sourc.* 217, 72–76. doi: 10.1016/j.jpowsour.2012.05.102

Evans, J., Vincent, C. A., and Bruce, P. G. (1987). Electrochemical measurement of transference numbers in polymer electrolytes. *Polymer* 28, 2324–2328. doi: 10.1016/0032-3861(87)90394-6

Fan, L., Wei, S., Li, S., Li, Q., and Lu, Y. (2018). Recent progress of the solid-state electrolytes for high-energy metal-based batteries. *Adv. Energy Mater.* 8:1702657. doi: 10.1002/aenm.201702657

Goodenough, J. B. (2018). How we made the Li-ion rechargeable battery. *Nat. Electr.* 1, 204–204. doi: 10.1038/s41928-018-0048-6

Hu, J., Tian, J., and Li, C. (2017). Nanostructured carbon nitride polymer reinforced electrolyte to enable dendrite-suppressed Li metal batteries. *ACS Appl. Mater. Interf.* 9, 11615–11625. doi: 10.1021/acsami.7b00478

Kumar, R. S., Raja, M., Kulandainathan, M. A., and Stephan, A. M. (2014). Metal organic framework-laden composite polymer electrolytes for efficient and durable all-solid-state-lithium batteries. *RSC Adv.* 4, 26171–26175. doi: 10.1039/C4RA03147D

Li, D., Chen, L., Wang, T., and Fan, L. Z. (2018). 3D fiber-network reinforced bicontinuous composite solid electrolyte for dendrite-free lithium metal batteries. *Acs Appl Mater Interf.* 10, 7069–7078. doi: 10.1021/acsami.7b18123

Li, W., Zhang, S., Wang, B., Gu, S., Xu, D., Wang, J., et al. (2018). Nanoporous adsorption effect on alteration of the Li^+ diffusion pathway by a highly ordered porous electrolyte additive for high-rate all-solid-state lithium metal batteries. *ACS Appl. Mater. Interf.* 10, 23874–23882. doi: 10.1021/acsami.8b06574

Lin, D., Liu, W., Liu, Y., Lee, H. R., Hsu, P. C., Liu, K., et al. (2016). High ionic conductivity of composite solid polymer electrolyte via *in situ* synthesis of monodispersed SiO_2 nanospheres in poly(ethylene oxide). *Nano Lett.* 16, 459–465. doi: 10.1021/acs.nanolett.5b04117

Manthiram, A., Yu, X., and Wang, S. (2017). Lithium battery chemistries enabled by solid-state electrolytes. *Nat. Rev. Mater.* 2:16103. doi: 10.1038/natrevmats.2016.103

Nie, K., Hong, Y., Qiu, J., Li, Q., Yu, X., Li, H., et al. (2018). Interfaces between cathode and electrolyte in solid state lithium batteries, challenges and perspectives. *Front. Chem.* 6:616. doi: 10.3389/fchem.2018.00616

Pan, Q., Zheng, Y., Kota, S., Huang, W., Wang, S., Qi, H., et al. (2019). 2D MXene-containing polymer electrolytes for all-solid-state lithium metal batteries. *Nanoscale Adv.* 395–402. doi: 10.1039/C8NA00206A

Shen, C., Yan, H., Gu, J., Gao, Y., Yang, J., and Xie, K. (2018). Li_2O-reinforced solid electrolyte interphase on three-dimensional sponges for dendrite-free lithium deposition. *Front. Chem.* 6:517. doi: 10.3389/fchem.2018.00517

Shi, Y., Jiang, S., Zhou, K., Bao, C., Yu, B., Qian, X., et al. (2014). Influence of g-C_3N_4 nanosheets on thermal stability and mechanical properties of biopolymer electrolyte nanocomposite films, a novel investigation. *ACS Appl. Mater. Interf.* 6:429. doi: 10.1021/am4044932

Sun, Z., Li, Y., Zhang, S., Shi, L., Wu, H., Bu, H., et al. (2019). g-C_3N_4 nanosheets enhanced solid polymer electrolytes with excellent electrochemical performance, mechanical properties, and thermal stability. *J. Mater. Chem. A* **7**, 11069–11076. doi: 10.1039/C9TA00634F

Tan, S. J., Zeng, X. X., Ma, Q., Wu, X. W., and Guo, Y. G. (2018). Recent advancements in polymer-based composite electrolytes for rechargeable lithium batteries. *Electrochem. Energy Rev.* 2018, 1–26. doi: 10.1007/s41918-018-0011-2

Wang, X., Yang, J., Shao, L., Li, J., Zhao, W., Ma, A., et al. (2019). A facile preparation of composite polymer electrolyte with high ionic conductivity by thermal treatment. *Sci. Sin. Chim.* 49, 360–367. doi: 10.1360/N032018-00121

Wang, Y., Wang, X., and Antonietti, M. (2012). Polymeric graphitic carbon nitride as a heterogeneous organocatalyst, from photochemistry to multipurpose catalysis to sustainable chemistry. *Angew. Chem. Int. Ed.* 51, 68–89. doi: 10.1002/anie.201101182

Wu, F., Yuan, Y.-X., Cheng, X.-B., Bai, Y., Li, Y., Wu, C., et al. (2018). Perspectives for restraining harsh lithium dendrite growth, Towards robust lithium metal anodes. *Energy Storage Mater.* 15, 148–170 doi: 10.1016/j.ensm.2018.03.024

Xiao, W., Wang, Z., Miao, C., Mei, P., Zhang, Y., Yan, X., et al. (2018). High performance composite polymer electrolytes doped with spherical-like and honeycomb structural $Li_{0.1}Ca_{0.9}TiO_3$ Particles. *Front. Chem.* 6:525. doi: 10.3389/fchem.2018.00525

Xue, Z., He, D., and Xie, X. (2015). Poly (ethylene oxide)-based electrolytes for lithium-ion batteries. *J. Mater. Chem. A* 3, 19218–19253. doi: 10.1039/c5ta03471j

Zhang, J., Li, X., Li, Y., Wang, H., Ma, C., Wang, Y., et al. (2018). Cross-linked nanohybrid polymer electrolytes with POSS cross-linker for solid-state lithium ion batteries. *Front. Chem.* 6:186. doi: 10.3389/fchem.2018.00186

Zhang, X., Xie, J., Shi, F., Lin, D., Liu, Y., Liu, W., et al. (2018). Vertically aligned and continuous nanoscale ceramic-polymer interfaces in composite solid polymer electrolytes for enhanced ionic conductivity. *Nano Lett.* 18, 3829–3838. doi: 10.1021/acs.nanolett.8b01111

Conflict of Interest Statement: LS was employed by the company Shaanxi Coal Chemical Industry Technology Research Institute Co. Ltd.

The remaining authors declare that the research was conducted in the absence of any commercial or financial relationships that could be construed as a potential conflict of interest.

frontiers in Chemistry

MINI REVIEW
published: 04 June 2019
doi: 10.3389/fchem.2019.00355

Advances in Microwave-Assisted Production of Reduced Graphene Oxide

Xinxin Xie[1,2], *Yanping Zhou*[1,2]* *and Kama Huang*[1,2]

[1] College of Electronics and Information Engineering, Sichuan University, Chengdu, China, [2] Key Laboratory of Wireless Power Transmission of Ministry of Education, Sichuan University, Chengdu, China

Efficient reduction of graphene oxide to obtain high-quality graphene nanosheets is desirable for energy storage, catalysis, electronics and environmental remediation. In this brief review, we mainly focus on the microwave-assisted production of reduced graphene oxide in three categories: (1) microwave-assisted chemical reduction of graphene oxide; (2) microwave-assisted thermal reduction of graphene oxide; (3) microwave-assisted simultaneous thermal exfoliation & thermal reduction of graphite oxide. We also summarize common techniques for characterizing reduction efficiency and quality of as-obtained rGO.

Keywords: microwave-assisted synthesis, reduced graphene oxide, chemical reduction, thermal reduction, exfoliation of graphite oxide

OPEN ACCESS

Edited by:
Wenping Sun,
University of Wollongong, Australia

Reviewed by:
Jiantie Xu,
South China University of Technology, China
Chao Wu,
University of Wollongong, Australia

***Correspondence:**
Yanping Zhou
ypzhou11@scu.edu.cn

Specialty section:
This article was submitted to Electrochemistry, a section of the journal Frontiers in Chemistry

Received: *21 February 2019*
Accepted: *30 April 2019*
Published: *04 June 2019*

Citation:
Xie X, Zhou Y and Huang K (2019) Advances in Microwave-Assisted Production of Reduced Graphene Oxide. Front. Chem. 7:355. doi: 10.3389/fchem.2019.00355

INTRODUCTION

Graphene is a two-dimensional sheet of sp2-hybridized carbon. Owing to its theoretically high mechanical strength (1,060 GPa), thermal conductivity (~5,000 W m^{-1} K^{-1}), electron mobility (2 × 105 cm^2 V^{-1} s^{-1}), Young's modulus (~1 TPa), surface area (2,630 m^2 g^{-1}), electrical conductivity (~2,000 S m^{-1}), and extraordinary optical properties, graphene has been attracting increasing application in various areas including energy storage [like fuel cells (Li et al., 2012; Hur and Park, 2013; Li and Wu, 2015), batteries (Li et al., 2015; Bak et al., 2016; Kaur et al., 2018), supercapacitors (Le et al., 2011; Akhavan, 2015)], sensors (Shao et al., 2010; Wang and Arash, 2014; Chatterjee et al., 2015), catalysis (Han et al., 2017; Hu et al., 2017), electronics (like liquid crystal displays (Novoselov et al., 2005; Lin et al., 2015; Basu et al., 2016; Narayan et al., 2016), touch panels (Das and Prusty, 2013; Liu et al., 2014; Katkov and Osipov, 2017), electromagnetic interference shielding (Eswaraiah et al., 2011; Thomassin et al., 2013; Song et al., 2014; Cao et al., 2015), environmental remediation (Bi et al., 2012; Qin and Brosseau, 2012; Chabot et al., 2014), and so on. Clearly, there will be an increasing demand for high quality graphene.

Currently, reduction of graphene oxide or simultaneous exfoliation and reduction of graphite oxide are regarded to be most promising for large scale production of chemically derived graphene, which can be defined as reduced graphene oxide (rGO). In general, there are mainly two strategies used for graphene oxide reduction: chemical reduction and thermal reduction, both of which are facing certain challenges. In chemical reduction methods, the reduction efficiency is unsatisfactory, requiring long treating time and yielding rGO with oxygen content usually higher than 15% (Stankovich et al., 2007; Shao et al., 2010; Mattevi et al., 2011; Park et al., 2011b; Xiao et al., 2013; Zhang et al., 2013; Wen et al., 2014). In thermal reduction process, long-time high-temperature treatment is not only energy consuming but also results in fragmentation of graphene and lots of structural defects (Jones et al., 2002; Chen and Yan, 2010; Chen et al., 2010; Gao et al., 2010; Lin et al., 2010; Zhu et al., 2010b; Zhang et al., 2011).

Microwave heats materials directly through dielectric loss rather than heat convection as in the conventional heating method, and hence can enable fast heating and selective heating. It is regarded to be promising in shortening the reaction time and yielding hot spots with extraordinary high temperature (Thostenson and Chou, 1999; Kappe, 2004; Tompsett et al., 2006; Schwenke et al., 2015). As such, material scientists have devoted much effort to explore the potential application of microwave in overcoming the current problems and facilitating the fabrication of high-quality rGO in large-scale. To this end, we present an up-to-date critical survey of literature relevant to MW-assisted production of rGO. This brief review is organized as follows. First, techniques for characterizing quality of as-obtained rGO are discussed. Next, we provide a comprehensive summary of microwave-assisted chemical reduction of graphene oxide, microwave-assisted thermal reduction of graphene oxide, and microwave-assisted simultaneous thermal exfoliation and reduction of graphite oxide**,** respectively.

TECHNIQUES FOR CHARACTERIZING QUALITY OF RGO

Generally, X-ray diffraction, X-ray photoelectron spectroscopy, Raman spectroscopy, electrical conductivity, thermal gravity analysis are common techniques used for characterizing reducing efficiency and quality of rGO.

X-Ray Diffraction

The X-ray diffraction (XRD) pattern of graphene/graphite oxide usually shows a characteristic diffraction peak at $2\theta = 10.9^{\circ}$ with the corresponding d-spacing of 0.81 nm (Stobinski et al., 2014; Strankowski et al., 2016), due to insertion of hydroxyl and epoxy groups between the carbon sheets. After reduction, two types of XRD spectra may be obtained: (1) The XRD pattern with no peaks, suggesting the complete reduction and the formation of single-layered rGO (Hassan et al., 2009). (2) The XRD pattern showing a broad peak around 26.5° (Zedan et al., 2010; Liu et al., 2011; Park et al., 2011b; Wang et al., 2011; Pokharel et al., 2014). Since the oxygen-containing functional groups could lead to a reduction in crystallinity, the higher the broad peak's intensity is, the higher the crystallinity degree is, and the better graphene/graphite oxide is reduced.

X-Ray Photoelectron Spectroscopy

X-ray photoelectron spectroscopy (XPS) could help to obtain qualitative and quantitative analysis results of the content of oxygenated groups. For example, the carbon/oxygen atomic ratio (C/O ratio) could be evaluated from the areas of C1s and O1s peaks and the atomic sensitivity factor. Usually, the C/O ratio of graphene oxide is ∼2.2–2.7 (Stankovich et al., 2007; Chen et al., 2010; Park et al., 2011a; Li et al., 2013; Wen et al., 2014; Han et al., 2015), attributed to the abundant oxygen-containing functional groups introduced during oxidation of graphite. Further, the C1s peak can be decomposed into three peaks: C=C (284.7 eV), C-O (286.9 eV), C=O (287.77 eV) (Zhao et al., 2014), through the areas of which existing statuses of oxygen could be analyzed in a quantitative manner.

Raman Spectroscopy

The D band around 1,350 cm^{-1} in Raman spectra could reflect the disorder degree of the crystal structure of carbon while the G band around 1,580 cm^{-1} represents a first-order scattering E_{2g} vibration mode for characterizing the sp2 bond structure of carbon. I_D/I_G is the ratio of D band intensity to G band intensity, which could be used to evaluate the quality of the graphene structure. The higher I_D/I_G is, the more defects of C atom crystal there are. In the Raman spectrum of graphene, the D-band peak could not be observed. However, the I_D/I_G of graphene oxide could be as high as ∼0.8–1 (Chen et al., 2010; Lin et al., 2010; Liu et al., 2011; Park et al., 2011a; Zhao et al., 2014). Besides, the number of rGO layers can be estimated by observing the shape and position of the 2D peak in Raman spectra which is the second-order two-phonon process. For example, single-layer graphene exhibits a single, sharp 2D band located below 2,700 cm^{-1}, while bilayer sheets have a broader 2D peak around 2,700 cm^{-1}, and sheets more than five layers have a broad 2D peak above 2,700 cm^{-1} (Hassan et al., 2009).

Electrical Conductivity

Though the conductivity of graphene is as high as 1×10^{8} S m^{-1}, that of graphene oxide is about 0.02–0.07 S m^{-1} (Li et al., 2010; Zhu et al., 2010a; Park et al., 2011a) due to the existence of oxygen-containing functional groups which disrupted sp2 bonding networks. During the reduction process, electrical conductivity can be recovered by restoring the p-network as oxygen-containing groups leave, leading to a conductivity improvement by 3–6 orders of magnitude (Chen et al., 2010; Dreyer et al., 2010; Zhao et al., 2014; Han et al., 2015). Therefore, the restoration degree of conductivity can indirectly reflect the reduction degree and quality of rGO.

Thermal Gravity Analysis

Graphene/Graphite has a very good thermal stability even when being heated up to 900°C (Bastiurea et al., 2015). For graphene oxide, it starts to have significant mass loss from ∼200°C due to the decomposition of labile oxygen functional groups leads to poor thermal stability (Hassan et al., 2009; Chen et al., 2010; Zhu et al., 2010a; Gannavarapu et al., 2018). Therefore, the removal of oxygen-containing functional groups can help to restore its thermal stability. The significant mass loss temperature of rGO usually happens around 500–800°C, depending on the reduction degree of rGO.

MICROWAVE-ASSISTED PRODUCTION OF REDUCED GRAPHENE OXIDE

Methods for producing rGO could generally be categorized into chemical reduction of graphene oxide, thermal reduction of graphene oxide, and simultaneous thermal exfoliation and reduction of graphite oxide. Here, we would also discuss microwave-assisted production of rGO in these three categories separately.

Microwave-Assisted Chemical Reduction of Graphene Oxide

Strong reducing reagents have been widely used to reduce graphene oxide. However, the reduction process is very slow. For example, hydrazine hydrate enabled reduction of graphene oxide in the oil bath for 12 h and 24 h resulted in a C/O ratio about 5 (Park et al., 2011b) and 10.3 (Stankovich et al., 2007), respectively. Microwave irradiation was found to be capable of accelerating the reducing rate significantly. For example, Hassan et al. (2009) reported microwave assisted hydrazine hydrate reduction of graphene oxide. After microwave treatment for 2 × 30 s (on for 10 s, off and stirring for 20 s), the I_D/I_G in Raman spectra was 0.1–0.12, indicating a high reduction degree even after such a short treating time This was confirmed by the improved thermal stability, showing no significant mass loss up to 750°C. Elazab et al. (2015) obtained Pd/Fe_3O_4 nanoparticles supported on graphene nanosheets by a one-pot microwave heating with the existence of hydrazine hydrate. After microwave irradiation for 2 min, the C/O of rGO was determined to be 8.1. Kumar et al. (2015) reported microwave-enhanced chemical reduction of graphene oxide using HI/CH_3COOH as reducing reagent. They found the effect of 4 h microwave irradiation was comparable to 48 h conventional reaction process.

Since strong reducing regents are very much expensive and hazardous, organic solvents have also been explored to reduce graphene oxide. Zedan et al. (2010) reported MW-assisted reduction of graphene oxide in dimethyl sulfoxide (DMSO), a solvent with high microwave absorbing capability. The reduction degree of the sample prepared from 2 min MW irradiation at 1,200 W is even much higher than that of the sample derived from 7 h conventional heating treatment, as evidenced by XRD results of both samples shown in **Figures 1a,b**. After 2 min of MW irradiation in DMSO, the color of the product changed to black (**Figure 1c**), and the XRD pattern showed no characteristic peak (10.9°) of GO, indicating that most of the GO has been converted into rGO. In contrast, under conventional heating at 180 °C, an apparent peak located at 10.9° was found even after 7 h treatment. It was not until 12th h that the GO was completely reduced, as can be seen from the disappearance of the peak at 10.9° in the XRD pattern and the color change of the sample to black (**Figure 1d**). Chen et al. (2010) reported the microwave-enhanced chemical reduction of graphene oxide to rGO in a mixed solution of N, N-dimethylacetamide (DMAc) and water without any additional reductant under nitrogen purge. The XRD pattern of the graphene oxide showed a wide peak, indicating the damage of the regular crystalline pattern of graphite during the oxidation. After microwave treatment for 2 min × 5 times (2.45 GHz, 800 W), no peak was observed indicating microwave-assisted formation of single-layered graphene. XPS results showed that C/O ratio changed from 2.09 to 5.46, confirming that the removal of oxygen containing groups happened. However, the I_D/I_G in Raman spectra changed from 0.95 to 0.96, suggesting that the reduction led to an increase of aromatic domains of smaller overall size in graphene. Similarly, Liu et al. (2011) also reported an increase of the product's I_D/I_G in Raman spectra from 0.80 to 0.94 after being treated by microwave at 750 W for 2 min in N, N-dimethylacetamide (DMF) solution. Zhao et al. (2014) applied DMF to reduce graphite oxide under microwave irradiation at 100 W for 30 min. The XPS results showed that C/O ratio rose from 2.13 to 6.13 while Raman results showed that I_D/I_G remained almost unchanged.

The characteristics of the as-obtained rGO products derived from different microwave-assisted chemical reduction methods are summarized and listed in **Table 1**. Since microwave heat rapidly, microwave-assisted rate enhancement in chemical reduction of graphene oxide has been widely observed, with most of the reaction time <10 min. However, as in the conventional heating method, the as-obtained rGO is still unsatisfactory, facing the same problem of containing a high oxygen content and a high I_D/I_G value when organic solvent was used as the reducing reagent. Microwave-enhanced quality of chemically reduced rGO is yet to be explored. Also, since the type and amount of reducing agents were different in different work, it is difficult to draw a conclusion regarding the effect of microwave power and treating time here.

Microwave-Assisted Thermal Reduction of Graphene Oxide

In conventional thermal reduction process, long-time high-temperature treatment in a protecting atmosphere (e.g., N_2/Ar) is usually required, which is not only very energy consuming but also leads to the formation of defects in the graphene basal plane because of the evolution of the oxygen functional groups during reduction, like nanoscopic holes brought by carbon loss as CO or CO_2 and Stone-Wales types of defects lead by rearrangement of carbon atoms in the graphene basal plane. Besides, the reducing efficiency is always suppressed by the highly stable ether and carbonyl groups formed between the oxygen functional groups.

In 2010, Li et al. (2010) for the first time reported a microwave-assisted thermal reduction of graphene oxide. Specifically, they made the graphene oxide into a free-standing film via filtration membrane, and then treated it with a microwave irradiation with a frequency of 6.425 ± 1.150 GHz at a power of 500 W without purging any inert gas. As shown in **Figures 2a,b**, after 1 s irradiation, the temperature rose only a little and no distinct difference were found in the electrical properties and the Raman spectra of the sample. However, after 2 s irradiation, the surface temperature of the graphene oxide film ramped up to 400°C and the conductivity of the graphene oxide film increased from 0.07 to 1 × 10^4 S m^{-1}; the I_D/I_G in Raman spectra decreased from 1 to 0.3; the mass loss temperature increased from 181 to 668°C (**Figure 2c**). In addition, they found that in the MW treatment process, fierce degassing and a high gas pressure inside the graphene oxide was generated, which was beneficial for exfoliating the graphene oxide into thinner graphene sheets. Afterwards, they also applied a household MW oven (with a frequency of 2.45 GHz and a power of 1,000 W) to treat the free-standing graphene oxide film. They found that there was an optimal irradiation time of 8 min as evidenced by Raman spectra (**Figure 2d**) and TGA results (**Figure 2e**). Longer treatment time (e.g., 10 min) caused lower mass loss temperature (from 700°C to around 800°C), which

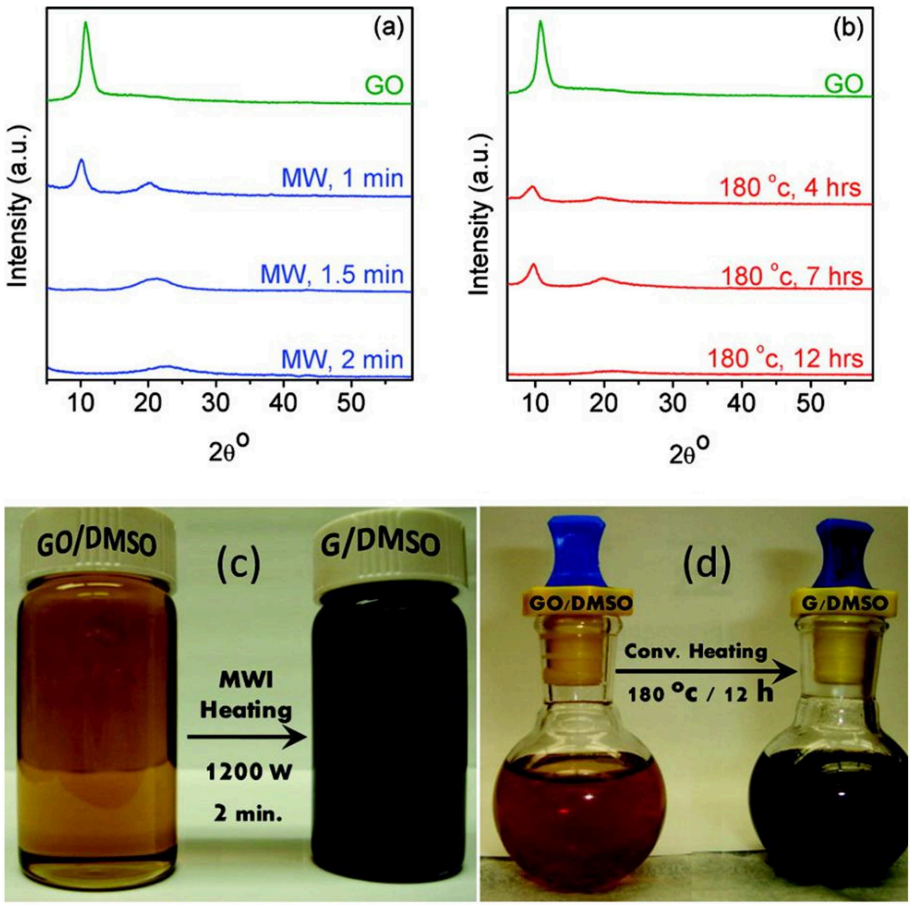

FIGURE 1 | (a) XRD pattern of graphene oxide after microwave reduction for 1, 1.5, and 2 min. **(b)** thermal reduction after 4, 7, and 12 h. Digital camera images of graphene oxide and graphene colloidal suspensions in DMSO for **(c)** microwave and **(d)** thermal syntheses. [Reprinted with permission from Zedan et al. (2010), copyright 2010 American Chemical Society].

could possibly be attributed to the oxidation by air when there was no protecting gas.

Considering the weak microwave absorption of graphene at low frequency, while 2.45 GHz and 915 MHz are most commonly used in industry, Voiry et al. (2016) introduced a conventional mild annealing process before the microwave irradiation process. Firstly, the single-layered graphene oxide solution was slowly injected into an aqueous solution that contained 1 wt% $CaCl_2$, which helps to coagulate GO nanosheets and promote solidification via bridging with the oxygen-containing groups from two GO nanosheets, yielding uniform and continuous gelatinous GO. The coagulated graphene oxide was then washed with DI water and dried, which was subsequently annealed at 300°C for 1 h under Argon to yield mildly reduced graphene oxide that was capable of absorbing microwaves at 2.45 GHz effectively. After 1–2 s long microwave irradiation in microwave oven at 1,000 W in argon, the efficient absorption of microwave led to rapid heating of the mildly reduced GO and consequently brought large arcing as shown in **Figure 3a**, causing desorption of oxygen functional groups and reordering of the graphene basal plane. As such, the as-obtained rGO exhibited pristine CVD graphene-like features in the Raman spectrum showing sharp G an 2D peaks and a nearly absence of D peak. In contrast, the rGO derived from conventional thermal reduction remains highly disordered, as indicated by the presence of an intense and broad disorder D band and the absence of the 2D band in the Raman spectra (**Figure 3b**). The XPS results were well in agreement with the Raman results. Owning to the large arcing which may possibly resulted in an extremely high temperature, the oxygen content of the MW-rGO was about 4%, lower than that theoretically predicted for rGO after annealing at 1,500 K (15–25%). Aberration corrected HR-TEM (**Figure 3c**) also suggested a highly ordered structure, which suggests that there is some reorganization of the carbon bonding during microwave reduction, along with removal of oxygen facilitated by achieving exceptionally high temperatures.

Jiang et al. (2018) further modified Voiry's strategy and developed a triggered microwave-assisted reduction of graphene oxide. In their work, 1 wt% $CaCl_2$ aqueous solution was used to treat one side of the filter paper while graphene oxide was dropped onto the other side of the filter paper. Subsequently,

TABLE 1 | Characteristics of rGO products derived from different microwave-assisted chemical reduction.

	Experiment conditions					Results					References
	Frequency	MW power	MW time	Atmosphere	Reducing agent	XRD (Peak location)	XPS (C/O)	Raman (I_D/I_G)	Conductivity (S m^{-1})	TGA (significant mass loss T)	
1	2.45 GHz	1,000 W	1 min	Air	hydrazine hydrate	No peak		0.12		750°C	Hassan et al., 2009
2	2.45 GHz	250 W	10 min	Air	hydrazine hydrate	~15°	8.1				Elazab et al., 2015
3	2.45 GHz	300 W	10 min	Air	hydrazine hydrate		5.28				Li et al., 2013
4	2.45 GHz	1,200 W	2 min	Air	DMSO	~24°					Zedan et al., 2010
5	2.45 GHz	800 W	10 min	N_2	DMAc	No peak	5.46	0.96	200	~500°C	Chen et al., 2010
6	2.45 GHz	750 W	2 min	Air	DMF			0.94			Liu et al., 2011
7	2.45 GHz	100 W	30 min	Air	DMF	13.4°	6.13	0.95	29.9		Zhao et al., 2014

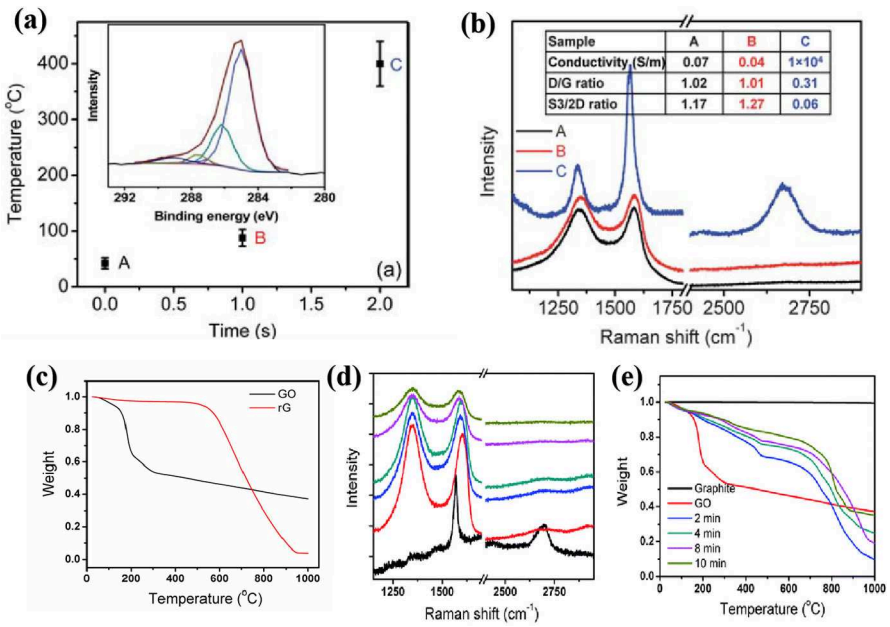

FIGURE 2 | (a) The temperature rises of graphite oxide film under 6.425 GHz, 500 W MW within 2 s. Inset is XPS data of rGO. **(b)** Raman spectroscopy of graphite oxide at (A) before MW; (B) imminent to transition state; (C) after being reduced to graphene, respectively. **(c)** The TGA data of GO and rGO reduced by 6.425 ± 1.150 GHz MW. Raman **(d)** and TGA **(e)** characteristics of graphite, graphite oxide and different types of rGO samples by 2.45 GHz MW irradiation. [Reprinted with permission from Li et al. (2010), copyright 2010 The Royal Society of Chemistry].

graphene oxide was treated with $CaCl_2$ solution and then washed with DI water, dried in air and pulled out from the filter paper. Finally, a small piece of rGO "paper" obtained by thermal annealing was placed on the as-obtained large graphene oxide paper to act as a trigger, as shown in **Figure 4a**. After 800 W microwave irradiation for 2 s in air, arc discharge process started. The irradiation was maintained for extra 3–5 s and high-quality microwave reduced graphene oxide paper was obtained. In XPS spectrum, the characteristic peak for C-O vanished, suggesting the significant removal efficiency of oxygen-containing group. Raman spectra of MW-rGO showed sharp G and 2D bands, and low-intensity D band. In contrast, the Raman spectra of rGO derived from conventional thermal reduction at 800°C showed a strong D band and none 2D band, indicating microwave heating is very beneficial for recovering the highly ordered graphene-like structures which was also confirmed by the conductivity. The sheet resistance of the MW-rGO was measured to be about 40 Ω cm^{-2}, far less than that (about 796 Ω cm^{-2}) of rGO prepared by 800°C annealing. They further examined the Raman spectra of graphene-triggered microwave reduction at different positions, and found the part of graphene oxide located nearest to the trigger was not reduced the best, as shown in **Figure 4b.** Hence, they proposed that the microwave reduction can be not only governed by a simple thermal

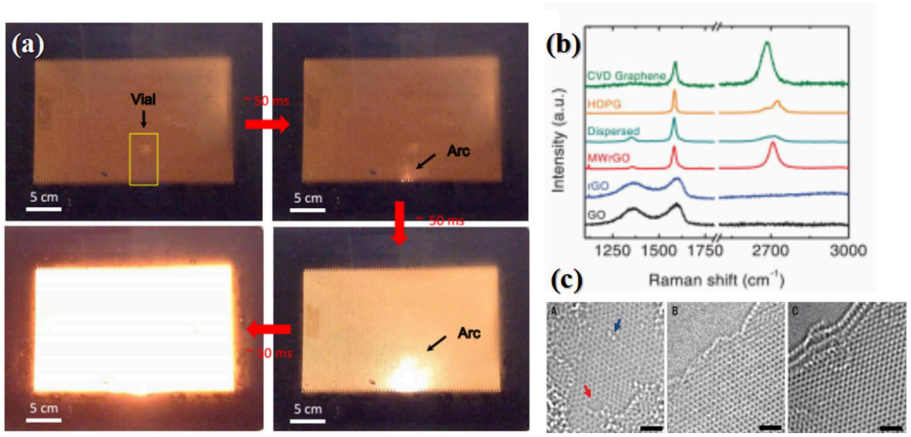

FIGURE 3 | (a) Digital picture showing the formation of arcs during graphene oxide microwaving. **(b)** Raman spectra of microwave-reduced GO (MW-rGO) and other different rGO samples. **(c)** HR-TEM of MW-rGO nanosheets. (A) single-layer rGO presenting high density of defects. HR-TEM of (B) Bilayer and (C) trilayer MW-rGO showing highly ordered structure. The red arrow denotes a hole; the blue arrow indicates an oxygen functional group, scale bars, 1 nm. [Reprinted with permission from Voiry et al. (2016), Copyright 2016 American Association for the Advancement of Science].

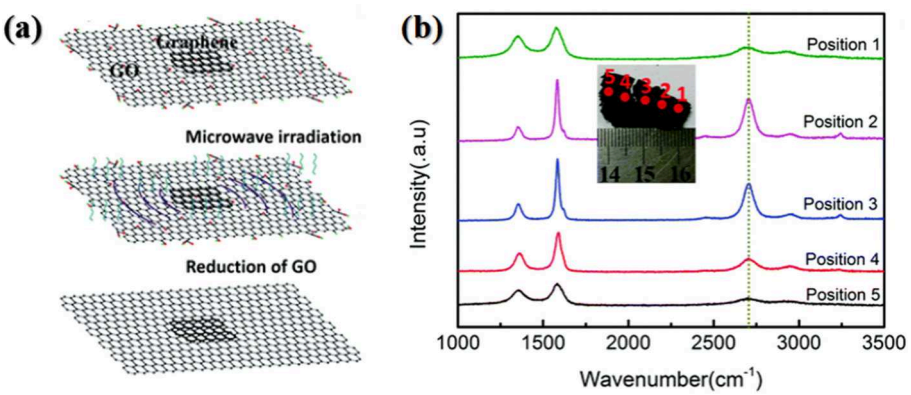

FIGURE 4 | (a) Schematic diagram of the fabrication process of graphene (rGO paper)-triggered microwave reduction. **(b)** Raman spectra of five measurement points on a strip MW-rGO sample. [Reprinted with permission from Jiang et al. (2018), copyright 2018 The Royal Society of Chemistry].

reduction process but the result of the thermal effect and arc discharge (Jiang et al., 2018).

Instead of putting a small piece of graphene as the trigger, Wan et al. (2018) put a fully bended copper wire inside graphene oxide to absorb 2.45 GHz microwave irradiation intensively and hence trigger immediate arcs and fire to reduce the graphene oxide, as shown in **Figures 5a,b**. Microwave treatment is applied for 2 s one time. The decreasing D band in Raman spectra under different microwave treating times indicate that high crystalline graphene was obtained after microwave treatment.

Low-temperature reduction of graphene oxide is of great importance when graphene oxide film was deposited on glass or plastic substrates. Han et al. (2015) demonstrated microwave-assisted low-temperature thermal reduction of few-layered graphene oxide film. Specifically, they put the graphene oxide film at the center of the highest magnetic field in a single mode microwave reactor which was operated at 2.45 GHz with a power of 42 W to ensure that the temperature was below 250°C during the whole process. After 5 min treatment in the air, I_D/I_G in the Raman spectrum of the product decreased from 2.89 to 1.56 and C/O derived from XPS results increased from 7.8 to 17.5. In addition, microwave-enabled exfoliation leading to thinner pieces was also observed in their work.

The characteristics of the as-obtained rGO products derived from different microwave-assisted thermal reduction of graphene oxide methods are summarized and listed in **Table 2**. Arc discharge caused by microwave irradiation is very beneficial for obtaining high-quality rGO, as evidence by the short reaction time, the low I_D/I_G values, the high C/O values and the conductivity values of most as-derived rGO. It is worth to note that rGO containing only 4% oxygen and exhibiting pristine CVD graphene-like features in the Raman spectrum was successfully fabricated via this reducing strategy. Besides, owning to the ultra-rapid treating process, protecting atmosphere is not always necessary. However, too long treatment time would result in re-oxidation and consequently rGO with worse quality when

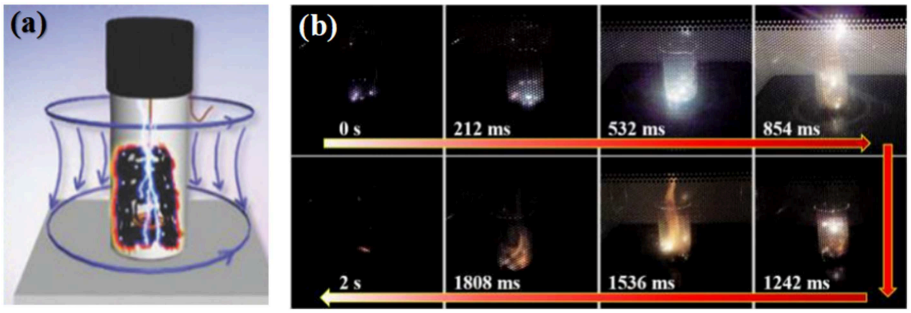

FIGURE 5 | (a) Schematic diagram of the microwave combustion system. **(b)** Digital picture showing the formation of arcs during microwave process. [Reprinted with permission from Wan et al. (2018), copyright 2018 John Wiley and Sons].

the reduction is done in the air. Since the amounts of GO samples and the microwave heating chambers in different work were different, which would affect the power intensity imposed on the GO, it is also difficult to draw a conclusion regarding the effect of microwave power here.

Microwave-Assisted Simultaneous Exfoliation and Reduction of Graphite Oxide

Beside of direct reduction of graphene oxide to yield rGO, thermal shock like flash-assisted simultaneous exfoliation and reduction of graphite oxide at temperatures up to 1,050°C has also been used. Theoretically, microwave heating which is well-known for its rapid heating feature is very promising in enabling simultaneous exfoliation and reduction of graphite oxide. In 2010, Zhu et al. (2010a) treated graphite oxide powder in microwave oven at 700 W for 1 min in ambient atmosphere. Large volume expansion as shown in **Figures 6a**,**b** accompanied with violent fuming followed by sparking was observed. They found that a minimum power of 280 W was required to expand the graphite oxide powder successfully, which was probably due to the insulating feature that resulted in inferior microwave absorption ability. After microwave treatment, the as-obtained rGO had a worm-like morphology, in which many regions are wrinkled and folded (**Figures 6c,d**). XPS results showed that C/O increased from 0.79 to 2.75 (**Figure 6e**). XRD spectrum showed a broad peak centered at $2\theta = 25°$. The conductivity was measured to be about 274 S m^{-1}.

Under microwave irradiation, graphite oxide itself might not be heated to a high enough temperature to cause its exfoliation and reduction efficiently due to its inferior microwave absorption ability. Scientists have tried several ways to come over this problem.

Park et al. (2011a) mixed graphite oxide powder with 10% graphene nanosheets to realized efficient exfoliation and reduction under microwave irradiation. The temperature rising rate was estimated to be 2,000°C/min, which was high enough to build up pressure to overcome the van der Waals forces between the graphene sheets in graphite oxide for exfoliation. Huge volume expansion was observed after 10 s, followed by arc after 40 s. SEM images (**Figure 7**) showed that the prepared rGO also had a worm-like structure composed of

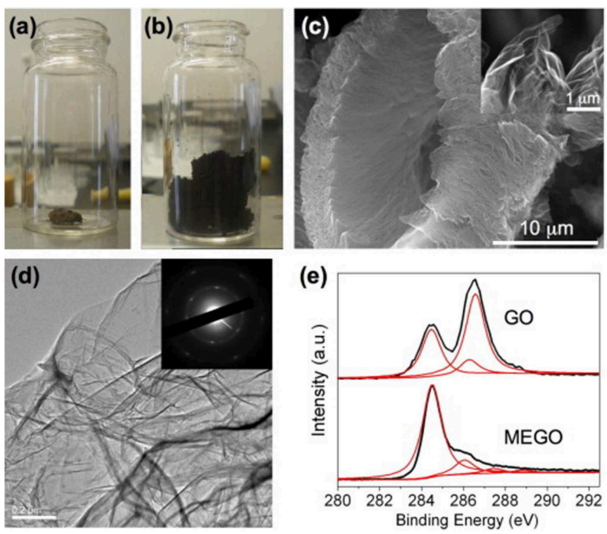

FIGURE 6 | Optical photos of graphite oxide before **(a)** and after **(b)** treatment in a microwave oven for 1 min. **(c)** Typical SEM image of as prepared microwave exfoliated graphite oxide (MEGO) by microwave irradiation with a high magnification SEM image in the inset showing the crumpled MEGO sheets. **(d)** Typical TEM image of the MEGO and the corresponding electron diffraction pattern. **(e)** XPS C1s spectra of GO and MEGO. [Reprinted with permission from Zhu et al. (2010a), Copyright 2010 Elsevier].

ultra-thin sheets, which is different from randomly agglomerated and wrinkled sheets prepared from solution-based reduction syntheses. HR-TEM images suggested the presence of single or a few layers of graphene nanosheets as shown in **Figure 7**. They further compared the effect of reduction atmosphere on the product quality. The rGO prepared in air, Ar, H_2+Ar (1:9) showed a C/O ratio of 3.6, 11.45, 18.5, respectively and I_D/I_G values of 0.853, 0.842, and 0.785, respectively in Raman spectra, respectively. The rGO prepared in Ar, H_2+Ar showed a conductivity of 7.41×10^2 and 1.25×10^3 S m^{-1}, respectively. Hydrogen containing atmosphere is the most effective because H_2O was formed instead of CO_2, which prevents the formation of vacancies and defects due to the loss of carbon atoms.

Wen et al. (2014) applied a sequential chemical reduction and microwave exfoliation and reduction of graphite oxide to

TABLE 2 | Characteristics of rGO products obtained by different microwave-assisted thermal reduction.

	Experiment conditions				Results					References
	Frequency	MW power	MW time	Atmosphere	XRD (peak location)	XPS (C/O)	Raman (I_D/I_G)	Conductivity	TGA (significant mass loss T)	
1	2.45 GHz	42 W	5 min	Air		17.5	1.56	6×10^3 Ω cm^{-2}		Han et al., 2015
2	6.425 GHz	500 W	2 s	Air			0.3	1×10^4 S m^{-1}	668°C	Li et al., 2010
3	2.45 GHz	800 W	5–7 s	Air	25.6°		0.32	40 Ω cm^{-2}		Jiang et al., 2018
				N_2			0.14			
4	2.45 GHz	1,000 W	1–2 s	Ar			<0.1			Voiry et al., 2016
5	2.45 GHz	1,000 W	8 min	Air					800°C	Li et al., 2010
6	2.45 GHz		2–40 s	Air	No peak					Wan et al., 2018

TABLE 3 | Characteristics of rGO products derived from different microwave-assisted simultaneous thermal exfoliation and reduction.

	Experiment conditions				Results					Additional information	References
	Frequency	MW power	MW time	Atmosphere	XRD (peak location)	XPS (C/O)	Raman (I_D/I_G)	Conductivity (S m^{-1})	TGA (significant mass loss T)		
1	2.45 GHz	700 W	1 min	Air	25°	2.75		274	~500°C		Zhu et al., 2010a
2	2.45 GHz	1,600 W	50 s	Air		3.6	0.853				Park et al., 2011b
				Ar		11.45	0.842	7.41×10^2			
				Ar+H_2		18.5	0.785	1.25×10^3			
3	5.8 GHz	1,400 W	10 min	N_2		7.24	~0.7	7.63×10^2			Wen et al., 2014
						10.33	~1.07	1.19×10^4		Pretreated by $NaBH_4$, and Raman beacomes worse. Maybe the MW not be sufficient to repair the large amount of defects caused by $NaBH_4$	
4	2.45 GHz	1,000 W	1 min	N_2	~12&24°	2.42			~450°C		Pokharel et al., 2014
			2 min		~22°	5.78					
			3 min		26.3°	10.39					

produce rGO. Specifically, graphite oxide powder was treated by $NaBH_4$ at 95°C for 2 h, and subsequently made into a film, which was microwave irradiated at 5.8 GHz with a power of 1,400 W for 10 min in N_2. After $NaBH_4$ treatment, a C/O value of 3.84, an I_D/I_G value of 1.05 in Raman, and a conductivity of 1.41×10^2 S m^{-1} were obtained. During the microwave treatment, the sample expanded to a loose floc and transmitted bright orange light, leading to ultrathin sheets with a C/O ratio of 10.33, an I_D/I_G ratio of 1.07 in the Raman spectrum and a conductivity of 1.19×10^4 S m^{-1}. Sole microwave irradiation at 5.8 GHz with a power of 1,400 W for 10 min without a preceding chemical reduction process gave yield to a C/O of 7.24 and an I_D/I_G of 0.89 in Raman spectrum. This demonstrated that solid-state microwave irradiation not only removed oxygen-containing groups, but also repaired defects on the graphene sheets while $NaBH_4$ though effective for removing oxygen-containing groups may induce more defects. Further, through XPS analysis of content of C-O and C=O groups, they found that microwave irradiation removed C=O more readily than C-O while the chemical reduction method removed C-O more efficiently.

Pokharel et al. (2014) developed a multi-step reduction technique to obtain rGO from graphite oxide. In the first step, graphite oxide with a C/O of 0.83 was exfoliated within 1 min under microwave irradiation at 2.45 GHz with a power of 1,000 W in N_2 without becoming red. The expanded graphite

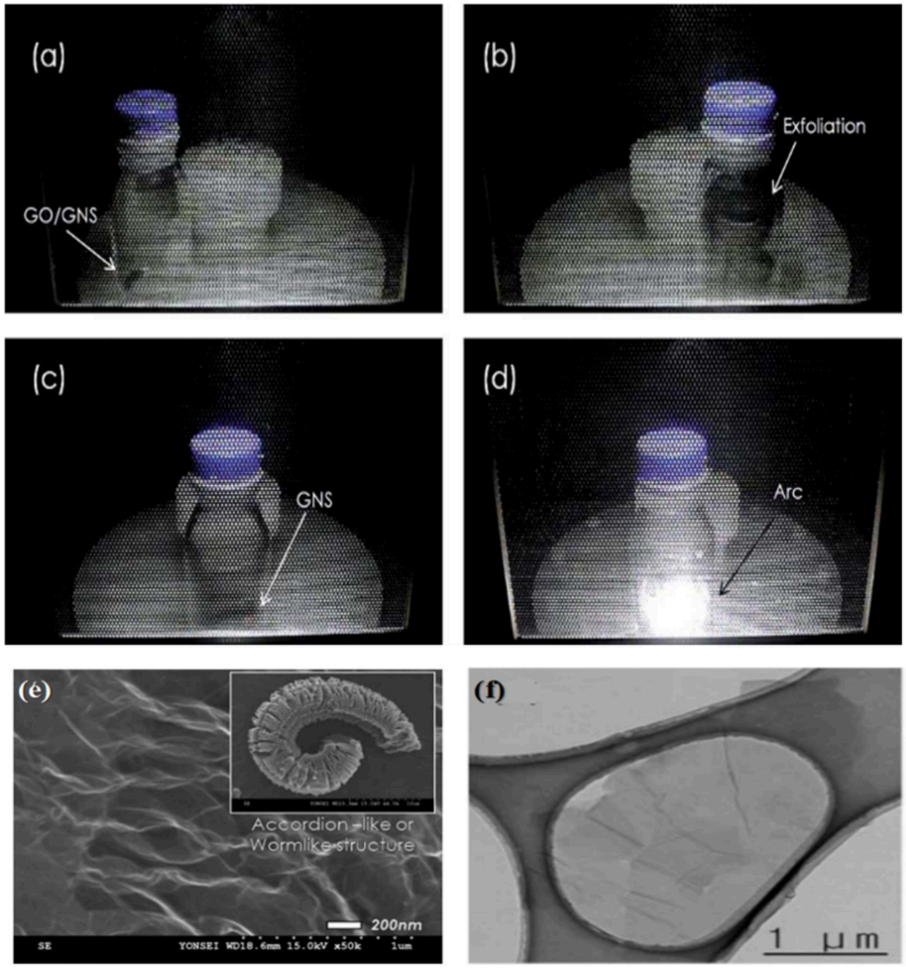

FIGURE 7 | Digital images of the sequence of the exfoliation process during solid-state microwave irradiation synthesis: **(a)** graphite oxide/graphene nanosheets (GNS) mixture powder, **(b)** exfoliation of graphite oxide/GNS powder. **(c)** GNS after exfoliation and **(d)** arc evolution from GNS. **(e)** SEM images of GNS by solid-state microwave irradiation synthesis. **(f)** HR-TEM images of GNS. [Reprinted with permission from Park et al. (2011a), copyright 2011 The Royal Society of Chemistry].

oxide had a C/O of 2.42. However, it was so loose that microwave could not concentrate on a definite area for further reduction of graphite oxide. Hence, in the second step, the expanded graphite oxide was collected and then exposed to additional microwave irradiation for 1 and 2 min, resulting in rGO showing a C/O ratio of 5.78 and 10.39, respectively.

The characteristics of the as-obtained rGO products derived from different microwave-assisted simultaneous thermal exfoliation and reduction of graphite oxide methods are summarized and listed in **Table 3**. As can be seen from the C/O values, I_D/I_G values, mass loss temperatures and conductivities, simultaneous exfoliation and reduction was not able to yield rGO with as high quality as those obtained from thermal reduction of graphene oxides. However, when combined with reducing atmosphere (i.e., H_2) or pretreatment with strong reducing reagents ($NaBH_4$), the reduction degree could be greatly enhanced.

PERSPECTIVES

It is expected that the explored methods for microwave-assisted reduction of graphene/graphite oxide into high-quality rGO could be extended to fabrication of graphene composites. The microwave-induced arc facilitated short reaction time at high temperature is not only beneficial for getting high-quality rGO, but also promising in facilitating the formation of high-quality nanomaterials (such as metal nanocrystals, metal oxides nanocrystals, and so on) with advanced performance. In addition, the methods could be extended to fabrication of other conductive materials that could trigger sparks under microwave irradiation, like graphene does.

AUTHOR CONTRIBUTIONS

All authors listed have made a substantial, direct and intellectual contribution to the work, and approved it for publication.

FUNDING

This work was financially supported by the National Natural Science Foundation of China (Grant No. 61801314), National Natural Science Foundation of China (Grant No. 61731013), Fundamental Research Funds for the Central Universities of China (Grant No. YJ201703).

REFERENCES

Akhavan, O. (2015). Bacteriorhodopsin as a superior substitute for hydrazine in chemical reduction of single-layer graphene oxide sheets. *Carbon* 81, 158–166. doi: 10.1016/j.carbon.2014.09.044

Bak, S., Kim, D., and Lee, H. (2016). Graphene quantum dots and their possible energy applications: a review. *Curr. Appl. Phys.* 16, 1192–1201. doi: 10.1016/j.cap.2016.03.026

Bastiurea, M., Rodeanu, M. S., Dima, D., Murarescu, M., and Andrei, G. (2015). Thermal and mechanical properties of polyester composites with graphene oxide and graphite. *Dig. J. Nanomater. Biostruct.* 10, 521–533.

Basu, R., Kinnamon, D., and Garvey, A. (2016). Graphene and liquid crystal mediated interactions. *Liq. Cryst.* 43, 2375–2390. doi: 10.1080/02678292.2016.1197429

Bi, H., Xie, X., Yin, K., Zhou, Y., Wan, S., He, L., et al. (2012). Hierarchical nanocomposites derived from nanocarbons and layered double hydroxides—properties, synthesis, and applications. *Adv. Funct. Mater.* 22, 4421–4425. doi: 10.1002/adfm.201102222

Cao, M.-S., Wang, X.-X., Cao, W.-Q., and Yuan, J. (2015). Ultrathin graphene: electrical properties and highly efficient electromagnetic interference shielding. *J. Mater. Chem. C* 3, 6589–6599. doi: 10.1039/c5tc01354b

Chabot, V., Higgins, D., Yu, A., Xiao, X., Chen, Z., and Zhang, J. (2014). A review of graphene and graphene oxide sponge: material synthesis and applications to energy and the environment. *Energ. Environ. Sci.* 7, 1564–1596. doi: 10.1039/c3ee43385d

Chatterjee, S. G., Chatterjee, S., Ray, A. K., and Chakraborty, A. K. (2015). Graphene-metal oxide nanohybrids for toxic gas sensor: a review. *Sensors Actuat. B Chem.* 221, 1170–1181. doi: 10.1016/j.snb.2015.07.070

Chen, W., and Yan, L. (2010). Preparation of graphene by a low-temperature thermal reduction at atmosphere pressure. *Nanoscale* 2, 559–563. doi: 10.1039/b9nr00191c

Chen, W., Yan, L., and Bangal, P. R. (2010). Preparation of graphene by the rapid and mild thermal reduction of graphene oxide induced by microwaves. *Carbon* 48, 1146–1152. doi: 10.1016/j.carbon.2009.11.037

Das, T. K., and Prusty, S. (2013). Graphene-based polymer composites and their applications. *Polym. Plast. Technol.* 52, 319–331. doi: 10.1080/03602559.2012.751410

Dreyer, D. R., Park, S., Bielawski, C. W., and Ruoff, R. S. (2010). The chemistry of graphene oxide. *Chem. Soc. Rev.* 39, 228–240. doi: 10.1039/B917103G

Elazab, H. A., Siamaki, A. R., Moussa, S., Gupton, B. F., and Elshall, M. S. (2015). Highly efficient and magnetically recyclable graphene-supported Pd/Fe_3O_4 nanoparticle catalysts for suzuki and heck cross-coupling reactions. *Appl. Catal. A Gen.* 491, 58–69. doi: 10.1016/j.apcata.2014.11.033

Eswaraiah, V., Sankaranarayanan, V., and Ramaprabhu, S. (2011). Functionalized graphene-PVDF foam composites for EMI shielding Macromol. *Mater. Eng.* 296, 894–898. doi: 10.1002/mame.201100035

Gannavarapu, K. P., Azizighannad, S., Muthukumar, S., Mitra, S., and Dandamudi, R. B. (2018). Microwave-assisted biogenic synthesis of metal-decorated reduced graphene oxide and their electrochemical properties. *ChemistrySelect* 3, 13438–13441. doi: 10.1002/slct.201803420

Gao, X., Jang, J., and Nagase, S. (2010). Hydrazine and thermal reduction of graphene oxide: reaction mechanisms, product structures, and reaction design. *J. Phys. Chem. C* 114, 832–842. doi: 10.1021/jp909284g

Han, H. J., Chen, Y. N., and Wang, Z. J. (2015). Effect of microwave irradiation on reduction of graphene oxide films. *Rsc Adv.* 5, 92940–92946. doi: 10.1039/c5ra19268d

Han, Q., Chen, N., Zhang, J., and Qu, L. (2017). Graphene/graphitic carbon nitride hybrids for catalysis. *Mater. Horiz.* 4, 832–850. doi: 10.1039/c7mh00379j

Hassan, H. M. A., Abdelsayed, V., Khder, A. E. R. S., Abouzeid, K. M., Terner, J., El-Shall, M. S., et al. (2009). Microwave synthesis of graphene sheets supporting metal nanocrystals in aqueous and organic media. *J. Mater. Chem.* 19, 3832–3837. doi: 10.1039/B906253J

Hu, M., Yao, Z., and Wang, X. (2017). Graphene-based nanomaterials for catalysis. *Ind. Eng. Chem. Res.* 56, 3477–3502. doi: 10.1021/acs.iecr.6b05048

Hur, S. H., and Park, J.-N. (2013). Graphene and its application in fuel cell catalysis: a review. *Asia Pac. J. Chen. Eng.* 8, 218–233. doi: 10.1002/apj.1676

Jiang, W. S., Yang, C., Chen, G. X., Yan, X. Q., Chen, S. N., Su, B. W., et al. (2018). Preparation of high-quality graphene using triggered microwave reduction under an air atmosphere. *J. Mater. Chem. C* 6, 1829–1835. doi: 10.1039/C7TC03957C

Jones, D. A., Lelyveld, T. P., Mavrofidis, S. D., Kingman, S. W., and Miles, N. J. (2002). Microwave heating applications in enviromnental engineering—a review. *Resour. Conserv. Recy.* 34, 75–90. doi: 10.1016/s0921-3449(01)00088-x

Kappe, C. O. (2004). Controlled microwave heating in modern organic synthesis. *Angew. Chem. Int. Edit.* 43, 6250–6284. doi: 10.1002/anie.200400655

Katkov, V. L., and Osipov, V. A. (2017). Journal of vacuum science & technology. *J. Vac. Sci. Technol. B* 2017, 35. doi: 10.1116/1.4995380

Kaur, M., Kaur, M., and Sharma, V. K. (2018). Nitrogen-doped graphene and graphene quantum dots: a review onsynthesis and applications in energy, sensors and environment. *Adv. Colloid Interfac.* 59, 44–64. doi: 10.1016/j.cis.2018.07.001

Kumar, D., Raghavan, C. M., Sridhar, C., Shin, J. H., Ryu, S. H., Jang, K., et al. (2015). Microwave-assisted synthesis, characterization of reduced graphene oxide, and its antibacterial activity. *B. Korean Chem. Soc.* 36, 2034–2038. doi: 10.1002/bkcs.10394

Le, L. T., Ervin, M. H., Qiu, H., Fuchs, B. E., and Lee, W. Y. (2011). Graphene supercapacitor electrodes fabricated by inkjet printing and thermal reduction of graphene oxide. *Electrochem. Commun.* 13, 355–358. doi: 10.1016/j.elecom.2011.01.023

Li, J., and Wu, N. (2015). Graphene-supported metal/metal oxide nanohybrids: synthesis and applications in heterogeneous catalysis. *Catal. Sci. Technol.* 5, 1360–1384. doi: 10.1002/chin.201537235

Li, J., Yang, Z., Qiu, H., Dai, Y., Zheng, Q., Zheng, G.-P., et al. (2013). Microwave-assisted simultaneous reduction and titanate treatment of graphene oxide. *J. Mater. Chem. A* 1, 11451–11456. doi: 10.1039/C3TA12228J

Li, X., Rui, M., Song, J., Shen, Z., and Zeng, H. (2015). Carbon and graphene quantum dots for optoelectronic and energy devices: a review. *Adv. Funct. Mater.* 25, 4929–4947. doi: 10.1002/adfm.201501250

Li, Z., Yao, Y., Lin, Z., Moon, K. S., Lin, W., and Wong, C. (2010). Ultrafast, dry microwave synthesis of graphene sheets. *J. Mater. Chem.* 20, 4781–4783. doi: 10.1039/c0jm00168f

Li,Y., Li, T., Yao, M., and Liu, S. (2012). Metal-free nitrogen-doped hollow carbon spheres synthesized by thermal treatment of poly(o-phenylenediamine) for oxygen reduction reaction in direct methanol fuel cell applications. *J. Mater. Chem.* 22, 10911–10917. doi: 10.1039/c2jm30781b

Lin, F., Tong, X., Wang, Y., Bao, J., and Wang, Z. M. (2015). Graphene oxide liquid crystals: synthesis, phase transition, rheological property, and applications in optoelectronics and display. *Nanoscale Res. Lett.* 10:435. doi: 10.1186/s11671-015-1139-1

Lin, Z., Yao, Y., Li, Z., Liu, Y., Li, Z., and Wong, C. P. (2010). Solvent-assisted thermal reduction of graphite oxide. *J. Phys. Chem. C* 114, 14819–14825. doi: 10.1021/jp1049843

Liu, S., Tian, J., Wang, L., and Sun, X. (2011). Microwave-assisted rapid synthesis of ag nanoparticles/graphene nanosheet composites and their application for hydrogen peroxide detection. *J. Nanopart. Res.* 13, 4539–4548. doi: 10.1007/s11051-011-0410-3

Liu, Y., Yuan, L., Yang, M., Zheng, Y., Li, L., Gao, L., et al. (2014). Giant enhancement in vertical conductivity of stacked CVD graphene sheets by self-assembled molecular layers. *Nat. Commun.* 2014, 5. doi: 10.1038/ncomms6461

Mattevi, C., Kim, H., and Chhowalla, M. (2011). A review of chemical vapour deposition of graphene on copper. *J. Mater. Chem.* 21, 3324–3334. doi: 10.1039/c0jm02126a

Narayan, R., Kim, J. E., Kim, J. Y., Lee, K. E., and Kim, S. O. (2016). Graphene oxide liquid crystals: discovery, evolution and applications. *Adv. Mater.* 28, 3045–3068. doi: 10.1002/adma.201505122

Novoselov, K. S., Jiang, D., Schedin, F., Booth, T. J., Khotkevich, V. V., Morozov, S. V., et al. (2005). Two-dimensional atomic crystals. *Proc. Natl. Acad. Sci. U.S.A.* 102, 10451–10453. doi: 10.1073/pnas.0502848102

Park, S., An, J., Potts, J. R., Velamakanni, A., Murali, S., and Ruoff, R. S. (2011b). Hydrazine-reduction of graphite- and graphene oxide. *Carbon* 49, 3019–3023. doi: 10.1016/j.carbon.2011.02.071

Park, S. H., Bak, S. M., Kim, K. H., Jegal, J. P., Lee, S. I., Lee, J., et al. (2011a). Solid-state microwave irradiation synthesis of high quality graphene nanosheets under hydrogen containing atmosphere. *J. Mater. Chem.* 21, 680–686. doi: 10.1039/c0jm01007c

Pokharel, P., Truong, Q. T., and Lee, D. S. (2014). Multi-step microwave reduction of graphite oxide and its use in the formation of electrically conductive graphene/epoxy composites. *Compos. Part B Eng.* 64, 187–193. doi: 10.1016/j.compositesb.2014.04.013

Qin, F., and Brosseau, C. (2012). A review and analysis of microwave absorption in polymer composites filled with carbonaceous particles. *J. Appl. Phys.* 111, 61301–61301. doi: 10.1063/1.3688435

Schwenke, A. M., Hoeppener, S., and Schubert, U. S. (2015). Synthesis and modification of carbon nanomaterials utilizing microwave heating. *Adv. Mater.* 27, 4113–4141. doi: 10.1002/adma.201500472

Shao, Y., Wang, J., Wu, H., Liu, J., Aksay, I. A., and Lin, Y. (2010). Graphene based electrochemical sensors and biosensors: a review. *Electroanalysis* 22, 1027–1036. doi: 10.1002/elan.200900571

Song, W.-L., Cao, M.-S., Lu, M.-M., Bi, S., Wang, C.-Y., Liu, J., et al. (2014). Flexible graphene/polymer composite films in sandwich structures for effective electromagnetic interference shielding. *Carbon* 66, 67–76. doi: 10.1016/j.carbon.2013.08.043

Stankovich, S., Dikin, D. A., Piner, R. D., Kohlhaas, K. A., Kleinhammes, A., Jia, Y., et al. (2007). Synthesis of graphene-based nanosheets via chemical reduction of exfoliated graphite oxide. *Carbon* 45, 1558–1565. doi: 10.1016/j.carbon.2007.02.034

Stobinski, L., Lesiak, B., Malolepszy, A., Mazurkiewicz, M., Mierzwa, B., Zemek, J., et al. (2014). Graphene oxide and reduced graphene oxide studied by the XRD, TEM and electron spectroscopy methods. *J. Electron Spectrosc.* 195, 145–154. doi: 10.1016/j.elspec.2014.07.003

Strankowski, M., Wlodarczyk, D., Piszczyk, A., and Strankowska, J. (2016). Polyurethane nanocomposites containing reduced graphene oxide, FTIR, Raman, and XRD studies. *J. Spectrosc.* doi: 10.1155/2016/7520741

Thomassin, J.-M., Jerome, C., Pardoen, T., Bailly, C., Huynen, I., and Detrembleur, C. (2013). Polymer/carbon based composites as electromagnetic interference (EMI) shielding materials. *Mat. Sci. Eng. R.* 74, 211–232. doi: 10.1016/j.mser.2013.06.001

Thostenson, E. T., and Chou, T. W. (1999). Microwave processing: fundamentals and applications. *Compos. Part A Appl. Sci. Manufact.* 30, 1055–1071. doi: 10.1016/s1359-835x(99)00020-2

Tompsett, G. A., Conner, W. C., and Yngvesson, K. S. (2006). Microwave synthesis of nanoporous materials. *ChemPhysChem* 7, 296–319. doi: 10.1002/cphc.200500449

Voiry, D., Yang, J., Kupferberg, J., Fullon, R., Lee, C., Jeong, H. Y., et al. (2016). High-quality graphene via microwave reduction of solution-exfoliated graphene oxide. *Science* 353, 1413–1416. doi: 10.1126/science.aah3398

Wan, J., Huang, L., Wu, J., Xiong, L., Hu, Z., Yu, H., et al. (2018). Microwave combustion for rapidly synthesizing pore-size-controllable porous graphene. *Adv. Funct. Mater.* 28:382. doi: 10.1002/adfm.201800382

Wang, K., Feng, T., Qian, M., Ding, H., Chen, Y., and Sun, Z. (2011). The field emission of vacuum filtered graphene films reduced by microwave. *Appl. Surf. Sci.* 257, 5808–5812. doi: 10.1016/j.apsusc.2011.01.109

Wang, Q., and Arash, B. (2014). A review on applications of carbon nanotubes and graphenes as nano-resonator sensors. *Comp. Mater. Sci.* 82, 350–360. doi: 10.1016/j.commatsci.2013.10.010

Wen, C., Zhao, N., Zhang, D. W., Wu, D., Zhang, Z.-B., and Zhang, S.-L. (2014). Efficient reduction and exfoliation of graphite oxide by sequential chemical reduction and microwave irradiation. *Synthetic Met.* 194, 71–76. doi: 10.1016/j.synthmet.2014.04.023

Xiao, L., Liao, L., and Liu, L. (2013). Chemical modification of graphene oxide with carbethoxycarbene under microwave irradiation. *Chem. Phys. Lett.* 556, 376–379. doi: 10.1016/j.cplett.2012.11.084

Zedan, A. F., Sappal, S., Moussa, S., and El-Shall, M. S. (2010). Ligand-controlled microwave synthesis of cubic and hexagonal cdse nanocrystals supported on graphene photoluminescence quenching by graphene. *J. Phys. Chem. C* 114, 19920–19927. doi: 10.1021/jp107297x

Zhang, H. B., Wang, J. W., Yan, Q., Zheng, W. G., Chen, C., and Yu, Z. Z. (2011). Vacuum-assisted synthesis of graphene from thermal exfoliation and reduction of graphite oxide. *J. Mater. Chem.* 21, 5392–5397. doi: 10.1039/C1JM10099H

Zhang, Y., Zhang, L., and Zhou, C. (2013). Review of chemical vapor deposition of graphene and related applications. *Accounts Chem. Res.* 46, 2329–2339. doi: 10.1021/ar300203n

Zhao, N., Wen, C. Y., Zhang, D. W., Wu, D. P., Zhang, Z. B., and Zhang, S. L. (2014). Liquid-phase and solid-phase microwave irradiations for reduction of graphite oxide. *Chinese Phys. B* 23:128101. doi: 10.1088/1674-1056/23/12/128101

Zhu, Y., Murali, S., Stoller, M. D., Velamakanni, A., Piner, R. D., and Ruoff, R. S. (2010a). Microwave assisted exfoliation and reduction of graphite oxide for ultracapacitors. *Carbon* 48, 2118–2122. doi: 10.1016/j.carbon.2010.02.001

Zhu, Y., Stoller, M. D., Cai, W., Velamakanni, A., Piner, R. D., Chen, D., et al. (2010b). Exfoliation of graphite oxide in propylene carbonate and thermal reduction of the resulting graphene oxide platelets. *Acs Nano* 4, 1227–1233. doi: 10.1021/nn901689k

Conflict of Interest Statement: The authors declare that the research was conducted in the absence of any commercial or financial relationships that could be construed as a potential conflict of interest.

frontiers in Chemistry

ORIGINAL RESEARCH
published: 12 June 2019
doi: 10.3389/fchem.2019.00421

Functional Ionic Liquid Modified Core-Shell Structured Fibrous Gel Polymer Electrolyte for Safe and Efficient Fast Charging Lithium-Ion Batteries

Xiaoxia Liu, Yufei Ren, Lan Zhang and Suojiang Zhang**

Beijing Key Laboratory of Ionic Liquids Clean Process, CAS Key Laboratory of Green Process and Engineering, Institute of Process Engineering, Chinese Academy of Sciences, Beijing, China

OPEN ACCESS

Edited by:
Oleksandr Malyi, University of Oslo, Norway

Reviewed by:
Xianhong Rui, Guangdong University of Technology, China
Weimin Kang, Tianjin Polytechnic University, China
Huarong Xia, Nanyang Technological University, Singapore

***Correspondence:**
Lan Zhang
zhangl@ipe.ac.cn
Suojiang Zhang
sjzhang@ipe.ac.cn

Specialty section:
This article was submitted to Electrochemistry, a section of the journal Frontiers in Chemistry

Received: 16 March 2019
Accepted: 21 May 2019
Published: 12 June 2019

Citation:
Liu X, Ren Y, Zhang L and Zhang S (2019) Functional Ionic Liquid Modified Core-Shell Structured Fibrous Gel Polymer Electrolyte for Safe and Efficient Fast Charging Lithium-Ion Batteries. Front. Chem. 7:421. doi: 10.3389/fchem.2019.00421

Fast charging is of enormous concerns in the development of power batteries, while the low conductivity and lithium ion transference number in current electrolytes degraded the charge balance, limited the rate performance, and even cause safety issues for dendrite growth. Combine inorganic fillers and ionic liquid plasticizer, here in this paper we prepared a core-shell structured nanofibrous membrane, by incorporating with carbonate based electrolyte, a gel polymer electrolyte (GPE) with high conductivity, outstanding Li^+ transference number was obtained. Notably, the Li/electrolyte/$LiNi_{0.6}Co_{0.2}Mn_{0.2}O_2$ (NCM622) half-cell with this composite electrolyte delivers a reversible capacity of 65 mAh/g at 20C, which is 13 times higher than that of with Celgard 2325 membrane. It also shows enhanced long-term cycle stability at both 3C and 5C for the suppression of lithium dendrite. This organic-inorganic co-modified GPE guarantees the fast charging ability and safety of LIBs, thus provides a promising method in high performance electrolyte design.

Keywords: lithium ion battery, fast charging, core-shell structure, nanofibrous separator, safety

INTRODUCTION

With the increasing demand for energy consumption and the continuous improvement for environmental protection, the development of sustainable and renewable energy is urgently needed currently. Lithium ion batteries (LIBs) have been widely used in the power battery, energy storage applications, portable electronic equipment and other fields, owing to its inherent advantages such as high energy density, high power density, long cycle life, no memory effect, and environmental friendliness (Gao et al., 2009; Goodenough and Kim, 2010; Etacheri et al., 2011; Scrosati et al., 2011; Lu et al., 2014a; Varzi et al., 2016; Tan et al., 2018). Nevertheless, high-capacity and high-power LIBs are facing more and more challenges such as high power output, rapid charge/discharge capability and safety under dynamic conditions (Zhu et al., 2013; Xie et al., 2014; Zhang J. et al., 2014; Li et al., 2018, 2019), and it is of particularly importance to investigate methods to guarantee the safety of LIBs with enhanced fast charge capability (Rui et al., 2016; Tan et al., 2018).

LIBs generally compose of anode, cathode, electrolyte, and packing material. The electrolyte, which including polymer separator and liquid electrolyte in commercial LIBs, mainly plays two key roles: blocking the direct contact between the electrodes to avoid internal electrical short circuit and

acting as the Li^+ transport passage (Tarascon and Armand, 2001; Xiao et al., 2009; Huang, 2010; Lee et al., 2014). Therefore, the electrolyte not only directly affects the LIB electrochemical performance, such as cycle stability and rate capability, but also, it has significant influence on the safety of LIBs. Most commercial LIBs adopt polyolefin [such as polyethylene (PE) and polypropylene (PP)] membranes (Huang, 2010; Kim et al., 2015; Shen et al., 2018) and $LiPF_6$/carbonates electrolyte, based on which satisfying cycle performances have achieved, while the rate capability and safety, especially during quick charge, is yet to be enhanced.

The major issue in fast charging LIBs is the poor kinetics caused by the sluggish ion transport in the cell, which will probably lead to large polarization and low reversible capacity, furthermore, when the anode potential is lower than that of Li plating, dendrite will be generated and may short the cell thus cause safety concerns.

Electrolyte holds significant influence on both rate capability and safety, on one hand, ionic conductivity and Li^+ transference number is the major factor to control the battery kinetics (Diederichsen et al., 2017), on the other hand, the separator, which blocks the direct contact between electrodes, should also work as a physical barrier to suppress the dendrite from shorting the battery (Jana et al., 2015; Shin et al., 2015; Zheng et al., 2018). Therefore, scientist made lots of efforts in electrolyte modification, including surface coating of the separator (Ghazi et al., 2017; Liu et al., 2017a,b; Zuo et al., 2017), doping inorganic nanoparticles in polymer to obtain composite electrolyte (Xiao et al., 2012; Chen et al., 2017; Kim et al., 2017; Wang et al., 2017; Shen et al., 2018), and electrostatic spinning to get nanofibrous membrane (Choi et al., 2003; Wu et al., 2015; Ma et al., 2017; Cheng et al., 2018). Thereinto, the nanofibrous membrane has large specific surface area, three-dimensional (3D) porous structure and high electrolyte uptake ability, on which the rate capability can be enhanced (Xiao et al., 2015; Liang et al., 2016; Park et al., 2017). What's more, functional groups can be easily introduced in the electrospining process, thereby endows the electrolyte with other properties, such as dendrite suppression (Lu et al., 2015a,b; Cheng et al., 2018; Deng et al., 2018), flame retardant (Lu et al., 2017; Jia et al., 2018; Sun et al., 2018), et al. Poly(vinylidene fluoride-co-hexafluoropropene) (PVDF-HFP) is considered as a potential polymer matrix for electrolyte not only as it has a low crystallinity which could promotes rapid ion conduction (Ali et al., 2018; Zhao et al., 2019), but also, it has high dielectric constant and low surface energy that may promote the compact deposition of metal Li (Lopez et al., 2018). It is reported the ionic conductivity of PVDF-HFP-based polymer electrolytes is up to 3.9 mS/cm (Xiao et al., 2012).

Ionic liquid modified gel polymer electrolytes (IL-GPE) have attracted much attention due to their good thermal stability and mechanical properties. Singh et al. studied imidazolyl ionic liquids and found that the EMIMFSI-based GPEs have excellent electrochemical stability, good compatibility and thermal stability(Singh et al., 2018). Guo et al. prepared the PVDF-HFP-LiTFSI/SiO_2/EMITFSI GPE with high thermal stability and good electrode compatibility (Guo et al., 2018). However, IL-GPE also has some shortcomings, such as lower ionic conductivity and lithium ion mobility (Zhou et al., 2015). In this work, a piperidine ionic liquid, 1-methyl-1-propylpiperidinium chloride (PPCl), and Li_2SiO_3 (LSO) nanoparticles were introduced into the PVDF-HFP matrix *via* coaxial electrospinning technology. The as prepared membrane has high porosity and electrolyte uptake, remarkable ionic conductivity, and outstanding electrochemical performance especially in quick charging. Commercial NCM622 cathode adopting this IL-GPE delivers a high reversible capacity of 65 mAh/g in 20C rate charge/discharging, which is 13 times higher than that of the cell adopting Celgard 2325 membrane.

EXPERIMENTAL SECTION

Materials

Poly (vinylidene fluoride-co-hexafluoropropene) (PVDF-HFP, Mw. ∼455,000), 1-methylpiperidine (97%), and (3-chloropropyl) trimethoxysilane (98%) were provided by Sigma-Aldrich. Li_2SiO_3 (LSO, 99%, Strem Chemicals), N, N-dimethylformamide (DMF, 99.5%, Beijing Chemical Works), $LiNi_{0.6}Co_{0.2}Mn_{0.2}O_2$ (NCM622, Beijing Dangsheng Material Technology Co., Ltd.), Super P (Imerys Graphite & Carbon), Polyvinylidene difluoride (PVDF, Solvay 5130), N-Methyl-2-pyrrolidone (NMP, 99.0%, Sinopharm Chemical Reagent Co., Ltd.), lithium tablet (Li, Tianjin Zhongneng Co., Ltd.), and polypropylene (PP, Japan Ube) were commercially available and used without further purification.

Preparation of the GPEs

The ionic liquid PPCl was synthesized according to the procedure reported before (Lu et al., 2012; Korf et al., 2014; Cheng et al., 2018), its structure and purity was also testified in our previous work (Xu et al., 2018). The core-shell structured 3D porous nanofiber membrane was prepared by the coaxial electrospinning technique on an ET-2535H machine (Ucalery Tech Inc., China), as shown in **Scheme 1**. To make composite nonwoven membrane, 80% (wt., similarly hereinafter) DMF was adopted in all the spinning solutions. The slurry for core spinning was prepared by mixing PPCl and PVDF-HFP in DMF solvent, wherein the weight ratio of PPCl: PVDF-HFP: DMF was fixed at 1:19:80. Correspondingly, the slurry for shell spinning was prepared by mixing LSO and PVDF-HFP in DMF solvent with a ratio of 2:18:80. The coaxial electrospinning equipment mainly contained a variable positive voltage of 15 kV and a negative voltage of −2kV, two syringe pumps, a spinneret consisting of two chambers and a collector. The pumped speed of the shell and core solutions supply were fixed at 0.25 and 0.15 mL/h, respectively, the distance between the needle tip and aluminum foil collector was 13 cm. The as prepared membrane has a thickness of 50 ± 5 μm, and was entitled by PHP@PHL. Accordingly, PVDF-HFP, PVDF-HFP-PPCl (PHP), and PVDF-HFP-LSO(PHL) nanofiber membrane was prepared by mixing PVDF-HFP in DMF (20:80), PPCl, and PVDF-HFP in DMF (1:19:80) or LSO and PVDF-HFP in DMF (2:18:80), respectively. The as-prepared nonwoven fiber membranes were cut into disc with a diameter of 16 mm, which were then dried in a vacuum oven at 60°C for 20 h to remove the residual solvent.

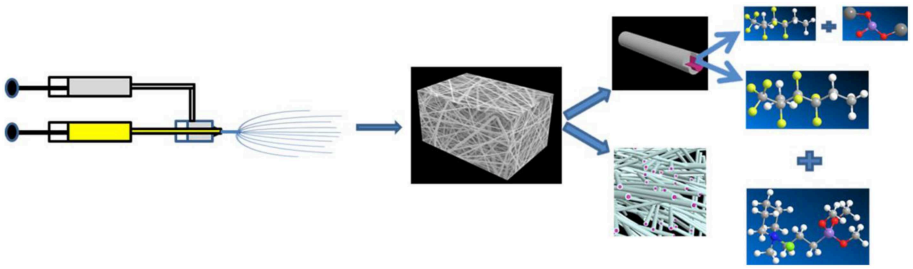

SCHEME 1 | Illustration of the preparation of the PHP@PHL membrane (Zhou et al., 2013).

In the end, the membranes were filled and swollen in a liquid electrolyte, 1.2 M $LiPF_6$ in ethylene carbonate (EC) and ethyl methyl carbonate (EMC) (3:7, weight ratio), for 30 min in an argon filled glove box to obtain the relevant GPEs.

Characterization of the Membranes and GPEs

The thickness of various films was recorded by measuring membrane apparatus (CH1ST, Shanghai Milite Precise Instrument Co., Ltd., China), and morphology of the membrane was studied by field-emission scanning electron microscopy (FE-SEM, JSM-7001F, JEOL, Japan). The field emission transmission electron microscopy (TEM, JEOL, JEM-2100) was used to test the core-shell structure of PHP@PHL nanoporous fiber membrane. The surface chemical composition of PHP@PHL was analyzed by X-ray photoelectron spectroscopy (XPS, ESCALAB 250Xi, Thermo Fisher Scientifec, America). Differential scanning calorimetry (DSC, Mettler-Toledo, Switzerland) was carried out to analyze the thermal behavior of all kinds of membranes. Samples were put into aluminum pans and the test temperature was set from 50 to 250°C with a heating rate of 5°C/min, under N_2 atmosphere. The porosity of various films was measured by soaking n-butanol for 2 h, then calculated using Equation (1): $P = (m_b/\rho_b)/(m_b/\rho_b + m_a/\rho_a) \times 100\%$, where m_a and m_b are the weights of separators and n-butanol, ρ_a and ρ_b are the density of separators and n-butanol, respectively (Xiao et al., 2012; Zhou et al., 2013). In an argon filled glove box, the electrolyte uptakes were analyzed by the mass difference of separators before and after soaking in electrolyte for 30 min and then calculated using Equation (2): $EU = (W–W_0)/W_0 \times 100\%$, in which W_0 and W are the weights of the films before and after immersing in the liquid electrolyte, respectively. Ten samples are tested to measure the electrolyte uptake and porosity of each membrane. Wettability of the separators were researched by contact angle measurements (DSA 100S, Germany KRUSS).

The various GPEs' effective ionic conductivities (σ) were calculated using Equation (3): $\sigma = d/(R_b \times S)$, where d is the thickness of the film, S is the area and R_b is the bulk impedance acquired by electrochemical impedance spectroscopy (EIS) in Stainless Steel (SS)/electrolyte/SS symmetric cells. The bulk resistances (R_b) were investigated by a CHI660E electrochemical workstation with a frequency range of 0.01–10^5Hz and an amplitude of 5 mV at room temperature. The lithium ion transference numbers (t_{Li}^+) of different electrolytes were tested using chronoamperometry (CA) and EIS (both by CHI660E), and then calculated using Equation (4): $t_{Li}^+ = I_S(\Delta v–I_0R_0)/I_0(\Delta v–I_SR_S)$ (Li et al., 2018), where I_0 and I_S are the initial and steady state currents obtained by CA testing of lithium symmetrical cell, R_0 and R_S are the interfacial impedance before and after polarization, and ΔV (10 mV) is the applied voltage difference (Yang et al., 2014; Zhang F. et al., 2014). The electrochemical performances were researched in coin cells with lithium foil anode and $LiNi_{0.6}Co_{0.2}Mn_{0.2}O_2$ (NCM622) cathode. The interfacial stability between the electrode and electrolytes was investigated using EIS after standing for 1, 10, 20, and 30 days, respectively. The long term cycling stability, as well as rate performances were tested in a voltage range between 2.8 and 4.4 V with different C rates by LAND battery cycle system (Wuhan Blue Electric Co., LTD, China).

RESULTS AND DISCUSSION

Morphologies of the Membranes

The morphologies of the Celgard 2325 (which is a PP/PE/PP trilayer separator), nanofibrous PVDF-HFP, PHL, and PHP@PHL membranes, as well as microscopic changes after the thermal stability analyze in 130–170°C temperature range, were tested by using SEM, as shown in **Figures 1A,D**. The Celgard 2325 membrane has tensile holes in the lamellar matrix, but the electrostatic spinning films show 3D porous structure with 80–160 nm diameter nanofiber which interlacing with each other to form interconnected networks. The energy dispersive X-ray spectroscopy (EDS) data shown in **Figure S1** gives the elemental distribution in PHL and PHP@PHL complex films. As shown in **Figure S1a**, Si and O are uniformly distributed in the membrane, which proves that Li_2SiO_3 is evenly dispersed in the polymer matrix. EDS results of PHP@PHL in **Figure S1b** shows little signal of N or Cl as the content of PPCl is pretty low (<2%). TEM image of PHP@PHL nanofiber further proved its core-shell structure, and the inorganic nanoparticle Li_2SiO_3 is dispersed in the out layer of the PVDF-HFP matrix, with the thickness of several to tens of nanometers as shown in **Figure 1B**. The XPS spectra in **Figure S2** detected no Cl element on the surface of PHP@PHL nanofiber, which further proves that the PPCl ionic liquid was fully encapsulated by the out PHL layer.

The thermal stability of various membranes was investigated by storing them in an air circulation oven at a series of temperatures between 130 and 170°C, each for 20 min. **Figure 1C**

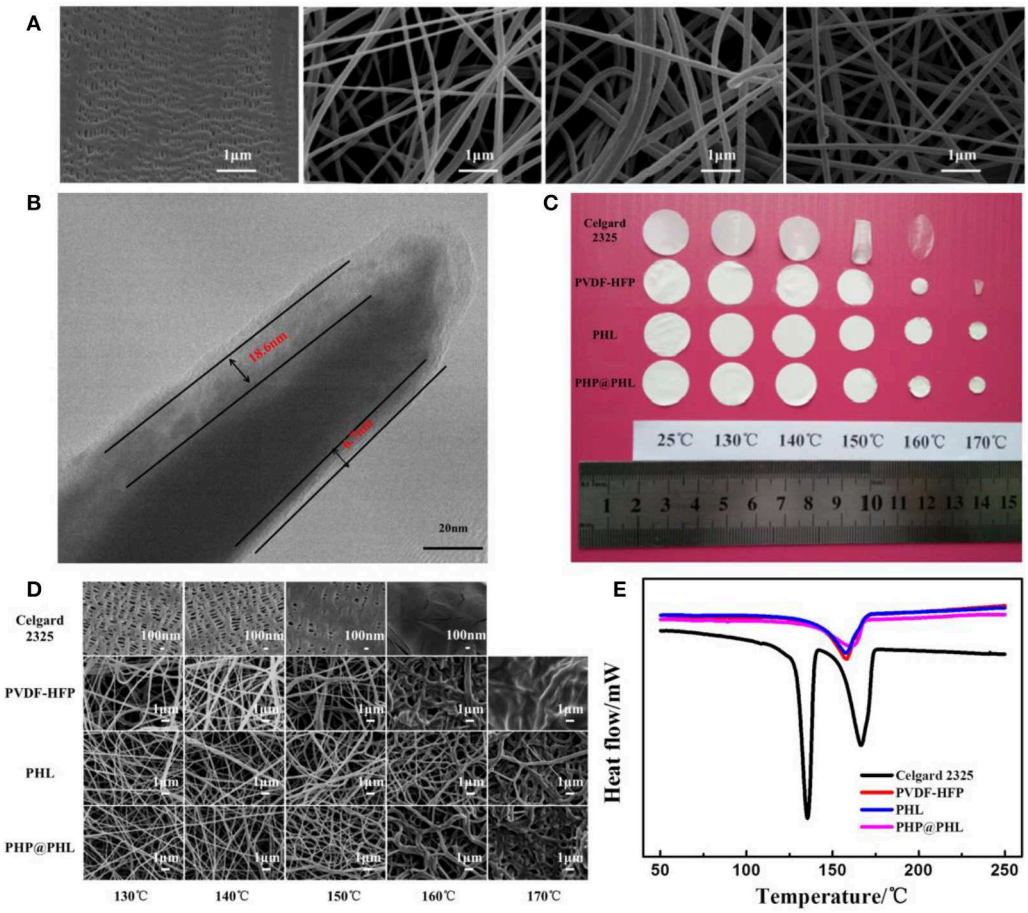

FIGURE 1 | (A) SEM images of the various separators, Celgard 2325, nanofibrous PVDF-HFP, PHL, and PHP@PHL; **(B)** TEM micrograph of the PHP@PHL fibers; **(C)** Picture of Celgard 2325, PVDF-HFP, PHL, and PHP@PHL separators and their macroscopic changes after heat treatment at different temperatures, **(D)** SEM pictures of Celgard 2325, PVDF-HFP, PHL, and PHP@PHL separators and their morphologies after heat treatment under different temperatures, **(E)** DSC curves of Celgard 2325, PVDF-HFP, PHL, and PHP@PHL separators.

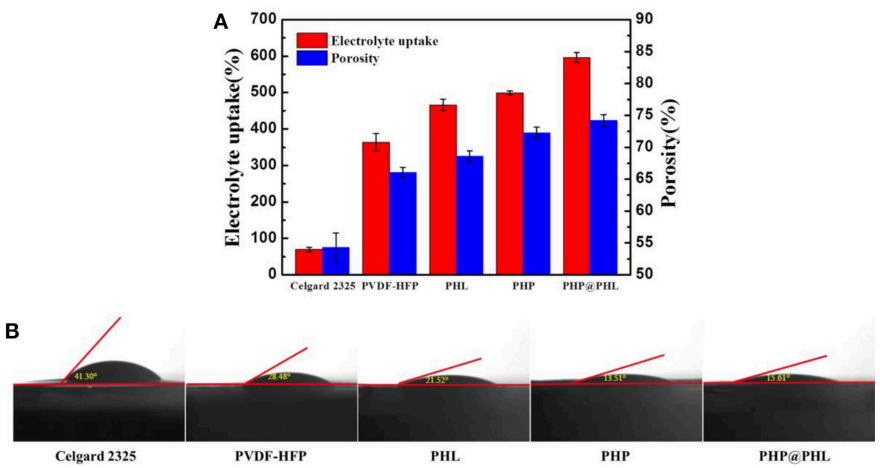

FIGURE 2 | Electrolyte uptake and porosity **(A)**, as well as the contact angle images with liquid electrolyte droplet **(B)** of the Celgard 2325, PVDF-HFP, PHL, PHP, and PHP@PHL separators.

shows that Celgard 2325 begins to curl for the melting of PE and molecular tanglement of polyolefin at about 135°C, it turns transparent at 160°C for the melt of PP, meanwhile PVDF-HFP shrink at 150°C and melt at 170°C. However, the PHL and PHP@PHL keeps their porous structure even at 170°C. It can be concluded that the inorganic nano-particle, Li_2SiO_3, in the shell structure significantly improved the thermal stability of the separator, which may potentially contribute in enhancing the safety of the battery. In order to further clarify the morphology changes of the films after heat treatment, FE-SEM pictures of the four separators are given in **Figure 1D** for microscopic description. Celgard 2325 was fully shutdown at 160°C, and PVDF-HFP nanofibrous films melt under 170°C, but the PHL and PHP@PHL films still keeps certain amount of pores remain in 170°C (**Figure 1D**). From the microscopic point of view, the core-shell structure nanofibrous membrane expresses excellent thermal stability, hence makes it have distinguished heat resistance and advance the safety of lithium battery under high temperature condition. According to DSC test results of four separators, membranes based on PVDF-HFP shows better thermal stability than that of Celgard 2325, and the core-shell structured PHP@PHL, released the least heat even on melting (**Figure 1E**) (Kang et al., 2016; Wang et al., 2019).

Porosity of the membranes are tested and calculated by Equation (1) as shown in **Figure 2A**, it's about 54.4, 66.1, 68.5, 72.5, and 74.0% for Celgard 2325, PVDF-HFP, PHL, PHP, and PHP@PHL, respectively. Obviously, fibrous separators have higher porosity than Celgard 2325, which may contribute in electrolyte uptake and thus enhance the rate capability. Contact angle of liquid electrolyte to various membranes were also studied and shown in **Figure 2B**. The contact angle of Celgard 2325, PVDF-HFP, PHL, PHP and PHP@PHL is 41.30, 28.48, 21.52 13.51, and 15.61°, respectively. All fibrous membranes showed smaller contact angle with electrolyte for the high dielectric constant of PVDF-HFP (Lopez et al., 2018), besides, they also beneficial from the fibrous structure. Smaller contact angle indicated that the PHP@PHL composite nanofibrous membrane has better affinity and is easier to be wetted by the liquid electrolyte, thus better rate capability might be obtained.

The effect ionic conductivity of the five separators was probed by EIS test at ambient temperature and calculated by Equation (3) as shown in **Figure 3A**. R_b obtained from EIS data is 2.1105, 3.8473, 2.5165, 3.3936, and 0.6801 Ω for Celgard 2325, PVDF-HFP, PHL, PHP, and PHP@PHL, respectively, and the corresponding effect ionic conductivity are 0.63, 0.64, 1.03, 1.02, and 4.05 mS/cm, respectively. Consistent with the results of porosity and wettability, this data further guaranteed the enhanced rate capability in cells.

The lithium ion transference number (t_{Li}^+) of Celgard 2325 and the as-prepared membranes with liquid electrolyte was tested and calculated via Equation (4) as shown in **Figures 3B–F**, where the corresponding t_{Li}^+ are 0.42, 0.39,

TABLE 1 | The film thickness, electrolyte uptake, porosity, effective ionic conductivity, and lithium ion transference number of Celgard 2325, PVDF-HFP, PHL, PHP, and PHP@PHL separators.

	Films thickness (μm)	Electrolyte uptake (%)	Porosity (%)	Conductivity (mS cm^{-1})	t_{Li}^+
Celgard 2325	25 ± 1	70 ± 3	54.4 ± 1.1	0.63	0.42
PVDF-HFP	50 ± 5	366 ± 12	66.1 ± 0.4	0.64	0.39
PHL	50 ± 5	466 ± 8	68.5 ± 0.4	1.03	0.56
PHP	50 ± 5	498 ± 3	72.5 ± 0.5	1.02	0.45
PHP@PHL	50 ± 5	597 ± 8	74.0 ± 0.5	4.05	0.62

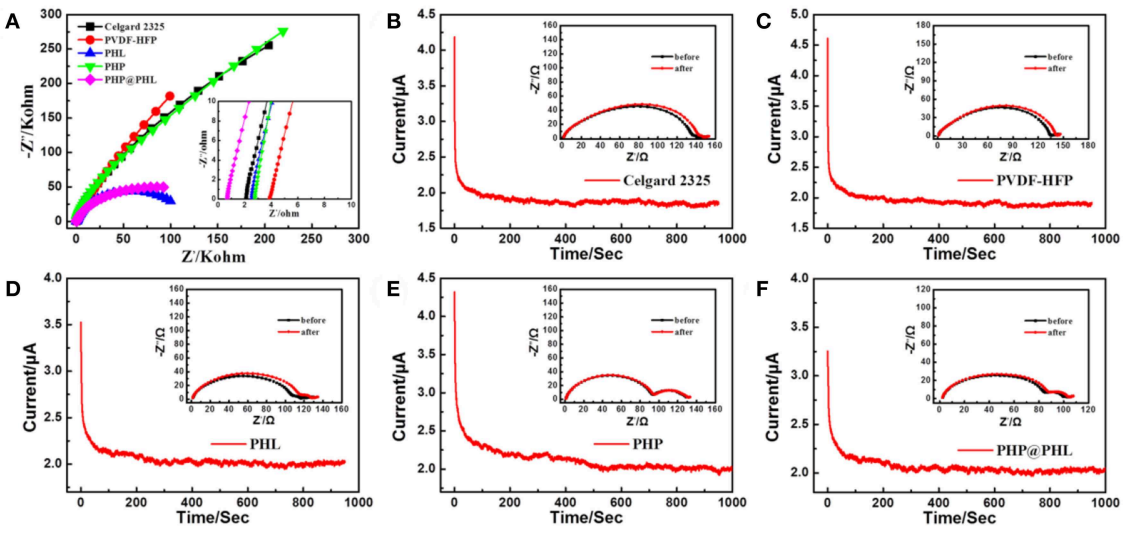

FIGURE 3 | (A) Nyquist plot of AC impedance measurements (SS/separator/SS) of the Celgard 2325, PVDF-HFP, PHL, and PHP@PHL separators; Lithium ion transference numbers of **(B)** the Celgard 2325, **(C)** PVDF-HFP, **(D)** PHL, **(E)** PHP, and **(F)** PHP@PHL membranes as demonstrated by CA polarization curves and EIS plots before and after polarization.

0.56, 0.45, and 0.62, respectively. t_{Li}^+ reduced from 0.42 to 0.39 when Celgard 2325 was replaced by PVDF-HFP, which proves that the polymer itself in fact has little contribute in Li^+ transference. The addition of Li_2SiO_3 enhanced the number to 0.56, which demonstrated that the inorganic nanoparticle may facilitate the desolvation of Li^+. While t_{Li}^+ of PHP is only 0.45, slightly higher than that of Clegard 2325 and PVDF-HFP, the reason lays on that although PPCl was mixed with PVDF-HPF and formed a membrane, but the Cl anion could still partly dissociated into the electrolyte thus influence the transportation of Li^+ (Xu et al., 2018). PHP@PHL shows the highest t_{Li}^+ among the five electrolytes for the synergistic effect of LSO and PPCl, encapsulated by the PHL layer, the Cl anion could not influence the Li^+ transport but adjust the polarization of the separator polymer matrix. Therefore, PHP@PHL nanofiber membrane prominently improves the t_{Li}^+, which may contribute in reduces anion aggregation near the electrode surface, thus reduces the concentration polarization and stabilizes the electrochemical deposition of lithium ions, improving the safety of LIB.

The film thickness, electrolyte uptake, porosity, ionic conductivity, and lithium ion transference number of the Celgard 2325, PVDF-HFP, PHL, and PHP@PHL separators summarized in **Table 1**. It is worth noting that the electrolyte uptake of PHP@PHL was about 597%, which is much higher than that of Celgard 2325 (70%), PVDF-HFP (366%), PHL (466%), and PHP (498%) and further contribute in the better rate capability when adopting in the LIBs. PHP@PHL composite membrane demonstrated the highest porosity and electrolyte uptake ability, the smallest electrolyte contact angle, and there are several factors that contribute to its remarkable performances. Firstly, the molecular structure of PVDF-HFP, as well as the 3D nanofibrous morphology facilitated the electrolyte uptake, for its high polarity and the nanoporous structure. Secondly, Li_2SiO_3 and PPCl reduced the order of molecular arrangement, which produced more chances for the electrolyte to be taken. Moreover, PPCl also worked as a plasticizer which has perfect affinity with the electrolyte, on which the contact angle is also reduced. Therefore, PHP@PHL shows the best physical performances. We also compare the ionic conductivity and the t_{Li}^+ with some of the previous publications as listed in **Table 2**, obviously, by the synergistic effect of LSO and PPCl, lithium ion transport efficiency was strongly enhanced.

TABLE 2 | Ionic conductivity and t_{Li+} in previous relevant works.

Type of GPE	Conductivity σ (mS/cm)	t_{Li}^+	References
PVDF-HFP@Al_2O_3 GPE	1.24	–	Shen et al., 2018
40 wt% IL GPE	0.15	0.39	Singh et al., 2018
PSA@PVDF-HFP	1.97	–	Zhou et al., 2013
PMMA/PVDF-HFP	1.31	–	Zhang J. et al., 2014
MS5 based GPE	3.2	0.62	Li et al., 2018
Gel PVDF–NWF	0.3	–	Zhu et al., 2013
SiO_2@Li^+ doped PVDF–HFP	3.9	0.44	Xiao et al., 2012
NanoIL GPE	0.64	0.6	Cheng et al., 2018
PHP@PHL	4.05	0.62	This work

Galvanostatic cycling measurements in Li/electrolyte/Li symmetrical cells can probed into lithium plating/stripping process and analyze the interfacial stability between the electrolyte and lithium electrode. The charge/discharge cycling test was performed at a fixed current density of 0.5 mA/cm^2 with a total capacity of 1 mAh/cm^2 and the results are shown in **Figure 4**. As can be seen from the Celgard 2325 voltage-time profile, it exhibits a gradual increase in hysteresis (overpotential between Li deposition and dissolution) as the time increases, and the voltage increases to 0.65 V after 300 h. In other words, the SEI film, or dead lithium is thickening with cycling, which means an out-off-balance lithium plating/stripping. The voltage-time profiles of PVDF-HFP, PHL, and PHP@PHL electrolytes were much stable compared with that of Celgard 2325. In particular, although the t_{Li}^+ of PVDF-HFP is lower than that of Celgard 2325, while it turns quite stable in the initial 500 h owing to the fibrous structure of the membrane which could balance the Li^+ flux adjacent to the electrode. PHL presents the least hysteresis after 1,000 h plating/stripping, while as it shows several abnormal convex during the cycling, therefore, we consider that the PHP@PHL cell demonstrated the best stability. As discussed before, the enhanced performance of PHP@PHL can be attributed to several reasons, firstly, the

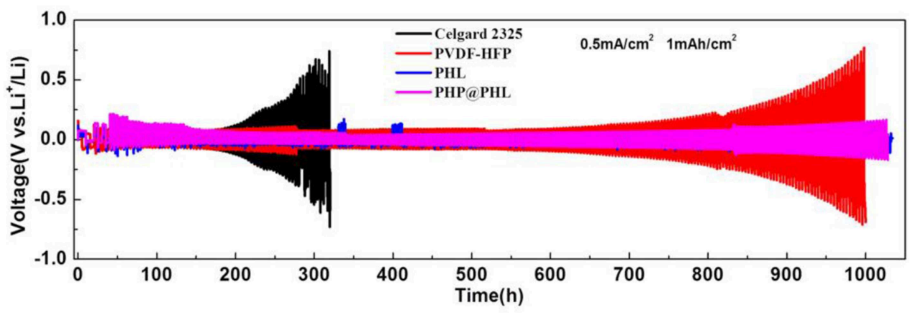

FIGURE 4 | Galvanostatic cycling performances of symmetric lithium cells with the Celgard 2325, PVDF-HFP, PHL, and PHP@PHL separators at a current density of 0.5 mA/cm^2 at 25°C.

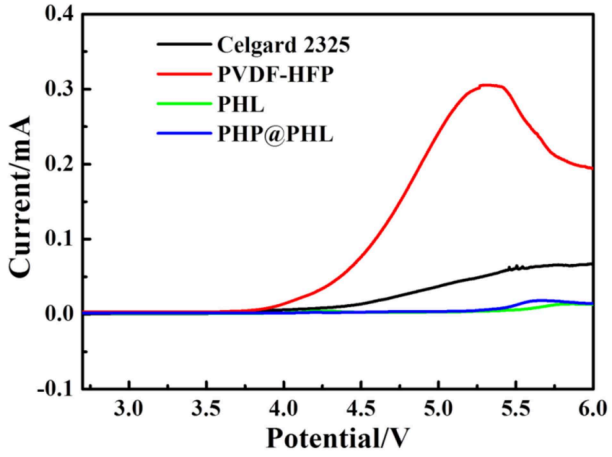

FIGURE 5 | Linear sweep voltammograms of the four electrolytes at a scan rate of 0.5 mV/s (Li/electrolyte/SS).

nanofibrous structure of PVDF-HFP balanced the Li^+ flux and suppressed the mossy deposition of Li; secondly, the synergistic effect of LSO and PPCl reduce the crystallinity of the polymer matrix, thus enhanced the Li^+ transportation efficiency; lastly, Cl anion from the IL may partly be involved in the formation of SEI, which further enhance the cycle stability of the symmetric cell. Hence, the formation of Li dendrites is inhibited and the speed of dendrite growth is reduced as well. These results manifest that using 3D porous electrostatic spinning nanofiber membrane could effectively lower the hysteresis, stabilize cycling behavior and elongate the cell lifetime.

The batteries tested with the above four electrolytes were then disassembled in an argon-protected glove box, the electrodes were cleaned with diethyl carbonate (DEC) and dried strictly, and then put into a vacuum transfer box before FE-SEM analysis. The experimental results are shown in **Figure S3**. For the symmetrical lithium battery assembled with Celgard 2325 after galvanostatic charge/discharge cycle for 300 h, the FE-SEM diagram indicates that a lot of clavate-shaped lithium dendrite is generated on the surface of the lithium electrode. These dendrites will eventually penetrate the separator, causing short circuit and safety problems. By contrast, the symmetrical lithium battery assembled with the electrostatic spinning films, PVDF-HFP, PHL, and PHP@PHL, even cycled for 1,000 h under the same current density, shows much smoother surface with smooth edges, which was not easy to penetrate the separators, greatly improved the safety of LIBs. The electrospinning separators have large specific surface area, which could balance the local current density on the electrode surface, thus inhibited the formation and growth of lithium dendrite. Therefore, the core-shell nanofiber separator prepared by coaxial electrostatic spinning can significantly improve the safety performance of LIB.

Linear sweep voltammetry (LSV) was used to investigate the electrochemical windows of the electrolytes with a scan rate of 0.5 mV/s over the range of 2.8–6 V in Li/electrolyte/SS battery, and the results are shown in **Figure 5**. The oxidation potentials of the Celgard 2325, PVDF-HFP, PHL, and PHP@PHL electrolyte is 4.27, 3.93, 5.5, and 5.45 V (vs. Li^+/Li), respectively. As all these membranes are plasticized by the same electrolyte, $LiPF_6$/EC+EMC, therefore, most parasitic reactions should origin from the membrane. Therefore, it can be concluded that both LSO and PPCl could prevent PVDF-HFP from being oxidized and effectively enhance the electrochemical stability of composite membrane, which is pivotal for practical application. No obvious decomposition of Li/PHP@PHL/SS battery was observed below 5.45 V, which manifested PHP@PHL may potentially be able to be coupled with high voltage cathode materials, such as NCM622.

The interfacial stability between the electrode and the electrolyte is fatal for long-term cycle stability and rate performance, therefore, the separators are adopted and Li/electrolyte/NCM622 half-cells were assembled to further test their compatibility with the electrode materials. Static EIS tests were performed in 1, 10, 20, and 30 days after cell assembled at room temperature and the data was deal with an equivalent circuit fitting (**Figure S4**), the results are shown in **Figure 6** and **Table S1**. R_b is corresponding to the bulk resistance originated from electrolyte and other cell components, R_1 and R_2 can be assigned to the interface resistance between electrolyte and anode or cathode, respectively. R_2 is smaller than R_1 because the battery is never charged after assembly and is left standing, therefore, little reaction would happen in the storage process. The cell with PHP@PHL shows the most stable R_1 value among the four cells, it is 18.32 Ω after 30 days of storage, while it is 61.40, 35.45, and 35.42 Ω for Celgard 2325, PVDF-HFP and PHL, respectively, which indicates that PHP@PHL has the best interfacial compatibility with Li among these electrolytes (Cheng et al., 2018). Its smallest increase in interface resistance is mainly attributed to the following reason: firstly, PVDF-HFP has higher dielectric constant than PP or PE, which endows it with better Li compatibility (Lopez et al., 2018); secondly, the introduction of Li_2SiO_3 partially suppresses the decomposition of $LiPF_6$ and carbonate solvents during long term storage (Fu et al., 2017); and the third, the slow dissociation of PPCl would generate some Cl anion, which would react with Li to form a more stable SEI component, LiCl, thus further stabilized the electrode/electrolyte interface and reduce its resistance (Lu et al., 2014b).

Electrochemical performances of the above mentioned GPEs were tested in Li/electrolyte/NCM622 half cells by different C rates. **Figure S5** shows the 0.5C rate performance of Celgard 2325 and PHP@PHL, we can see that the cells delivers quite similar capacity in the initial 300 cycles, both cells kept more than 100 mAh/g reversible capacity in 500 cycles, which proves that the cathode material works well in this electrolyte system. It also can be notice that the Celgard one shows lower coulombic efficiency after about 350 cycles, which might cause by the mossy Li deposition after long term striping/plating. High rate tests were performed to testify the performance of nanofibrous GPEs. **Figures 7A,B** show the long term cycle performances of the Li/electrolyte/NCM622 half cells at 3C and

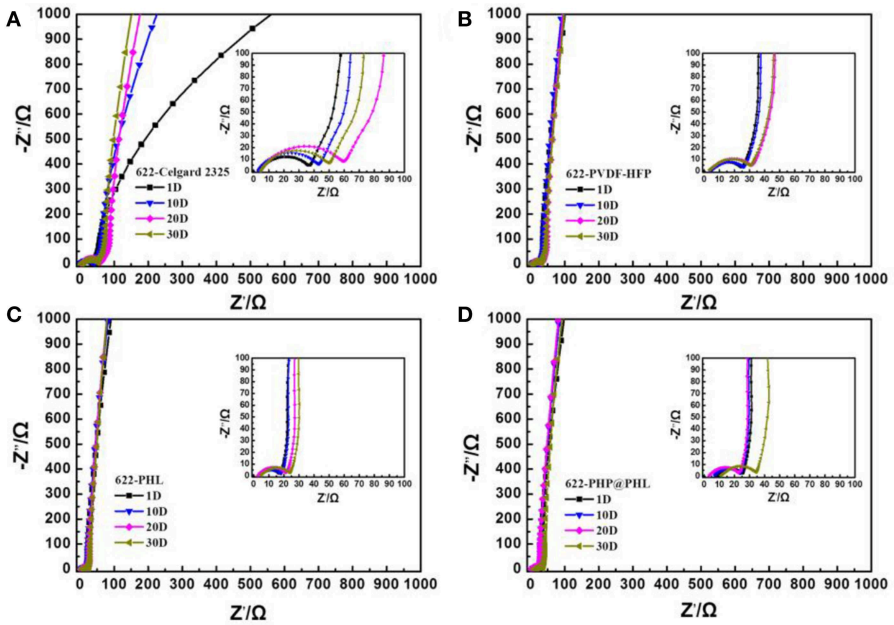

FIGURE 6 | Impedance evolution of the NCM622/Li half-cells with **(A)** the Celgard 2325, **(B)** PVDF-HFP, **(C)** PHL, and **(D)** PHP@PHL membranes at open circuit potential as a function of storage time at 25°C for 1, 10, 20, and 30 days.

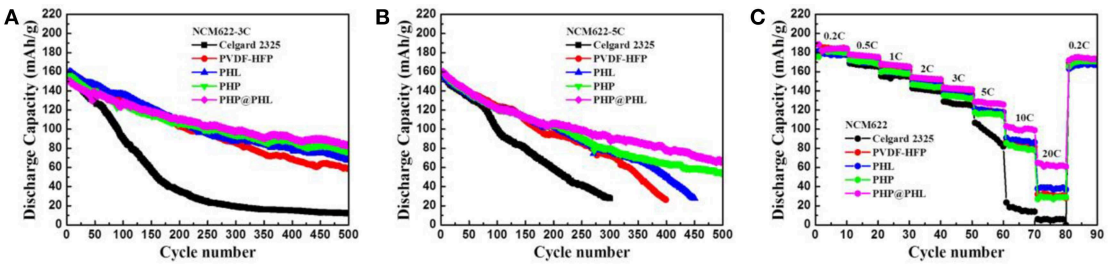

FIGURE 7 | Long-term cycling stability of the NCM622/Li cells with different membranes (Celgard 2325, PVDF-HFP, PHL, PHP, and PHP@PHL) at 3C rate **(A)**, 5C rate **(B)**, and their rate capability **(C)**.

5C, respectively. Obviously, the reversible capacity and cycle stability of PHP@PHL system were significantly improved at these C rates. The initial discharge capacities of Celgard 2325, PVDF-HFP, PHL, PHP, and PHP@PHL were 156.6, 160.6, 161.4, 156.5, and 150.6 mAh/g at 3C rate, respectively. It drops sharply to 15.8 mAh/g after 300 cycles for the Celgard 2325 one, while that of PVDF-HFP, PHL, PHP, and PHP@PHL maintained at 85.3, 87.9, 84.1, and 98.5 mAh/g, respectively. The initial discharge capacities of Celgard 2325, PVDF-HFP, PHL, PHP, and PHP@PHL at 5C rate were 156.0, 156.0, 156.2, 158.7, and 160.2 mAh/g, respectively. It declined dramatically to 27.8 mAh/g after 300 cycles for Celgard 2325, and that of PVDF-HFP and PHL were also significantly reduced to 26.3 and 27.2 mAh/g after 400 cycles, respectively. But the one with PHP@PHL remained 78.5 mAh/g even after 500 cycles. The rate performances (from 0.2 to 20C) of Li/electrolyte/NCM622 half-cells are shown in **Figure 7C**. It can be seen that the difference between the electrospining GPEs and the Celgard separator was not obvious under low current density, but the diversity significantly improved under large current density, especially for PHP@PHL. The Li/electrolyte/NCM622 half-cell with PHP@PHL can still deliver a reversible capacity of 65 mAh/g at 20C, while that of Celgard 2325, PVDF-HFP, PHL, and PHP were 5, 30, 38, and 29 mAh/g, respectively, which means the PHP@PHL delivers 13 times higher capacity than that of Celgard 2325. Charge-discharge profiles of the Li/electrolyte/NCM622 half-cells with Celgard 2325 and PHP@PHL at different C rates were compared in **Figure S6**. It can be easily conclude from these results that the as prepared core-shell structure PHP@PHL nanofibrous electrolyte has the best electrochemical performances, which can realize safe and efficient quick charging, thus has great potential in the application of high-power density LIBs.

CONCLUSIONS

In summary, a core-shell structured nanofibrous membrane with PPCl ionic liquid plasticizer in the core and inorganic nano-particle Li_2SiO_3 as the filler in shell, PHP@PHL, was prepared by a facile coaxial electrospining method. The electrolyte uptake, porosity, ionic conductivity and lithium ion transference number of PHP@PHL nanofiber membrane were about 597%, 74.0%, 4.05 mS/cm, and 0.62, respectively. By the introduction of PPCl and Li_2SiO_3, ionic conductivity of the electrolyte increases by an order of magnitude and wettability between the separator and liquid electrolyte also significantly improved compared to commercial Celgard 2325 or even electrospining PVDF-HFP separator. In addition, it has good thermal stability, low interfacial impedance and wide electrochemical window. Symmetrical lithium cells with PHP@PHL demonstrated excellent plating/stripping cycling stability for about 1,000 h without short-circuit, which is 5 times longer than that of Celgard 2325. Moreover, the PHP@PHL electrolyte presents outstanding rate capability, it delivers a reversible capacity of 65 mAh/g at 20C compared to the 5 mAh/g in the case of Celgard 2325. The long term cycle performance was also significantly improved, as demonstrated in 3C and 5C. The core-shell structured nanofibrous membrane, in which different fillers or plasticizers could be used thus different functions can be realized in one single membrane, provides and effective method to enhance the overall performances of LIBs.

DATA AVAILABILITY

The raw data supporting the conclusions of this manuscript will be made available by the authors, without undue reservation, to any qualified researcher.

AUTHOR CONTRIBUTIONS

SZ helps to improve ideas and experimental platform. LZ helps to solve some problems of experience. XL helps to do mainly works. YR helps to do any experience.

FUNDING

This work was financially supported by the National Key Research and Development Program of China (No. 2016YFB0100303), National Natural Science Foundation of China (No. 21706261), Beijing Natural Science Foundation (No. L172045), and the Ford-China University Research Program.

SUPPLEMENTARY MATERIAL

The Supplementary Material for this article can be found online at: https://www.frontiersin.org/articles/10.3389/fchem.2019.00421/full#supplementary-material

REFERENCES

Ali, S., Tan, C., Waqas, M., Lv, W., Wei, Z., Wu, S., et al. (2018). Highly efficient PVDF-HFP/colloidal alumina composite separator for high-temperature lithium-ion batteries. *Adv. Mater. Interfaces* 5:1701147. doi: 10.1002/admi.201701147

Chen, N., Dai, Y., Xing, Y., Wang, L., Guo, C., Chen, R., et al. (2017). Biomimetic ant-nest ionogel electrolyte boosts the performance of dendrite-free lithium batteries. *Energy Environ. Sci.* 10, 1660–1667. doi: 10.1039/C7EE00988G

Cheng, Y., Zhang, L., Xu, S., Zhang, H., Ren, B., Li, T., et al. (2018). Ionic liquid functionalized electrospun gel polymer electrolyte for use in a high-performance lithium metal battery. *J. Mater. Chem. A* 6, 18479–18487. doi: 10.1039/C8TA06338A

Choi, S. W., Jo, S. M., Lee, W. S., and Kim, Y. R. (2003). An electrospun poly(vinylidene fluoride) nanofibrous membrane and its battery applications. *Adv. Mater.* 15, 2027–2032. doi: 10.1002/adma.200304617

Deng, K., Qin, J., Wang, S., Ren, S., Han, D., Xiao, M., et al. (2018). Effective suppression of lithium dendrite growth using a flexible single-ion conducting polymer electrolyte. *Small.* 14:e1801420. doi: 10.1002/smll.201801420

Diederichsen, K. M., McShane, E. J., and McCloskey, B. D. (2017). Promising routes to a high Li+ transference number electrolyte for lithium ion batteries. *ACS Energy Lett.* 2, 2563–2575. doi: 10.1021/acsenergylett.7b00792

Etacheri, V., Marom, R., Elazari, R., Salitra, G., and Aurbach, D. (2011). Challenges in the development of advanced Li-ion batteries: a review. *Energy Environ. Sci.* 4, 3243–3262. doi: 10.1039/c1ee01598b

Fu, J., Mu, D., Wu, B., Bi, J., Liu, X., Peng, Y., et al. (2017). Enhanced electrochemical performance of $LiNi_{0.6}Co_{0.2}Mn_{0.2}O_2$ cathode at high cutoff voltage by modifying electrode/electrolyte interface with lithium metasilicate. *Electrochim. Acta* 246, 27–34. doi: 10.1016/j.electacta.2017.06.038

Gao, Y., Shan, D. C., Cao, F., Gong, J., Li, X., Ma, H. Y., et al. (2009). Silver/polyaniline composite nanotubes: one-step synthesis and electrocatalytic activity for neurotransmitter dopamine. *J. Phys. Chem. C* 113, 15175–15181. doi: 10.1021/jp904788d

Ghazi, Z. A., He, X., Khattak, A. M., Khan, N. A., Liang, B., Iqbal, A., et al. (2017). MoS2 /celgard separator as efficient polysulfide barrier for long-life lithium-sulfur batteries. *Adv. Mater.* 29:1606817. doi: 10.1002/adma.201606817

Goodenough, J. B., and Kim, Y. (2010). Challenges for rechargeable Li batteries. *Chem. Mater.* 22, 587–603. doi: 10.1021/cm901452z

Guo, Q., Han, Y., Wang, H., Xiong, S., Liu, S., Zheng, C., et al. (2018). Preparation and characterization of nanocomposite ionic liquid-based gel polymer electrolyte for safe applications in solid-state lithium battery. *Solid State Ionics* 321, 48–54. doi: 10.1016/j.ssi.2018.03.032

Huang, X. (2010). Separator technologies for lithium-ion batteries. *J. Solid State Electr.* 15, 649–662. doi: 10.1007/s10008-010-1264-9

Jana, A., Ely, D. R., and García, R. E. (2015). Dendrite-separator interactions in lithium-based batteries. *J. Power Sources* 275, 912–921. doi: 10.1016/j.jpowsour.2014.11.056

Jia, H., Onishi, H., Wagner, R., Winter, M., and Cekic-Laskovic, I. (2018). Intrinsically safe gel polymer electrolyte comprising flame-retarding polymer matrix for lithium ion battery application. *ACS Appl. Mater. Interfaces* 10, 42348–42355. doi: 10.1021/acsami.8b15505

Kang, W., Deng, N., Ma, X., Ju, J., Li, L., Liu, X., et al. (2016). A thermostability gel polymer electrolyte with electrospun nanofiber separator of organic F-doped poly-m-phenyleneisophthalamide for lithium-ion battery. *Electrochim. Acta* 216, 276–286. doi: 10.1016/j.electacta.2016.09.035

Kim, S., Han, T., Jeong, J., Lee, H., Ryou, M.-H., and Lee, Y. M. (2017). A flame-retardant composite polymer electrolyte for lithium-ion polymer batteries. *Electrochim. Acta* 241, 553–559. doi: 10.1016/j.electacta.2017.04.129

Kim, Y. B., Tran-Phu, T., Kim, M., Jung, D. W., Yi, G. R., and Park, J. H. (2015). Facilitated ion diffusion in multiscale porous particles: application in battery separators. *ACS Appl. Mater. Interfaces* 7, 4511–4517. doi: 10.1021/am506797d

Korf, K. S., Lu, Y., Kambe, Y., and Archer, L. A. (2014). Piperidinium tethered nanoparticle-hybrid electrolyte for lithium metal batteries. *J. Mater. Chem. A* 2, 11866–11873. doi: 10.1039/C4TA02219J

Lee, H., Yanilmaz, M., Toprakci, O., Fu, K., and Zhang, X. (2014). A review of recent developments in membrane separators for rechargeable lithium-ion batteries. *Energy Environ. Sci.* 7, 3857–3886. doi: 10.1039/C4EE01432D

Li, M., Liao, Y., Liu, Q., Xu, J., Sun, P., Shi, H., et al. (2018). Application of the imidazolium ionic liquid based nano-particle decorated gel polymer electrolyte for high safety lithium ion battery. *Electrochim. Acta* 284, 188–201. doi: 10.1016/j.electacta.2018.07.140

Li, Q., Chen, D., Tan, H., Zhang, X., Rui, X., and Yu, Y. (2019). 3D porous V2O5 architectures for high-rate lithium storage. *J. Energy Chem.* 40, 15–21. doi: 10.1016/j.jechem.2019.02.010

Liang, H.-q., Wan, L.-s., and Xu, Z.-k. (2016). Poly(vinylidene fluoride) separators with dual-asymmetric structure for high-performance lithium ion batteries. *Chin. J. Polym. Sci.* 34, 1423–1435. doi: 10.1007/s10118-016-1860-y

Liu, K., Bai, P., Bazant, M. Z., Wang, C.-A., and Li, J. (2017a). A soft non-porous separator and its effectiveness in stabilizing Li metal anodes cycling at 10 mA cm^{-2} observed *in situ* in a capillary cell. *J. Mater. Chem. A* 5, 4300–4307. doi: 10.1039/C7TA00069C

Liu, K., Zhuo, D., Lee, H.-W., Liu, W., Lin, D., Lu, Y., et al. (2017b). Extending the life of lithium-based rechargeable batteries by reaction of lithium dendrites with a novel silica nanoparticle sandwiched separator. *Adv. Mater.* 29:1603987. doi: 10.1002/adma.201603987

Lopez, J., Pei, A., Oh, J. Y., Wang, G. N., Cui, Y., and Bao, Z. (2018). Effects of polymer coatings on electrodeposited lithium metal. *J. Am. Chem. Soc.* 140, 11735–11744. doi: 10.1021/jacs.8b06047

Lu, Q., He, Y. B., Yu, Q., Li, B., Kaneti, Y. V., Yao, Y., et al. (2017). Dendrite-free, high-rate, long-life lithium metal batteries with a 3D cross-linked network polymer electrolyte. *Adv. Mater.* 29:1604460. doi: 10.1002/adma.201604460

Lu, Y., Korf, K., Kambe, Y., Tu, Z., and Archer, L. A. (2014a). Ionic-liquid-nanoparticle hybrid electrolytes: applications in lithium metal batteries. *Angew. Chem. Int. Edit.* 53, 488–492. doi: 10.1002/anie.201307137

Lu, Y., Moganty, S. S., Schaefer, J. L., and Archer, L. A. (2012). Ionic liquid-nanoparticle hybrid electrolytes. *J. Mater. Chem.* 22, 4066–4072. doi: 10.1039/c2jm15345a

Lu, Y., Tu, Z., and Archer, L. A. (2014b). Stable lithium electrodeposition in liquid and nanoporous solid electrolytes. *Nat. Mater.* 13, 961–969. doi: 10.1038/nmat4041

Lu, Y., Tu, Z., Shu, J., and Archer, L. A. (2015a). Stable lithium electrodeposition in salt-reinforced electrolytes. *J. Power Sources* 279, 413–418. doi: 10.1016/j.jpowsour.2015.01.030

Lu, Y., Xu, S., Shu, J., Aladat, W. I. A., and Archer, L. A. (2015b). High voltage LIB cathodes enabled by salt-reinforced liquid electrolytes. *Electrochem. Commun.* 51, 23–26. doi: 10.1016/j.elecom.2014.11.010

Ma, X., Kolla, P., Yang, R., Wang, Z., Zhao, Y., Smirnova, A. L., et al. (2017). Electrospun polyacrylonitrile nanofibrous membranes with varied fiber diameters and different membrane porosities as lithium-ion battery separators. *Electrochim. Acta* 236, 417–423. doi: 10.1016/j.electacta.2017.03.205

Park, S.-R., Jung, Y.-C., Shin, W.-K., Ahn, K. H., Lee, C. H., and Kim, D.-W. (2017). Cross-linked fibrous composite separator for high performance lithium-ion batteries with enhanced safety. *J. Membrane Sci.* 527, 129–136. doi: 10.1016/j.memsci.2017.01.015

Rui, X., Tang, Y., Malyi, O. I., Gusak, A., Zhang, Y., Niu, Z., et al. (2016). Ambient dissolution–recrystallization towards large-scale preparation of V_2O_5nanobelts for high-energy battery applications. *Nano Energy* 22, 583–593. doi: 10.1016/j.nanoen.2016.03.001

Scrosati, B., Hassoun, J., and Sun, Y.-K. (2011). Lithium-ion batteries. A look into the future. *Energy Environ. Sci.* 4, 3287–3295. doi: 10.1039/c1ee01388b

Shen, X., Li, C., Shi, C., Yang, C., Deng, L., Zhang, W., et al. (2018). Core-shell structured ceramic nonwoven separators by atomic layer deposition for safe lithium-ion batteries. *Appl. Surf. Sci.* 441, 165–173. doi: 10.1016/j.apsusc.2018.01.222

Shin, W. K., Kannan, A. G., and Kim, D. W. (2015). Effective suppression of dendritic lithium growth using an ultrathin coating of nitrogen and sulfur codoped graphene nanosheets on polymer separator for lithium metal batteries. *ACS Appl. Mater. Inter.* 7, 23700–23707. doi: 10.1021/acsami.5b07730

Singh, S. K., Shalu, B. L., Gupta, H., Singh, V. K., Tripathi, A. K., and Singh, R. K. (2018). Improved electrochemical performance of EMIMFSI ionic liquid based gel polymer electrolyte with temperature for rechargeable lithium battery. *Energy* 150, 890–900. doi: 10.1016/j.energy.2018.03.024

Sun, G., Dong, G., Kong, L., Yan, X., Tian, G., Qi, S., et al. (2018). Robust polyimide nanofibrous membrane with porous-layer-coated morphology by *in situ* self-bonding and micro-crosslinking for lithium-ion battery separator. *Nanoscale* 10, 22439–22447. doi: 10.1039/C8NR07548D

Tan, H., Xu, L., Geng, H., Rui, X., Li, C., and Huang, S. (2018). Nanostructured $Li_3V_2(PO_4)_3$ cathodes. *Small* 14:e1800567. doi: 10.1002/smll.201800567

Tarascon, J. M., and Armand, M. (2001). Issues and challenges facing rechargeable lithium batteries. *Nature* 414, 359–367. doi: 10.1038/35104644

Varzi, A., Raccichini, R., Passerini, S., and Scrosati, B. (2016). Challenges and prospects of the role of solid electrolytes in the revitalization of lithium metal batteries. *J. Mater. Chem. A* 4, 17251–17259. doi: 10.1039/C6TA07384K

Wang, L., Deng, N., Ju, J., Wang, G., Cheng, B., and Kang, W. (2019). A novel core-shell structured poly-m-phenyleneisophthalamide@polyvinylidene fluoride nanofiber membrane for lithium ion batteries with high-safety and stable electrochemical performance. *Electrochim. Acta* 300, 263–273. doi: 10.1016/j.electacta.2019.01.115

Wang, M., Chen, X., Wang, H., Wu, H., Jin, X., and Huang, C. (2017). Improved performances of lithium-ion batteries with a separator based on inorganic fibers. *J. Mater. Chem. A* 5, 311–318. doi: 10.1039/C6TA08404D

Wu, D., Shi, C., Huang, S., Qiu, X., Wang, H., Zhan, Z., et al. (2015). Electrospun nanofibers for sandwiched polyimide/poly (vinylidene fluoride)/polyimide separators with the thermal shutdown function. *Electrochim. Acta* 176, 727–734. doi: 10.1016/j.electacta.2015.07.072

Xiao, Q., Li, Z., Gao, D., and Zhang, H. (2009). A novel sandwiched membrane as polymer electrolyte for application in lithium-ion battery. *J. Membrane Sci.* 326, 260–264. doi: 10.1016/j.memsci.2008.10.019

Xiao, W., Li, X., Guo, H., Wang, Z., Zhang, Y., and Zhang, X. (2012). Preparation of core–shell structural single ionic conductor $SiO^2@Li^+$ and its application in PVDF–HFP-based composite polymer electrolyte. *Electrochim. Acta* 85, 612–621. doi: 10.1016/j.electacta.2012.08.120

Xiao, W., Zhao, L., Gong, Y., Liu, J., and Yan, C. (2015). Preparation and performance of poly(vinyl alcohol) porous separator for lithium-ion batteries. *J. Membrane Sci.* 487, 221–228. doi: 10.1016/j.memsci.2015.04.004

Xie, H., Liao, Y., Sun, P., Chen, T., Rao, M., and Li, W. (2014). Investigation on polyethylene-supported and nano-SiO_2 doped poly(methyl methacrylate-co-butyl acrylate) based gel polymer electrolyte for high voltage lithium ion battery. *Electrochim. Acta* 127, 327–333. doi: 10.1016/j.electacta.2014.02.038

Xu, S., Cheng, Y., Zhang, L., Zhang, K., Huo, F., Zhang, X., et al. (2018). An effective polysulfides bridgebuilder to enable long-life lithium-sulfur flow batteries. *Nano Energy* 51, 113–121. doi: 10.1016/j.nanoen.2018.06.044

Yang, P., Liu, L., Li, L., Hou, J., Xu, Y., Ren, X., et al. (2014). Gel polymer electrolyte based on polyvinylidenefluoride-co-hexafluoropropylene and ionic liquid for lithium ion battery. *Electrochim. Acta* 115, 454–460. doi: 10.1016/j.electacta.2013.10.202

Zhang, F., Ma, X., Cao, C., Li, J., and Zhu, Y. (2014). Poly(vinylidene fluoride)/SiO_2 composite membranes prepared by electrospinning and their excellent properties for nonwoven separators for lithium-ion batteries. *J. Power Sources* 251, 423–431. doi: 10.1016/j.jpowsour.2013.11.079

Zhang, J., Chen, S., Xie, X., Kretschmer, K., Huang, X., Sun, B., et al. (2014). Porous poly(vinylidene fluoride-co-hexafluoropropylene) polymer membrane with sandwich-like architecture for highly safe lithium ion batteries. *J. Membrane Sci.* 472, 133–140. doi: 10.1016/j.memsci.2014.08.049

Zhao, H., Deng, N., Ju, J., Li, Z., Kang, W., and Cheng, B. (2019). Novel configuration of heat-resistant gel polymer electrolyte with electrospun poly (vinylidene fluoride-co-hexafluoropropylene) and poly-m-phenyleneisophthalamide composite separator for high-safety lithium-ion battery. *Mater. Lett.* 236, 101–105. doi: 10.1016/j.matlet.2018.10.067

Zheng, H., Xie, Y., Xiang, H., Shi, P., Liang, X., and Xu, W. (2018). A bifunctional electrolyte additive for separator wetting and dendrite suppression in lithium metal batteries. *Electrochim. Acta* 270, 62–69. doi: 10.1016/j.electacta.2018.03.089

Zhou, R., Liu, W., Yao, X., Leong, Y. W., and Lu, X. (2015). Poly(vinylidene fluoride) nanofibrous mats with covalently attached SiO_2 nanoparticles

as an ionic liquid host: enhanced ion transport for electrochromic devices and lithium-ion batteries. *J. Mater. Chem. A* 3, 16040–16049. doi: 10.1039/C5TA02154E

Zhou, X., Yue, L., Zhang, J., Kong, Q., Liu, Z., Yao, J., et al. (2013). A core-shell structured polysulfonamide-based composite nonwoven towards high power lithium ion battery separator. *J. Electrochem. Soc.* 160, A1341–A1347. doi: 10.1149/2.003309jes

Zhu, Y., Wang, F., Liu, L., Xiao, S., Chang, Z., and Wu, Y. (2013). Composite of a nonwoven fabric with poly(vinylidene fluoride) as a gel membrane of high safety for lithium ion battery. *Energy Environ. Sci.* 6, 618–624. doi: 10.1039/C2EE23564A

Zuo, P., Hua, J., He, M., Zhang, H., Qian, Z., Ma, Y., et al. (2017). Facilitating the redox reaction of polysulfides by an electrocatalytic layer-modified separator for lithium–sulfur batteries. *J. Mater. Chem. A* 5, 10936–10945. doi: 10.1039/C7TA02245J

Conflict of Interest Statement: The authors declare that the research was conducted in the absence of any commercial or financial relationships that could be construed as a potential conflict of interest.

frontiers in Chemistry

ORIGINAL RESEARCH
published: 19 June 2019
doi: 10.3389/fchem.2019.00449

Bimetallic Metal-Organic Framework-Derived Carbon Nanotube-Based Frameworks for Enhanced Capacitive Deionization and Zn-Air Battery

Wenhui Shi[1†], Xilian Xu[2†], Chenzeng Ye[1†], Dongyong Sha[2], Ruilian Yin[2], Xuhai Shen[2], Xiaoyue Liu[1], Wenxian Liu[2], Jiangnan Shen[1], Xiehong Cao[2*] and Congjie Gao[1]*

[1] Center for Membrane Separation and Water Science and Technology, Ocean College, Zhejiang University of Technology, Hangzhou, China, [2] College of Materials Science and Engineering, Zhejiang University of Technology, Hangzhou, China

OPEN ACCESS

Edited by:
Yuxin Tang,
University of Macau, China

Reviewed by:
Xihong Lu,
Sun Yat-Sen University, China
Shengjie Peng,
Nanjing University of Aeronautics and Astronautics, China
Xingtao Xu,
Hohai University, China

***Correspondence:**
Jiangnan Shen
shenjn@zjut.edu.cn
Xiehong Cao
gcscaoxh@zjut.edu.cn

†These authors have contributed equally to this work

Specialty section:
This article was submitted to Electrochemistry, a section of the journal Frontiers in Chemistry

Received: *03 May 2019*
Accepted: *04 June 2019*
Published: *19 June 2019*

Citation:
Shi W, Xu X, Ye C, Sha D, Yin R, Shen X, Liu X, Liu W, Shen J, Cao X and Gao C (2019) Bimetallic Metal-Organic Framework-Derived Carbon Nanotube-Based Frameworks for Enhanced Capacitive Deionization and Zn-Air Battery. Front. Chem. 7:449. doi: 10.3389/fchem.2019.00449

Carbon-based materials have attracted intensive attentions for a wide range of energy and environment-related applications. Energy storage/conversion devices with improved performance have been achieved by utilization of metal-organic-framework (MOF)-derived carbon structures as active materials in recent years. However, the effects of MOF precursors on the performance of derived carbon materials are rarely investigated. Here, we report that the incorporation of small amount of Fe or Ni in Co-based MOFs leads to a significant enhancement for the derived carbon nanotube-based frameworks (CNTFs) in Na^+/Cl^- ion electrosorption. Further investigation revealed the enhanced performance can be attributed to the improved specific surface area, electrical conductivity, and electrochemical activity. Notably, the CoFe-CNTF derived from bimetallic CoFe-MOFs achieves a high ion adsorption capacity of 37.0 mg g^{-1}, superior to most of recently reported carbon-based materials. Furthermore, the CoFe-CNTF also demonstrates high catalytic activity toward oxygen evolution reaction (OER) with a Tafel slope of 87.7 mV dec^{-1}. After combination with three-dimensional graphene foam (3DG), the resultant CoFe-CNTF-coated 3DG is used as air-cathode to fabricate a flexible all-solid-state Zn-air battery, which exhibits a high open circuit potential of 1.455 V. Importantly, the fabricated flexible battery can light a light-emitting diode (LED) even when it is bent. This work provides new insights into designs of high-performance and flexible electrode based on MOF-derived materials.

Keywords: metal-organic frameworks, carbon nanotubes, capacitive deionization, oxygen evolution reaction, Zn-air battery, flexible devices, three-dimensional graphene, hierarchical structures

INTRODUCTION

Metal-organic frameworks (MOFs), as a group of porous crystalline materials with tailorable composition and structure, are versatile precursors for carbon-based porous materials (Tang et al., 2015; Xu et al., 2017, 2018). MOF-derived carbon-based materials have attracted intensive attentions for a wide range of applications, benefiting from their high surface area and well-defined porosity (Wang et al., 2016, 2017b, 2019; Li et al., 2018b; Liu et al., 2019a). Capacitive deionization

(CDI) has emerged as a potential water treatment technology owing to its low cost and energy consumption (Song et al., 2019; Xu et al., 2019). In the CDI process, upon the application of an external voltage, ions in the solution are adsorbed and stored in the electrodes by forming electrical double layers (Suss et al., 2015; Hassanvand et al., 2018). A series of carbon-based materials have been extensively studied as CDI electrodes, such as activated carbon (Wu et al., 2016; Tang et al., 2019), graphene (Cao et al., 2014; Shi et al., 2016; Liu et al., 2017a; Li et al., 2018a), mesoporous carbon (Tsouris et al., 2011; Wang et al., 2014; Gao et al., 2019b), carbon nanotubes (Nie et al., 2012; Liu et al., 2015) and their composites (Xu et al., 2016b; Huang et al., 2017; Hu et al., 2018). Recently, MOF-derived porous carbon has demonstrated great potential for CDI applications. However, MOF-derived carbon materials generally have poor electrical conductivity because of low crystallinity of carbon (Gao et al., 2018, 2019a). Furthermore, abundant micropores within MOF-derived carbon structures limit the diffusion of ions into the electrode, leading to unsatisfactory CDI performance (Ding et al., 2017; Shi et al., 2018, 2019a). Therefore, novel strategies are required to further improve electron and ion transport of MOF-derived carbons (Wang et al., 2017a; Shi et al., 2019b).

In addition, MOF-derived nanostructured carbons are also attractive noble-metal-free electrocatalysts, which are promising in oxygen evolution reaction (OER) and have been used as cathode materials for Zn-air batteries recently (Liu et al., 2018, 2019b; Zhang et al., 2018b; Fang et al., 2019; Guo et al., 2019). Although the bright prospects of MOF-derived carbon materials, their practical applications are still restricted. First, micropores within MOF-derived porous carbon materials contribute to the majority of specific surface area, which have limited diffusion rate for electrolyte ions. Second, the development of next-generation flexible energy storage/conversion devices requires electrode materials with robust structure and strong mechanical properties under deformation (Han et al., 2018; Lv et al., 2018; Peng et al., 2018; Zhu et al., 2018; Ji et al., 2019). However, MOF-derived carbons are normally in powder form, which is difficult to form a firm interaction within a flexible electrode. Third, previous reports have shown that metallic content within MOF-derived carbons play an essential role in their catalytic properties (Liu et al., 2017b; Zhang et al., 2018a; Zheng et al., 2019). The effects of bimetallic MOF precursors on the performance of derived carbon materials are rarely investigated. Therefore, it is still a challenge to develop hierarchically porous, flexible, high-ion/charge-transport-rate MOF-derived carbon-based materials for high-performance Zn-air battery.

In this work, unique carbon nanotube-based frameworks (CNTFs) were obtained by a facile annealing process of rationally designed bimetallic MOF crystals (i.e., CoFe and CoNi-MOFs) as precursors. By the incorporation of a small amount of Fe or Ni in Co-based frameworks, the obtained CoFe- and CoNi-CNTFs both exhibited improved specific surface area and electrical conductivity, as compared to those of Co-CNTF. Due to the hierarchically porous structure with abundant exposed active sites, high conductivity for fast electron transfer, and unique nanostructures with metal nanoparticle embedded in CNTs, the CoFe- and CoNi-CNTF electrodes exhibited remarkably enhanced Na^+/Cl^- ions adsorption property. Furthermore, high catalytic activity toward oxygen evolution reaction (OER) was also achieved by CoFe-CNTF. As a proof-of-concept application, an air-cathode based on CoFe-CNTF coated 3D graphene foam (CoFe-CNTF@3DG) was fabricated, and then used for flexible all-solid-state Zn-air battery, which displayed a high open circuit potential of 1.455 V.

EXPERIMENTAL SECTION

Material Synthesis

Preparation of Co-MOF: Typically, 1.4553 g of $Co(NO_3)_2{\cdot}6H_2O$ was dissolved in 50 mL of methanol, which was mixed with 50 mL of methanol containing 3.2860 g of 2-methylimidazole. The obtained mixture was stirred at room temperature for 12 h. The sample was collected by centrifugation and washed with methanol for several times, followed by drying at 60°C for 12 h in vacuum oven.

Preparation of bimetallic CoFe and CoNi-MOFs: CoFe-MOF was synthesized by using $Co(NO_3)_2{\cdot}6H_2O$ and $Fe(NO_3)_3{\cdot}6H_2O$ with a molar ratio of 9:1. Typically, 1.3097 g of $Co(NO_3)_2{\cdot}6H_2O$ and 0.2019 g of $Fe(NO_3)_3{\cdot}6H_2O$ were dissolved in 50 mL of methanol. Then, 50 mL of methanol dissolved with 3.2860 g of 2-methylimidazole was added into the above solution followed by continuously stirring for 12 h at room temperature. CoFe-MOF was collected by centrifugation and washed with methanol for several times, followed by drying at 60°C for 12 h in vacuum oven. CoNi-MOF was synthesized by a similar procedure using $Co(NO_3)_2{\cdot}6H_2O$ and $Ni(NO_3)_2{\cdot}6H_2O$ with a molar ratio of 9:1.

Preparation of CNTFs: The as-prepared MOF precursors were pyrolyzed in a tube furnace by a two-step annealing process. The MOF precursors were first heated to 500°C with a heating rate of 5°C min^{-1}, followed by bubbling ethanol vapor using H_2 for 30 min. Then, the samples were heated at 800°C for 1 h under N_2 atmosphere, followed by immersing the sample in 1 M HCl for 12 h to obtain CNTFs.

Preparation of CoFe-CNTF@3DG: 3D graphene foam (3DG) was obtained by using our previously reported method (Cao et al., 2011). Then 3DG was treated with a concentrated HNO_3 solution at 80°C for 4 h, followed by washing with deionized water to obtain hydrophilic 3DG. The 3DG was placed into the precursor solution for CoFe-MOF and reacted for 12 h at room temperature. The CoFe-MOF@3DG composite was obtained by washing with methanol and then drying at 60°C for 12 h. The CoFe-CNTF@3DG was obtained according to the aforementioned annealing procedures for CNTF samples.

Material Characterization

The morphologies of the samples were investigated by field-emission scanning electron microscopy (FE-SEM, Hitachi SU-8010), equipped with energy-dispersive X-ray spectroscopy (EDX) and transmission electron microscopy (TEM, JEM-100CX II). The crystal structures were characterized by powder X-ray diffraction (XRD, PNAlytical X'Pert PRO) with Cu Kα radiation. Nitrogen adsorption/desorption measurements were carried out by Micromeritics ASAP 2020. The specific surface

areas were calculated by the multipoint Brunauer-Emmett-Teller (BET) method.

Electrosorption Measurements

Batch-mode CDI tests were conducted by a circulating system, which includes a CDI module, a peristaltic pump (Longer Pump, YZ-1515x), a conductivity meter (Leici, DDSJ-308F) and a source meter (Keithley, SMU-2,400) (**Figure S1A**). The CDI electrodes were fabricated by coating a mixture of active materials, carbon black and poly(vinylidene fluoride) (PVDF) with a mass ratio of 8:1:1 in n-methylpyrrolidone (NMP) solution onto graphite paper, followed by drying at 60°C for 12 h in vacuum oven. As shown in **Figure S1B**, the CDI module was assembled with a CDI electrode, cation exchange membrane (Hangzhou Grion Environmental Technology Co., Ltd., LEHeCM-1, Type 1), spacer, anion exchange membrane (Hangzhou Grion Environmental Technology Co., Ltd., LE-HeAM-I, Type 1) and another CDI electrode. The total volume of NaCl aqueous solution is maintained at 50 mL. The electrosorption performance was measured at a flow rate of 30 mL min^{-1}, varied applied voltages (1.0–1.6 V) and concentrations of NaCl solution (125–1,000 mg L^{-1}). The electrosorption capacity, Γ (mg g^{-1}), is calculated based on the following equation:

$$\Gamma = \frac{(C_0 - C_t)\, V}{m}$$

where C_0 is the initial concentration of NaCl solution (mg L^{-1}), C_t is the final concentration (mg L^{-1}), V is the total volume of the solution (L), and m is the total mass of the electrodes (g).

Electrochemical Measurements

The electrochemical properties were measured by an electrochemical workstation (Chenhua, China, CHI760E) in a three-electrode system at room temperature, using a carbon paper coated with prepared catalyst as the working electrode, a graphite rod as the counter electrode, a Saturated Calomel Electrode (SCE) as the reference electrode and 1.0 M KOH as the electrolyte. The catalyst slurry was obtained by adding 5 mg of CoFe-CNTF powder into a mixed solution of 768 μL DI water, 200 μL ethanol and 32 μL nafion, followed by ultrasonication for 30 min. The electrode was fabricated by coating the obtained slurry onto carbon paper with a loading mass of 1 mg cm^{-2}. The Linear Sweep Voltammetry (LSV) was tested at a scan rate of 5 mV s^{-1} with a potential range from 1.2 to 1.7 V vs. Reversible Hydrogen Electrode (RHE). The Electrochemical Impedance Spectroscopy (EIS) measurement was conducted by an electrochemical station (Autolab PGSTAT302N) at a potential of 1.33 V vs. RHE in a frequency range from 100 kHz to 0.01 Hz with an amplitude of 5 mV.

Fabrication of Zn-Air Battery

Zn-air battery was assembled using a carbon paper loaded with CoFe-CNTF catalyst as the air cathode, Zn plate as the anode, and a mixed solution of 6 M KOH and 0.2 M $Zn(Ac)_2$ as the electrolyte, which was tested on a battery testing system (Land CT2001A). The flexible solid-state Zn-air battery was assembled by using CoFe-CNTF@3DG as the air electrode, nickel foam as the current collector, Zn plate as the anode, and polyacrylic acid (PAA) gel containing 11.25 M KOH and 0.25 M ZnO as the solid electrolyte.

RESULTS AND DISCUSSION

The preparation of CNTF is schematically shown in **Scheme 1**. Bimetallic MOF crystals (i.e., CoFe- and CoNi-MOFs) were first synthesized using the mixtures of metal salts with a proper molar ratio (route 1, see Experimental Section). For comparison, monometallic Co-MOF was also prepared. Then, the as-prepared MOF precursors were undergone a two-step annealing process for pyrolysis of MOFs and catalytic growth of CNTs, followed by an acid treatment to obtain the CNT-based frameworks (i.e., CoFe-CNTF, CoNi-CNTF, and Co-CNTF). Furthermore, CoFe-MOFs were *in-situ* grown on 3D graphene foam (3DG) followed by similar annealing process to produce a flexible air cathode (CoFe-CNTF@3DG, route 2, see Experimental Section).

The scanning electron microscopy (SEM) images of prepared bimetallic MOF crystals exhibit typical dodecahedron shape (**Figures S2A–C**), which is similar with that of Co-MOF. In addition, the energy-dispersive X-ray spectroscopy (EDX) spectra in **Figures S2D–F** indicate all of the MOFs show signals of C, N, O, and Co. Besides, CoFe- and CoNi-MOFs contain additional Fe or Ni elements, suggesting the successful incorporation of Fe/Ni in the Co-based frameworks. The X-ray diffraction (XRD) patterns in **Figure S3** show the same diffraction peaks for CoFe-, CoNi-MOFs, and Co-MOF, demonstrating the same crystal structure (Kaur et al., 2016). SEM images in **Figure S4** further reveal that CNTFs derived from CoFe, CoNi, and Co-MOFs maintained a similar dodecahedron shape after the annealing process, which consist of interconnected CNT frameworks. Further investigations on the morphology and microstructure of CNTFs were performed by transmission electron microscopy (TEM). As shown in **Figures 1A–C**, the obtained CNTFs exhibited hierarchically porous structures assembled by CNTs, which have nanoparticles with diameters of 10–18 nm encapsulated on the top of tubes (Li et al., 2016). XRD patterns of all CNTFs exhibit similar characteristic peaks located at ∼26 and 44° (**Figure 1D**), which can be assigned to the (002) and (101) planes of graphitic carbon (JCPDS: 41-1487) (Xu et al., 2016a).

The electrosorption performance of the prepared three CNTFs samples for Na^+/Cl^- ions were evaluated by measuring change of solution conductivity at applied voltages using a CDI device (**Figure S1**, see experimental section). As displayed in **Figure 1E**, when an external voltage was applied, Na^+/Cl^- ions were adsorbed and trapped in the electrodes, along with the gradually decreased solution conductivity. The NaCl electrosorption capacity of the CoFe-CNTF electrode is 37.0 mg g^{-1}, which is much higher than that of Co-CNTF (19.9 mg g^{-1}). **Figure 1F** depicts CDI Ragone plot of the three electrodes, in which the adsorption

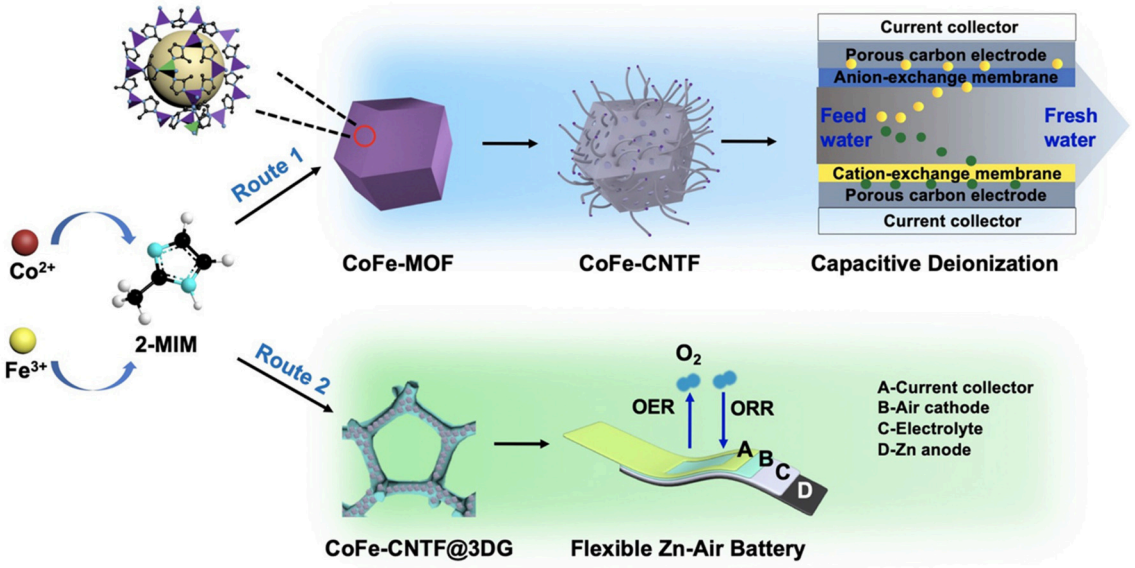

SCHEME 1 | Schematic illustration of the synthetic processes of CoFe-CNTF and CoFe-CNTF@3DG as well as their applications for CDI and Zn-air battery.

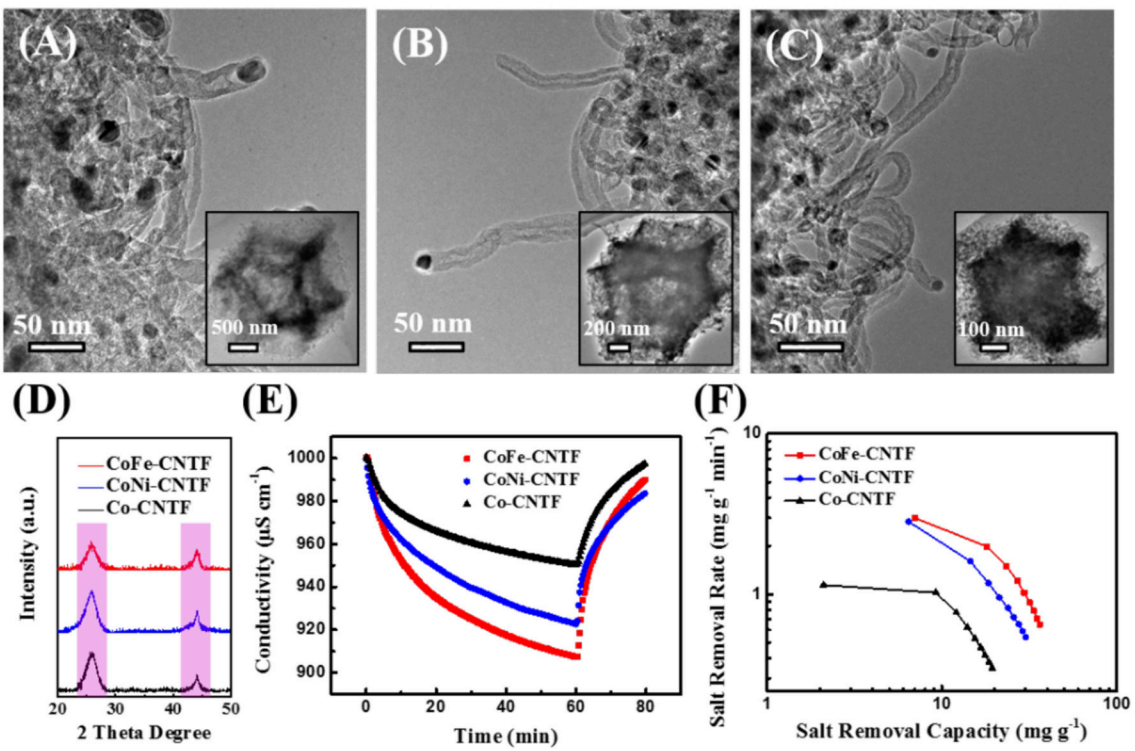

FIGURE 1 | TEM images of **(A)** CoFe-CNTF, **(B)** CoNi-CNTF, and **(C)** Co-CNTF. Insets in **(A–C)**: corresponding low-magnification TEM images. **(D)** XRD patterns of CoFe-CNTF, CoNi-CNTF, and Co-CNTF. **(E)** Electrosorption behaviors and **(F)** CDI Ragone plots of CoFe-CNTF, CoNi-CNTF, and Co-CNTF in 500 mg L^{-1} NaCl solution at 1.2 V.

capacity and rate for Na^+/Cl^- ions are used to assess the electrosorption behavior of the electrodes. Notably, in the CDI Ragone plot, the curve of CoFe-CNTF electrode is located in the upper right corner, suggesting both the highest Na^+/Cl^- ions adsorption capacity and adsorption rate (Lee et al., 2018).

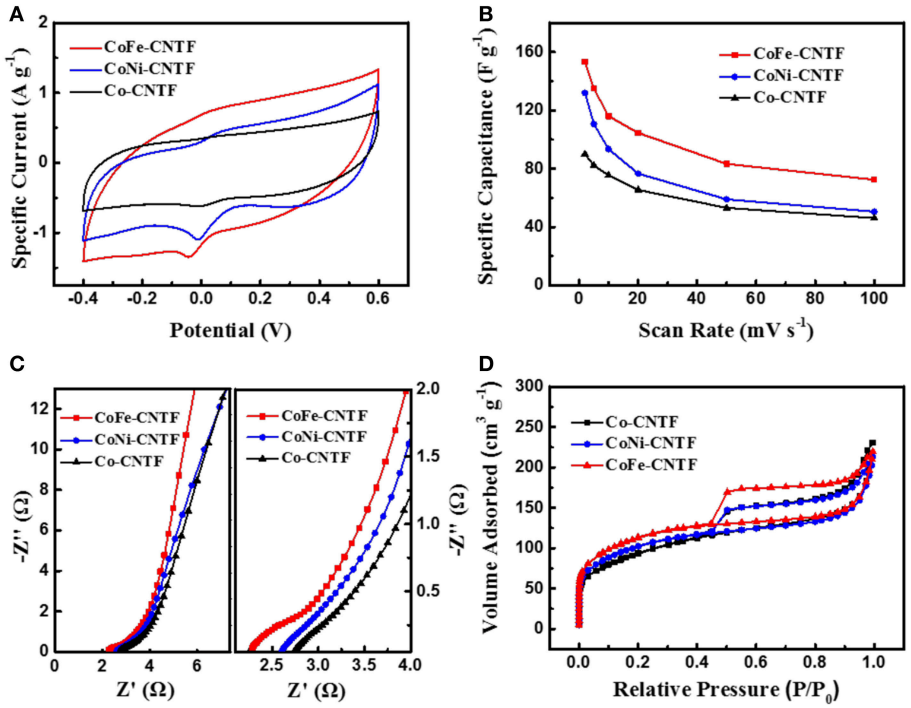

FIGURE 2 | (A) CV curves of CoFe-CNTF, CoNi-CNTF, and Co-CNTF electrodes at a scan rate of 5 mV s^{-1}. **(B)** Specific capacitances of CoFe-CNTF, CoNi-CNTF, and Co-CNTF at different scan rates. **(C)** Nyquist plots and **(D)** Nitrogen adsorption-desorption isotherms of CoFe-CNTF, CoNi-CNTF, and Co-CNTF.

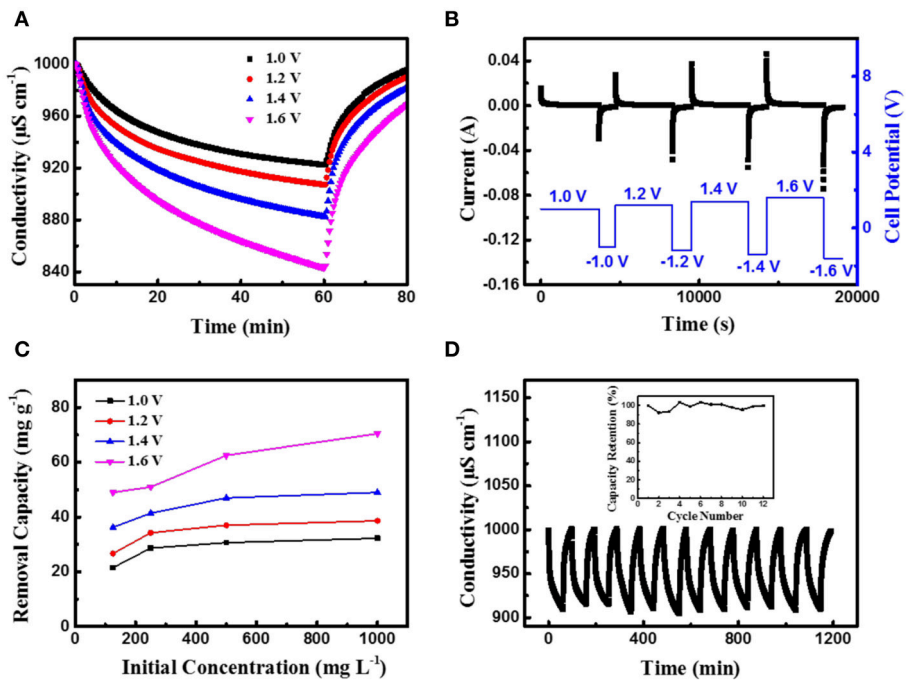

FIGURE 3 | (A) Electrosorption behaviors and **(B)** the corresponding current curves of CoFe-CNTF in 500 mg L^{-1} NaCl solution at various cell voltages. **(C)** The electrosorption capacity of CoFe-CNTF at various cell voltages and concentrations of NaCl solution. **(D)** Cycling performance of CoFe-CNTF in 500 mg L^{-1} NaCl solution at 1.2 V. Inset is the capacity retention of CoFe-CNTF.

The aforementioned results demonstrate that the remarkably enhanced Na^+/Cl^- ions adsorption performance was achieved by the bimetallic MOF-derived CNTFs. To further reveal the origins of the improvement of CDI performance, further investigations on the properties of samples in terms of electrochemical capacitance, electrical conductivity, and specific surface area were carried out. The cyclic voltammetry (CV) profiles of CoFe-, CoNi-, and Co-CNTF electrodes are shown in **Figure 2A**. Obviously, the CoFe-CNTF electrode exhibited the largest integrated area of CV curve, which is consistent with the calculated specific capacitances. The CoFe-CNTF electrode showed the highest specific capacitance at various scan rates, i.e., 153 F g^{-1} at 2 mV s^{-1} and 72 F g^{-1} at 100 mV s^{-1} (see **Figure 2B**). To further study the electrical conductivity and internal resistivity of CNTF electrodes, electrochemical impedance spectroscopy (EIS) measurement was conducted. **Figure 2C** exhibits the Nyquist plots of CoFe-, CoNi-, and Co-CNTF electrodes in 1 M NaCl solution, which include a semicircle in the high frequency region and an inclined line in the low frequency region. The inclined line of the CoFe-CNTF electrode shows the largest slope, suggesting faster ion diffusion into the porous structure. In addition, the intercept of the curve in the high-frequency region with the real axis represents the equivalent series resistance (ESR) of the electrodes. The CoFe-CNTF electrode showed an ESR value of 2.38 Ω, smaller than that of Co-CNTF (2.83 Ω). The smaller ESR and fast ion diffusion of CoFe-CNTF electrode enhance the capacitive performance. Additionally, to investigate the specific surface area and pore structure of CNTFs, N_2 adsorption-desorption measurements were carried out. As shown in **Figure 2D**, both CoFe- and CoNi-CNTFs displayed type-IV isotherms with sharply increased adsorption at low pressures and distinct hysteresis loops at medium pressure region, indicating existence of micropores, and abundant mesopores (Ding et al., 2018). Compared with CoFe- and CoNi-CNTFs, Co-CNTF exhibited a smaller hysteresis loop at high relative pressure, indicating that CoFe- and CoNi-CNTFs possesses more mesopores. Moreover, the pore size distributions of Co-CNTF, CoNi-CNTF, and CoFe-CNTF in **Figure S5** also suggest more mesopores existed in CoNi-CNTF and CoFe-CNTF than that of Co-CNTF. The Brunauer-Emmett-Teller (BET) surface areas of CoFe and CoNi-CNTF are 410 and 369 m^2 g^{-1}, respectively, which is higher than that of Co-CNTF (334 m^2 g^{-1}). Obviously, the CoFe-CNTF with the highest specific surface area and abundant mesopore is in favor of the diffusion of ions, thus, it is promising electrode materials for CDI.

The CDI performance of the CoFe-CNTF electrode was further studied in terms of the effects of various applied voltages and concentrations of NaCl solution. As shown in **Figure 3A**, with the increase of the applied voltage, the electrosorption capacity was increased, indicating that a larger amount of ions were removed from the solution due to stronger electrostatic interaction. The corresponding transient current curves at different applied voltages in **Figure 3B** also show an increased current at higher voltages. Furthermore,

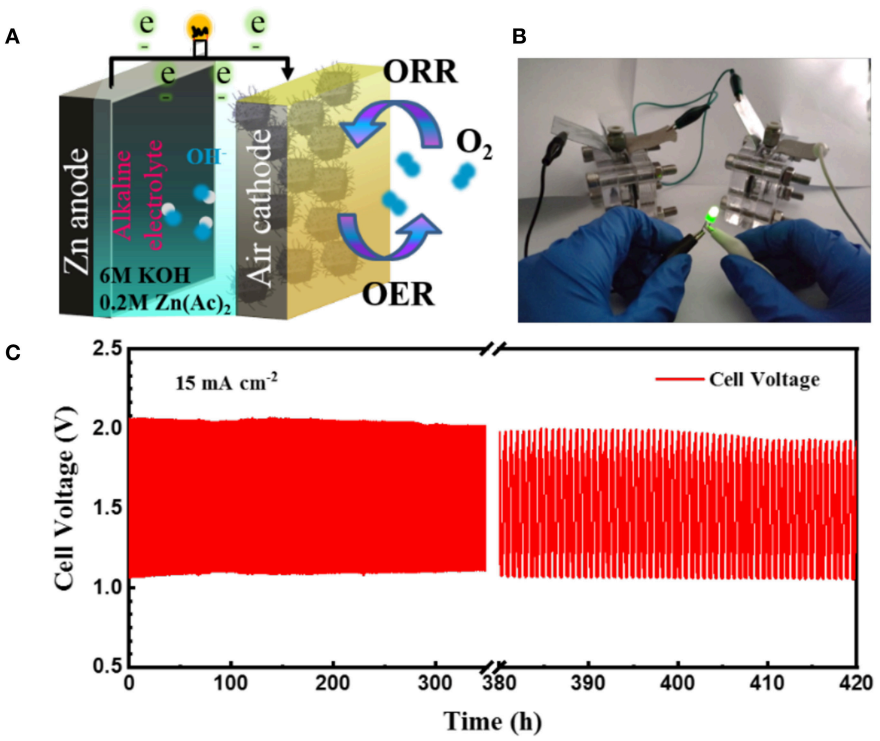

FIGURE 4 | (A) Schematic illustration of Zn-air battery. **(B)** Photograph of the lightened LED bulb by two Zn-air batteries connected in series. **(C)** Discharge-charge cycling curves at a current density of 15 mA cm^{-2}.

electrosorption experiments in NaCl solutions of various initial concentrations ranging from 125 to 1,000 mg L^{-1} were carried out. **Figure 3C** demonstrates the calculated adsorption capacities of CoFe-CNTF electrode in different concentrations of NaCl solution at cell voltages of 1.0, 1.2, 1.4, and 1.6 V, respectively. With increment of the concentration of NaCl solution, the adsorption capacity increases as well. Notably, the CoFe-CNTF electrode exhibited a superior adsorption capacity of 37.0 mg g^{-1} in a 500 mg L^{-1} NaCl solution at 1.2 V, which is superior to most of the recently reported CDI electrode materials (see **Table S1**). Furthermore, the regeneration stability of the electrode was investigated by repeated electrosorption-desorption experiments at a voltage of 1.2 V. As shown in **Figure 3D**, CoFe-CNTF electrode exhibited excellent stability for 12 cycles without obvious capacity drop.

The above studies clearly demonstrate that CoFe-CNTF has an extraordinary specific surface area, conductivity, and electrochemical activity. This could be attributed to the hierarchically porous structure with abundant exposed active sites, high electrical conductivity for fast electron transfer, and unique nanostructures with Co/Fe nanoparticles embedded in CNTFs. These excellent properties endow them promising performance as air electrode of Zn-air batteries. As shown in **Scheme 1**, in order to apply it in flexible Zn-air batteries, the OER performance of CoFe-CNTF was first investigated. The OER activity of the as-obtained CoFe-CNTF was evaluated by a conventional three-electrode cell in 1.0 M KOH solution. Commercial IrO_2 was also tested for comparison. As shown in **Figure S6A**, the CoFe-CNTF catalyst require a potential of 1.574 V vs. RHE (corresponding to overpotential of 344 mV) to achieve a current density of 10 mA cm^{-2}, which is better than that of commercial IrO_2 (1.658 V). Moreover, the Tafel slope of CoFe-CNTF is 87.7 mV dec^{-1}, which is much smaller than that of commercial IrO_2 (106.5 mV dec^{-1}), suggesting faster OER catalytic kinetics of CoFe-CNTF (see **Figure S6B**). The Nyquist plots in **Figure S6C** demonstrate that the charge transfer resistance of CoFe-CNTF is much smaller than that of commercial IrO_2, indicating that charge transfer process within CoFe-CNTF is more effective. Notably, CoFe-CNTF also exhibits excellent OER stability. As shown in **Figure S6D**, CoFe-CNTF shows nearly constant operating potential with a current density of 10 mA cm^{-2} for 12 h.

To demonstrate the practical application of the obtained CoFe-CNTF, a rechargeable Zn-air battery was fabricated. **Figure 4A** shows a schematic diagram of the configuration of rechargeable Zn-air battery, in which CoFe-CNTF catalyst loaded on carbon paper was used as air-cathode, Zn plate as anode, and a mixed solution of 6 M KOH and 0.2 M $Zn(Ac)_2$ as electrolyte. Two rechargeable Zn-air batteries connected in series can light up a light-emitting diode (LED) bulb successfully (**Figure 4B**). Furthermore, the fabricated Zn-air battery exhibited remarkable cycling stability after operation for 420 h at a current density of 15 mA cm^{-2} (**Figure 4C**). In addition, a flexible Zn-air battery based on CoFe-CNTF is also demonstrated. CoFe-MOFs were grown on 3DG (see **Figure S7**) followed by a similar annealing process to produce the flexible air cathode

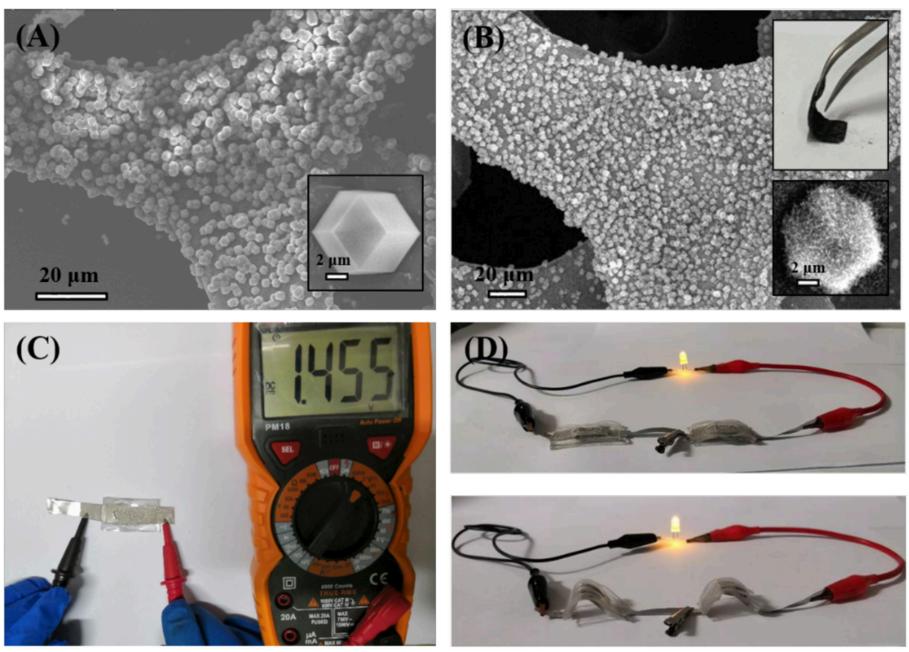

FIGURE 5 | (A) SEM image of CoFe-MOF@3DG. Inset is high-magnification SEM image showing a CoFe-MOF crystal grown on the surface of 3DG. **(B)** SEM image of CoFe-CNTF@3DG. Insets: photograph of a bent CoFe-CNTF@3DG, and high-magnification SEM image (Bottom). **(C)** Open-circuit voltage of a fabricated all-solid-state Zn-air battery based on CoFe-CNTF@3DG. **(D)** Photographs of the lightened LED by two Zn-air batteries connected in series under different blending status.

of CoFe-CNTF@3DG. The morphologies and XRD patterns of obtained CoFe-MOF@3DG and CoFe-CNTF@3DG are shown in **Figures 5A,B** and **Figure S8**. The photograph in the top inset of **Figure 5B** clearly demonstrates good flexibility of the obtained CoFe-CNTF@3DG electrode. The open-circuit voltage of the fabricated all-solid-state Zn-air battery is 1.455 V (**Figure 5C**). Importantly, a LED bulb could be successfully lightened by two Zn-air batteries connected in series under different blending status (**Figure 5D**), demonstrating its excellent flexibility and promising application in Zn-air batteries.

CONCLUSION

In summary, we developed hierarchically porous carbon nanotube-based frameworks (CNTFs), which were derived from rationally designed bimetallic MOFs followed by a two-step annealing process. The CNTFs showed excellent Na^+/Cl^- ion adsorption property. Especially, the CoFe-CNTF exhibited a remarkable adsorption capacity of 37.0 mg g^{-1} in a 500 mg L^{-1} NaCl solution at 1.2 V, superior to that of Co-CNTF (19.9 mg g^{-1}). Such enhanced performance can be attributed to the larger surface area and improved electrical conductivity of the CoFe-CNTF. Moreover, due to the unique porous framework structure and abundant metal active sites, the CoFe-CNTF displayed excellent electrocatalytic performance in OER. CoFe-CNTF@3DG as air electrode demonstrated excellent flexibility and potential application for flexible all-solid-state Zn-air battery. We believe our work paves a way for the design of nanostructured carbon materials for the applications in sustainable energy conversion and storage.

DATA AVAILABILITY

All datasets generated for this study are included in the manuscript and/or the **Supplementary Files**.

AUTHOR CONTRIBUTIONS

WS, XC, JS, CG, and WL designed the project. WS, CY, XS, and XL performed the synthesis, CDI experiment, and data analysis. XX, DS, and RY performed the Zn-air battery experiment and data analysis. All authors contribute to editing and discussion of the manuscript.

FUNDING

This work was supported by the financial support from Zhejiang Provincial Natural Science Foundation of China (LQ17B030002, LR19E020003) and the National Natural Science Foundation of China (51702286, 51602284), General Scientific Research Project of the Department of Education of Zhejiang Province, China (Y201839638), and the Thousand Talent Program and Qianjiang Scholars program of Zhejiang Province in China.

SUPPLEMENTARY MATERIAL

The Supplementary Material for this article can be found online at: https://www.frontiersin.org/articles/10.3389/fchem.2019.00449/full#supplementary-material

REFERENCES

Cao, X., Shi, Y., Shi, W., Lu, G., Huang, X., Yan, Q., et al. (2011). Preparation of novel 3D graphene networks for supercapacitor applications. *Small* 7, 3163–3168. doi: 10.1002/smll.201100990

Cao, X., Yin, Z., and Zhang, H. (2014). Three-dimensional graphene materials: preparation, structures and application in supercapacitors. *Energy Environ. Sci.* 7, 1850–1865. doi: 10.1039/C4EE00050A

Ding, M., Bannuru, K. K. R., Wang, Y., Guo, L., Baji, A., and Yang, H. Y. (2018). Free-standing electrodes derived from metal-organic frameworks/nanofibers hybrids for membrane capacitive deionization. *Adv. Mater. Technol.* 3:1800135. doi: 10.1002/admt.201800135

Ding, M., Shi, W., Guo, L., Leong, Z. Y., Baji, A., and Yang, H. Y. (2017). Bimetallic metal–organic framework derived porous carbon nanostructures for high performance membrane capacitive desalination. *J. Mater. Chem. A* 5, 6113–6121. doi: 10.1039/C7TA00339K

Fang, G., Wang, Q., Zhou, J., Lei, Y., Chen, Z., Wang, Z., et al. (2019). Metal organic framework-templated synthesis of bimetallic selenides with rich phase boundaries for sodium-ion storage and oxygen evolution reaction. *ACS Nano*. 13, 5635–5645. doi: 10.1021/acsnano.9b00816

Gao, T., Du, Y., and Li, H. (2019a). Preparation of nitrogen-doped graphitic porous carbon towards capacitive deionization with high adsorption capacity and rate capability. *Sep. Purif. Technol.* 211, 233–241. doi: 10.1016/j.seppur.2018.09.085

Gao, T., Li, H., Zhou, F., Gao, M., Liang, S., and Luo, M. (2019b). Mesoporous carbon derived from ZIF-8 for high efficient electrosorption. *Desalination* 451, 133–138. doi: 10.1016/j.desal.2017.06.021

Gao, T., Zhou, F., Ma, W., and Li, H. (2018). Metal-organic-framework derived carbon polyhedron and carbon nanotube hybrids as electrode for electrochemical supercapacitor and capacitive deionization. *Electrochim. Acta* 263, 85–93. doi: 10.1016/j.electacta.2018.01.044

Guo, Q., Li, X., Wei, H., Liu, Y., Li, L., Yang, X., et al. (2019). Sr, Fe Co-doped perovskite oxides with high performance for oxygen evolution reaction. *Front. Chem.* 7:224. doi: 10.3389/fchem.2019.00224

Han, Y., Lu, Y., Shen, S., Zhong, Y., Liu, S., Xia, X., et al. (2018). Enhancing the capacitive storage performance of carbon fiber textile by surface and structural modulation for advanced flexible asymmetric supercapacitors. *Adv. Mater. Funct.* 29:1806329. doi: 10.1002/adfm.201806329

Hassanvand, A., Chen, G. Q., Webley, P. A., and Kentish, S. E. (2018). A comparison of multicomponent electrosorption in capacitive deionization and membrane capacitive deionization. *Water Res.* 131, 100–109. doi: 10.1016/j.watres.2017.12.015

Hu, C., Liu, Z., Lu, X., Sun, J., Liu, H., and Qu, J. (2018). Enhancement of the donnan effect through capacitive ion increase using an electroconductive rGO-CNT nanofiltration membrane. *J. Mater. Chem. A* 6, 4737–4745. doi: 10.1039/C7TA11003K

Huang, Z.-H., Yang, Z., Kang, F., and Inagaki, M. (2017). Carbon electrodes for capacitive deionization. *J. Mater. Chem. A* 5, 470–496. doi: 10.1039/C6TA06733F

Ji, D., Fan, L., Li, L., Peng, S., Yu, D., Song, J., et al. (2019). Atomically transition metals on self-supported porous carbon flake arrays as binder-free air-cathode for wearable zinc-air batteries. *Adv. Mater.* 31:e1808267. doi: 10.1002/adma.201808267

Kaur, G., Rai, R. K., Tyagi, D., Yao, X., Li, P.-Z., Yang, X.-C., et al. (2016). Room-temperature synthesis of bimetallic Co-Zn based zeolitic imidazolate frameworks in water for enhanced CO_2 and H_2 uptakes. *J. Mater. Chem. A* 4, 14932–14938. doi: 10.1039/C6TA04342A

Lee, J., Jo, K., Lee, J., Hong, S. P., Kim, S., and Yoon, J. (2018). Rocking-chair capacitive deionization for continuous brackish water desalination. *ACS Sustain Chem. Eng.* 6, 10815–10822. doi: 10.1021/acssuschemeng.8b02123

Li, H., Su, Y., Sun, W., and Wang, Y. (2016). Carbon nanotubes rooted in porous ternary metal sulfide@N/S-doped carbon dodecahedron: bimetal-organic-frameworks derivation and electrochemical application for high-capacity and long-life lithium-ion batteries. *Adv. Funct. Mater.* 26, 8345–8353. doi: 10.1002/adfm.201601631

Li, J., Ji, B., Jiang, R., Zhang, P., Chen, N., Zhang, G., et al. (2018a). Hierarchical hole-enhanced 3D graphene assembly for highly efficient capacitive deionization. *Carbon* 129, 95–103. doi: 10.1016/j.carbon.2017.11.095

Li, Y., Kim, J., Wang, J., Liu, N. L., Bando, Y., Alshehri, A. A., et al. (2018b). High performance capacitive deionization using modified ZIF-8-derived, N-doped porous carbon with improved conductivity. *Nanoscale* 10, 14852–14859. doi: 10.1039/C8NR02288G

Liu, P., Yan, T., Shi, L., Park, H. S., Chen, X., Zhao, Z., et al. (2017a). Graphene-based materials for capacitive deionization. *J. Mater. Chem. A*, 5 13907–13943. doi: 10.1039/C7TA02653F

Liu, R., Sui, Y., and Wang, X. (2019a). Metal–organic framework-based ultrafltration membrane separation with capacitive-type for enhanced phosphate removal. *Chem. Eng. J.* 371, 903–913. doi: 10.1016/j.cej.2019.04.136

Liu, W., Huang, J., Yang, Q., Wang, S., Sun, X., Zhang, W., et al. (2017b). Multi-shelled hollow metal-organic frameworks. *Angew. Chem. Int. Edit.* 56, 5512–5516. doi: 10.1002/anie.201701604

Liu, W., Yin, R., Shi, W., Xu, X., Shen, X., Yin, Q., et al. (2018). Gram-scale preparation of 2D transition metal hydroxide/oxide assembled structures for oxygen evolution and Zn-air battery. *ACS Appl. Energy Mater.* 2, 579–586. doi: 10.1021/acsaem.8b01613

Liu, W., Yin, R., Xu, X., Zhang, L., Shi, W., and Cao, X. (2019b). Structural engineering of low-dimensional metal-organic frameworks: synthesis, properties, and applications. *Adv. Sci.* 1802373. doi: 10.1002/advs.201802373

Liu, Y., Lu, T., Sun, Z., Chua, D. H. C., and Pan, L. (2015). Ultra-thin carbon nanofiber networks derived from bacterial cellulose for capacitive deionization. *J. Mater. Chem. A* 3, 8693–8700. doi: 10.1039/C5TA00435G

Lv, Z., Tang, Y., Zhu, Z., Wei, J., Li, W., Xia, H., et al. (2018). Honeycomb-lantern-inspired 3D stretchable supercapacitors with enhanced specific areal capacitance. *Adv. Mater.* 30:1805468. doi: 10.1002/adma.201805468

Nie, C., Pan, L., Liu, Y., Li, H., Chen, T., Lu, T., et al. (2012). Electrophoretic deposition of carbon nanotubes–polyacrylic acid composite film electrode for capacitive deionization. *Electrochim. Acta* 66, 106–109. doi: 10.1016/j.electacta.2012.01.064

Peng, S., Han, X., Li, L., Chou, S., Ji, D., Huang, H., et al. (2018). Electronic and defective engineering of electrospun $CaMnO_3$ nanotubes for enhanced oxygen electrocatalysis in rechargeable zinc-air batteries. *Adv. Energy Mater.* 8:1800612. doi: 10.1002/aenm.201800612

Shi, W., Li, H., Cao, X., Leong, Z. Y., Zhang, J., Chen, T., et al. (2016). Ultrahigh performance of novel capacitive deionization electrodes based on a three-dimensional graphene architecture with nanopores. *Sci. Rep.* 6:18966. doi: 10.1038/srep18966

Shi, W., Liu, X., Ye, C., Cao, X., Gao, C., and Shen, J. (2019a). Efficient lithium extraction by membrane capacitive deionization incorporated with monovalent selective cation exchange membrane. *Sep. Purif. Technol.* 210, 885–890. doi: 10.1016/j.seppur.2018.09.006

Shi, W., Mao, J., Xu, X., Liu, W., Zhang, L., Cao, X., et al. (2019b). An ultra-dense NiS2/reduced graphene oxide composite cathode for high-volumetric/gravimetric energy density nickel-zinc *batteries. J. Mater. Chem. A*. doi: 10.1039/c9ta04900b. [Epub ahead of print].

Shi, W., Ye, C., Xu, X., Liu, X., Ding, M., Liu, W., et al. (2018). High-performance membrane capacitive deionization based on metal-organic framework-derived hierarchical carbon structures. *ACS Omega* 3, 8506–8513. doi: 10.1021/acsomega.8b01356

Song, J., Ma, J., Zhang, C., He, C., and Waite, D. (2019). Implication of non-electrostatic contribution to deionization in flow-electrode CDI: case study of nitrate removal from contaminated source waters. *Front. Chem.* 7:146. doi: 10.3389/fchem.2019.00146

Suss, M. E., Porada, S., Sun, X., Biesheuvel, P. M., Yoon, J., and Presser, V. (2015). Water desalination via capacitive deionization: what is it and what can we expect from it? *Energy Environ. Sci.* 8, 2296–2319. doi: 10.1039/C5EE00519A

Tang, J., Salunkhe, R. R., Liu, J., Torad, N. L., Imura, M., Furukawa, S., et al. (2015). Thermal conversion of core-shell metal-organic frameworks: a new method for selectively functionalized nanoporous hybrid carbon. *J. Am. Chem. Soc.* 137, 1572–1580. doi: 10.1021/ja511539a

Tang, W., Liang, J., He, D., Gong, J., Tang, L., Liu, Z., et al. (2019). Various cell architectures of capacitive deionization: recent advances and future trends. *Water Res.* 150, 225–251. doi: 10.1016/j.watres.2018.11.064

Tsouris, C., Mayes, R., Kiggans, J., Sharma, K., Yiacoumi, S., DePaoli, D., et al. (2011). Mesoporous carbon for capacitive deionization of saline water. *Environ. Sci. Technol.* 45, 10243–10249. doi: 10.1021/es201551e

Wang, H., Shi, L., Yan, T., Zhang, J., Zhong, Q., and Zhang, D. (2014). Design of graphene-coated hollow mesoporous carbon spheres as high performance electrodes for capacitive deionization. *J. Mater. Chem. A* 2, 4739–4750. doi: 10.1039/C3TA15152B

Wang, M., Xu, X., Liu, Y., Li, Y., Lu, T., and Pan, L. (2016). From metal-organic frameworks to porous carbons: a promising strategy to prepare high-performance electrode materials for capacitive deionization. *Carbon* 108, 433–439. doi: 10.1016/j.carbon.2016.07.047

Wang, M., Xu, X., Tang, J., Hou, S., Hossain, M. S. A., Pan, L., et al. (2017a). High performance capacitive deionization electrodes based on ultrathin nitrogen-doped carbon/graphene nano-sandwiches. *Chem. Commun.* 53, 10784–10787. doi: 10.1039/C7CC05673G

Wang, Z., Xu, X., Kim, J., Malgras, V., Mo, R., Li, C., et al. (2019). Nanoarchitectured metal-organic framework/polypyrrole hybrids for brackish water desalination using capacitive deionization. *Mater. Horiz.* doi: 10.1039/C9MH00306A. [Epub ahead of print].

Wang, Z., Yan, T., Shi, L., and Zhang, D. (2017b). *In situ* expanding pores of dodecahedron-like carbon frameworks derived from MOFs for enhanced capacitive deionization. *ACS Appl. Mater. Interfaces* 9, 15068–15078. doi: 10.1021/acsami.7b02712

Wu, T., Wang, G., Zhan, F., Dong, Q., Ren, Q., Wang, J., et al. (2016). Surface-treated carbon electrodes with modified potential of zero charge for capacitive deionization. *Water Res.* 93, 30–37 doi: 10.1016/j.watres.2016.02.004

Xu, X., Allah, A., Wang, C., Tan, H., Farghali, A., Khedr, M., et al. (2019). Capacitive deionization using nitrogen-doped mesostructured carbons for highly efficient brackish water desalination. *Chem. Eng. J.* 362, 887–896. doi: 10.1016/j.cej.2019.01.098

Xu, X., Li, J., Wang, M., Liu, Y., Lu, T., and Pan, L. (2016a). Shuttle-like porous carbon rods from carbonized metal-organic frameworks for high-performance capacitive deionization. *Chemelectrochem* 3, 993–998. doi: 10.1002/celc.201600051

Xu, X., Shi, W., Li, P., Ye, S., Ye, C., Ye, H., et al. (2017). Facile fabrication of three-dimensional graphene and metal-organic framework composites and their derivatives for flexible all-solid-state supercapacitors. *Chem. Mater.* 29, 6058–6065. doi: 10.1021/acs.chemmater.7b01947

Xu, X., Shi, W., Liu, W., Ye, S., Yin, R., Zhang, L., et al. (2018). Preparation of two-dimensional assembled NiMn-C ternary composites for high-performance all-solid-state flexible supercapacitors. *J. Mater. Chem. A* 6, 24086–24091. doi: 10.1039/C8TA06412A

Xu, X., Wang, M., Liu, Y., Lu, T., and Pan, L. (2016b). Metal–organic framework-engaged formation of a hierarchical hybrid with carbon nanotube inserted porous carbon polyhedra for highly efficient capacitive deionization. *J. Mater. Chem. A* 4, 5467–5473. doi: 10.1039/C6TA00618C

Zhang, L., Liu, W., Shi, W., Xu, X., Mao, J., Li, P., et al. (2018a). Boosting lithium storage properties of MOF derivatives through a wet-spinning assembled fiber strategy. *Chem-Eur. J.* 24, 13792–13799. doi: 10.1002/chem.201802826

Zhang, W., Ma, X., Zhong, C., Ma, T., Deng, Y., Hu, W., et al. (2018b). Pyrite-type CoS_2 nanoparticles supported on nitrogen-doped graphene for enhanced water splitting. *Front. Chem.* 6:569. doi: 10.3389/fchem.2018.00569

Zheng, X., Cao, Y., Liu, D., Cai, M., Ding, J., Liu, X., et al. (2019). Bimetallic metal-organic-framework/reduced graphene oxide composites as bifunctional electrocatalysts for rechargeable Zn-air batteries. *ACS Appl. Mater. Interfaces* 11, 15662–15669. doi: 10.1021/acsami.9b02859

Zhu, L., Zheng, D., Wang, Z., Zheng, X., Fang, P., Zhu, J., et al. (2018). A confinement strategy for stabilizing ZIF-derived bifunctional catalysts as a benchmark cathode of flexible all-solid-state zinc-air batteries. *Adv. Mater.* 30:1805268. doi: 10.1002/adma.201805268

Conflict of Interest Statement: The authors declare that the research was conducted in the absence of any commercial or financial relationships that could be construed as a potential conflict of interest.

frontiers in Chemistry

ORIGINAL RESEARCH
published: 12 July 2019
doi: 10.3389/fchem.2019.00499

$CsPbBr_3$/CdS Core/Shell Structure Quantum Dots for Inverted Light-Emitting Diodes Application

Xiaosheng Tang, Jie Yang, Shiqi Li, Weiwei Chen, Zhiping Hu and Jing Qiu**

Key Laboratory of Optoelectronic Technology and Systems, College of Optoelectronic Engineering, Chongqing University, Ministry of Education, Chongqing, China

Novel $CsPbBr_3$/CdS core/shell structure quantum dots (QDs) were successfully synthesized using a facile hot-injection method. The corresponding $CsPbBr_3$/CdS QDs based light-emitting diodes (QLEDs) were further prepared, which demonstrated the maximum luminance of 354 cd/m^2 and an external quantum efficiency (EQE) of 0.4% with the current efficiency (CE) of 0.3 cd/A. Moreover, the optoelectronic performance of the $CsPbBr_3$/CdS QDs based QLEDs exhibited a comparable enhancement in contrast to the pure $CsPbBr_3$ QDs based QLEDs. Hypothetically, the novel $CsPbBr_3$/CdS structure QDs introduced one new route for advanced light emission applications of perovskite materials.

Keywords: semiconductors, luminescence, core/shell structure, quantum dots, light-emitting diode

OPEN ACCESS

Edited by:
Yuxin Tang,
University of Macau, China

Reviewed by:
Du Yuan,
Nanyang Technological University, Singapore
Jin Zhao,
Nanyang Technological University, Singapore
Wang Hui Bo,
University of Macau, China

****Correspondence:***
Shiqi Li
shiqili@cqu.edu.cn
Jing Qiu
jingqiu@cqu.edu.cn

Specialty section:
This article was submitted to Electrochemistry, a section of the journal Frontiers in Chemistry

Received: *25 April 2019*
Accepted: *28 June 2019*
Published: *12 July 2019*

Citation:
Tang X, Yang J, Li S, Chen W, Hu Z and Qiu J (2019) $CsPbBr_3$/CdS Core/Shell Structure Quantum Dots for Inverted Light-Emitting Diodes Application. Front. Chem. 7:499. doi: 10.3389/fchem.2019.00499

INTRODUCTION

During the past two decades, huge efforts have been devoted to various QDs as the light-emitting layer of QLEDs (Coe et al., 2002; Sun et al., 2007; Kwak et al., 2012; Seth and Samanta, 2016; Chen et al., 2017). Recently, perovskite QDs have attracted great attention due to their excellent optoelectronic performance, due to their tunable bandgap, high absorbance coefficient, and high photoluminescence quantum yield (PLQY) (Protesescu et al., 2015; Song et al., 2015; Tang et al., 2016; Heejae et al., 2017). However, the electroluminescence (EL) EQE of halide perovskite QLEDs is relatively lower to that of CdSe based QLEDs, which seriously limits further commercial application (Shirasaki et al., 2013; Dai et al., 2014; Wang et al., 2018). It is known that the photoluminescence (PL) performance of the QDs emitting layer plays a crucial role in QLED. Therefore, how to synthesize QDs with high quality is one critical step for preparing high performance QLEDs. It was recognized that the formation of core/shell structure between semiconductors is one effective approach to improve the performance of nanocrystals and QLEDs devices (Hines and Guyot-Sionnest, 1996; Li et al., 2011). Many research groups have reported that the non-radiative Auger recombination of CdSe QDs could be efficiently suppressed by being coated with larger bandgap materials such as CdS and ZnS, where better optical properties have been achieved (Chen et al., 2008; Bae et al., 2013; Efros and Nesbitt, 2016). However, few studies on the core/shell structure for perovskite materials have been reported. Therefore, it is still a challenge to investigate a perovskite-based core/shell structure and the corresponding QLEDs.

Herein, we synthesized novel colloidal perovskite core/shell QDs by covering $CsPbBr_3$ QDs with a CdS shell. Moreover, the inverted QLEDs (ITO/ZnO:Mg/QDs/CBP(4,4′-Bis(N-carbazolyl)-1,1′-biphenyl)/MoO_3/Al) based on $CsPbBr_3$/CdS core/shell QDs and pure $CsPbBr_3$ QDs were fabricated, respectively. The $CsPbBr_3$/CdS QDs based QLED exhibited the maximum luminance of 354 cd/m^2 with a CE of 0.3 cd/A and the best EQE of 0.4% was 5.4 times of the pure $CsPbBr_3$ QDs based QLEDs.

MATERIALS AND METHODS

Chemicals

Cs_2CO_3 (Aldrich, 99.9%), $PbBr_3$ (ABCR, 98%), Cadmium (II) oxide (Sigma Aldrich, 99.5%), Oleic Acid (OA, Sigma Aldrich, 90%), 1-octadecene (ODE, Sigma Aldrich, tech. 90%), Sulfur (Sigma Aldrich, 99.98%), Oleylamine (OME, Sigma Aldrich, tech. 70%), Toluene (Sigma Aldrich, 99.8%), CBP (Xi'an Polymer Light Technology Co., Ltd.), Molybdenum Oxide (MoO_3, from Aladdin-reagent), ZnO:Mg (Xingshuo Nano Technology Co., Ltd.).

Cd-oleate Solution Synthesis

For the synthesis of Cd-oleate solution a protocol by Li et al. (2011) was adopted. A 0.38 M Cd-oleate solution was made by dissolving 383 mg CdO in 3.9 ml oleic acid and 3.9 ml ODE at 280°C under N_2 flow. After 1 h the CdO was dissolved and the clear solution was degassed for 30 min at 110°C.

$CsPbBr_3$/CdS Core/Shell QDs Synthesis

For the synthesis of $CsPbBr_3$ core QDs a protocol by Protesescu et al. (2015) was adopted. One hundred milligram Cs_2CO_3 was loaded into a 100 ml 3-neck flask along with 4 ml 1-octadecene, and 0.5 ml OA (oleic acid), then heated under N_2 to 120°C until the powder was completely dissolved. Five milliliter ODE and 69 mg $PbBr_2$ were loaded into a 100 ml 3-neck flask and heated under N_2 to 120°C 1 h. 0.5 ml OME and 0.5 ml OA was injected at 120°C under N_2. After the $PbBr_2$ salt was completely dissolved, the temperature was raised to 150°C and the Cs-oleate solution (0.4 ml, 0.125 M in ODE, prepared as described above) was quickly injected and, 5 s later, the reaction finished. Four milliliter ODE, 1 ml Cd-oleate solution, and 0.4 ml 1 M sulfur in OME solution, was mixed when the reaction for $CsPbBr_3$ QDs finished and added dropwise over 20 min to the $CsPbBr_3$ solution at 150°C under N_2 flow. After the addition was complete, the mixture was allowed to react for 20 min at 150°C and was subsequently cooled by an ice-water bath, washed with toluene several times, and dispersed in toluene.

Preparation of QLED

The cleaned ITO/glass was treated under UV–ozone for 30 min. The ZnO:Mg nanoparticles were spin-coated onto ITO/glass at 3,000 rpm for 40 s, and annealed at 100°C for 10 min. The perovskite QDs were deposited by spin-coating at 2,000 rpm for 60 s. CBP (40 nm), MoO_3 (10 nm), and Al (100 nm) electrodes were deposited using a thermal evaporation system through a shadow mask under a high vacuum of $\approx 1 \times 10^{-4}$ Pa. All device operations were performed in a nitrogen-filled glove box.

Optical Characterization

Photoluminescence spectra were measured by Agilent Cary Eclipse spectrograph FLS920P. XRD characterization was done by Shimadzu/6100 X-ray diffractometer, using a Cu Kα radiation source (wavelength at 1.5405 Å). TEM images were recorded on a Zeiss/Libra 200 FE. The PLQY measurements were carried out in solutions with an Edinburgh Instruments fluorescence spectrometer (FLS920), which included a xenon lamp with monochromator for steady-state PL excitation. A calibrated integrating sphere was used for PLQY measurements. The EL spectra and luminance (L)—current density (J)—voltages (V)

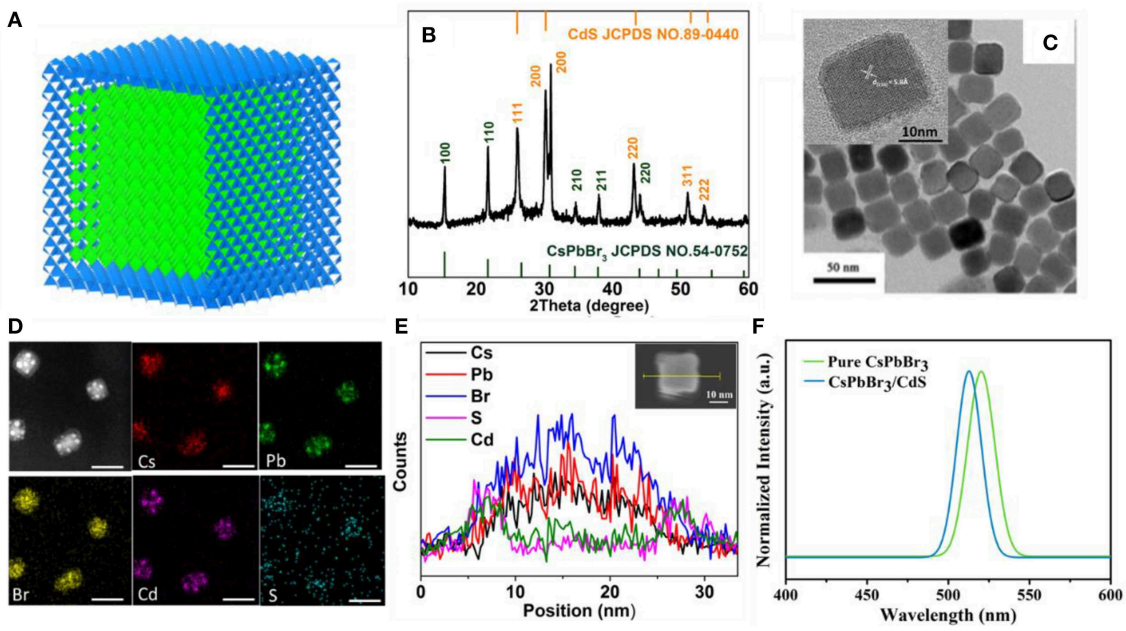

FIGURE 1 | (A,B) Schematic diagram and XRD patterns of $CsPbBr_3$/CdS QDs (orange). The stick patterns show the standard peak positions of $CsPbBr_3$ (green) and CdS (blue). **(C)** TEM images of $CsPbBr_3$/CdS QDs, the inset shows a high resolution TEM image of $CsPbBr_3$/CdS QDs. **(D,E)** The mapping images and EDX line profiles of Cs, Pb, Br, Cd, and S for $CsPbBr_3$/CdS QDs. Scale bars correspond to 30 nm in **(D)**. **(F)** PL spectra of pure $CsPbBr_3$ QDs (green curve) and $CsPbBr_3$/CdS QDs (blue curve) in toluene, the excitation light is 350 nm.

characteristics were collected using a Keithley 2400 source and a PR-670 Spectra Scan spectrophotometer (Photo Research) at room temperature.

RESULTS AND DISCUSSION

Based on the continuous injection method, a novel approach to overcome a non-radiative recombination of $CsPbBr_3$ QDs was developed by growing a thin CdS shell on the surface of the $CsPbBr_3$ core. **Figure 1A** shows the simulation of the $CsPbBr_3$/CdS core/shell structure. The X-ray diffraction (XRD) patterns of the $CsPbBr_3$/CdS core/shell QDs clearly show that two types of crystalline structures were formed (**Figure 1B**). Compared to the pure $CsPbBr_3$ QDs (**Figure S2**), the extra peaks of the $CsPbBr_3$/CdS XRD patterns are fairly consistent with the standard XRD patterns of a CdS-liked zinc blende structure. From the transmission electron microscope (TEM) images of $CsPbBr_3$ (**Figure S1b**) and $CsPbBr_3$/CdS QDs (**Figure 1C),** it can be seen that the point angle of the cubic shape become a circular arc. The high resolution TEM image of $CsPbBr_3$ (the inset of **Figure S1b**) and $CsPbBr_3$/CdS QDs (the inset of **Figure 1C)** clearly exhibit the crystal lattice (110) of the $CsPbBr_3$ nanoparticles and further verify the $CsPbBr_3$/CdS core/shell structure. In addition, the $CsPbBr_3$/CdS QDs exhibited a typical cubic shape with a larger average size (22.1 nm) than that of the $CsPbBr_3$ QDs (12.7 nm; **Figure S1**). To further demonstrate the successful formation of the $CsPbBr_3$ core and CdS shell, the mapping analysis and energy dispersive X-ray (EDX) spectroscopy of $CsPbBr_3$/CdS QDs was employed (**Figures 1D,E**) with the S and Cd elements uniformly distributed on the surface of the $CsPbBr_3$ core. Moreover, the PL spectra of $CsPbBr_3$/CdS QDs has a slightly blueshift (from 519 to 514 nm) compared with pure $CsPbBr_3$ QD (**Figure 1F**), which was probably induced by the CdS shell. A similar phenomenon was found and ascribed for the cationic inter-diffusion at the interface between the $CsPbBr_3$ core and CdS shell (Oladeji and Chow, 2005; Li et al., 2011; Kwak et al., 2015). On the other side, the $CsPbBr_3$/CdS showed a high photoluminescence quantum yield (PLQY) of 88% (**Figure S3**) and the full width at half-maximum (FWHM) was as narrow as 19 nm, which is similar to pure $CsPbBr_3$ QDs.

As shown in **Figure 2A**, the inverted QLEDs structure was fabricated with a sandwich structure of ITO (In_2O_3-SnO_2)/ZnO:Mg/QDs/CBP/MoO_3/Al, which was constituted by the transparent electrode ITO as a cathode, Mg doped ZnO as an electron transport layer, perovskite QDs as the light-emitting layer, CBP as a hole transport layer, Al as an anode, and MoO_3 as a hole injection layer. The flat-band energy levels of devices are shown in **Figures 2B,C**. After perovskite QDs were coated on the ZnO:Mg electron transport layer, the perovskite film was still soluble in organic solvents due to the presence of aliphatic ligands on the QDs. The structure above the light emitting layer was prepared by evaporation (**Materials and Methods section**).

As shown in **Figures 2D,E**, the peaks of the QLEDs EL spectra based on $CsPbBr_3$ QDs and $CsPbBr_3$/CdS QDs were consistent with the PL spectra, and the luminescence intensity

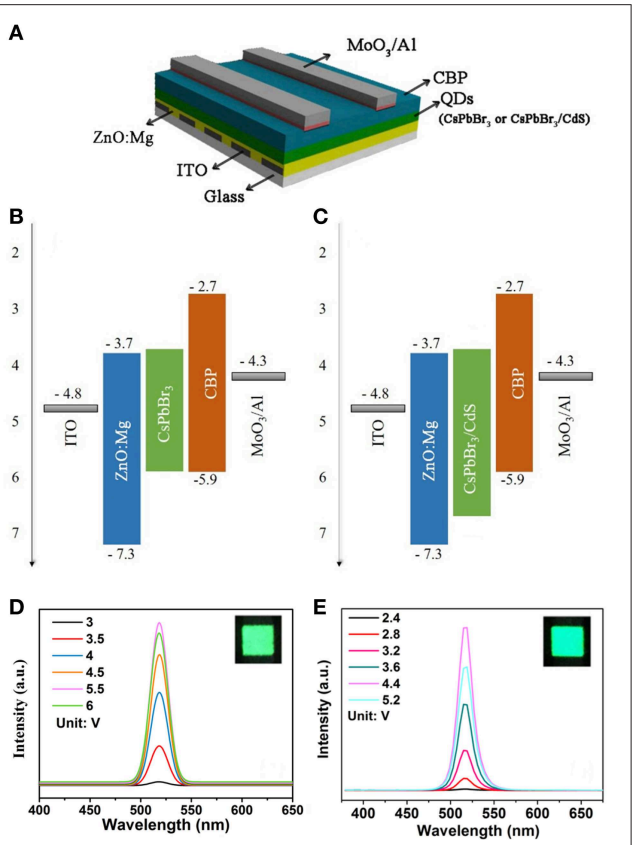

FIGURE 2 | (A) Inverted QLEDs structure schematic. Energy-level diagram of $CsPbBr_3$ QDs **(B)** and $CsPbBr_3$/CdS QDs **(C)** based QLEDs. The EL spectra of $CsPbBr_3$ QDs **(D)** and $CsPbBr_3$/CdS QDs **(E)** based QLED, the insets shows an operating device driven at 4 V.

increased with the voltage increase. The EL of pure $CsPbBr_3$ QDs based LEDs (**Figure 2D**), peaking at 519 nm with a FWHM of ∼20 nm, was observed. And there is no emission peak from the hole/electron transport layer. The $CsPbBr_3$/CdS QDs based QLEDs also performed with a peak at 516 nm with a FWHM of ∼20 nm. As depicted in **Figure 2E**, the emission from the hole/electron transport layer was hardly shown. The insets showed an operating device driven at 4 V, and the devices both exhibited a saturated and pure green color.

For the potential application in a light emission device, the characteristic of emitter layers is extremely important. For the inverted QLEDs with the $CsPbBr_3$ QDs emitting layer, the pure $CsPbBr_3$ QDs worked with poorer luminous characteristics, exhibiting a lower maximum luminance intensity of 65 cd/m^2 and the maximum CE of 0.14 cd/A (**Figures 3A,B**). It is worth mentioning that a maximum luminance of 354 cd/m^2 was obtained when the $CsPbBr_3$/CdS QDs were used as the emitting layer, and the maximum CE was boosted to 0.3 cd/A (**Figures 3C,D**). The overall performance of two kinds of devices were also described with the average EQE. The EQE of QLEDs with the $CsPbBr_3$ QDs emitting layer (0.4%) was 5.4 times larger than the pure $CsPbBr_3$ QDs (0.07%). The results are tabulated in

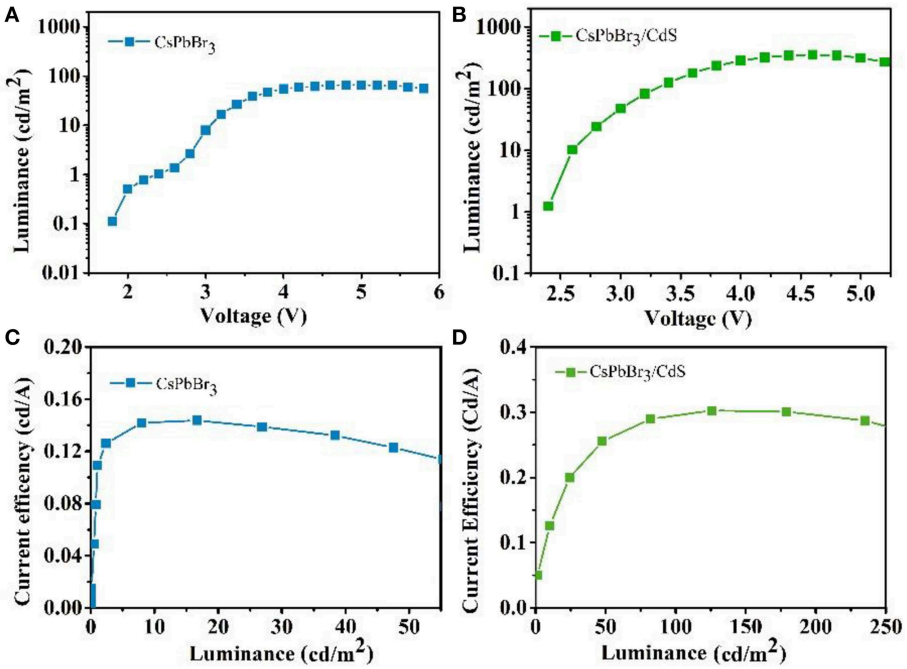

FIGURE 3 | Luminance vs. driving voltage characteristics for pure CsPbBr$_3$ QDs **(A)** and CsPbBr$_3$/CdS QDs **(B)** based QLEDs. CE luminance curve for pure CsPbBr$_3$ QDs **(C)** and CsPbBr$_3$/CdS QDs **(D)** based QLEDs.

TABLE 1 | Comparison of performance parameters between CsPbBr$_3$ QDs and CsPbBr$_3$ QDs based QLED.

Devices	Max. L (cd/m^2)	Max. CE (cd/A)	MAX. EQE (%)
CsPbBr$_3$ based QLED	65	0.14	0.07
CsPbBr$_3$/CdS based QLED	354	0.3	0.4

Table 1 for comparison. Based on the same device structure with a different emitting layer, the turn-on voltage of CsPbBr$_3$/CdS based QLEDs was slightly lower than CsPbBr$_3$ based QLEDs. Moreover, the maximum CE of the CsPbBr$_3$/CdS based QLEDs was 2.1 times larger than the pure CsPbBr$_3$ based QLEDs, which could be ascribed to the valence bands (conduction bands) of the CdS shell which are lower (or higher) than that of CsPbBr$_3$ core, and a non-radiative Auger recombination of CsPbBr$_3$ was effectively suppressed (Park et al., 2014; Nasilowski et al., 2015; Niu et al., 2017). Additionally, the probable reason could be attributed to the fact that the extra carriers cannot escape from the surface of the QDs as the protecting layer of CdS, which leads to a higher radiative recombination rate, higher luminance and EQE.

CONCLUSION

In conclusion, we have developed novel all-inorganic core/shell perovskite QDs and applied it as an emitting layer in inverted QLEDs (ITO/ZnO:Mg/QDs/CBP/MoO_3/Al). The results show that the fabricated CsPbBr$_3$/CdS QDs based QLEDs exhibited enhanced performance compared with pure CsPbBr$_3$ QDs based QLEDs. The EQE of CsPbBr$_3$/CdS QDs was 5.4 times higher than that of pure CsPbBr$_3$ QDs, which demonstrates that the introduction of a CdS shell can increase the optoelectronic performance. The core/shell structure perovskite QDs present a new route of perovskite materials for light emission applications.

DATA AVAILABILITY

All datasets generated for this study are included in the manuscript and/or the **Supplementary Files**.

AUTHOR CONTRIBUTIONS

XT and JY contributed equally to this work. XT and JQ designed the experiment. JY and SL conducted the experiments and characterization. XT and JQ wrote and revised the paper. JY, WC, and ZH participated in the discussion. XT funded some of the subject experiments.

FUNDING

This work is supported by the Fundamental Research Funds for the Central Universities (Grant No. 2018CDYJSY0055, 106112017CDJQJ128837), the National Natural Science Foundation of China (Grant Nos. 61520106012, 61674023, 51775070, and 51602033), the Chongqing Research

Program of Basic Research and Frontier Technology (Grant Nos. cstc2017jcyjB0127, cstc2017jcyjAX0197), and the Open Fund of the State Key Laboratory of High Field Laser Physics (Shanghai Institute of Optics and Fine Mechanics).

SUPPLEMENTARY MATERIAL

The Supplementary Material for this article can be found online at: https://www.frontiersin.org/articles/10.3389/fchem.2019.00499/full#supplementary-material

REFERENCES

Bae, W. K., Padilha, L. A., Park, Y.-S., McDaniel, H., Robel, I., Pietryga, J. M. (2013).Controlled alloying of the core–shell interface in CdSe/CdS quantum dots for suppression of auger recombination. *ACS Nano* 7, 3411–3419. doi: 10.1021/nn4002825

Chen, W. W., Hao, J. Y., Hu, W., Zang, Z. G., Tang, X. S., Fang, L., et al. (2017). Enhanced stability and tunable photoluminescence in perovskite CsPbX3 /ZnS quantum dot heterostructure. *Small* 13:1604085. doi: 10.1002/smll.201604085

Chen, Y., Vela, J., Htoon, H., Casson, J. L., Werder, D. J., Bussian, D. A., et al. (2008). "Giant" multishell CdSe nanocrystal quantum dots with suppressed blinking. *J. Am. Chem. Soc.* 130, 5026–5027. doi: 10.1021/ja711379k

Coe, S., Woo, W. K., Bawendi, M., and Bulovic, V. (2002). Electroluminescence from single monolayers of nanocrystals in molecular organic devices. *Nature* 420, 800–803. doi: 10.1038/nature01217

Dai, X. L., Zhang, Z. X., Jin, Y. Z., Niu, Y., Cao, H. J., Liang, X. Y., et al. (2014). Solution-processed, high-performance light-emitting diodes based on quantum dots. *Nature* 515, 96–99. doi: 10.1038/nature13829

Efros, A. L., and Nesbitt, D. J. (2016). Origin and control of blinking in quantum dots. *Nat. Nanotechnol.* 11, 661–671. doi: 10.1038/nnano.2016.140

Heejae, C., Il, J. S., Jin, K. H., Wonhee, C., Eunji, S., Dongho, K., et al. (2017). Composition-dependent hot carrier relaxation dynamics in cesium lead halide (CsPbX3, X=Br and I) perovskite nanocrystals. *Angew. Chem.* 129, 4224–4228. doi: 10.1002/ange.201611916

Hines, M. A., and Guyot-Sionnest, P. (1996). Synthesis and characterization of strongly luminescing ZnS-Capped CdSe nanocrystals. *J. Phys. Chem.* 100, 468–471. doi: 10.1021/jp9530562

Kwak, J., Bae, W. K., Lee, D., Park, I., Lim, J., Park, M., et al. (2012). Bright and efficient full-color colloidal quantum dot light-emitting diodes using an inverted device structure. *Nano Lett.* 12, 2362–2366. doi: 10.1021/nl3003254

Kwak, J., Lim, J., Park, M., Lee, S., Char, K., and Lee, C. (2015). High-power genuine ultraviolet light-emitting diodes based on colloidal nanocrystal quantum dots. *Nano Lett.* 15, 3793–3799. doi: 10.1021/acs.nanolett.5b00392

Li, L., Pandey, A., Werder, D. J., Khanal, B. P., Pietryga, J. M., and Klimov, V. I. (2011). Efficient synthesis of highly luminescent copper indium sulfide-based core/shell nanocrystals with surprisingly long-lived emission. *J. Am. Chem. Soc.* 133, 1176–1179. doi: 10.1021/ja108261h

Nasilowski, M., Spinicelli, P., Patriarche, G., and Dubertret, B. (2015). Gradient CdSe/CdS quantum dots with room temperature biexciton unity quantum yield. *Nano Lett.* 15, 3953–3958. doi: 10.1021/acs.nanolett.5b00838

Niu, Y., Pu, C. D., Lai, R. C., Meng, R. Y., Lin, W. Z., Qin, H. Y., et al. (2017). One-pot/three-step synthesis of zinc-blende CdSe/CdS core/shell nanocrystals with thick shells. *Nano Res.* 10, 1149–1162. doi: 10.1007/s12274-016-1287-3

Oladeji, I. O., and Chow, L. (2005). Synthesis and processing of CdS/ZnS multilayer films for solar cell application. *TSF* 474, 77–83. doi: 10.1016/j.tsf.2004.08.114

Park, Y. S., Bae,W. K., Pietryga, J. M., and Klimov, V. I. (2014). Auger recombination of biexcitons and negative and positive trions in individual quantum dots. *ACS Nano* 8, 7288–7296. doi: 10.1021/nn5023473

Protesescu, L., Yakunin, S., Bodnarchuk, M. I., Krieg, F., Caputo, R., Hendon, C. H., et al. (2015). Nanocrystals of cesium lead halide perovskites (CsPbX(3), X = Cl, Br, and I): novel optoelectronic materials showing bright emission with wide color gamut. *Nano Lett.* 15, 3692–3696. doi: 10.1021/nl5048779

Seth, S., and Samanta, A. (2016). A facile methodology for engineering the morphology of CsPbX3 perovskite nanocrystals under ambient condition. *Sci. Rep.* 6:37693. doi: 10.1038/srep37693

Shirasaki, Y., Supran, G. J., Bawendi, M. G., and Bulovic, V. (2013). Emergence of colloidal quantum-dot light-emitting technologies. *Nat.Photon.* 7, 13–23. doi: 10.1038/nphoton.2012.328

Song, J. Z., Li, J. H., Li, X. M., Xu, L. M., Dong,Y. H., and Zeng, H.B. (2015). Quantum dot light-emitting diodes based on inorganic perovskite cesium lead halides (CsPbX3). *Adv. Mater.* 27, 7162–7167. doi: 10.1002/adma.201502567

Sun, Q., Wang, Y. A., Li, L. S., Wang, D., Zhu, T., Xu, J., et al. (2007). Bright, multicoloured light-emitting diodes based on quantum dots. *Nat. Photon.* 1, 717–722. doi: 10.1038/nphoton.2007.226

Tang, X. S., Hu, Z. P., Chen, W. W., Xing, X., Zang, Z. G., Hu, W., et al. (2016). Room temperature single-photon emission and lasing for all-inorganic colloidal perovskite quantum dots. *Nano Energy* 28, 462–468. doi: 10.1016/j.nanoen.2016.08.062

Wang, H.-C., Bao, Z., Tsai, H.-Y., Tang, A.-C., and Liu, R.-S. (2018). Perovskite quantum dots and their application in light-emitting diodes. *Small* 14:1702433. doi: 10.1002/smll.201702433

Conflict of Interest Statement: The authors declare that the research was conducted in the absence of any commercial or financial relationships that could be construed as a potential conflict of interest.

frontiers in Chemistry

ORIGINAL RESEARCH
published: 16 July 2019
doi: 10.3389/fchem.2019.00512

In-situ Functionalization of Metal Electrodes for Advanced Asymmetric Supercapacitors

Leimeng Sun[1], Xinghui Wang[2], Yurong Wang[1], Dongyang Xiao[1], Weifan Cai[3], Yuan Jing[3], Yanrong Wang[3], Fangjing Hu[1]* and Qing Zhang[3]**

[1] MOE Key Laboratory of Fundamental Physical Quantities Measurement & Hubei Key Laboratory of Gravitation and Quantum Physics, PGMF and School of Physics, Huazhong University of Science and Technology, Wuhan, China, [2] College of Physics and Information Engineering, Institute of Micro-Nano Devices and Solar Cells, Fuzhou University, Fuzhou, China, [3] NOVITAS, Nanoelectronics Centre of Excellence, School of Electrical and Electronic Engineering, Nanyang Technological University, Singapore, Singapore

OPEN ACCESS

Edited by:
Yuxin Tang,
University of Macau, China

Reviewed by:
Xiehong Cao,
Zhejiang University of Technology, China
Cao Guan,
National University of Singapore, Singapore
Xiaolei Sun,
Leibniz-Institut für Festkörper- und Werkstoffforschung (IFW Dresden), Germany
Baihua Qu,
Xiamen University, China

***Correspondence:**
Leimeng Sun
sunleimeng@hust.edu.cn
Fangjing Hu
fangjing_hu@hust.edu.cn
Qing Zhang
eqzhang@ntu.edu.sg

Specialty section:
This article was submitted to Electrochemistry, a section of the journal Frontiers in Chemistry

Received: 26 May 2019
Accepted: 03 July 2019
Published: 16 July 2019

Citation:
Sun L, Wang X, Wang Y, Xiao D, Cai W, Jing Y, Wang Y, Hu F and Zhang Q (2019) In-situ Functionalization of Metal Electrodes for Advanced Asymmetric Supercapacitors. Front. Chem. 7:512. doi: 10.3389/fchem.2019.00512

Nanostructured metal-based compound electrodes with excellent electrochemical activity and electrical conductivity are promising for high-performance energy storage applications. In this paper, we report an asymmetric supercapacitor based on Ti and Cu coated vertical-aligned carbon nanotube electrodes on carbon cloth. The active material is achieved by *in-situ* functionalization using a high-temperature annealing process. Scanning and transmission electron microscopy and Raman spectroscopy confirm the detailed nanostructures and composition of the electrodes. The TiC@VCC and Cu_xS@VCC electrodes show a high specific capacity of 200.89 F g^{-1} and 228.37 F g^{-1}, respectively, and good capacitive characteristics at different scan speeds. The excellent performance can be attributed to a large surface area to volume ratio and high electrical conductivity of the electrodes. Furthermore, an asymmetric supercapacitor is assembled with TiC@VCC as anode and Cu_xS@VCC as cathode. The full device can operate within the 0–1.4 V range, and shows a maximum energy density of 9.12 Wh kg^{-1} at a power density of 46.88 W kg^{-1}. These findings suggest that the metal-based asymmetric electrodes have a great potential for supercapacitor applications.

Keywords: asymmetric supercapacitors, carbon nanotubes, carbon cloth, *in-situ* functionalization, metal electrode

INTRODUCTION

Supercapacitors (SCs) with outstanding power densities and cycling performances have become one of the most promising power sources for next generation microelectronics and portable electronic products (Wang, 2010). However, their low energy density is one of major barriers for commercialization and practical applications of SCs. For example, the SCs based on carbon materials could hardly satisfy the energy demands for most practical applications in comparison with metal ion batteries. According to the energy (E) and capacitance (C) relationship, i.e., $E = \frac{1}{2}CV^2$, where V stands for the working voltage of SC, asymmetric supercapacitors (ASCs) based on novel materials are considered to be capable of improving the energy densities from two aspects. One is that the operation potential window is effectively broadened through the asymmetric design. The other one is that, by applying functional nanomaterials to electrodes to introduce the faradic capacitance, the specific capacitance of the electrodes can be significantly enhanced. As a result, ASCs based on nanostructured metal oxides have shown a significant improvement in energy

density, and an operating potential of 2.0 V for ASCs have been achieved (Xiao et al., 2012). However, the metal oxides based ASCs suffer from poor conductivities and low power densities (Zhu et al., 2015). In order to solve these problems, new electroactive materials apart from transition metal oxides need to be investigated, to optimize the performance of electrodes in ASCs.

Transition metal oxides were considered as promising candidates for new energy storage material due to the introduction of pseudo capacitance that was able to significantly increase specific capacitance when compared with traditional carbon based electrodes. However, transition metal oxide are usually of poor conductivity and could not deliver high current and power densities. Transition metal carbides exhibit both fascinating energy storage performances and outstanding conductivities, when compared with transition metal oxides. Two-dimensional metal carbides have demonstrated ultrahigh specific volumetric capacitances (Lukatskaya et al., 2013). In addition, compared with metal oxides, transition metal carbides usually have better cycling performances. For example, supercapacitor based on a tubular TiC fiber nanostructured electrode was fabricated and tested for more than 150,000 cycles at a high temperature of 65°C (Xia et al., 2015). Moreover, layered titanium carbide Ti_3C_2 has also been proved to be a promising negative electrode material with a high mass loading of 7.6 mg cm^{-2} and a high specific capacitance of 112 F g^{-1} in a stable potential window (−0.9 to −0.3 V refer to Ag/AgCl electrode) (Lin and Zhang, 2015). Transition metal sulfides (e.g., MoS_2, $NiCo_2S_4$, Ni_3S_2) based electrodes have also been extensively studied with ever improving intrinsic conductivity (Acerce et al., 2015; Fu et al., 2015; Li et al., 2015). Copper sulfides (Cu_xS) have been used in electrochemical devices for gas sensing application (Sagade and Sharma, 2008) and lithium-ion batteries (Chung and Sohn, 2002), owing to their superior conductivity and great specific capacitance. Furthermore, acting as positive electrodes of supercapacitors, Cu_xS presents a metal-like conductivity of $\sim 1 \times 10^3$ S cm^{-1} (Mazor et al., 2009) and remarkable specific capacitance of 110 F g^{-1} (Zhu et al., 2012). To better evaluate the capacitance of CuS based electrodes, an asymmetric supercapacitor cell, constructed with nanostructured CuS networks as the cathode and activated carbon as anode, was demonstrated with a high specific capacity of 49.8 mAh g^{-1} at a current density of 1 A g^{-1}, and the maximum energy density is 17.7 Wh kg^{-1} at a power density of 504 W kg^{-1} (Fu et al., 2016).

The structures of electrodes are also important for optimizing the performance of supercapacitors. Recently, three-dimensional nanocarbon electrodes made from carbon nanotubes (CNTs) on carbon cloth (CC) were applied to electrochemical cells. A nickel-zinc battery based on a 3D hierarchical carbon nanofiber-CC electrode was reported to have a power density of 6.09 mWh cm^{-3} and an energy density of 355.7 Wh kg^{-1} (Liu et al., 2016). A lithium-ion battery with 3D carbon nanostructures as its electrodes can be consistently operated for more than 8,000 cycles (Wang et al., 2015). Furthermore, low-dimensional metal-organic frameworks (LD MOFs) have attracted increasing attention in recent years, which successfully combine the unique properties of MOFs, with the distinctive physical and chemical properties of LD nanomaterials (Xu et al., 2017, 2018; Liu et al., 2019).

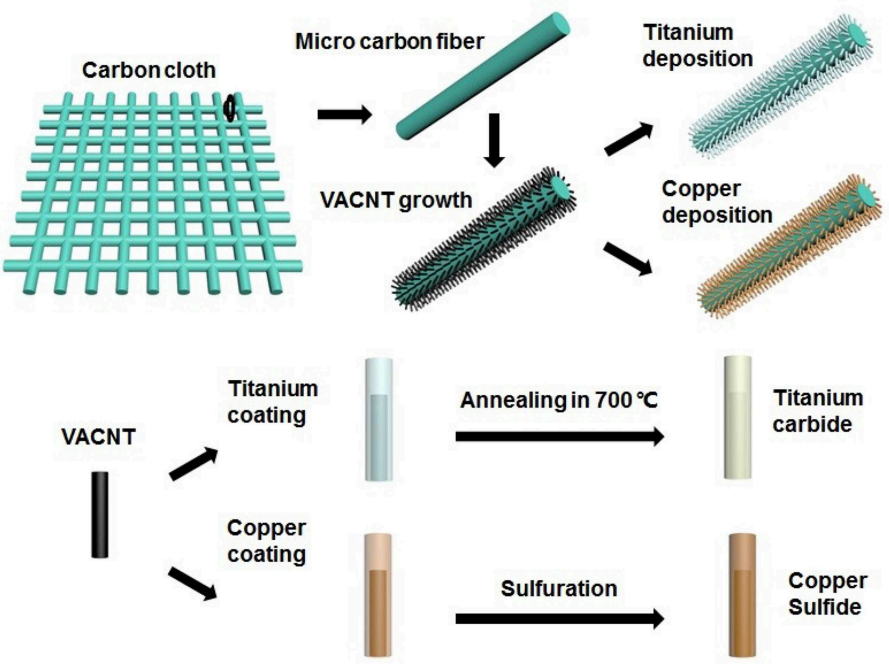

FIGURE 1 | Schematics of the fabrication processes of the cathode and anode electrode.

Herein, we report on an asymmetric supercapacitor constructed with TiC and Cu_xS as its anode and cathode, respectively. TiC@VCC and CuxS@VCC are chosen as negative and positive electrode, respectively, due to the potential window of the materials. To optimize the electrochemical performance of the device, we have incorporated a vertical-aligned carbon nanotube (VACNT) array on carbon cloth as the electrodes. Different from other reported CNT arrays, the VACNT array employed here is of low density and superior conductivity, and has demonstrated as promising electrochemical electrodes (Sun et al., 2015, 2016, 2017). The array with well-distributed VACNTs on carbon cloth (VCC) forms a 3D nanostructure with a large surface to volume ratio and ultra-straight morphology (Wang et al., 2016). A high-temperature annealing process is conducted to *in-situ* functionalize the metal-coated VCC electrodes for the anode and cathode. A large specific capacitance of 200.89 F g^{-1} in a potential window of −0.7–0.1 V and 228.37 F g^{-1} in −0.1–0.7 V are obtained. Moreover, a full device based on these electrodes shows a high energy density of 9.12 Wh kg^{-1} and power density of 46.88 W kg^{-1}. Our findings suggest a feasible approach to achieve SCs with both high energy densities and high power densities.

EXPERIMENTAL

Preparation of VACNT Array on Carbon Cloth

Well-distributed VACNTs were grown on a piece of flexible carbon cloth as current collectors. Firstly, an ultrathin Ni/Al_2O_3 bi-layer catalyst was deposited through a plasma-enhanced CVD (PECVD) system (Wang et al., 2014a) and the CNT grew in a mixture of ammonia/acetylene (240/60 sccm) gas atmosphere under 120 W plasma at 800°C.

Preparation of TiC@VCC and Cu_xS@VCC Electrodes

After the fabrication of VCC, 500 nm titanium and copper were coated on the VACNT array using a Denton RF/DC magnetron sputtering system in which a Ti target (99.999%) and a Cu target (99.99%) were sputtered at a current of 0.7 A and 0.4 A under a pure Argon atmosphere, respectively. *In-situ* functionalization processes for both electrodes were conducted in a thermal chemical vapor deposition (TCVD) furnace. The sulfur powder was placed in an Al_2O_3 ceramic boat and heated in a low temperature zone and the two metal-coated VCC electrodes were

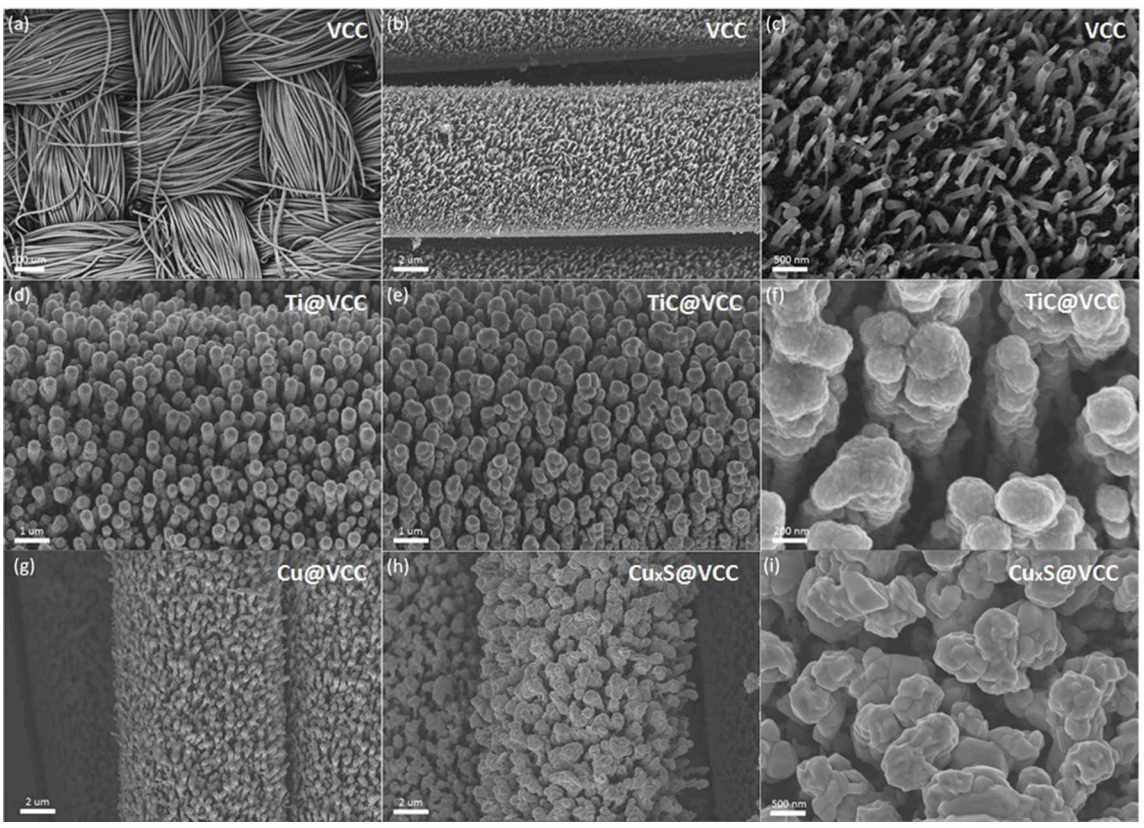

FIGURE 2 | Morphology characterizations of VCC electrodes before and after the metal coating and thermal anneal functionalization. SEM images of VCC with different magnifications of 80 **(a)**, 5,000 **(b)** and 20,000 **(c)**. SEM images of Ti@VCC electrode before **(d)** and after **(e,f)** the functionalization. SEM images of Cu@VCC electrode before **(g)** and after **(h,i)** the functionalization.

placed in a high temperature zone of 700°C for about 30 min in a mixed gas (Ar/H_2) atmosphere.

Materials Characterization and Electrochemical Measurement

The structure and morphology of the electrodes were characterized with a SEM system (LEO 1550 Gemini) and TEM (JEM 2100 FJEOL), respectively. A Raman system (WITec) with a 532 nm wavelength excitation was applied for Raman spectrum measurements. The mass loading of these as-grown TiC or Cu_xS nanocomposite were 0.12 and 0.65 mg/cm^2, respectively, which were determined by the difference before and after material deposition and functionalization with an analytical balance (Mettler Toledo XP 26, 0.002 mg).

Electrochemical measurements of the electrode were carried out through an electrochemical workstation (Autolab/M101) in a 1.0 M LiCl aqueous electrolyte under a three-electrode measurement setup with a standard Ag/AgCl reference electrode. For full device test, a standard CR-2032 coin cell testing system was built and tested as a whole, in which TiC@VCC and Cu_xS@VCC electrodes were used as the anode and cathode, respectively. A membrane was used as the separator and 1.0 M LiCl as the aqueous electrolyte.

RESULTS AND DISCUSSION

The fabrication process of the TiC@VCC and Cu_xS@VCC electrodes is shown in **Figure 1**. A 20 nm nickel thin film functioning as catalyst for VACNT growth was deposited on the carbon cloth substrate through an electron beam evaporation system. The VACNT array synthesis was conducted in a plasma-enhanced chemical vapor deposition system (Wang et al., 2014b) to form 3D nanostructured VCC electrodes.

SEM images of the VCC substrate in **Figures 2a–c** show that VACNTs were well distributed on the surface of the carbon cloth. The density and uniformity of the as-prepared VACNTs are much better than randomly grown carbon nanotube networks (De Volder et al., 2013) and common carbon nanotube arrays grown via thermal CVD system (Jiang et al., 2013). In addition, large interspacings in the VACNT array in **Figure 2c** can reserve space for later accommodation of active materials.

After the fabrication of VCC electrodes, titanium and copper were deposited on these VCC substrates via sputtering. SEM

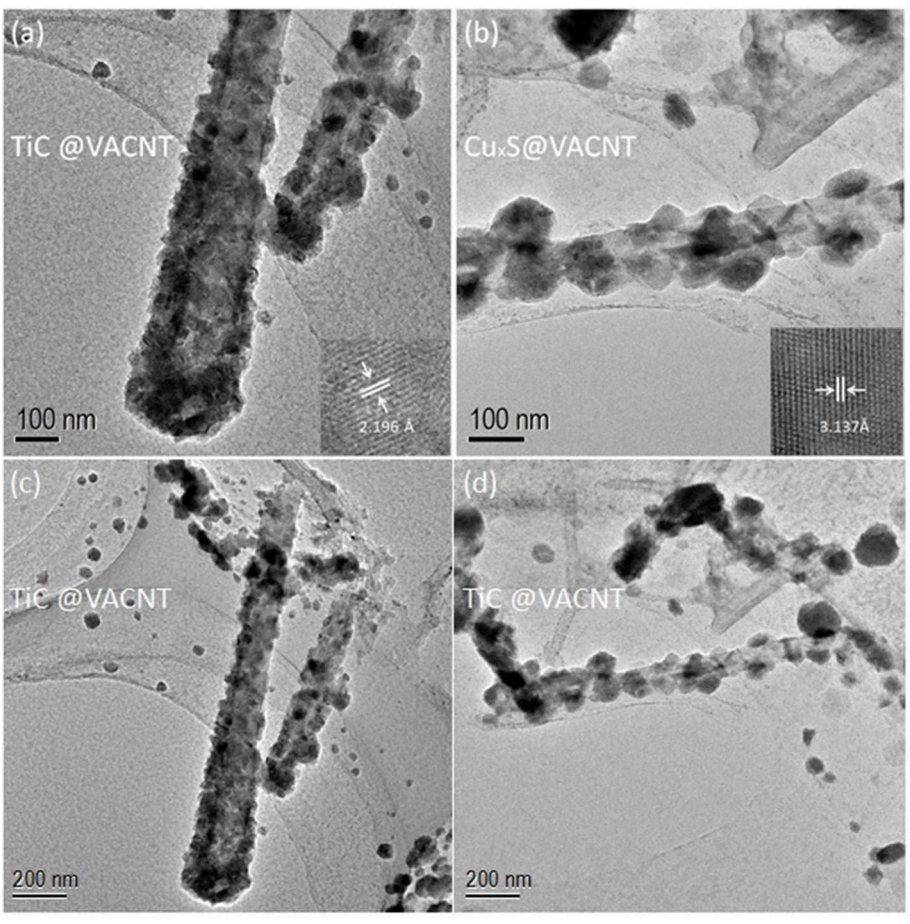

FIGURE 3 | TEM images of electrodes: TiC@VACNT **(a,c)**, and Cu_xS@VACNT **(b,d)**. (Insets: corresponding high resolution TEM images.

images of Ti@VCC (**Figure 2d**) and Cu@VCC (**Figure 2g**) electrodes suggest that the diameters of 1D nanostructures in both electrodes were uniformly increased, indicating that conformable coatings of titanium and copper on VCC electrodes have been achieved. Subsequently, high temperature annealing processes were conducted for Ti@VCC and Cu@VCC electrodes, as described in Section Preparation of TiC@VCC and CuxS@VCC electrodes. It is confirmed that the proposed *in-situ* functionalization process has successfully converted the two metal-coated VCC electrodes into TiC@VCC (Yildirim and Ciraci, 2005) and Cu_xS@VCC (Vas-Umnuay et al., 2015) electrodes, respectively. In **Figures 2e,h**, it is seen that the diameters of metal coated VACNTs have not been significantly changed. From zoom-in images as seen in **Figures 2f,j**, the surface morphologies of 1D nanostructures in both electrodes have been altered, especially for the Cu_xS@VCC electrode. It is also noticed that a notable aggregation occurred in the functionalized VACNT array during the annealing process, and part of the nanowires have stick together to form thicker bundles (Sun et al., 2015). Nevertheless, enough interspacing and porosity were reserved inside of these 3D nanostructured electrodes although the 1D nanostructured array would aggregate during the annealing step.

To obtain detailed nanostructures and materials compositions of the electrodes, transmission electron microscopy (TEM) characterizations were performed. **Figures 3a,c** reveil the core-shell nanostructure within a single TiC-coated VACNT. The inset of a high resolution TEM (HRTEM) image indicates a lattice interspacing of 2.196 Å, corresponding to the (002) planes of TiC (Xia et al., 2015). TEM image of a single Cu_xS-coated VACNT (**Figure 3d**) is consistent with the SEM characterization results, and the aggregation phenomenon in Cu_xS@VCC further escalated during the high-temperature functionalization. In this process, as-deposited Cu thin film was converted into Cu_xS nanoparticles attached to the VACNTs with an approximate average diameter of 100 nm. The inset of **Figure 3b** shows a d-spacing of 3.127 Å, which coincides with other findings of high-temperature fabricated Cu_xS (Quintana-Ramirez et al., 2014; Bulakhe et al., 2016). Low-magnification images of TiC@VCC and Cu_xS@VCC are further provided as shown in **Figures 4C,D** to confirm the material of electrodes.

The Raman spectra of the TiC@VCC electrode and bare VCC electrodes are shown in **Figures 4A,B**, respectively. Strong characteristic peaks of 258, 430, and 620 cm^{-1} are attributed to TiC after functionalization (Lohse et al., 2005; Xia et al., 2015). Concurrently, the intensities of the Raman disordered band (D band) and graphitic band (G band) are significantly reduced, confirming that the TiC thin film shell was conformably coated on VACNTs. The Raman spectra of Cu_xS@VCC electrodes illustrate a strong copper sulfide peak at 470 cm^{-1} (**Figure 4C**), and weakened D and G band (**Figure 4D**), which are well-consistent with other reported results (Munce et al., 2007; Quintana-Ramirez et al., 2014; Bulakhe et al., 2016).

The electrochemical characterizations of the proposed electrodes were performed in a standard three-electrode testing system with Pt plate as a counter electrode, and Ag/AgCl as

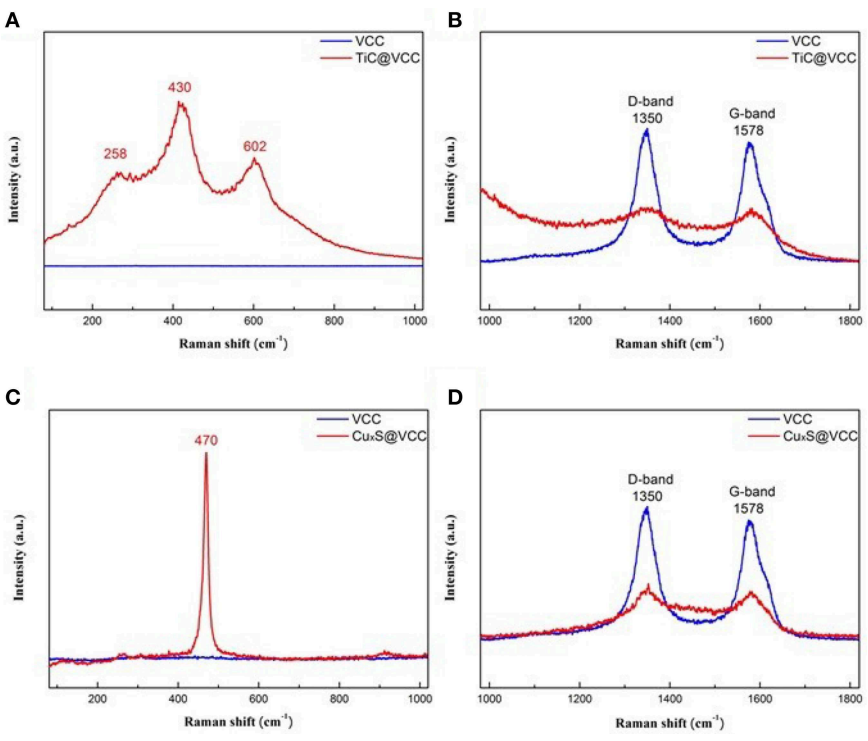

FIGURE 4 | Raman spectra of TiC@VACNT electrode **(A,B)** and Cu_xS@VACNT electrode **(C,D)**.

a reference electrode. TiC@VCC anode/Cu_xS@VCC cathode were used as the working electrodes, and LiCl as an electrolyte. For comparison purpose, the CV curves of VCC electrodes at different scan speeds from 20 to 5,000 mV s^{-1} are first shown in **Figures 5A,D**. Correspondingly, the CV curves of the TiC@VCC anode (from −0.7–0.1 V, vs. Ag/AgCl) and Cu_xS@VCC cathode (from −0.1–0.7 V, vs. Ag/AgCl) are presented in **Figures 5B,E,C,F**, respectively. It is confirmed that both TiC@VCC and Cu_xS@VCC electrodes exhibit good capacitive behaviors at these scan speeds. **Figure 5G** further shows the real and imaginary parts of the electrochemical impedance for both electrodes, validating highly conductive properties with small impedance. The specific capacitance of TiC@VCC and Cu_xS@VCC electrodes can be calculated from these CV curves, yielding much higher values in comparison with VCC electrodes for a scan rate up to 200 mV/s (**Figure 5H**). It is noticed that the specific capacitance of the CuxS electrode decreases sharply after 200 mV/s, which may limit the applications of the proposed electrode at lower scan rate. This is attributed to the limited migration of electrolyte ions at higher scan rates, and some similar results have been observed in other metal sulfide based electrodes (Choudhary et al., 2015). Nevertheless, the specific capacitance is still higher than carbon only electrodes at higher scan rates. Measured CV curves of TiC@VCC and Cu_xS@VCC electrodes in the range of −0.7–0.7 V and scan speeds at 10 and 500 mV/s (**Figure 5I**) show a better rectangular shape than those of the VCC electrodes, suggesting dominating capacitive characteristics.

To evaluate the applicability of the proposed electrodes, a full device was assembled using the TiC@VCC as anode and the Cu_xS@VCC as cathode, having a working range from 0 to 1.4 V. **Figures 6A,B** illustrate the measured CV curves of the full device at scan rates from 2 to 100 mV/s. At these scan speeds, good rectangular shapes and large curve areas are obtained. The CV curves as a function of the bias voltage (from 0.7 to 1.4 V) at a scan rate of 10 mV/s (**Figure 6C**) confirm that the full device can operate at different bias voltages, and therefore, can operate effectively as a micro-supercapacitor. After the charging and discharging test of 3,000 cycles, it is found that the specific capacitance retention is from ∼80% to 110% of its original value (**Figure 6D**), which is relatively unstable when compared with other demonstrated micro-supercapacitors. This phenomenon is attributed to the side electrochemical reactions occurred during the first several hundred cycles within the

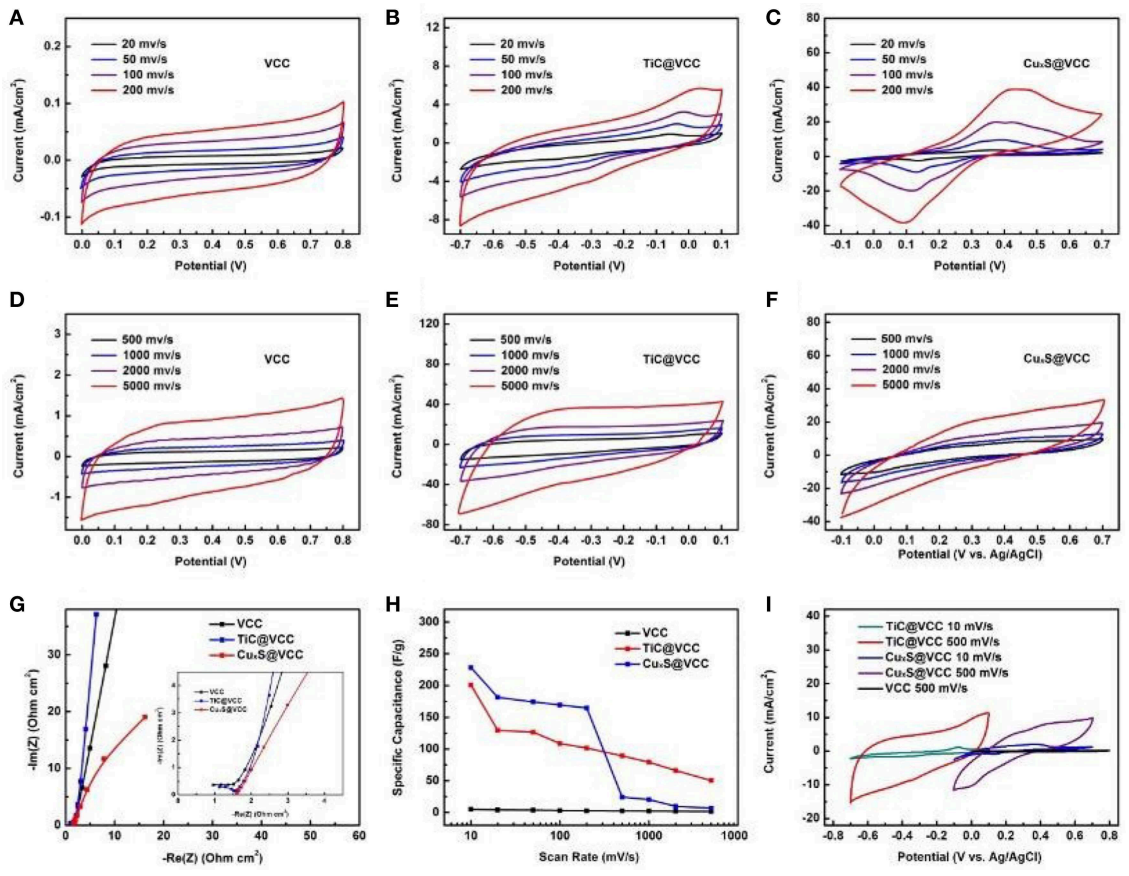

FIGURE 5 | Electrochemical properties of the proposed electrodes. CV curves of the VCC **(A,D)**, TiC@VCC **(B,E)** and Cu_xS@VCC **(C,F)** at different scan speeds from 10 to 5,000 mV/s. Electrochemical impedance **(G)**, Specific capacitance of electrodes **(H)** at different scan rates calculated from the CV curves **(A,F)**. Comparative CV curves of VCC, TiC@VCC and Cu_xS@VCC electrodes performed in a three-electrode cell **(I)**.

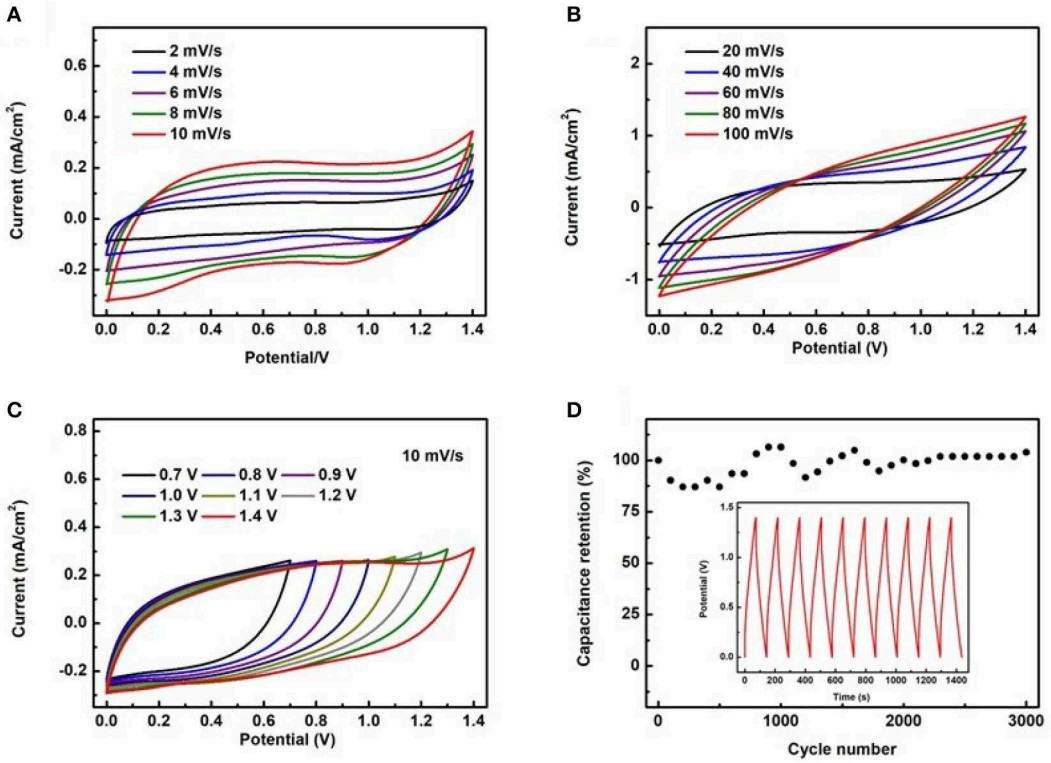

FIGURE 6 | The electrochemical properties of the full device. CV curves of the full device at different scan rates **(A,B)**, CV curves at different bias voltages under a scan rate of 10 mV/s **(C)**, capacitance retention vs. cycle number for the full device **(D)**.

copper sulfide in positive electrode (Zhu et al., 2012; Hsu et al., 2014; Bulakhe et al., 2016). Experimental results of copper sulfide based supercapacitors suggest that the unstable cycling performance in full device was a common issue and usually only 1,000∼2,000 stable cycles of electrochemical test can be achieved. Nevertheless, all these results suggest that the full device shows an excellent electrochemical performance when compared to other recently reported full micro-supercapacitors.

CONCLUSIONS

In this paper, we designed, fabricated and experimentally demonstrated a metal-based asymmetric supercapacitor using TiC@VCC as anode and Cu_xS@VCC as cathode. TiC and Cu_xS were prepared through *in-situ* functionalizations on the VCC substrate, providing a large interspacing and porosity to the 3D nanostructured electrodes. The electrodes showed a specific capacitance of 200.89 and 228.37 F g^{-1} in the potential window of −0.7 to 0.1 V and −0.1 to 0.7V, respectively. A full device assembled from the electrodes was able to work within a potential window of 0–1.4 V at a scan speed up to 100 mV/s, and demonstrated a maximum energy density of 9.12 Wh kg^{-1} at a power density of 46.88 W kg^{-1}. Cycling measurements showed that the capacitance retention was between 80 and 110% of its original value. The proposed all-solid-state asymmetric supercapacitor demonstrated a high applicability and can be used as efficient energy-storage devices.

DATA AVAILABILITY

The datasets generated for this study are available on request to the corresponding author.

AUTHOR CONTRIBUTIONS

LS and QZ conceived the idea. LS, XW, and YuW designed and fabricated the sample, and conducted the experiment. All the authors contributed to the analysis of data and the draft of the manuscript.

FUNDING

The project was financially supported by the National Key R&D Program of China (No. 2018YFC0603301), the National Natural Science Foundation of China (Nos. 11704071, 61801185), MOE AcRF Tier1 (MOE 2016-T1-001-197, RG102/16), MOE AcRF Tier1 (2018-T1-005-001) and MOE Tier2 (MOE2018-T2-2-005), Singapore.

ACKNOWLEDGMENTS

LS, XW, and YuW contributed equally to this work. The project was financially supported by the National Key R&D Program of China (No. 2018YFC0603301), the National Natural

Science Foundation of China (Nos. 11704071, 61801185), MOE AcRF Tier1 (MOE 2016-T1-001-197, RG102/16), MOE AcRF Tier1 (2018-T1-005-001) and MOE Tier2 (MOE2018-T2-2-005), Singapore.

REFERENCES

Acerce, M., Voiry, D., and Chhowalla, M. (2015). Metallic 1T phase MoS_2 nanosheets as supercapacitor electrode materials. *Nat. Nanotecch*. 10:313. doi: 10.1038/nnano.2015.40

Bulakhe, R. N., Sahoo, S., Nguyen, T. T., Lokhande, C. D., Roh, C., Lee, Y. R., Shim, J., et al. (2016). Chemical synthesis of 3D copper sulfide with different morphologies for high performance supercapacitors application. *RSC Adv*. 6, 14844–14851. doi: 10.1039/C5RA25568F

Choudhary, N., Patel, M., Ho, Y.-H., Dahotre, N. B., Lee, W., Hwang J. Y., et al. (2015). Directly deposited MoS 2 thin film electrodes for high performance supercapacitors. *J. Mater. Chem. A*, 3, 24049–24054. doi: 10.1039/C5TA08095A

Chung, J.-S., and Sohn, H.-J. (2002). Electrochemical behaviors of CuS as a cathode material for lithium secondary batteries. *J. Power Sources* 108, 226–231. doi: 10.1016/S0378-7753(02)00024-1

De Volder, M. F., Tawfick, S. H., Baughman, R. H., and Hart, A. J. (2013). Carbon nanotubes: present and future commercial applications. *Science* 339, 535–539. doi: 10.1126/science.1222453

Fu, W., Han, W., Zha, H., Mei, J., Li, Y., Zhang, Z., et al. (2016). Nanostructured CuS networks composed of interconnected nanoparticles for asymmetric supercapacitors. *Phys. Chem. Chem. Phys* 18, 36524471–36524476. doi: 10.1039/C6CP02228F

Fu, W., Zhao, C., Han, W., Liu, Y., Zhao, H., Ma, Y., et al. (2015). Cobalt sulfide nanosheets coated on $NiCo_2S_4$ nanotube arrays as electrode materials for high-performance supercapacitors. *J. Mater. Chem. A* 3, 10492–11049. doi: 10.1039/C5TA00742A

Hsu, Y. K., Chen, Y. C., and Lin, Y. G. (2014). Synthesis of copper sulfide nanowire arrays for high-performance supercapacitors. *Electrochimica Acta* 139, 401–407. doi: 10.1016/j.electacta.2014.06.138

Jiang, Y., Wang, P., Zang, X., Yang, Y., Kozinda, A., and Lin, L. (2013). Uniformly embedded metal oxide nanoparticles in vertically aligned carbon nanotube forests as pseudocapacitor electrodes for enhanced energy storage. *Nano Lett*. 13, 3524–3530. doi: 10.1021/nl400921p

Li, R., Wang, S., Wang, J., and Huang, Z. (2015). Ni_3S_2@CoS core–shell nano-triangular pyramid arrays on Ni foam for high-performance supercapacitors. *Phys. Chem. Chem. Phys*. 17, 16434–16442. doi: 10.1039/C5CP01945A

Lin, S.-Y., and Zhang, X. (2015). Two-dimensional titanium carbide electrode with large mass loading for supercapacitor. *J. Power Sources* 294, 354–359. doi: 10.1016/j.jpowsour.2015.06.082

Liu, J., Guan, C., Zhou, C., Fan, Z., Ke, Q., Zhang, G., et al. (2016). A flexible quasi-solid-state nickel-zinc battery with high energy and power densities based on 3D electrode design. *Adv. Mater*. 28, 8732–8739. doi: 10.1002/adma.201603038

Liu, W., Yin, R., Xu, X., Zhang, L., Shi, W., and Cao, X. (2019). Structural engineering of low-dimensional metal-organic frameworks: synthesis, properties, and applications. *Adv. Science*. 6:1802373. doi: 10.1002/advs.201802373

Lohse, B., Calka, A., and Wexler, D. (2005). Raman spectroscopy as a tool to study TiC formation during controlled ball milling. *J. Appl. Phys*. 97:114912. doi: 10.1063/1.1927282

Lukatskaya, M. R., Mashtalir, O., Ren, C. E., Dall'Agnese, Y., Rozier, P., Taberna, P. L., et al. (2013). Cation intercalation and high volumetric capacitance of two-dimensional titanium carbide. *Science* 341, 1502–1505. doi: 10.1126/science.1241488

Mazor, H., Golodnitsky, D., Burstein, L., and Peled, E. (2009). Highpower copper sulfide cathodes for thin-film microbatteries. *Electrochem. Solid-State Lett*. 12, A232–A235. doi: 10.1149/1.3240921

Munce, C. G., Parker, G. K., Holt, S. A., and Hope, G. A. (2007). A raman spectroelectrochemical investigation of chemical bath de-posited Cu_xS thin films and their modification. *Colloids Surf. A* 295,152–158. doi: 10.1016/j.colsurfa.2006.08.045

Quintana-Ramirez, P. V., Arenas-Arrocena, M. C., Santos-Cruz, J., Vega-González, M., Martínez-Alvarez, O., Castaño-Meneses, V. M., et al. (2014). Growth evolution and phase transition from chalcocite to digenite in nanocrystalline copper sulfide: morphological, optical and electrical properties. *Beilstein J. Nanotechnol*. 5, 1542–1552. doi: 10.3762/bjnano.5.166

Sagade, A. A., and Sharma, R. (2008). Copper sulphide (Cu_xS) as an ammonia gas sensor working at room temperature. *Sens. Actuators B* 133, 135–143. doi: 10.1016/j.snb.2008.02.015

Sun, L., Wang, X., Liu, W., Zhang, K., Zou, J., and Zhang, Q. (2016). Optimization of coplanar high rate supercapacitors. *J. Power Sources* 315, 1–8. doi: 10.1016/j.jpowsour.2016.03.019

Sun, L., Wang, X., Susantyoko, R. A., and Zhang, Q. (2015). High performance binder-free Sn coated carbon nanotube array anode. *Carbon* 82, 282–287. doi: 10.1016/j.carbon.2014.10.072

Sun, L., Wang, X., Wang, Y., and Zhang, Q. (2017). Roles of carbon nanotubes in novel energy storage devices. *Carbon* 122, 462–474. doi: 10.1016/j.carbon.2017.07.006

Vas-Umnuay, P., Kim, K.-J., Kim, D.-H., and Chang, C.-H. (2015). Conformal growth of copper sulfide thin films on highly textured surface via microreactor-assisted solution deposition. *Cryst. Eng. Comm*. 17, 2827–2836. doi: 10.1039/C4CE02374A

Wang, X., Sun, L., Susantyoko, R. A., Fan, Y., and Zhang, Q. (2014a). Ultrahigh volumetric capacity lithium ion battery anodes with CNT–Si film. *Nano Energy* 8, 71–77. doi: 10.1016/j.nanoen.2014.05.020

Wang, X., Sun, L., Susantyoko, R. A., and Zhang, Q. (2016). A hierarchical 3D carbon nanostructure for high areal capacity and flexible lithium ion batteries. *Carbon* 98, 504–509. doi: 10.1016/j.carbon.2015.11.049

Wang, X., Susantyoko, R. A., Fan, Y., Sun, L., Xiao, Q., and Zhang, Q. (2014b). Vertically aligned CNT-supported thick Ge films as high-performance 3D anodes for lithium ion batteries. *Small* 10, 2826–2829. doi: 10.1002/smll.201400003

Wang, X. H., Guan, C., Sun, L. M., Susantyoko, R. A., Fan, H. J., and Zhang, Q. (2015). Highly stable and flexible Li-ion battery anodes based on TiO_2 coated 3D carbon nanostructures. *J. Mater. Chem. A* 3, 15394–15398. doi: 10.1039/C5TA04436G

Wang, Z. L. (2010). Toward self-powered sensor networks. *Nano Today* 5, 512–514. doi: 10.1016/j.nantod.2010.09.001

Xia, X., Zhang, Y., Chao, D., Xiong, Q., Fan, Z., Tong, X., et al. (2015). Tubular TiC fibre nanostructures as supercapacitor electrode materials with stable cycling life and wide-temperature performance. *Energy Environ. Sci*. 8, 1559–1568. doi: 10.1039/C5EE00339C

Xiao, X., Ding, T., Yuan, L., Shen, Y., Zhong, Q., Zhang, X., et al. (2012). WO_{3-x}/MoO_{3-x} core/shell nanowires on carbon fabric as an anode for all-solid-state asymmetric supercapacitors. *Adv. Energy Mater*. 2, 1328–1332. doi: 10.1002/aenm.201200380

Xu, X., Shi, W., Li, P., Ye, S., Ye, C., Ye, H., et al. (2017). Facile fabrication of three-dimensional graphene and metal-organic framework composites and their derivatives for flexible all-solid-state supercapacitors. *Chem. Mater*. 29, 6058–6065. doi: 10.1021/acs.chemmater.7b01947

Xu, X., Shi, W., Liu, W., Ye, S., Yin, R., Zhang, L., et al. (2018). Preparation of two-dimensional assembled Ni-Mn-C ternary composites for high-performance all-solid-state flexible supercapacitors. *J. Mater. Chem. A* 6 24086–24091. doi: 10.1039/C8TA06412A

Yildirim, T., and Ciraci, S. (2005). Titanium-decorated carbon nanotubes as a potential high-capacity hydrogen storage medium. *Phys. Rev. Lett*. 94:175501. doi: 10.1103/PhysRevLett.94.175501

Zhu, C., Yang, P., Chao, D., Wang, X., Zhang, X., Chen, S., et al. (2015). All metal nitrides solid-state asymmetric supercapacitors. *Adv. Mater*. 27, 4566–4571. doi: 10.1002/adma.201501838

Zhu, T., Xia, B., Zhou, L., and Lou, X. W. D. (2012). Arrays of ultrafine CuS nanoneedles supported on a CNT backbone for application in supercapacitors. *J. Mater. Chem*. 36022, 7851–7855. doi: 10.1039/c2jm30437f

Conflict of Interest Statement: The authors declare that the research was conducted in the absence of any commercial or financial relationships that could be construed as a potential conflict of interest.

frontiers in Chemistry

ORIGINAL RESEARCH
published: 25 July 2019
doi: 10.3389/fchem.2019.00511

Hollow Mesoporous Fe_2O_3 Nanospindles/CNTs Composite: An Efficient Catalyst for High-Performance Li-O_2 Batteries

Hairong Xue[1], Yiou Ma[1], Tao Wang[1], Hao Gong[1], Bin Gao[1], Xiaoli Fan[1], Juanjuan Yan[1], Xianguang Meng[2], Songtao Zhang[3] and Jianping He[1]**

[1] *Jiangsu Key Laboratory of Materials and Technology for Energy Conversion, College of Materials Science and Technology, Nanjing University of Aeronautics and Astronautics, Nanjing, China,* [2] *Photofunctional Materials Research Platform, College of Materials Science and Engineering, North China University of Science and Technology, Tangshan, China,* [3] *Testing Center, Yangzhou University, Yangzhou, China*

OPEN ACCESS

Edited by:
Jianqing Zhao, Soochow University, China

Reviewed by:
Yuxin Tang, University of Macau, China
Bo Jiang, National Institute for Materials Science, Japan
Jianhua Zhou, Guilin University of Electronic Technology, China

***Correspondence:**
Tao Wang
wangtao0729@nuaa.edu.cn
Jianping He
jianph@nuaa.edu.cn

Specialty section:
This article was submitted to Electrochemistry, a section of the journal Frontiers in Chemistry

Received: *16 May 2019*
Accepted: *03 July 2019*
Published: *25 July 2019*

Citation:
Xue H, Ma Y, Wang T, Gong H, Gao B, Fan X, Yan J, Meng X, Zhang S and He J (2019) Hollow Mesoporous Fe_2O_3 Nanospindles/CNTs Composite: An Efficient Catalyst for High-Performance Li-O_2 Batteries. Front. Chem. 7:511. doi: 10.3389/fchem.2019.00511

The design of mesoporous or hollow transition metal oxide/carbon hybrid catalysts is very important for rechargeable Li-O_2 batteries. Here, spindle-like Fe_2O_3 with hollow mesoporous structure on CNTs backbones (Fe_2O_3-HMNS@CNT) are prepared by a facile hydrolysis process combined with low temperature calcination. Within this hybrid structure, the hollow interior and mesoporous shell of the Fe_2O_3 nanospindles provide high specific surface area and abundant catalytical active sites, which is also beneficial to facilitating the electrolyte infiltration and oxygen diffusion. Furthermore, the crisscrossed CNTs form a three-dimensional (3D) conductive network to accelerate and stabilize the electron transport, which leads to the decreasing internal resistance of electrode. As a cathodic catalyst for Li-O_2 batteries, the Fe_2O_3-HMNS@CNT composite exhibits high specific capacity and excellent cycling stability (more than 100 cycles).

Keywords: hollow mesoporous structure, carbon support, transition metal oxides, cathodic catalyst, Li-O_2 batteries

INTRODUCTION

To meet the global energy demand, the development of the clean and sustainable energy storage or conversion devices is very important (Tarascon and Armand, 2011; Lu et al., 2014; Wang et al., 2017; Zhang et al., 2018; Gao et al., 2019). Rechargeable Li-O_2 battery has attracted wide attention as a new energy storage device, due to its high theoretical energy density (~3,500 Wh kg^{-1}) (Tarascon and Armand, 2011; Lu et al., 2014). However, the practical application of Li-O_2 batteries still suffer a series of problems, including high overpotentials, low rate capacity and poor cycle stability, which primarily originates from its sluggish kinetics for oxygen reduction reaction (ORR) and oxygen evolution reaction (OER) (Bruce et al., 2012; Wang et al., 2014). At the cathode (air electrode), the gradual formation of the insoluble discharge products Li_2O_2 may block the inward oxygen diffusion of and electrolyte infiltration, which results in the rapid decline of battery performance (Zhao et al., 2015; Wang et al., 2016). To overcome these challenges, the design and development of the high-performance catalysts for oxygen-involved reactions are highly desired for the Li-O_2 batteries.

In recent years, a lot of the efforts have been devoted to investigate the highly active and stable catalysts for the Li-O_2 batteries, such as carbons, precious metals, and transition metal oxides. As the common catalysts, the inexpensive carbon materials have high surface area, nevertheless, their

limited catalytic activity for both OER and ORR restricts the battery performance of the Li-O_2 batteries (Girishkumar et al., 2010; Shui et al., 2013). Since the nanoporous gold (NPG) was used as a cathode catalyst, various precious metals (e.g., Ru, RuO, and Pd) have been adopted in the Li-O_2 batteries (Peng et al., 2012; Lu et al., 2013; Ottakam Thotiyl et al., 2013; Li et al., 2014, 2015). Although the cyclic stability can be distinctly enhanced by precious metal catalysts, the battery capacity is severely restricted because of the highly chemical formula weight. Moreover, high price of precious metals also hinders the large-scale commercialization in the Li-O_2 batteries. Benefiting from the low cost, high stability and good catalytic performance, transition metal oxides have been proposed as the promising catalysts for the Li-O_2 batteries (Wang H. et al., 2012; Chen et al., 2016; Gong et al., 2016, 2018a,b; Xue et al., 2016a,c; Dai et al., 2017; Tan et al., 2017; Feng et al., 2019). Many researches have indicated that Fe-based materials possess high catalytic activities for ORR in fuel cells and OER in water electrolysis (Bates et al., 2016; Song et al., 2019). Recently, some reports began to focus on iron oxides (Fe_2O_3), which can serve as the cathode catalyst in Li-O_2 batteries (Zhang et al., 2014). These works show the enhanced electrochemical performance (e.g., higher capacity and lower overpotentials) of the Li-O_2 batteries, however the cycling performance still needs to further improve. Therefore, it is necessary to explore an effective approach to enhance the catalytic performance of Fe_2O_3-based materials.

Tailoring of the morphology is an important method for obtaining the high-performance catalysts in various electrochemical application. Mesoporous hollow architectures show high surface area and large pore volume, which offers fast electron transfer paths and facilitates the electrolyte infiltration (Kresge et al., 1992; Inagaki et al., 2002; Malgras et al., 2016). Normally, mesoporous or hollow metallic oxide are prepared through the template-based methods, using either hard templates (e.g., carbon sphere and mesoporous silica) or soft templates (e.g., surfactants and polymer) (Attard et al., 1997; Crossland et al., 2013; Liu et al., 2015; Xue et al., 2016d). For these template methods, the multi-step processes are unavoidable, and the mesoporous of hollow structures may be damaged after removing the templates. Moreover, the resultant mesoporous or hollow frameworks often show poor crystalline degree and even amorphous, which limits their electrochemical performance (Lin et al., 2015). It should be noted that the low electronic conductivity is an intrinsical characteristic of the most metallic oxides. Although most of pure carbon materials possess low catalytic activity for OER and ORR, they are identified as the good catalyst support due to their high electric conductivity and large specific surface area (Hsin et al., 2007; Stein et al., 2009; Wu et al., 2009; Xia et al., 2018). Among various carbon materials, the carbon nanotubes (CNTs) show low density, very high strength, high chemical stability, and excellent conductivity (Sathiya et al., 2011; Wang Z. et al., 2012; Ma et al., 2018). These advantages are beneficial to fabricate hybrid or composite materials in many applications by using CNTs as useful substrates. However, the fabrication of mesoporous hollow Fe_2O_3 with high crystalline degree supported on CNTs by a simple and effective method is still an important challenge.

Inspired by the above idea, we proposed a Fe_2O_3/CNTs composite (denoted as Fe_2O_3-HMNS@CNT) prepared by using a simple hydrolysis reaction combined with heat treatment, in which spindle-like Fe_2O_3 with hollow mesoporous structure grown on CNTs backbones. Their hollow interior and mesoporous shell with high specific surface area offer abundant catalytical active sites for OER and ORR, which also promotes the diffusion and infiltration of electrolyte. Furthermore, a great deal of the crisscrossed CNTs form the three-dimensional (3D) conductive network, which benefits the fast and stable electron transport. As a cathodic catalyst for Li-O_2 batteries, the Fe_2O_3-HMNS@CNT exhibits good battery performance, especially excellent outstanding cycling stability (100 cycles).

EXPERIMENTAL METHODS

Hollow Mesoporous Fe_2O_3 Nanospindles on CNT Backbones

Carbon nanotubes (CNTs, 30–60 nm in diameter and 5–15 μm in length) were purchased from Shenzhen Nanotech Port Co. Ltd (Shenzhen, China). CNTs were refluxed in HNO_3 and then rinsed with distilled water. After drying, the obtained CNTs (10 mg) was dispersed in $FeCl_3$ solution (20 mL, 0.12 M) under sonication for 1 h. Then, the suspension was heated at 75°C for 6 h in an oil bath with stirring. After several rinsing combined with sonication, the products were dried at 60°C. Finally, the above products were annealed at 400°C for 4 h in air by using a slow heating rate (0.5°C min^{-1}) to form hollow mesoporous Fe_2O_3 nanospindles on CNT backbones.

Materials Characterization

The X-ray diffraction (XRD, Bruker D8 advance) with Cu Ka radiation ($\lambda = 1.5406$ Å) is used to analyze the crystal structure of the sample. The N_2 adsorption–desorption measurements conducted on a ASAP-2010 analyzer to investigate the pore structure. The Brunauer-Emmet-Teller (BET) method is used to calculate the specific surface area. The morphology and microstructure are observed by using field-emission scanning electron microscope (FE-SEM, Hitachi S-4800) and high-resolution transmission electron microscope (HR-TEM, JEOL JEM-2100), respectively.

Electrochemical Measurement

The electrochemical measurements are tested under two-electrode system at room temperature in the pure O_2 atmosphere, using Li plate as the counter and reference electrode. The work electrode is prepared by mixing Fe_2O_3-HMNS@CNT catalyst (50 wt %), Super P (45 wt %) and polytetrafluoroethylene (PTFE) binder (5 wt %), followed by vacuum drying at 100°C for 12 h. The capacity and current density of the sample is calculated by the whole electrode' weight. For the assembling of Li-O_2 battery, the working electrode and Li plate are separated by a glass-fiber separator in coin cell. The tetraethylene glycol dimethyl ether (TEGDME) containing lithium bis(tri-fluoromethane-sulfonyl)imide (LiTFSI) (1 M) is used as electrolyte. The Land 2100 Charge/Discharge instruments are carried to test the electrochemical measurements.

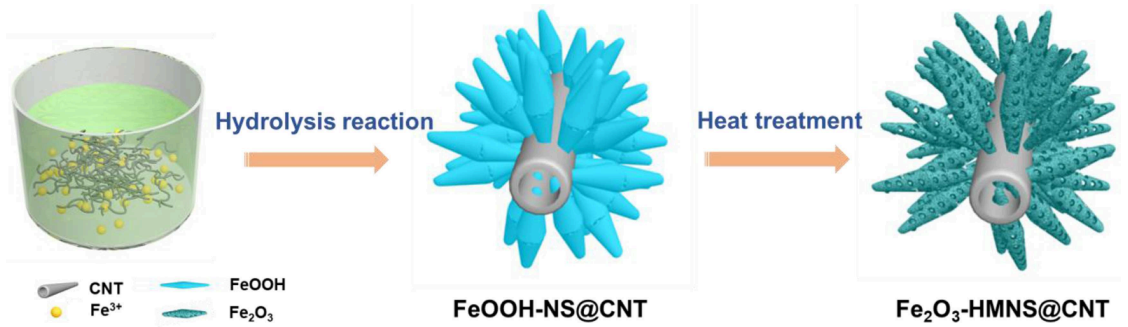

FIGURE 1 | Schematic illustration of the preparation of the Fe_2O_3-HMNS@CNT composite.

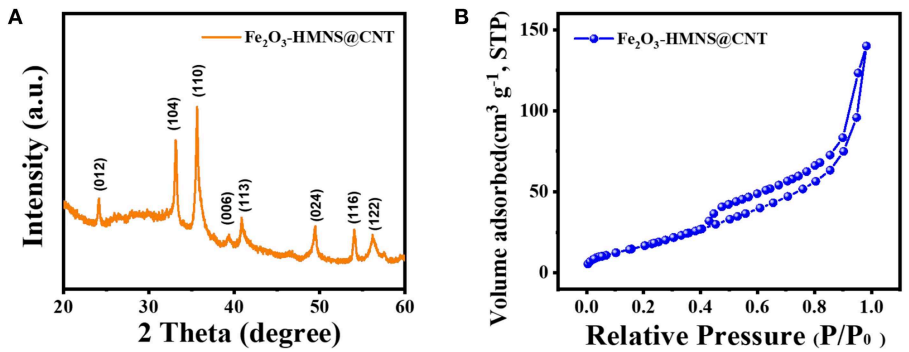

FIGURE 2 | (A) XRD patterns, **(B)** N_2 adsorption–desorption isotherms of the Fe_2O_3-HMNS@CNT composite.

RESULTS AND DISCUSSION

Figure 1 illustrates the fabrication of the mesoporous hollow Fe_2O_3 nanocrystals covered on CNT by a simple hydrolysis reaction combined with heat treatment. In order to facilitate the nucleation and anchoring of the nanocrystals on the CNT surface, these CNTs are functionally modified with carboxylic or hydroxyl groups under acidic reflux. During the subsequent stirring process, the electropositive Fe^{3+} ions can preferential adsorb the electronegative oxygen-containing groups on CNTs by the electrostatic attraction. Due to the hydrolysis of Fe^{3+} ions followed by the olation/oxolation of the FeO_6 units, the formed spindle-like β-FeOOH nanocrystals can be spontaneously grown on CNT backbones, which avoids the addition of any structure-directing agent. The TG/DSC is used to explore the reactions in the final annealing step (**Figure S1**). The TG curve show two mainly weight loss processes at 300°C and 300∼400°C during the annealing step, which are attributed to the conversion from FeOOH into Fe_2O_3. The slowly intramolecular dehydration results in the slow weight loss before 300°C. After 300°C, a distinct weight loss can be found, which is originated from the fast removal of the H_2O molecules. After annealing treatment in air, the spindle-like β-FeOOH nanocrystals are converted to hollow mesoporous α-Fe_2O_3 nanospindles on CNT backbones (denoted as Fe_2O_3-HMNS@CNT) by the thermal dehydroxylation together with the lattice shrinkage.

The crystalline structure of the Fe_2O_3-HMNS@CNT composite is confirmed by XRD analysis. As shown in **Figure 2A**, the XRD pattern exhibits several intensively diffraction peaks at the 2θ values of about 24.2, 33.2, 35.6, 39.3, and 40.9°, which are indexed to the (012), (104), (110), (006), and (113) facets of the hexagonal α-Fe_2O_3. This result of XRD is in accord with the standard card of α-Fe_2O_3 (JCPDS no. 33-0664). The pore structure of the Fe_2O_3-HMNS@CNT composite is analyzed by N_2 adsorption–desorption isotherms (**Figure 2B**). It can be seen that there is a type-IV curve of the Fe_2O_3-HMNS@CNT with a distinctly hysteresis loop on N_2 adsorption–desorption isotherms, which indicates the typically mesoporous structure (Deng et al., 2007; Xue et al., 2016b). Moreover, the nitrogen uptake is found from 0.40 to 0.70 (P/P_o), which can be attributed to the mesoporous materials' capillary condensation of nitrogen. Based on N_2 adsorption–desorption isotherms, the specific surface area is calculated to be 97 $m^2\ g^{-1}$. The above results indicate that the Fe_2O_3-HMNS@CNT has a typically mesoporous structure with high specific surface area.

The morphologies and structures of the Fe_2O_3-HMNS@CNT composite are observed by scanning electron microscopy (SEM) and transmission electron microscopy (TEM). As shown in **Figure S2**, the CNT shows the typical one-dimensional tubular structure with a diameter of ∼40 nm. **Figure 3a** reveals a panoramic view of the sample, in which the spindle-like nanocrystals grown on the entire surface of the sinuous CNTs

backbones. It can be noted that there are many obvious porous within the Fe_2O_3 nanospindles, as shown in **Figures 3b,c**. TEM observation is used to further investigate the internal structure of the sample. The spindle-like Fe_2O_3 nanocrystals have a diameter of around 80 nm and a length of about 250 nm (**Figure 3d**), which show a well-developed hollow interior (marked by orange dotted line) and a typically mesoporous shell (marked by purple dotted line) (**Figure 3e**). During the calcining process, the decomposition-oxidation of the FeOOH can release abundant H_2O and gases, which leads to the formation of mesoporous structure. On the other hand, the density of FeOOH (3 g cm^{-3}) is lower than that of the hematite (Fe_2O_3, 5.3 g cm^{-3}), so some internal mesoporous slowly forms the larger porous to maintain the spindle-like structure during the lattice shrinkage process, thus leading to the formation of the hollow interior together with the mesoporous shell. As shown in **Figure 3f**, some clear lattice

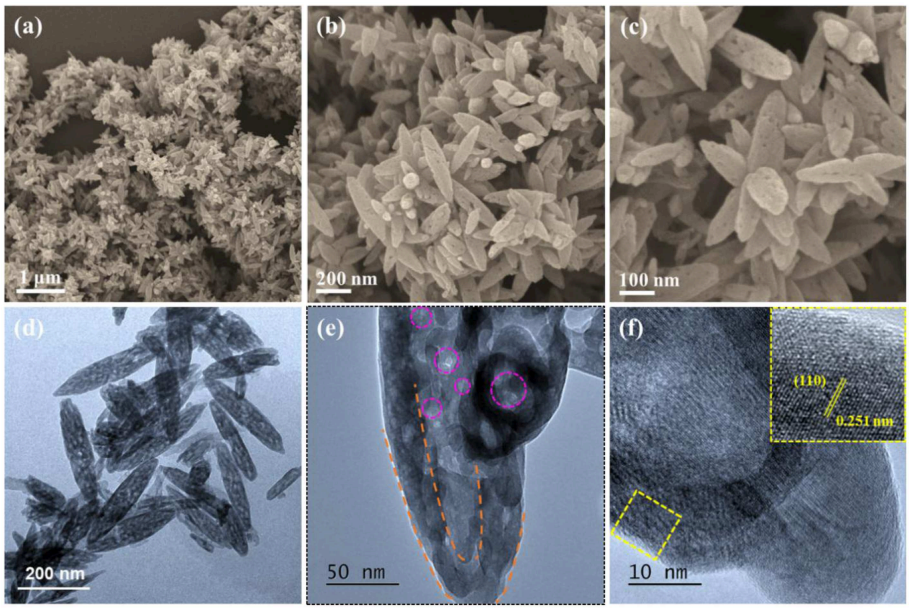

FIGURE 3 | (a–c) FESEM, **(d–f)** HRTEM images of the Fe_2O_3-HMNS@CNT composite.

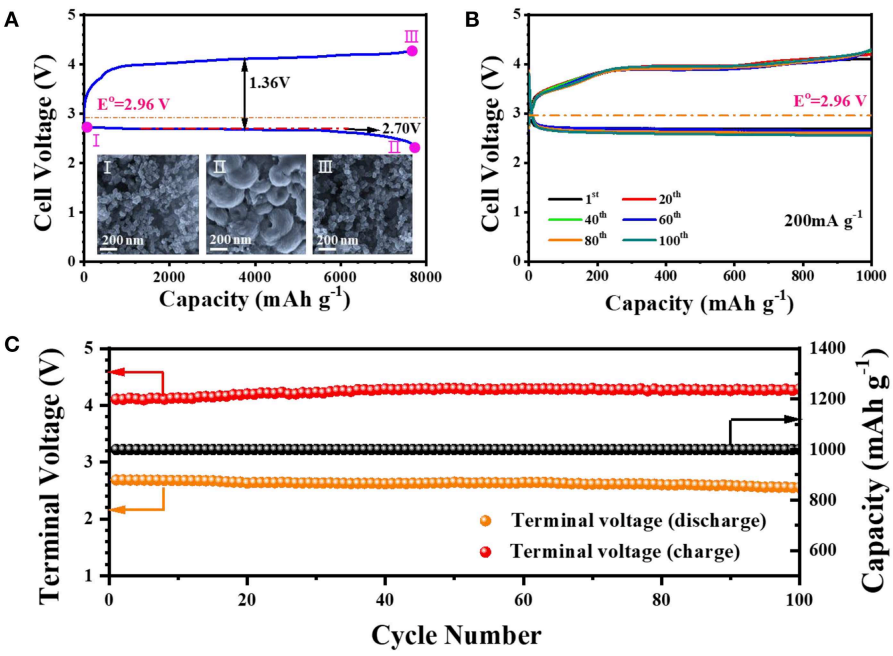

FIGURE 4 | (A) The fully discharging and charging curves in the first cycle and the SEM images [inset of **(A)**], **(B)** cyclic stability tested under a limited capacity (1,000 mAh g^{-1}), and **(C)** the variation of the terminal charge/discharge voltages and specific capacity over 100 cycles of the Fe_2O_3-HMNS@CNT-based cathode.

fringes with an interplanar spacing of 0.251 nm in a single Fe_2O_3 nanospindle, corresponding to the (110) planes of the hexagonal α-Fe_2O_3, which confirms the formation of the α-Fe_2O_3 with high crystallinity.

Inspired by the superiorities of material and structure, the Fe_2O_3-HMNS@CNT composite is investigated as the cathodic catalyst for rechargeable Li-O_2 batteries. **Figure 4A** shows the discharge and charge curves of the sample, which is tested under O_2 atmosphere with a current density of 200 mA g^{-1}. The Fe_2O_3-HMNS@CNT-based cathode exhibits a large discharge capacity of 7,730 mAh g^{-1} and a high discharge plateau (∼2.70 V) with the low overpotential for discharging (0.26 V). Owing to the low overpotential (1.10 V) for the charge process, the coulombic efficiency of the sample is closed to 100%. The reversible formation/decomposition of the discharging product Li_2O_2 can be confirmed by SEM (inset of **Figure 4A**). After fully discharging (defined as II), it is seen that a mass of the Li_2O_2 particles with the typically toroid-like shape uniformly cover on the electrode surface, which is observably different from the fresh electrode (defined as I). When the electrode is fully charged, the formed Li_2O_2 particles is rarely observed (defined as III), indicating high reversibility of the Fe_2O_3-HMNS@CNT-based cathode. We further evaluate the cycling performance of the Fe_2O_3-HMNS@CNT-based cathode, tesed under the limited capacity (1,000 mAh g^{-1}). It can be found that the sample has the small discharge and charge overpotentials of 0.24 and 0.93 V in the first cycle, respectively, which implies the high catalytic activity for both OER and ORR (**Figure 4B**). After 100 cycles, no distinct change of the specific capacities of the sample is observed in discharging/charging curves. Moreover, the discharging and charging terminal voltages can still maintain in 2.6 and 4.3 V. These results exhibit the excellent cycling stability of the Fe_2O_3-HMNS@CNT-based cathode (**Figure 4C**). As a reference, the cycling stability of the Fe_2O_3-HMNS@CNT-based cathode is much better than those of previously reported non-precious metal/metal oxide-based materials (**Table S1**).

As the cathodic catalyst for rechargeable Li-O_2 batteries, the as-prepared Fe_2O_3-HMNS@CNT composite exhibits the excellent cycling stability, which not only benefits by the intrinsic material characteristics but also dependents on the morphology and structure. On the one hand, these largely separated Fe_2O_3 nanospindles directly grown on the CNT backbones, which makes them accessible to the electrolyte. Different from the conventional nanoparticle catalysts, the adverse agglomeration of the Fe_2O_3-HMNS@CNT can be effectively decreased, avoiding the elimination of the active interfaces. The Fe_2O_3 with a hollow interior and a mesoporous shell offers high specific surface area and a mass of catalytical active sites, which also facilitates the diffusion and infiltration of electrolyte. On the other hand, the 3D conductive network composed of the crisscrossed CNTs ensures the fast and stable electron transport, leading to the lower internal resistance of electrode.

CONCLUSION

In summary, we successfully fabricated hollow mesoporous Fe_2O_3 nanospindles on CNTs (Fe_2O_3-HMNS@CNT) though a simple hydrolysis reaction followed by a heat treatment, which are served as cathodic catalyst for Li-O_2 batteries. In this catalyst design concept, the spindle-like Fe_2O_3 nanocrystals possess the hollow interior and mesoporous shell, which not only provides high specific surface area and abundant catalytical active sites but also facilitates the diffusion and infiltration of electrolyte. Moreover, the 3D conductive network formed by the crisscrossed CNTs ensures the fast and stable electron transport, reducing internal resistance of electrode. Benefiting from the intrinsic material characteristics and structural superiorities, the Fe_2O_3-HMNS@CNT catalyst shows high specific capacity and excellent cyclic stability.

DATA AVAILABILITY

All datasets generated for this study are included in the manuscript/**Supplementary Files**.

AUTHOR CONTRIBUTIONS

HX, TW, and JH conceived this research work. HX performed the experiments and wrote the manuscript. YM, HX, HG, BG, XF, and JY tested the electrochemical performance. XM and SZ contributed to analyze the experimental results. All authors read and approved the final manuscript.

FUNDING

This work was financially supported by the Zhejiang Provincial Natural Science Foundation of China under Grant no. LQ18B010005, National Natural Science Foundation of China (51602153, 11575084, and 21703065), the Natural Science Foundation of Jiangsu Province (BK20160795), the Fundamental Research Funds for the Central Universities (no. NE2018104), and a project funded by the Priority Academic Program Development of Jiangsu Higher Education Institutions (PAPD).

SUPPLEMENTARY MATERIAL

The Supplementary Material for this article can be found online at: https://www.frontiersin.org/articles/10.3389/fchem.2019.00511/full#supplementary-material

REFERENCES

Attard, G., Bartlett, P., Coleman, N., Elliott, J., Owen, J., and Wang, J. (1997). Mesoporous platinum films from lyotropic liquid crystalline phases. *Science*. 278, 838–840. doi: 10.1126/science.278.5339.838

Bates, M., Jia, Q., Doan, H., Liang, W., and Mukerjee, S. (2016). Charge-transfer effects in Ni-Fe and Ni-Fe-Co mixed-metal oxides for the alkaline oxygen evolution reaction. *ACS Catal.* 6, 155–161. doi: 10.1021/acscatal.5b01481

Bruce, P. G., Freunberger, S. A., Hardwick, L. J., and Tarascon, J. M. (2012). Li-O2 and Li-S batteries with high energy storage. *Nat. Mater.* 11, 19–29. doi: 10.1038/nmat3191

Chen, Y., Pang, W. K., Bai, H., Zhou, T., Liu, Y., Li, S., et al. (2016). Enhanced structural stability of nickel-cobalt hydroxide via intrinsic pillar effect of metaborate for high-power and long-life supercapacitor electrodes. *Nano Lett*. 17, 429–436. doi: 10.1021/acs.nanolett.6b04427

Crossland, E. J., Noel, N., Sivaram, V., Leijtens, T., Alexander-Webber, J. A., and Snaith, H. J. (2013). Mesoporous TiO2 single crystals delivering enhanced mobility and optoelectronic device performance. *Nature* 495, 215–219. doi: 10.1038/nature11936

Dai, Z., Geng, H., Wang, J., Luo, Y., Li, B., Zong, Y., et al. (2017). Hexagonal-phase cobalt monophosphosulfide for highly efficient overall water splitting. *ACS. Nano* 11, 11031–11040. doi: 10.1021/acsnano.7b05050

Deng, Y., Liu, C., Yu, T., Liu, F., Zhang, F., Wan, Y., et al. (2007). Facile synthesis of hierarchically porous carbons from dual colloidal crystal/block copolymer template approach. *Chem. Mater*. 19, 3271–3277. doi: 10.1021/cm070600y

Feng, Y., Xue, H., Wang, T., Gong, H., Gao, B., Xia, W., et al. (2019). Enhanced Li2O2 decomposition in rechargeable Li-O2 battery by incorporating WO3 nanowire array photocatalyst. *ACS Sustain. Chem. Eng*. 7, 5931–5939. doi: 10.1021/acssuschemeng.8b05944

Gao, B., Wang, T., Fan, X., Gong, H., Li, P., Feng, Y., et al. (2019). Enhanced water oxidation reaction kinetics on a BiVO4 photoanode by surface modification with Ni4O4 cubane. *J. Mater. Chem. A* 7, 278–288. doi: 10.1039/C8TA09404G

Girishkumar, G., McCloskey, B., Luntz, A., Swanson, S., and Wilcke, W. (2010). Lithium-air battery: promise and challenges. *J. Phys. Chem. Lett*. 1, 2193–2203. doi: 10.1021/jz1005384

Gong, H., Wang, T., Guo, H., Fan, X., Liu, X., Song, L., et al. (2018a). Fabrication of perovskite-based porous nanotubes as efficient bifunctional catalyst and application in hybrid lithium-oxygen batteries. *J. Mater. Chem. A* 6, 16943–16949. doi: 10.1039/C8TA04599B

Gong, H., Wang, T., Xue, H., Fan, X., Gao, B., Zhang, H., et al. (2018b). Photo-enhanced lithium oxygen batteries with defective titanium oxide as both photo-anode and air electrode. *Energy Storage Mater*. 13, 49–56. doi: 10.1016/j.ensm.2017.12.025

Gong, H., Xue, H., Wang, T., Guo, H., Fan, X., Song, L., et al. (2016). High-loading nickel cobaltate nanoparticles anchored on three-dimensional N-doped graphene as an efficient bifunctional catalyst for lithium-oxygen batteries. *ACS Appl. Mater. Interfaces* 8, 18060–18068. doi: 10.1021/acsami.6b04810

Hsin, Y. L., Hwang, K. C., and Yeh, C. T. (2007). Poly (vinylpyrrolidone)–modified graphite carbon nanofibers as promising supports for PtRu catalysts in direct methanol fuel cells. *J. Am. Chem. Soc*. 129, 9999–10010. doi: 10.1021/ja072367a

Inagaki, S., Guan, S., Ohsuna, T., and Terasaki, O. (2002). An ordered mesoporous organosilica hybrid material with a crystal-like wall structure. *Nature* 416, 304–307. doi: 10.1038/416304a

Kresge, C., Leonowicz, M., Roth, W., Vartuli, J., and Beck, J. (1992). Ordered mesoporous molecular sieves synthesized by a liquid-crystal template mechanism. *Nature* 359, 710–712. doi: 10.1038/359710a0

Li, F., Tang, D., Jian, Z., Liu, D., Golberg, D., Yamada, A., et al. (2014). Li-O2 battery based on highly efficient Sb-doped Tin oxide supported Ru nanoparticles. *Adv. Mater*. 26, 4659–4664. doi: 10.1002/adma.201400162

Li, F., Tang, D., Zhang, T., Liao, K., He, P., Golberg, D., et al. (2015). Superior performance of a Li-O2 battery with metallic RuO2 hollow spheres as the carbon-free cathode. *Adv. Energy Mater*. 5:1500294. doi: 10.1002/aenm.201500294

Lin, J., Zhao, L., Heo, Y., Wang, L., Bijarbooneh, F., Mozer, A., et al. (2015). Mesoporous anatase single crystals for efficient Co(2+/3+)-based dye-sensitized solar cells. *Nano Energy* 11, 557–567. doi: 10.1016/j.nanoen.2014.11.017

Liu, J., Wickramaratne, N. P., Qiao, S. Z., and Jaroniec, M. (2015). Molecular-based design and emerging applications of nanoporous carbon spheres. *Nat. Mater*. 14, 763–774. doi: 10.1038/nmat4317

Lu, J., Lei, Y., Lau, K. C., Luo, X., Du, P., Wen, J., et al. (2013). Nanostructured cathode architecture for low charge overpotential in lithium-oxygen batteries. *Nat. Commun*. 4:2383. doi: 10.1038/ncomms3383

Lu, J., Li, L., Park, J., Sun, Y., Wu, F., and Amine, K. (2014). Aprotic and aqueous Li-O2 batteries. *Chem. Rev*. 114, 5611–5640. doi: 10.1021/cr400573b

Ma, L., Zhang, W., Wang, L., Hu, Y., Zhu, G., Wang, Y., et al. (2018). Strong capillarity, chemisorption, and electrocatalytic capability of crisscrossed nanostraws enabled flexible, high-rate, and long-cycling lithium-sulfur batteries. *ACS Nano* 12, 4868–4876. doi: 10.1021/acsnano.8b01763

Malgras, V., Ataee-Esfahani, H., Wang, H., Jiang, B., Li, C., Wu, K. C., et al. (2016). Nanoarchitectures for mesoporous metals. *Adv. Mater*. 28, 993–1010. doi: 10.1002/adma.201502593

Ottakam Thotiyl, M. M., Freunberger, S. A., Peng, Z., Chen, Y., Liu, Z., and Bruce, P. G. (2013). A stable cathode for the aprotic Li-O2 battery. *Nat. Mater*. 12, 1050–1056. doi: 10.1038/nmat3737

Peng, Z., Freunberger, S., Chen, Y., and Bruce, P. (2012). A reversible and higher-rate Li-O2 battery. *Science* 373, 563–566. doi: 10.1126/science.1223985

Sathiya, M., Prakash, A. S., Ramesha, K., Tarascon, J. M., and Shukla, A. K. (2011). V2O5-anchored carbon nanotubes for enhanced electrochemical energy storage. *J. Am. Chem. Soc*. 133, 16291–16299. doi: 10.1021/ja207285b

Shui, J. L., Okasinski, J. S., Kenesei, P., Dobbs, H. A., Zhao, D., Almer, J. D., et al. (2013). Reversibility of anodic lithium in rechargeable lithium-oxygen batteries. *Nat. Commun*. 4:2255. doi: 10.1038/ncomms3255

Song, L., Wang, T., Li, L., Wu, C., and He, J. (2019). [Fe(CN)6]2 derived Fe/Fe5C2@ N-doped carbon as a highly effective oxygen reduction reaction catalyst for zinc-air battery. *Appl. Catal. B Environ*. 244, 197–205. doi: 10.1016/j.apcatb.2018.11.005

Stein, A., Wang, Z., and Fierke, M. (2009). Functionalization of porous carbon materials with designed pore architecture. *Adv. Mater*. 21, 265–293. doi: 10.1002/adma.200801492

Tan, G., Chong, L., Amine, R., Lu, J., Liu, C., Yuan, Y., et al. (2017). Toward highly efficient electrocatalyst for Li-O2 batteries using biphasic N-doping cobalt@graphene multiple-capsule heterostructures. *Nano Lett*. 17, 2959–2966. doi: 10.1021/acs.nanolett.7b00207

Tarascon, J. M., and Armand, M. (2011). Issues and challenges facing rechargeable lithium batteries. *Nature* 414, 359–367. doi: 10.1038/35104644

Wang, H., Yang, Y., Liang, Y., Zheng, G., Li, Y., Cui, Y., et al. (2012). Rechargeable Li-O2 batteries with a covalently coupled MnCo2O4-graphene hybrid as an oxygen cathode catalyst. *Energy Environ. Sci*. 5, 7931–7935. doi: 10.1039/c2ee21746e

Wang, J., Zhang, Y., Guo, L., Wang, E., and Peng, Z. (2016). Identifying reactive sites and transport limitations of oxygen reactions in aprotic lithium-O2 batteries at the stage of sudden death. *Angew. Chem. Int. Ed*. 55, 5201–5205. doi: 10.1002/anie.201600793

Wang, X., Wang, Y., Bu, Y., Yan, X., Wang, J., Cai, P., et al. (2017). Influence of doping and excitation powers on optical thermometry in Yb3+-Er3+ doped CaWO4. *Sci. Rep*. 7:43383. doi: 10.1038/srep43383

Wang, Z., Luan, D., Madhavi, S., Hu, Y., and Lou, X. (2012). Assembling carbon-coated a-Fe2O3 hollow nanohorns on the CNT backbone for superior lithium storage capability. *Energy Environ. Sci*. 5, 5252–5256. doi: 10.1039/C1EE02831F

Wang, Z. L., Xu, D., Xu, J. J., and Zhang, X. B. (2014). Oxygen electrocatalysts in metal-air Batteries: from aqueous to nonaqueous electrolytes. *Chem. Soc. Rev*. 43, 7746–7786. doi: 10.1039/C3CS60248F

Wu, B., Hu, D., Kuang, Y., Liu, B., Zhang, X., and Chen, J. (2009). Functionalization of carbon nanotubes by an ionic-liquid polymer: dispersion of Pt and PtRu nanoparticles on carbon nanotubes and their electrocatalytic oxidation of methanol. *Angew. Chem. Int. Ed*. 48, 4751–4654. doi: 10.1002/anie.200900899

Xia, W., Li, J., Wang, T., Song, L., Guo, H., Gong, H., et al. (2018). The synergistic effect of Ceria and Co in N-doped leaf-like carbon nanosheets derived from a 2D MOF and their enhanced performance in the oxygen reduction reaction. *Chem. Commun*. 54, 1623–1626. doi: 10.1039/C7CC09212A

Xue, H., Mu, X., Tang, J., Fan, X., Gong, H., Wang, T., et al. (2016a). A nickel cobaltate nanoparticle-decorated hierarchical porous N-doped carbon nanofiber film as a binder-free self-supported cathode for non-aqueous Li-O2 batteries. *J. Mater. Chem. A* 4, 9106–9112. doi: 10.1039/C6TA01712F

Xue, H., Tang, J., Gong, H., Guo, H., Fan, X., Wang, T., et al. (2016b). Fabrication of PdCo bimetallic nanoparticles anchored on three-dimensional ordered N-doped porous carbon as an efficient catalyst for oxygen reduction reaction. *ACS Appl. Mater. Interfaces*. 8, 20766–20771. doi: 10.1021/acsami.6b05856

Xue, H., Wu, S., Tang, J., Gong, H., He, P., He, J., et al. (2016c). Hierarchical porous nickel cobaltate nanoneedle arrays as flexible carbon-protected cathodes for high-performance lithium-oxygen batteries. *ACS. Appl. Mater. Interfaces*. 8, 8427–8435. doi: 10.1021/acsami.5b10856

Xue, H., Zhao, J., Tang, J., Gong, H., He, P., Zhou, H., et al. (2016d). High-loading Nano-SnO2 encapsulated *in situ* in three-dimensional rigid porous

carbon for superior lithium-ion batteries. *Chem. Eur. J.* 22, 4915–4923. doi: 10.1002/chem.201504420

Zhang, T., Wang, Y., Song, T., Miyaoka, H., Shinzato, K., Miyaoka, H., et al. (2018). Ammonia, a switch for controlling high ionic conductivity in lithium borohydride ammoniates. *Joule* 2, 1522–1533. doi: 10.1016/j.joule.2018.04.015

Zhang, Z., Zhou, G., Chen, W., Lai, Y., and Li, J. (2014). Facile synthesis of Fe2O3 nanoflakes and their electrochemical properties for Li-air batteries. *ECS Electrochem. Lett.* 3, A8–A10. doi: 10.1149/2.006401eel

Zhao, C., Yu, C., Liu, S., Yang, J., Fan, X., Huang, H., et al. (2015). 3D porous N-doped graphene frameworks made of interconnected nanocages for ultrahigh-rate and long-life Li-O2 batteries. *Adv. Funct. Mater.* 25, 6913–6920. doi: 10.1002/adfm.201503077

Conflict of Interest Statement: The authors declare that the research was conducted in the absence of any commercial or financial relationships that could be construed as a potential conflict of interest.

frontiers in Chemistry

ORIGINAL RESEARCH
published: 19 December 2019
doi: 10.3389/fchem.2019.00878

Free-Standing SnO_2@rGO Anode via the Anti-solvent-assisted Precipitation for Superior Lithium Storage Performance

Shuli Jiang [1,2], Ruiming Huang [3], Wenchang Zhu [1,2], Xiangyi Li [1,2], Yue Zhao [1,2], Zhixiang Gao [1,2], Lijun Gao [1,2]* and Jianqing Zhao [1,2]**

[1] College of Energy, Soochow Institute for Energy and Materials Innovations, Soochow University, Suzhou, China, [2] Key Laboratory of Advanced Carbon Materials and Wearable Energy Technologies of Jiangsu Province, Soochow University, Suzhou, China, [3] Department of Chemistry, Rutgers-Newark, The State University of New Jersey, Newark, NJ, United States

Metal oxides have been attractive as high-capacity anode materials for lithium-ion batteries. However, oxide anodes encounter drastic volumetric changes during lithium ion storage through the conversion reaction and alloying/dealloying processes, leading to rapid capacity decay and poor cycling stability. Here, we report a free-standing SnO_2@reduced graphene oxide (SnO_2@rGO) composite anode, in which SnO_2 nanoparticles are tightly wrapped within wrinkled rGO sheets. The SnO_2@rGO sheet is assembled in high porosity via an anti-solvent-assisted precipitation of dispersed SnO_2 nanoparticles and graphene oxide sheets in the distilled water, followed by the filtration and post-annealing processes. Significantly enhanced lithium storage performance has been obtained of the SnO_2@rGO anode compared with the bare SnO_2 anode material. A high charge capacity above 700 mAh g^{-1} can be achieved with a satisfying 95.6% retention after 50 cycles at a current density of 500 mA g^{-1}, superior to reserved 126 mAh g^{-1} and a much lower 16.8% retention of the bare SnO_2 anode. XRD pattern and HRTEM images of the cycled SnO_2@rGO anode material verify the expected oxidation of Sn to SnO_2 at the fully-charged state in the 50th cycle. In addition, FESEM and TEM images reveal the well-preserved free-standing structure after cycling, which accounts for high reversible capacity and excellent cycling stability of such a SnO_2@rGO anode. This work provides a promising SnO_2-based anode for high-capacity lithium-ion batteries, together with an effective fabrication adoptable to prepare different free-standing composite materials for device applications.

Keywords: SnO_2, rGO, anti-solvent-assisted precipitation, free-standing anode, lithium-ion battery

OPEN ACCESS

Edited by:
Vito Di Noto,
University of Padova, Italy

Reviewed by:
Abhishek Lahiri,
Clausthal University of Technology, Germany
Xiaosheng Tang,
Chongqing University, China

****Correspondence:***
Ruiming Huang
ruiming407@gmail.com
Lijun Gao
gaolijun@suda.edu.cn
Jianqing Zhao
jqzhao@suda.edu.cn

Specialty section:
This article was submitted to Electrochemistry, a section of the journal Frontiers in Chemistry

Received: *06 September 2019*
Accepted: *05 December 2019*
Published: *19 December 2019*

Citation:
Jiang S, Huang R, Zhu W, Li X, Zhao Y, Gao Z, Gao L and Zhao J (2019) Free-Standing SnO_2@rGO Anode via the Anti-solvent-assisted Precipitation for Superior Lithium Storage Performance. Front. Chem. 7:878. doi: 10.3389/fchem.2019.00878

INTRODUCTION

With the rapid development of portable electronic devices, pure electric vehicles and emerging large-scale energy storage systems, lithium-ion batteries are required to at least have high energy and power densities, in order to meet high-grade demands for various practical applications. The exploration of alternative anode materials has become an urgent task to pursue high lithium storage capacity, together with excellent rate capability and cycling stability, because the specific capacity of

the commercial graphite anode has been reached to the theoretical limit of 372 mAh g^{-1}. The tin-based oxides have been widely reported as promising anode candidates, due to the high capacity, non-toxicity, and natural abundance (Hu et al., 2017; Sahoo and Ramaprabhu, 2018; Cao et al., 2019; Hong et al., 2019). As reported in the literature (Zhao et al., 2016; Ahmed et al., 2017; Cui et al., 2017), lithium storage capacity of the SnO_2 anode material is on the basis of reversible alloying/dealloying processes of Sn_xLi ($0 < x \leq 4.4$, corresponding to the maximum theoretical capacity of 782 mAh g^{-1} when the $x = 4.4$) after an initial irreversible conversion reaction from original SnO_2 to the metallic Sn (Wang et al., 2012). An impressive capacity up to 1,493 mAh g^{-1} based on $x = 8.4$ has been achieved by Wang and co-authors (Wang et al., 2015) through realizing the fully reversible oxidation from the reduced Sn back to SnO intermediate then to SnO_2. In addition, increased capacities can also be obtained via a partial Sn to SnO_2 conversion, coupled with synergistic effects from different carbonaceous materials or functional nanomaterials (Kim et al., 2014, 2017; Sun et al., 2015). However, the practical application of SnO_2-based anode materials is impeded by severe volumetric expansion/contraction up to 259% during alloying/dealloying processes of Sn_xLi variants, leading to the structural degradation and poor electronic conductivity of the anode. Additionally, the undesirable aggregation of reduced Sn nanoparticles into clusters together with the Sn pulverization occurs during prolonged electrochemical cycling, which further brings about the deactivation of active Sn particles, and thus the rapid capacity loss and poor cycling stability (Li et al., 2015; Liu et al., 2015; Min et al., 2019).

Compared with extensively-reported strategies, such as reducing particles size (Park et al., 2007; Wang et al., 2015; Xia et al., 2016; Yao et al., 2019) and dispersing active anode materials into a solid matrix (Xu et al., 2012; Zheng et al., 2016), few attention has been devoted to the binders in the anode (Zhang et al., 2014). The traditional binder, i.e., polyvinylidene fluoride (PVDF) is insulating and electrochemically inactive, which is used to strengthen mechanical connections between active anode materials, conductive additives, and the current collector. However, the presence of the binder decreases the overall electronic conductivity, but increases the electrochemical polarization in the anode. As reported in the literature (Kumar et al., 2019; Pan et al., 2019), polymetric conductive binders with strong mechanical binding force and even self-healing capability have been demonstrated to address detrimental volume effects of oxide/metal-based anode materials. Moreover, such polymetric binders play an additional role in offering the desired pathway for the charge transfer, resulting in free conductive carbon additives in the anode. However, the synthesis of those conductive polymers is expensive and time-consuming, which requires complex coupling reactions, noble metal catalysts and stringent reaction conditions. In addition to the binders, the metallic current collector, i.e., the copper foil is also needed for the anode fabrication. Within the typical anode, inactive components involving the binder, conductive additive and current collector exceed 50 wt.% of the total electrode mass. Therefore, an advanced electrode structure should be rationally designed to increase the energy density of the anode.

The graphene and reduced graphene oxide (rGO) have been extensively used for energy storage and conversion applications, especially in lithium-ion batteries, owing to their unique two-dimensional structures with excellent flexibility, mechanical strength, chemical stability, and thermal and electronic conductivities (Rong et al., 2014; Deng et al., 2016; Ahn et al., 2019; Riyanto et al., 2019). Both graphene and rGO materials have been demonstrated to act as reliable supporting and buffering matrixes to improve electrochemical performance of high-capacity anode materials, such as SnO_2 and Si, by accommodating their drastic volume changes during the lithium storage (Jiang et al., 2017; Ma et al., 2017; Chen et al., 2018; Deng et al., 2019). Tri-dimensional hybrid materials consisting of graphene (or rGO) sheets and active anode particles can be served as promising free-standing anodes with free conductive additives and binders. The wrinkled structure of graphene or rGO sheets may be also fabricated, in order to ensure the "buffering" capability. On the other hand, active particles are required to distribute in the graphene-based matrix uniformly (Li et al., 2015; Wang et al., 2018). As reported in the literature (Li et al., 2011, 2019), either aerosol spray drying process or solution ionic strength engineering has been demonstrated as an effective route to obtain desired composite materials, but the conductive additive and polymer binder are still added for the electrode preparation. It would be very interesting to explore assembly methods for the preparation of free-standing graphene-based anodes full of pores and wrinkles, in which active particles are uniformly distributed free of the conductive carbon and binder components, resulting in the maximum capacity contribution of such the anode (Xia et al., 2019; Xing et al., 2020).

In this work, we report an effective approach to fabricate a free-standing SnO_2@rGO composite anode through an anti-solvent-assisted precipitation followed by the suction filtration. The resulting SnO_2@rGO anode has sufficient wrinkles and internal channels, which are expected to favor not only the electrolyte permeation but also the accommodation of large volume expansion during cyclic lithium storage of the SnO_2 anode material, and thus contribute to enhanced electrochemical performance compared with the bare SnO_2 anode material. The assembly method developed in this study may be adopted to prepare different free-standing composite materials consisting of a flexible matrix and functional nanoparticles for device applications beyond lithium-ion batteries.

EXPERIMENTAL

Preparation of the Graphene Oxide (GO) and Free-Standing SnO_2@rGO Electrode

Graphene oxide was prepared via a modified Hammond method (Marcano et al., 2010). Typically, 0.75 g graphite flakes and 4.5 g $KMnO_4$ were added to a 100 mL concentrated H_2SO_4 and H_3PO_4 solution at a volume ratio of 90:10. After heating at 50°C for 12 h under continuous stirring, the mixed solution was cooled to room temperature and poured onto a 100 mL ice with 1 mL

30 wt.% H_2O_2. The obtained slurry was then centrifuged and washed repeatedly with 10% HCl to remove Mn^{2+} ion, followed by removing the majority of Cl^- ion via the successive washing using the acetone. For the complete removal of all the ions, deionized water was used to wash GO until no precipitate was observed when the GO solution was mixed the 10 mM $AgNO_3$ solution.

In order to prepare the free-standing SnO_2@rGO electrode, 4 mg SnO_2 (Sigma Aldrich) and 8.8 mg GO were co-dispersed in 15 mL de-ionized water for 15 min. Twenty milligrams LiCl powder was directly added. The suspension was then sonicated for an additional 1 min. Sixty milliliters acetone was poured into the above suspension at one time shot. The resulted mixture was then collected via vacuum filtration using the PTFE filter paper with the pore size of 0.2 μm and the diameter of 15 mm (Sterlitech). The obtained free-standing SnO_2@GO sheet on the PTFE paper was then together dried in vacuum at 60°C for 2 h. After peeling off from the PTFE paper, the dried SnO_2@GO sheet was subjected to post-annealing processes to reduce the GO and obtain SnO_2@rGO. The heating temperature was increased 100°C per step with a duration time of 1 h up to 400°C, followed by heating at 500°C for 3 h in the Ar flow. The typical mass of as-prepared SnO_2@rGO electrode is 5.6 mg, corresponding to the loading density of 3.1 mg/cm^2

Material Characterizations

Crystallographic structures of as-prepared materials were identified by X-ray diffraction (XRD) on a Bruker D8 Advance automatic diffractometer with Cu Kα radiation. Morphology and structure of different samples were observed by using scanning electron microscopy (SEM, Hitachi S-4800) and transmission electron microscopy (TEM, FEI Tecnai G2T20) at an acceleration voltage of 200 kV, respectively. The chemical environment and valent states of anions and cations within different materials were characterized by X-ray photoelectron spectroscopic (XPS) measurements on an ESCALAB 250Xi XPS equipment. All XPS spectra were calibrated according to the binding energy of the C 1s peak at 284.8 eV. The degree of graphitization of the GO and rGO materials were characterized by Raman spectra on a Horiba JY LabRAM Aramis equipment. The rGO content within the SnO_2@rGO electrode was determined by the thermogravimetric analysis on a TG/DTA-7300 thermal analyzer (Seko) in air flow at a temperature range between room temperature and 900°C.

Electrochemical Measurements

Electrochemical measurements were carried out in a two-electrode system for lithium-ion battery testing. The free-standing SnO_2@rGO sheet was directly used as the working anode. All CR2025-type coin cells were assembled in an Ar-filled glove box, using the lithium metal as the counter and reference electrode, and Celgard3501 as the separator. The electrolyte was 1 M $LiPF_6$ dissolved in a mixture of ethylene carbonate (EC), dimethyl carbonate (DMC) and diethyl carbonate (DEC) at a volumetric ratio of 4:3:3. Galvanostatic charge/discharge of the cells were performed on the MTI BST8-MA-battery analyzer in a voltage range of 0.01–3.0 V vs. Li^+/Li. Cyclic voltammetric (CV) curves were recorded at a scanning rate of 0.1 mV s^{-1} between 0.01 and 3 V vs. Li^+/Li, and electrochemical impedance spectroscopy (EIS) was conducted from the open circuit voltage of testing cells in a frequency range of 10 mHZ-100 kHZ with an AC amplitude of 5 mV using an electrochemical analyzer (CHI 760C).

RESULTS AND DISCUSSION

The SnO_2 oxide has been extensively reported as a high-capacity anode material for lithium-ion batteries, but suffers from fast capacity decay during cycling, due to drastic volume changes for the lithium storage on the basis of the reversible initial conversion reaction (Equation 1) and successive alloying/dealloying processes (Equation 2) as follows (Huang et al., 2010; Wang et al., 2011; Zhang et al., 2012; Jiang et al., 2017):

$$4Li^+ + SnO_2 + 4e^- \leftrightarrow 2Li_2O + Sn \quad \text{(capacity delivered: 711 mAh/g)} \tag{1}$$

$$xLi^+ + Sn + xe^- \leftrightarrow Li_xSn \ (0 \le x \le 4.4) \quad \text{(capacity delivered: 782 mAh/g)} \tag{2}$$

However, it is difficult to maintain the full reversibility of the conversion reaction as shown in Equation (1), resulting in a capacity range of 782–1,493 mAh/g for the SnO_2 anode material (Wang et al., 2013; Deng et al., 2016; Cao et al., 2019). In order to obtain the maximum capacity with excellent cycling stability, a carbon-based framework should be employed to support active SnO_2 nanoparticles by serving as a conductive network and a structural cushion to release mechanical strains during lithiation/delithiation of such the oxide anode. In addition, the uniform dispersion of SnO_2 nanoparticles in the carbonaceous framework is also highly required to restrict from the unfavorable aggregation and pulverization of the reduced Sn nanoparticles. The as-prepared GO nanosheets are here used to accommodate commercial SnO_2 nanoparticles, and a free-standing SnO_2@rGO anode is obtained through an effective anti-solvent-assisted precipitation followed by a post-annealing process. **Figure 1** shows schematic illustrations for the synthesis of the free-standing SnO_2@rGO sheet, together with photographs taken in different stages. Notably, an anti-solvent-assisted precipitation, which is inspired by a frequently used method to purify and/or concentrate RNA and DNA in biochemistry (Zeugin and Hartley, 1985), is adopted to assemble the SnO_2@GO composite material. The synergy of ionic strength and dielectric constant change induced by a low concentrated salt and an organic solvent (such as ethanol and acetone) allows for the controllable assembly of well-dispersed graphene oxide (GO) nanosheets and SnO_2 nanoparticles in an aqueous solution. SEM images as shown at **Stage I** reveal distinct aggregations of both original GO nanosheets and SnO_2 nanoparticles. The brown solution-like suspension can be obtained through simply dispersing GO and SnO_2 powders in the deionized (DI) water by the ultrasonic treatment at **Stage II**, on account of numerous hydrophilic groups involving -COOH and -OH ends at the surface of GO

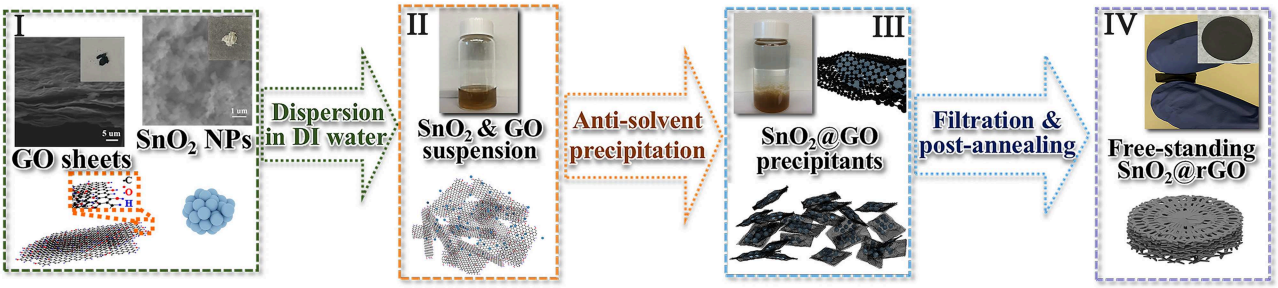

FIGURE 1 | Schematic illustrations for the synthesis of the free-standing SnO_2@rGO sheet.

sheets and nano-sized SnO_2 particles. The assembly of GO sheets and SnO_2 nanoparticles can be implemented at **Stage III** by adding a small amount of LiCl salt and subsequently the acetone as an anti-solvent, resulting in the rapid precipitation as shown in the vial. The instant formation of SnO_2@GO precipitant is attributed to the considerably strengthened electrostatic force between negatively-charged GO sheets and positively-charged Li^+ ion induced by the anti-solvent acetone. Thus, the stable GO dispersion is disturbed, and GO sheets crumple and fold to minimize the surface energy. With the co-existence of well-distributed SnO_2 nanoparticles in the GO solution, SnO_2 nanoparticles are all wrapped in wrinkled GO nanosheets, resulting in the SnO_2@GO precipitation. As shown at **Stage IV**, the free-standing SnO_2@rGO sheet is obtained via the facile vacuum filtration of all SnO_2@GO precipitants, followed by a post-annealing process.

Morphologic and structural characteristics of resulting SnO_2@rGO composite material are examined in **Figure 2**. **Figures 2a,b** show SEM images taken at the intersection area (the side view) and the surface (the top view) of the free-standing SnO_2@rGO sheet, respectively, indicating a distinct porous structure. The zoom-in FESEM image as shown in **Figure 2c** clarifies that all SnO_2 nanoparticles are tightly wrapped within rGO sheets full of expected wrinkles, which is very similar to the assembled structure of original SnO_2@GO material (**Figure 2d**). The post-annealing process only results in the reduction of GO component to rGO material, while encased SnO_2 nanoparticles are stabilized without the particle growth and phase reduction to either SnO or Sn (will be discussed in **Figure 3**). As captured in TEM observation (**Figure 2e**), SnO_2 nanoparticles all show spherical shapes in a particle size range of 10–50 nm. The HRTEM image of the SnO_2@rGO material is also captured as displayed in **Figure 2f**, coupled with corresponding selected area electron diffraction (SAED) pattern as shown in **Figure 2f$_I$**, indicating the single crystal property of SnO_2 particles and a high graphitization degree of the rGO sheet. Lattice fringes of two selected SnO_2 particles (squared in red and pink dashed lines in **Figure 2f**) with the corresponding *d*-space distance of 0.26 and 0.33 nm can be indexed to (101) and (110) planes of the SnO_2 in a tetragonal rutile structure, as shown in **Figures 2f$_{II}$, f$_{III}$**, respectively. Additionally, **Figure 2f$_{IV}$** shows the enlarged selected lattice fringe of the rGO sheet (squared in the navy dashed line in **Figure 2f**), corresponding to (004) planes of the hexagonal graphite phase with an interplanar distance of 0.17 nm. Overall, SEM and TEM observations demonstrate the desired structural integrity of the free-standing SnO_2@rGO sheet with the high porosity.

Figure 3 further analyzes the composition, crystallographic structure and chemical environment of the SnO_2@rGO composite material. The rGO content within the SnO_2@rGO is determined to be 33.1 wt.%, according to the TG analysis as shown in **Figure 3a**. However, XRD pattern of the SnO_2@rGO is identical to that of the pure SnO_2 powder (**Figure 3b**), which can be well indexed to the rutile SnO_2 phase in the tetragonal structure (PDF: 41–1445). The absence of characteristic diffraction peaks from the rGO component implies the homogeneous dispersion of SnO_2 nanoparticles between each rGO layer, in accordance with SEM and TEM observations (**Figures 2c,e**). By contrast, the typical (002) peak can be detected at $2\theta = 12^0$ in the XRD pattern of GO powder, indicating the ordered stack of original GO sheets. The other broad peak located at $2\theta = 23^0$ is resulted from the partial reduction of the GO material, possibly owing to the drying process during the material collection. Accordingly, the Raman spectrum of rGO sheets shows an intensity ratio of the D band over G band, i.e., the I_D/I_G equal to 1.06, also indicating a certain degree of graphitization, because the G band peak located near 1,589 cm^{-1} is related to the vibration of sp^2-bonded carbon atoms in an ordered two-dimensional hexagonal lattice of carbon-based materials, while the D band peak around 1,339 cm^{-1} is associated with defects and disorder formed in the hexagonal graphitic layers (Wang et al., 2012). However, it is interesting to see that the rGO component in the SnO_2@rGO composite material gives a higher ratio of $I_D/I_G = 1.14$, although it was subjected to the post-annealing process for reducing defects in original GO sheets. The increased disordered domains in the rGO component are probably caused by wrapped SnO_2 nanoparticles through the possible chemical bonding; hence, XPS spectra were carried out on the SnO_2@rGO powder to study chemical environments of Sn, O, and C elements. Characteristic C 1s, Sn 3d, and O 1s XPS peaks are plotted in **Figures 3d–f**, respectively. According to fitting patterns, the C 1s peak can be deconvoluted to one dominant C=C contribution at 284.7 eV, together with two weak effects from the C-O at 285.2 eV and C=O at 286.5 eV (**Figure 3d**), indicating a typical chemical environment of the rGO component as reported in the literature (Min et al., 2019).

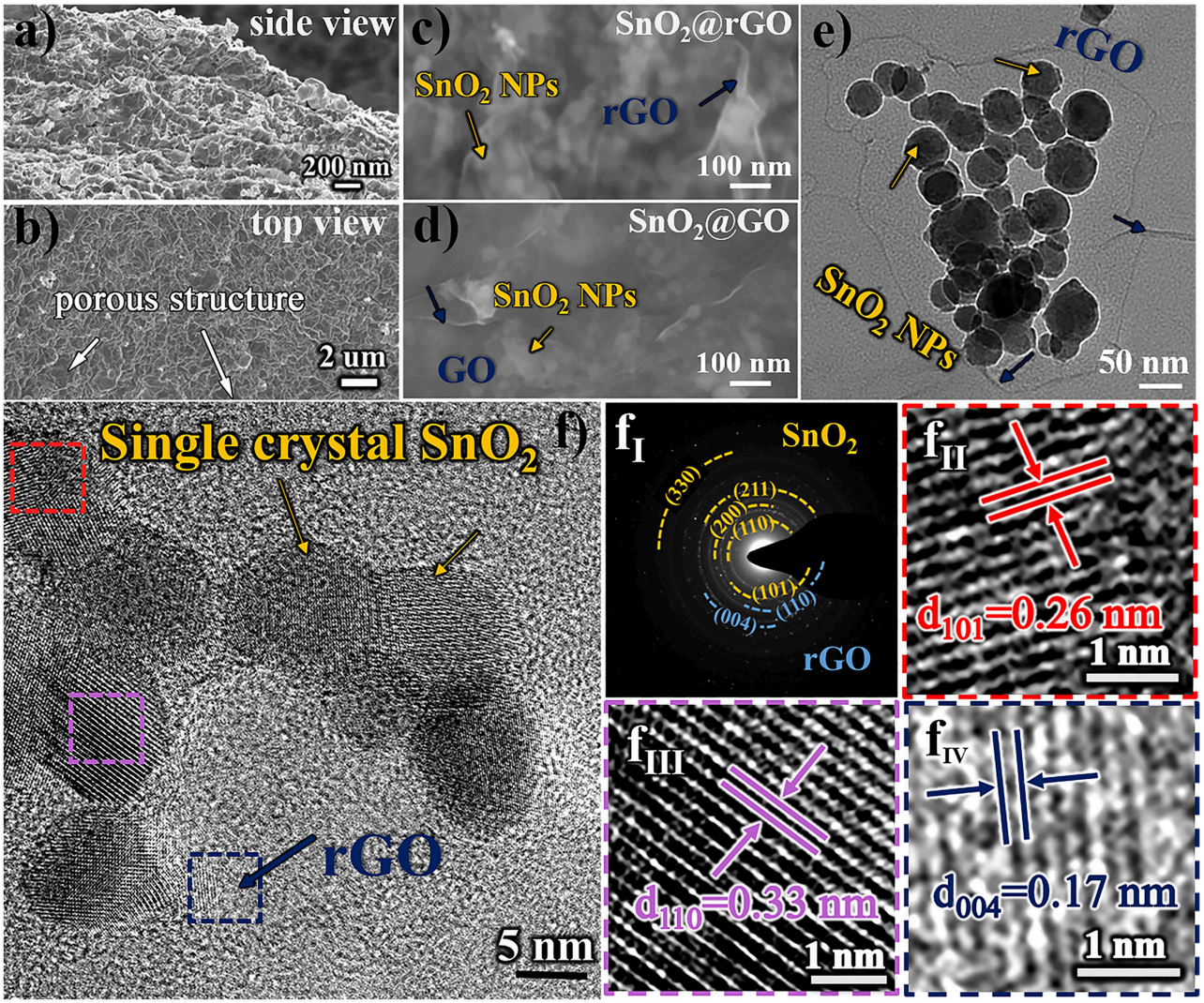

FIGURE 2 | Morphologic and structural characteristics of resulting SnO_2@rGO composite material: SEM images of **(a)** the side view and **(b)** the top view, **(c)** zoom-in FESEM image in comparison with **(d)** the original SnO_2@GO material before the reduction, **(e)** TEM image, **(f)** HRTEM image, coupled with **(f_I)** SAED pattern and **(f_{II}–f_{IV})** enlarged lattice fringes as squared in red, pink and navy dashed lines, respectively.

It is worth noting that two Sn 3d XPS peaks in **Figure 3e** shift to the higher binding energies for 0.8 eV compared with the reported pure SnO_2 powder (Yao et al., 2019). Furthermore, different contributions of O-Sn bond at 531.3 eV, Sn-O-C bond at 532.4 eV and O-O bond at 533.3 eV can be identified in the O 1s peak on the basis of fitting patterns as shown in **Figure 3f**, respectively. Thus, Raman and XPS spectra together indicate the favorable chemical bonding formed between SnO_2 and rGO components within the SnO_2@rGO composite material.

The resulting SnO_2@rGO sheet (**Figure 1IV**) is directly used as the free-standing anode for lithium storage performance evaluations without adding the conductive carbon, polymer binder and even the copper current collector. For the comparative propose, the bare rGO film is also fabricated as the other free-standing anode, and the bare SnO_2-based anode is composed of 70 wt.% SnO_2 nanoparticles as the active material, 20 wt.% acetylene black as the conductive carbon and 10 wt.% polyvinylidene fluoride (PVDF) as the binder. **Figures 4a–c** show cyclic voltammetric (CV) curves of the SnO_2@rGO, SnO_2 and bare rGO anodes in the first five cycles recorded at a scanning rate of 0.1 mV s^{-1} in a voltage range of 0.01–3.0 V vs. Li^+/Li. As referred to CV characteristics of bare rGO and SnO_2 anode materials, the initial cathodic peak at 0.74 V in the first CV discharge of the SnO_2@rGO anode is attributed to the conversion reaction of SnO_2 to the metallic Sn and Li_2O, as described in Equation (1). The subsequent broad cathodic peak below 0.5 V reveals combined effects from the successive formation of Li_xSn ($0 < x < 4.4$) alloys (Equation 2), lithiation of the rGO material (**Figure 4b**) and the formation of solid electrolyte interphase (SEI) film at the surface of the working electrode. Correspondingly, a weak anodic shoulder peak at 0.2 V in the following charge process can be probably assigned to the

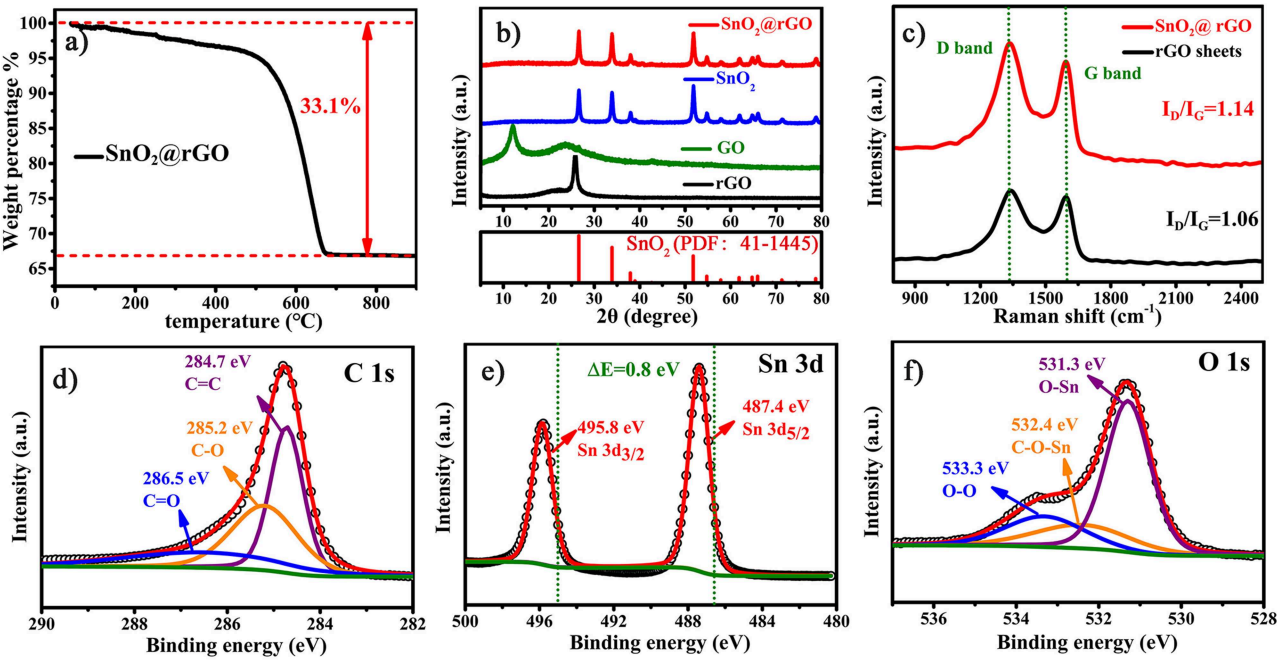

FIGURE 3 | Composition, crystallographic structure, and chemical environment of the SnO_2@rGO composite material: **(a)** TG analysis to determine the content of SnO_2 component, **(b)** XRD patterns, **(c)** Raman spectra compared with rGO sheets, and characteristic XPS spectra of **(d)** C 1s, **(e)** Sn 3d, and **(f)** O 1s.

reversible delithiation from the rGO component. The dominant anodic peak positioned at 0.55 V corresponds to the dealloying process of as-formed Li_xSn compounds. It is interesting to find a very wide anodic park cross a voltage range between 1.0 and 2.5 V. As reported in the literature (Chen and Yano, 2013; Kim et al., 2014; Hong et al., 2019), such electrochemical CV behaviors result from the reversible reaction from the reduced Sn to the SnO intermediate near 1.3 V and then to the SnO_2 near 1.9 V. Accordingly, a wide anodic peak appears in a voltage range of 0.75–1.5 V in the second CV cycle, which supports our speculation of the reversible conversion reaction between SnO_2 and Sn as shown in Equation (1). Two following cathodic peaks located at 0.2 and 0.01 V are ascribed to the alloying process of Li_xSn and lithium ion storage of the rGO, respectively, together with the continuous growth of SEI film. Notably, CV profiles of this SnO_2@rGO composite anode in next cycles are almost identical to each other after initial electrochemical activations in the first two cycles, indicating the excellent electrochemical reversibility similar to that of the bare rGO anode (**Figure 4c**). By contrast, the reversible $SnO_2 \leftrightarrow SnO \leftrightarrow Sn$ conversion reaction cannot be well-maintained in the bare SnO_2 anode, leading to the gradual disappearance of anodic/cathodic CV peaks around 1.5/1.0 V in its CV curves after initial two cycles (**Figure 4b**), which may account for the drastic capacity decay of the bare SnO_2 anode material in initial 10 of charge/discharge cycles. In a short summary, CV results indicate the satisfied electrochemical reversibility for stable lithium ion storage of the free-standing SnO_2@rGO anode on the basis of synergistic effects from SnO_2 and rGO components (Cong et al., 2015; Huang et al., 2016).

Figures 4d,f plot galvanostatic charge/discharge curves at different cycles of these three anodes at a current density of 500 mA g^{-1} between 0.01 and 3.0 V vs. Li^+/Li, and corresponding cycling performance are compared as shown in **Figure 4g**. The SnO_2@rGO anode can deliver initial discharge and charge capacities of 1,169 and 744 mAh g^{-1} in the first cycle, respectively. The moderate initial columbic efficiency of 63.6% is mainly attributed to the undesirable SEI formation and the lithium consumption during the conversion reaction from SnO_2 to metallic Sn and lithiated Li_2O in the first discharge process. By contrast, the lower columbic efficiency of 54.6% in the bare SnO_2 anode may result from the limited reversibility from the reduced Sn and Li_2O back to SnO_2 and Li^+ ion in the charge process, and the inferior columbic efficiency of 23.5% in the bare rGO anode should be caused by considerably aggravated side reactions. As a result, the SnO_2@rGO anode can retain a desired charge capacity of 711 mAh g^{-1} in the 50th cycle, corresponding to the capacity retention of 95.6%, much higher than that of the bare SnO_2 anode (reserved 126 mAh g^{-1} and 16.8% retention in the 50th cycle as shown in **Figure 4g**). Significantly enhanced cycling stability of the SnO_2@rGO anode can be attributed to the free-standing structure, in which active SnO_2 nanoparticles are well-accommodated in the flexible rGO buffer with excellent conductivity and sufficient porosity. **Figure 4h** compares EIS spectra of both the bare SnO_2 and SnO_2@rGO anodes before and after cycling. The SnO_2@rGO composite anode shows a distinctly lower charge-transfer resistance after 50 cycles compared with that of the bare SnO_2 anode, which can be attributed to high electronic conductivity of the rGO framework even without any carbon additives. In addition, side

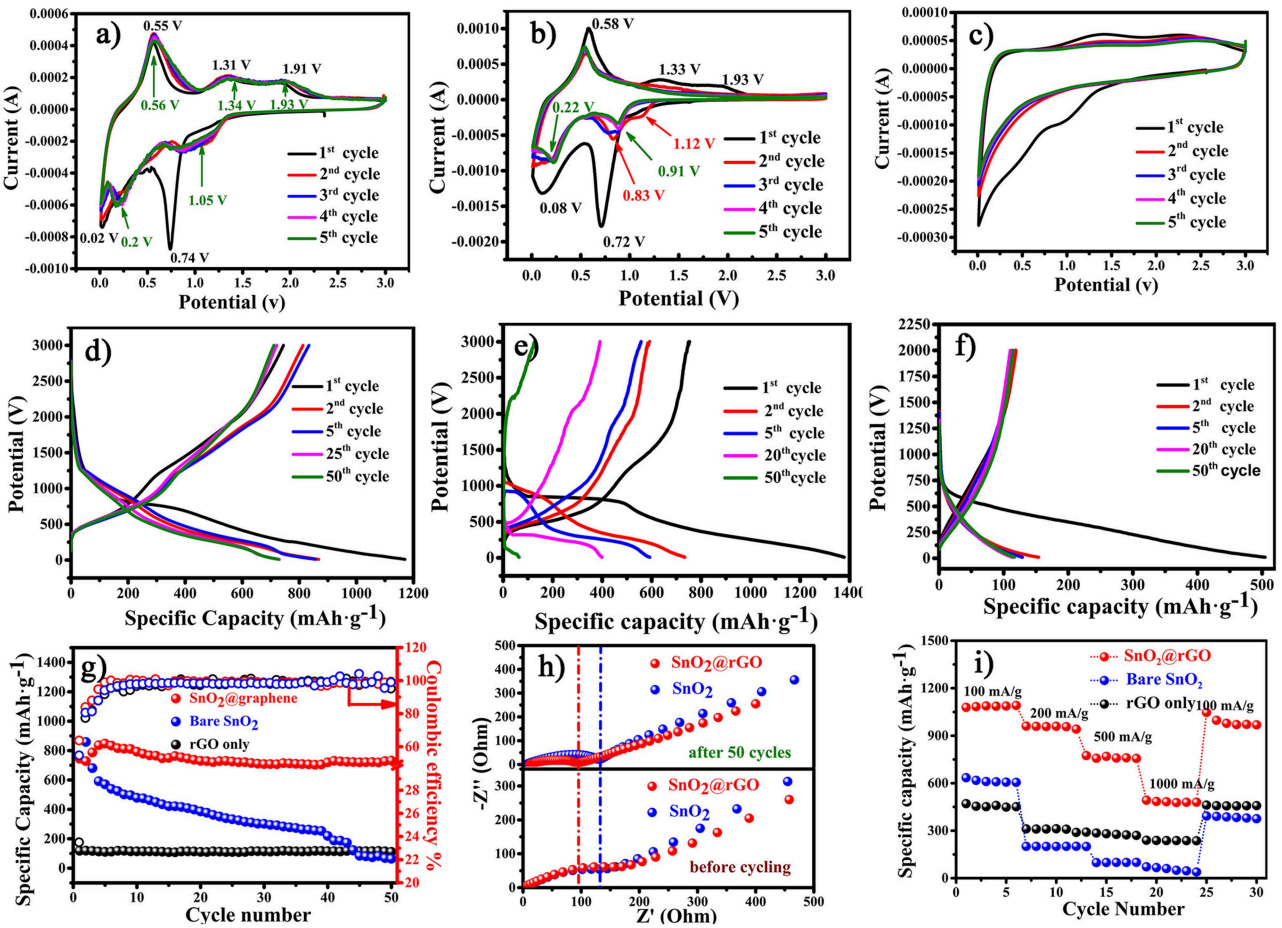

FIGURE 4 | Electrochemical performance of the free-standing SnO_2@rGO anode in a voltage range of 0.01–3.0 V vs. Li^+/Li: CV curves of **(a)** SnO_2@rGO, **(b)** bare SnO_2, and **(c)** bare rGO anodes in the first five cycles at a scanning rate of 0.1 mV s^{-1}, galvanostatic charge/discharge curves in different cycles at a current density of 500 mA g^{-1} of **(d)** SnO_2@rGO, **(e)** bare SnO_2, and **(f)** bare rGO anodes, **(g)** cycling performance at a current density of 500 mA g^{-1}, **(h)** EIS spectra of both the bare SnO_2 and SnO_2@rGO anodes before and after cycling and **(i)** comparative high-rate performance of three anodes.

reactions of active SnO_2 and/or Li_xSn materials may also be impeded in the composite anode through the rGO protection. It is noting that the SnO_2@rGO anode has the reduced resistance after cycling in comparison with its original state, possibly owing to the electrolyte infiltration into its internal structure during cycling. Furthermore, improved rate capability is also achieved of the SnO_2@rGO anode, which delivers high charge capacities of 1,085, 958, 758, and 480 mAh g^{-1} at gradually-increased current densities of 100, 200, 500, and 1,000 mA g^{-1}, respectively. The specific capacity around 1,000 mAh g^{-1} can be reversed, when such the free-standing anode is cycled back to a low current density of 100 mA g^{-1} after high-rate trials (**Figure 4i**). Electrochemical performance verifies that the free-standing SnO_2@rGO anode supported by the rGO framework results in enhanced cycling stability and rate capability of SnO_2-based anode materials for superior lithium storage.

In order to deeply understand the relationship between the designed structure and superior electrochemical performance of free-standing SnO_2@rGO composite material, the cycled anode is reexamined after 50 cycles in the full-charged state. **Figure 5a** shows the SEM image of cycled SnO_2@rGO anode, which preserves the well free-standing structure. Tin-based nanoparticles are expectedly localized between rGO sheets as shown in the cross-section view. The cycled electrode shows compressed pores and channels by contrast with the initial structure (**Figures 2a,b**), which can be attributed to the SEI formation during cycling, together with the high-pressure effect from the coin cell assembly on the anode. As shown in **Figure 5b**, XRD pattern of the cycled anode reveals the co-existence of three rGO, SnO_2 and Sn components in the fully-charged state. The reformation of SnO_2 component verifies the partial oxidation of Sn to SnO_2 during the charge reaction, in consistence with CV results (**Figure 4a**), which significantly accounts for high lithium storage capacity of the SnO_2@rGO anode as illustrated in Equation (1). TEM and HRTEM images are recaptured on the cycled SnO_2@rGO material. The TEM observation in **Figure 5c** clarifies the structural stability of such an assembled composite material, in which tin-based nanoparticles are uniformly and

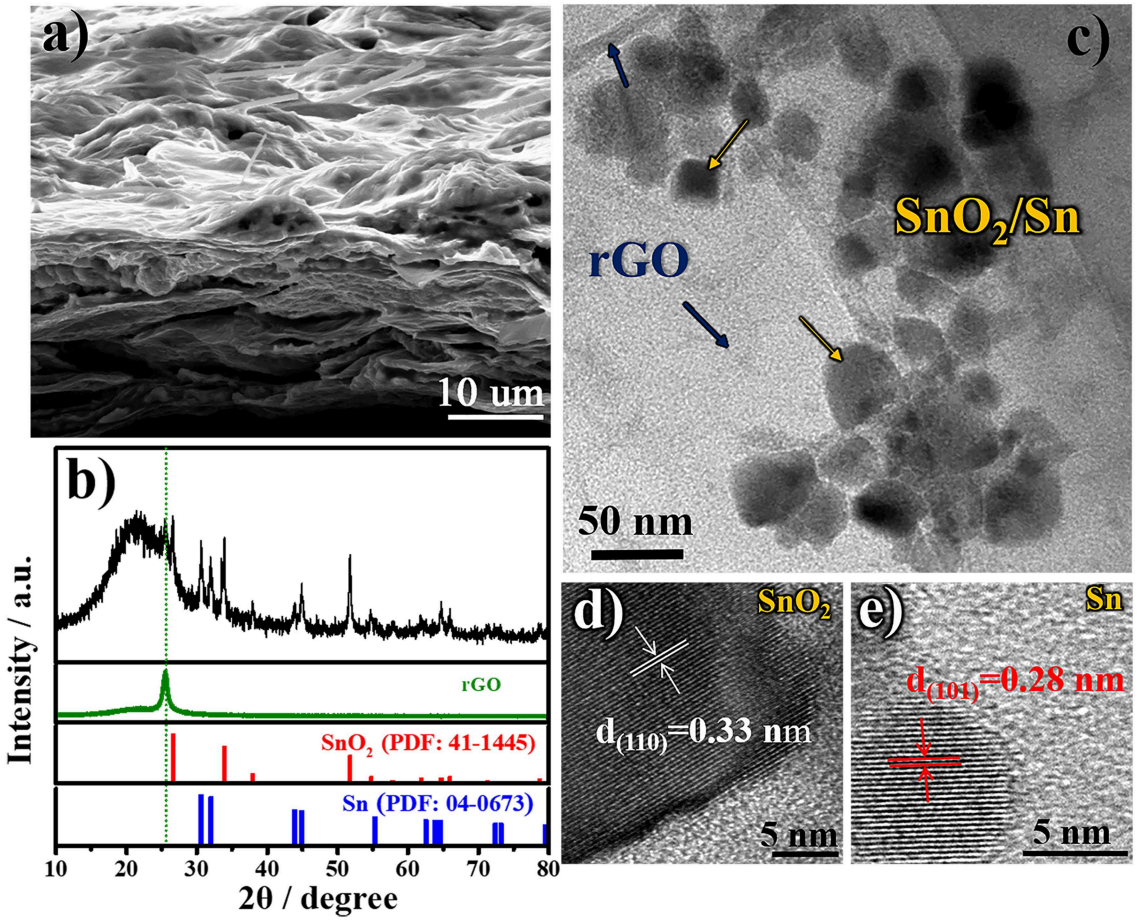

FIGURE 5 | Morphologic and structural characteristics of cycled SnO_2@rGO composite anode material in the fully-charged state after 50 cycles at a current density of 500 mA g^{-1}: **(a)** FESEM image, **(b)** XRD pattern, **(c)** TEM image, and HRTEM images of **(d)** SnO_2 and **(e)** Sn particles, respectively.

tightly wrapped within rGO sheets, in accordance with the SEM image (**Figure 5a**). **Figures 5d,e** presents HRTEM images of SnO_2 and Sn particles through indexing their different lattice fringes, respectively, which is consistent with the XRD results (**Figure 5b**). All characterizations of the cycled anode demonstrate the desired structural stability and the Sn to SnO_2 oxidation reaction during the charge reaction of the free-standing SnO_2@rGO anode; hence, improved cycling stability with high specific capacity can be obtained for prolonged cycles.

CONCLUSIONS

An anti-solvent precipitation method has been developed to effectively assemble SnO_2 nanoparticles and graphene oxide sheets for the fabrication of a free-standing electrode, which is free of the conductive additive, polymer binder and current collector. The resulting SnO_2@rGO composite anode shows significantly improved lithium storage performance compared with the bare SnO_2 anode material. It can deliver an impressive charge capacity of ~500 mAh g^{-1} at a high current density of 1 A g^{-1}, and an attractive capacity above 700 mAh g^{-1} can be retained after 50 cycles at a moderate current density of 500 mA/g. Enhanced cycling stability and rate capability of the composite anode can be attributed to the unique free-standing structure, in which all SnO_2 nanoparticles are tightly wrapped within rGO sheets full of wrinkles. Material characterizations of the cycled anode indicate the desired structural stability of such a free-standing SnO_2@rGO anode, accounting for superior lithium storage performance. This work offers a facile assembly method for the preparation of free-standing composite materials with enhanced performance for device applications.

DATA AVAILABILITY STATEMENT

The datasets generated for this study are available on request to the corresponding author.

AUTHOR CONTRIBUTIONS

JZ, LG, and RH conceived the idea and designed the work. SJ, RH, WZ, XL, YZ, and ZG carried out materials synthesis, characterizations, and performance measurements. SJ, JZ, and

RH wrote and revised the paper. All authors have made substantial, direct and intellectual contributions to the work.

FUNDING

This work was supported by the National Natural Science Foundation of China [grant number 21703147, U1401248]; the Jiangsu Provincial Natural Science Foundations for the Young Scientist [grant number BK20170338]. The Open Fund of Jiangsu Key Laboratory of Materials and Technology for Energy Conversion [grant number MTEC-2017M01]. The authors also acknowledge Suzhou Key Laboratory for Advanced Carbon Materials and Wearable Energy Technologies, Suzhou 215006, China, and Testing and Analysis Center, Soochow University, Suzhou 215123, China.

REFERENCES

Ahmed, B., Anjum, D. H., Gogotsi, Y., and Alshareef, H. N. (2017). Atomic layer deposition of SnO_2 on MXene for Li-ion battery anodes. *Nano Energy* 34, 249–256. doi: 10.1016/j.nanoen.2017.02.043

Ahn, W., Seo, M. H., Pham, T. K., Nguyen, Q. H., Luu, V. T., Cho, Y., et al. (2019). High lithium ion transport through rGO-wrapped $LiNi_{0.6}Co_{0.2}Mn_{0.2}O_2$ cathode material for high-rate capable lithium ion batteries. *Front. Chem.* 7:361. doi: 10.3389/fchem.2019.00361

Cao, B., Liu, Z., Xu, C., Huang, J., Fang, H., and Chen, Y. (2019). High-rate-induced capacity evolution of mesoporous C@SnO_2@C hollow nanospheres for ultra-long cycle lithium-ion batteries. *J. Power Sources* 414, 233–241. doi: 10.1016/j.jpowsour.2019.01.001

Chen, H., Zhang, B., Zhang, J., Yu, W., Zheng, J., Ding, Z., et al. (2018). *In-situ* grown SnS_2 nanosheets on rGO as an advanced anode material for lithium and sodium ion batteries. *Front. Chem.* 6:629. doi: 10.3389/fchem.2018.00629

Chen, J., and Yano, K. (2013). Highly monodispersed tin oxide/mesoporous starbust carbon composite as high-performance Li-ion battery anode. *ACS Appl. Mater. Interfaces* 5, 7682–7687. doi: 10.1021/am4021846

Cong, H.-P., Xin, S., and Yu, S.-H. (2015). Flexible nitrogen-doped graphene/SnO_2 foams promise kinetically stable lithium storage. *Nano Energy* 13, 482–490. doi: 10.1016/j.nanoen.2015.03.016

Cui, D., Zheng, Z., Peng, X., Li, T., Sun, T., and Yuan, L. (2017). Fluorine-doped SnO_2 nanoparticles anchored on reduced graphene oxide as a high-performance lithium ion battery anode. *J. Power Sources* 362, 20–26. doi: 10.1016/j.jpowsour.2017.07.024

Deng, B., Xu, R., Wang, X., An, L., Zhao, K., and Cheng, G. J. (2019). Roll to roll manufacturing of fast charging, mechanically robust 0D/2D nanolayered Si-graphene anode with well-interfaced and defect engineered structures. *Energy Storage Mater.* 22, 1–460. doi: 10.1016/j.ensm.2019.07.019

Deng, Y., Fang, C., and Chen, G. (2016). The developments of SnO_2/graphene nanocomposites as anode materials for high performance lithium ion batteries: A review. *J. Power Sources* 304, 81–101. doi: 10.1016/j.jpowsour.2015.11.017

Hong, Y., Mao, W., Hu, Q., Chang, S., Li, D., Zhang, J., et al. (2019). Nitrogen-doped carbon coated SnO_2 nanoparticles embedded in a hierarchical porous carbon framework for high-performance lithium-ion battery anodes. *J. Power Sources* 428, 44–52. doi: 10.1016/j.jpowsour.2019.04.093

Hu, R., Ouyang, Y., Liang, T., Wang, H., Liu, J., Chen, J., et al. (2017). Stabilizing the nanostructure of SnO_2 anodes by transition metals: a route to achieve high initial coulombic efficiency and stable capacities for lithium storage. *Adv. Mater. Weinheim.* 29:1605006. doi: 10.1002/adma.201605006

Huang, B., Li, X., Pei, Y., Li, S., Cao, X., Masse, R. C., et al. (2016). Novel carbon-encapsulated porous SnO_2 anode for lithium-ion batteries with much improved cyclic stability. *Small* 12, 1945–1955. doi: 10.1002/smll.201503419

Huang, J. Y., Zhong, L., Wang, C. M., Sullivan, J. P., Xu, W., Zhang, L. Q., et al. (2010). *In situ* observation of the electrochemical lithiation of a single SnO_2 nanowire electrode. *Science* 330, 1515–1520. doi: 10.1126/science.1195628

Jiang, B., He, Y., Li, B., Zhao, S., Wang, S., He, Y. B., et al. (2017). Polymer-templated formation of polydopamine-coated SnO_2 nanocrystals: anodes for cyclable lithium-ion batteries. *Angew. Chem. Int. Ed Engl.* 56, 1869–1872. doi: 10.1002/anie.201611160

Kim, H. W., Na, H. G., Kwon, Y. J., Kang, S. Y., Choi, M. S., Bang, J. H., et al. (2017). Microwave-assisted synthesis of graphene-SnO_2 nanocomposites and their applications in gas sensors. *ACS Appl. Mater. Interfaces* 9, 31667–31682. doi: 10.1021/acsami.7b02533

Kim, W.-S., Hwa, Y., Kim, H.-C., Choi, J.-H., Sohn, H.-J., and Hong, S.-H. (2014). SnO_2@Co_3O_4 hollow nano-spheres for a Li-ion battery anode with extraordinary performance. *Nano Res.* 7, 1128–1136. doi: 10.1007/s12274-014-0475-2

Kumar, R., Sahoo, S., Joanni, E., Singh, R. K., Tan, W. K., Kar, K. K., et al. (2019). Recent progress in the synthesis of graphene and derived materials for next generation electrodes of high performance lithium ion batteries. *Prog. Energy Combust. Sci.* 75:100786. doi: 10.1016/j.pecs.2019.100786

Li, H., Wang, J., Zhang, Y., Wang, Y., Mentbayeva, A., and Bakenov, Z. (2019). Synthesis of carbon coated Fe_3O_4 grown on graphene as effective sulfur-host materials for advanced lithium/sulfur battery. *J. Power Sources* 437. doi: 10.1016/j.jpowsour.2019.226901

Li, X., Huang, X., Liu, D., Wang, X., Song, S., Zhou, L., et al. (2011). Synthesis of 3D hierarchical Fe_3O_4/graphene composites with high lithium storage capacity and for controlled drug delivery. *J. Phys. Chem. C* 115, 21567–21573. doi: 10.1021/jp204502n

Li, Z., Ding, J., Wang, H., Cui, K., Stephenson, T., Karpuzov, D., et al. (2015). High rate SnO_2 –graphene dual aerogel anodes and their kinetics of lithiation and sodiation. *Nano Energy* 15, 369–378. doi: 10.1016/j.nanoen.2015.04.018

Liu, L., An, M., Yang, P., and Zhang, J. (2015). Superior cycle performance and high reversible capacity of SnO_2/graphene composite as an anode material for lithium-ion batteries. *Sci. Rep.* 5, 9055. doi: 10.1038/srep09055

Ma, T., Yu, X., Li, H., Zhang, W., Cheng, X., Zhu, W., et al. (2017). High volumetric capacity of hollow structured SnO_2@Si nanospheres for lithium-ion batteries. *Nano Lett.* 17, 3959–3964. doi: 10.1021/acs.nanolett.7b01674

Marcano, D. C., Kosynkin, D. V., Berlin, J. M., Sinitskii, A., Sun, Z., et al. (2010). Improved synthesis of graphene oxide. *ACS nano* 4, 4806–4814. doi: 10.1021/nn1006368

Min, X., Sun, B., Chen, S., Fang, M., Wu, X., Liu, Y., et al. (2019). A textile-based SnO_2 ultra-flexible electrode for lithium-ion batteries. *Energy Storage Mater.* 16, 597–606. doi: 10.1016/j.ensm.2018.08.002

Pan, L., Zhang, Y., Lu, F., Du, Y., Lu, Z., Yang, Y., et al. (2019). Exposed facet engineering design of graphene-SnO_2 nanorods for ultrastable Li-ion batteries. *Energy Storage Mater.* 19, 39–47. doi: 10.1016/j.ensm.2018.10.007

Park, M. S., Wang, G. X., Kang, Y. M., Wexler, D., Dou, S. X., and Liu, H. K. (2007). Preparation and electrochemical properties of SnO_2 nanowires for application in lithium-ion batteries. *Angew. Chem. Int. Ed Engl.* 46, 750–753. doi: 10.1002/anie.200603309

Riyanto, Sahroni, I., Bindumadhavan, K., Chang, P. Y., and Doong, R.A. (2019). Boron doped graphene quantum structure and MoS_2 nanohybrid as anode materials for highly reversible lithium storage. *Front. Chem.* 7:116. doi: 10.3389/fchem.2019.00116

Rong, J., Ge, M., Fang, X., and Zhou, C. (2014). Solution ionic strength engineering as a generic strategy to coat graphene oxide (GO) on various functional particles and its application in high-performance lithium-sulfur (Li-S) batteries. *Nano Lett.* 14, 473–479. doi: 10.1021/nl403404v

Sahoo, M., and Ramaprabhu, S. (2018). One-pot environment-friendly synthesis of boron doped graphene-SnO_2 for anodic performance in Li ion battery. *Carbon N. Y.* 127, 627–635. doi: 10.1016/j.carbon.2017.11.056

Sun, J., Xiao, L., Jiang, S., Li, G., Huang, Y., and Geng, J. (2015). Fluorine-doped SnO_2@Graphene porous composite for high capacity lithium-ion batteries. *Chem. Mater.* 27, 4594–4603. doi: 10.1021/acs.chemmater.5b00885

Wang, B., Ryu, J., Choi, S., Song, G., Hong, D., Hwang, C., et al. (2018). Folding graphene film yields high areal energy storage in lithium-ion batteries. *ACS Nano* 12, 1739–1746. doi: 10.1021/acsnano.7b08489

Wang, D., Yang, J., Li, X., Geng, D., Li, R., Cai, M., et al. (2013). Layer by layer assembly of sandwiched graphene/SnO_2 nanorod/carbon nanostructures with ultrahigh lithium ion storage properties. *Energy Environ. Sci.* 6, 2900–2906. doi: 10.1039/c3ee40829a

Wang, X., Cao, X., Bourgeois, L., Guan, H., Chen, S., Zhong, Y., et al. (2012). N-doped graphene-SnO_2 sandwich paper for high-performance lithium-ion batteries. *Adv. Funct. Mater.* 22, 2682–2690. doi: 10.1002/adfm.201103110

Wang, X., Zhou, X., Yao, K., Zhang, J., and Liu, Z. (2011). A SnO_2/graphene composite as a high stability electrode for lithium ion batteries. *Carbon N. Y.* 49, 133–139. doi: 10.1016/j.carbon.2010.08.052

Wang, Y., Huang, Z. X., Shi, Y., Wong, J. I., Ding, M., and Yang, H. Y. (2015). Designed hybrid nanostructure with catalytic effect: beyond the theoretical capacity of SnO_2 anode material for lithium ion batteries. *Sci. Rep.* 5:9164. doi: 10.1038/srep09164

Xia, J., Liu, L., Jamil, S., Xie, J., Yan, H., Yuan, Y., et al. (2019). Free-standing SnS/C nanofiber anodes for ultralong cycle-life lithium-ion batteries and sodium-ion batteries. *Energy Storage Mater.* 17, 1–11. doi: 10.1016/j.ensm.2018.08.005

Xia, L., Wang, S., Liu, G., Ding, L., Li, D., Wang, H., et al. (2016). Flexible SnO_2/N-doped carbon nanofiber films as integrated electrodes for lithium-ion batteries with superior rate capacity and long cycle life. *Small* 12, 853–859. doi: 10.1002/smll.201503315

Xing, T., Ouyang, Y., Zheng, L., Wang, X., Liu, H., Chen, M., et al. (2020). Free-standing ternary metallic sulphides/Ni/C-nanofiber anodes for high-performance lithium-ion capacitors. *J. Energy Chem.* 42, 108–115. doi: 10.1016/j.jechem.2019.06.002

Xu, Y., Guo, J., and Wang, C. (2012). Sponge-like porous carbon/tin composite anode materials for lithium ion batteries. *J. Mater. Chem.* 22, 9562–9567. doi: 10.1039/c2jm30448a

Yao, W., Wu, S., Zhan, L., and Wang, Y. (2019). Two-dimensional porous carbon-coated sandwich-like mesoporous SnO_2/graphene/mesoporous SnO_2 nanosheets towards high-rate and long cycle life lithium-ion batteries. *Chem. Eng. J.* 361, 329–341. doi: 10.1016/j.cej.2018.08.217

Zeugin, J. A., and Hartley, J. L. (1985). Ethanol precipitation of DNA. *Focus* 7, 1–2. doi: 10.1108/eb015969

Zhang, C., Peng, X., Guo, Z., Cai, C., Chen, Z., Wexler, D., et al. (2012). Carbon-coated SnO_2/graphene nanosheets as highly reversible anode materials for lithium ion batteries. *Carbon N. Y.* 50, 1897–1903. doi: 10.1016/j.carbon.2011.12.040

Zhang, L., Zhang, L., Chai, L., Xue, P., Hao, W., and Zheng, H. (2014). A coordinatively cross-linked polymeric network as a functional binder for high-performance silicon submicro-particle anodes in lithium-ion batteries. *J. Mater. Chem. A* 2, 19036–19045. doi: 10.1039/C4TA04320K

Zhao, K., Zhang, L., Xia, R., Dong, Y., Xu, W., Niu, C., et al. (2016). SnO_2 quantum Dots@graphene oxide as a high-rate and long-life anode material for lithium-ion batteries. *Small* 12, 588–594. doi: 10.1002/smll.201502183

Zheng, Y., Zhou, T., Zhang, C., Mao, J., Liu, H., and Guo, Z. (2016). Boosted charge transfer in SnS/SnO_2 heterostructures: toward high rate capability for sodium-ion batteries. *Angew. Chem. Int. Ed Engl.* 55, 3408–3413. doi: 10.1002/anie.201510978

Conflict of Interest: The authors declare that the research was conducted in the absence of any commercial or financial relationships that could be construed as a potential conflict of interest.

frontiers in Chemistry

ORIGINAL RESEARCH
published: 08 January 2020
doi: 10.3389/fchem.2019.00869

A Hierarchical Copper Oxide–Germanium Hybrid Film for High Areal Capacity Lithium Ion Batteries

Liying Deng[1], Wangyang Li[1], Hongnan Li[1], Weifan Cai[2], Jingyuan Wang[2], Hong Zhang[1], Hongjie Jia[1], Xinghui Wang[1,3] and Shuying Cheng[1,3]**

[1] College of Physics and Information Engineering, Institute of Micro-Nano Devices and Solar Cells, Fuzhou University, Fuzhou, China, [2] NOVITAS, Nanoelectronics Centre of Excellence, School of Electrical and Electronics Engineering, Nanyang Technological University, Singapore, Singapore, [3] Jiangsu Collaborative Innovation Center of Photovolatic Science and Engineering, Changzhou, China

Self-supported electrodes represent a novel architecture for better performing lithium ion batteries. However, lower areal capacity restricts their commercial application. Here, we explore a facial strategy to increase the areal capacity without sacrificing the lithium storage performance. A hierarchical CuO–Ge hybrid film electrode will not only provide high areal capacity but also outstanding lithium storage performance for lithium ion battery anode. Benefiting from the favorable structural advance as well as the synergic effect of the Ge film and CuO NWs array, the hybrid electrode exhibits a high areal capacity up to 3.81 mA h cm^{-2}, good cycling stability (a capacity retention of 90.5% after 150 cycles), and superior rate performance (77.4% capacity remains even when the current density increased to 10 times higher).

Keywords: self-supported electrode, lithium ion battery, CuO, Ge, areal capacity

OPEN ACCESS

Edited by:
Jianqing Zhao,
Soochow University, China

Reviewed by:
Wangwang Xu,
Louisiana State University, United States
Qingshui Xie,
Xiamen University, China

****Correspondence:***
Xinghui Wang
seaphy23@fzu.edu.cn
Shuying Cheng
sycheng@fzu.edu.cn

Specialty section:
This article was submitted to Electrochemistry, a section of the journal Frontiers in Chemistry

Received: *16 October 2019*
Accepted: *03 December 2019*
Published: *08 January 2020*

Citation:
Deng L, Li W, Li H, Cai W, Wang J, Zhang H, Jia H, Wang X and Cheng S (2020) A Hierarchical Copper Oxide–Germanium Hybrid Film for High Areal Capacity Lithium Ion Batteries. Front. Chem. 7:869. doi: 10.3389/fchem.2019.00869

INTRODUCTION

Rechargeable lithium ion batteries (LIBs) are identified as the ideal sources of power for wide applications ranging from portable electronic devices to large-scale products on account of their long-life span and high energy density (Liu et al., 2018b; Xu et al., 2018; Zhang et al., 2018; Yan et al., 2019). However, the specific capacity of the electrodes severely restricts their energy density. As a solution to this problem, different anode materials with higher specific capacities have been investigated to take the place of the present commercial graphite (Kim et al., 2017). To date, Ge and CuO have aroused increasing interest as the novel anodes for new generation LIBs due to their high theoretical capacities. Compared with commercial graphite (theoretical gravimetric capacity is 372 mA h g^{-1}), Ge has a high theoretical capacity of 1,624 mA h g^{-1}, while CuO has a capacity of 674 mA h g^{-1}. Ge has been widely studied because of its high ionic conductivity and low lithiation potential and CuO, as one of the transition metal oxides, has demonstrated to be a promising material for the substitute anodes in LIBs for its earth abundance, commercial benefit, and environmental friendly (Chan et al., 2008; Xiaojun et al., 2012; Huang et al., 2015; Susantyoko et al., 2015; Mironovich et al., 2017).

However, the considerable capacities of Ge and CuO are generally accompanied by drastic volume change upon Li intercalation and deintercalation, thus causing the poor cycling performance (Liu et al., 2015; So et al., 2018). Great efforts have been made to solve the pulverization

problem during the Li insertion and extraction process using nanomaterials such as nanoparticles (Hyojin et al., 2005; Mi-Hee et al., 2010; Yang et al., 2010), nanowires (Chan et al., 2008; Chockla et al., 2012; Yuan et al., 2012; Mullane et al., 2013), nanotubes (Chen et al., 2009; Cao et al., 2015; Liu et al., 2018a; Sun et al., 2018), and so on. For example, Li et al. synthesized mesoporous and hollow Ge@C nanostructures via carbon coating and reduced the hollow ellipsoidal GeO_2 precursor into Ge. A stable cycling performance (capacity retention remained 100% at 0.2 C rate for 200 cycles) and high rate capability (805 mA h g^{-1} at 20°C) is finally obtained (Li et al., 2013). Wang et al. fabricated self-supported CuO nanowires (NWs) on Cu foam (CF). The obtained electrodes delivered a specific capacity of 461.5 mA h g^{-1} after 100 cycles at a current density of 100 mA g^{-1}, and a capacity of 150.6 mA h g^{-1} even at a high rate of 1,000 mA g^{-1} (Wang et al., 2018).

Although these nanoengineering strategies have effectively improved the Li^+ ions storage performance of these high-capacity electrodes (Sun et al., 2018), most of these nanoscale metal oxides/group-IV elements and corresponding composites are mixed with organic binders and conductive carbon and then fabricate into electrode, which complicate the fabrication process (Wang et al., 2012). The bonding force between traditionally used binders and high-capacity active materials is too weak to maintain a stable performance after long-term cycling (Chang et al., 2019).

Recently, self-supported active nanomaterials which is *in situ* grown on current collectors without any inactive materials represent an unique architecture, which can offer many advantages for LIBs such as large contact area with electrolyte, great electrical conductivity, fast Li-ion transportation, and better performance for the electrodes (Wang et al., 2016). Susantyoko et al. fabricated amorphous Ge on the multiwall carbon nanotube arrays (MWCNT/a-Ge) by the combination of facial chemical vapor deposition and a physical sputtering method, which could give a specific areal capacity of 0.405 mA h cm^{-2} at the rate of 0.1 C after 100 cycles (Susantyoko et al., 2014). Kim et al. synthesized nano-Ge/C composite via electrochemical deposition method; the obtained electrode exhibits a capacity of 1 mA h cm^{-2} at 0.1 C over 50 cycles (Kim et al., 2017). Ji et al. fabricated binder-free electrodes, which is composed of 3D graphene network and octahedral CuO, the obtained 3D GN/CuO composites, yielding an areal capacity of 0.39 mA h cm^{-2} at 0.095 mA cm^{-2} (Dong et al., 2016). Xu et al. synthesized CuO mesocrystal entangled with MWCNT composites through a combination of precipitation and an oriented aggregation process. The CuO-MWCNT composites could deliver an areal capacity of 1.11 mA h cm^{-2} after 400 cycles at the current density of 0.39 mA cm^{-2} (Xu et al., 2016). Great progress for CuO- and Ge-based self-supporting electrodes has been achieved by the above-mentioned effects. Areal capacity is one of the important parameters for practical LIB application. Especially for self-supporting electrodes, it is very important and hard to obtain both high areal capacity and good electrochemical performance. However, the areal capacities of the most obtained electrodes are <2 mA h cm^{-2}, which is lower than the commercial specification of 3–4 mA h cm^{-2} (Cong et al., 2017). Normally, larger mass loading of active materials will make contribution to higher areal capacities but meanwhile sacrificing electrochemical performance (Chang et al., 2019). There is an increasing concern about fabricating self-supporting electrodes with high areal capacity as well as good electrochemical performance.

Usually, the self-supporting electrodes cannot maintain good electrochemical performance at very high areal capacity. Herein, we report a hierarchical CuO–Ge hybrid film on CF as a self-supporting electrode with ultrahigh areal capacity for LIB application. As shown in **Figure 1**, the integrated film was formed by physical vapor deposition of Ge film on CuO NWs array, which were grown directly on the CF via a facial and scalable solution approach. CuO NWs array with well-defined nanostructure serves as both the active materials and conductive connection for Ge film. The porous feature will not only alleviate the drastic volume change during the Li insertion and extraction process but also facilitate the diffusion of electrolyte into the electrode. Benefiting from the favorable nanostructures as well as the synergic effect of the Ge film and CuO NWs

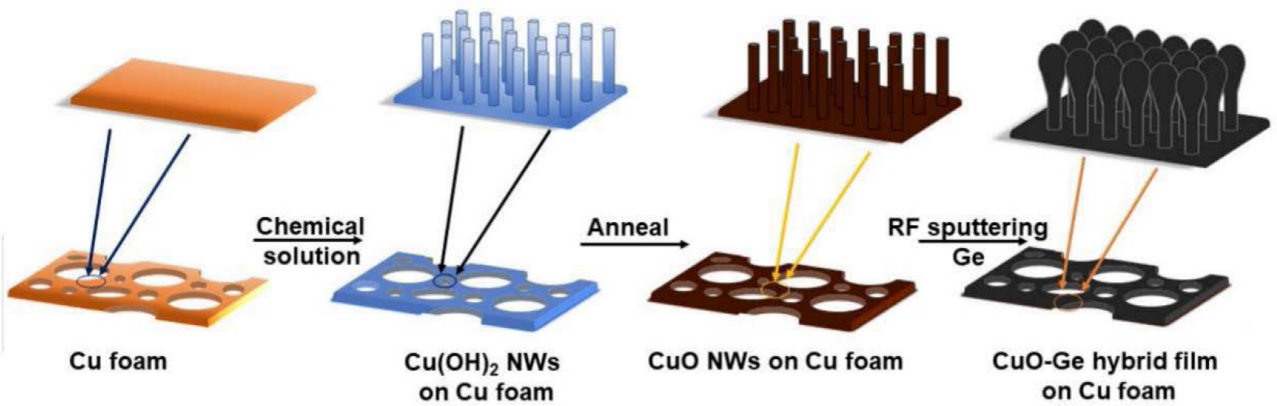

FIGURE 1 | Schematic illustration of the fabrication processes of the CuO–Ge hybrid film on Cu foam (CF).

array, the integrated electrode delivers ultrahigh areal capacity, extraordinary rate capability, and stable cycling performance. Moreover, this is the first time that CuO NWs combined with Ge film hybrid anode achieved a high areal capacity. It could deliver an ultrahigh charge areal capacity up to 3.45 mA h cm^{-2} after 150 cycles at a current density of 0.8 mA cm^{-2} and a capacity ~2.98 mA h cm^{-2} at a current density as high as 4 mA cm^{-2}.

EXPERIMENTAL

Fabrication Procedure

Fabrication of CuO NWs Array

Typically, the growth of CuO NWs array on CF is fabricated from a simple and scalable method. The CF with dimension of 2 × 2 cm^2 (1 mm, 100 PPI) was first degreased in 1.0 mol L^{-1} HCl for 15 min and then washed in ethanol, acetone, and deionized water by ultrasonication for 15 min, respectively. The rinsed CF was then submerged in the mixed solution, which was prepared by adding 8 ml of freshly obtained 10 M NaOH into $(NH_4)_2S_2O_8$ solution [0.913 g $(NH_4)_2S_2O_8$ added into 22 ml of deionized water] with magnetically stirring. After 15 min reaction time, the light blue CF can be obtained, which means the formation of $Cu(OH)_2$ NWs. After rinsing with deionized water for several times, the light blue CF was dried under N_2 gas flow and annealed at 180°C in air at a ramp rate of 2°C min^{-1} for 2 h. Then, the final product CuO NWs array was obtained with dark brown color. The principal of CuO NWs array *in situ* grown on CF could be described as following reactions (Cheng et al., 2016):

$$Cu + 4OH^- + (NH_4)_2S_2O_8 \rightarrow Cu(OH)_2 + 2SO_4^{2-} + 2NH_3 \uparrow + 2H_2O \quad (1)$$

$$Cu(OH)_2 \rightarrow CuO + H_2O \quad (2)$$

Fabrication of Hierarchical CuO–Ge Hybrid Film

The CuO NWs array on CF was placed into an radio frequency (RF) sputtering system (Verios G4 UC, Shenyang Lining Co.) using 99.999% pure Ge target. The base pressure was 7.8 × 10^{-4} Pa. Then, argon flowed at 50 sccm, and pressure remained at 2.2 Pa. The RF power was 100 W, and the deposition time was 400 min. The mass loading of CuO NWs supported Ge (typically ~0.67 mg cm^{-2}), CuO NWs array (typically ~3.64 mg cm^{-2}) and Ge on pristine CF (typically ~0.45 mg cm^{-2}) were weighed before and after sputtering using a microbalance (OHAUS, AX224ZH) with an accuracy of 0.1 mg. Besides, the Ge film was also deposited on pristine CF under the same deposition parameters.

Structural Characterization

The samples were characterized using X-ray diffraction (Rigaku Ultima IV) and Raman spectroscopy (WITEC alpha300 R Confocal Raman system), and the structure and morphology characterization of them were carried out by field-emission scanning electron microscopy (SEM, FEI Inspect F50) with accelerating voltage of 5.00 kV and transmission electron microscopy (TEM, FEI Tecnai G2).

Electrochemical Characterization

CR 2032-type coin cells was used to test electrochemical characterizations, test cells were assembled in a high-purity argon filled glove box (Mikrouna Technology) with oxygen and moisture level <0.5 ppm. The fabricated self-supporting electrodes were used as the working electrode and a Li foil as the counter and reference electrode. Lithium hexafluorophosphate ($LiPF_6$) (1 M) in a mixture of ethylene carbonate and diethyl carbonate (1:1 in volume) was used as the electrolyte. All the cells were aged for 12 h so that the electrolyte can fully infiltrate the whole cell before measurement. Lithium storage performance were evaluated by a multichannel battery tester (Neware, BTS-610) in the voltage range of 3.0–0.01 V (Li/Li^+). An electrochemical workstation (CHI660c, Shanghai Chenhua Co.) was used to evaluate the cyclic voltammetry (CV) at scan rate of 0.1 mV s^{-1}. All the tests were carried out in the thermotank at fixed temperature of 25°C.

RESULTS AND DISCUSSION

The Raman spectra analyses of the Ge film, CuO NWs array, and CuO–Ge hybrid film are shown in **Figure 2A**. For Ge film, a broad peak at 290 cm^{-1} was observed, which can be indexed to amorphous form of Ge (Susantyoko et al., 2014). There are three Raman peaks at 280, 324, and 618 cm^{-1} for CuO NWs array samples, which can be indexed to the A_g, $B_g^{(1)}$, and $B_g^{(2)}$ modes of CuO (Xu et al., 2015). All the peaks can be found on the CuO–Ge hybrid film samples, demonstrating that the hybrid structure was successfully fabricated. The X-ray diffraction patterns are shown in **Figure 2B**. One can note that the strong diffraction peaks of 43.3, 50.4, and 74.1°, which could be indexed to the CF with JCPDS card no. 70-3039. There are two weak but identifiable peaks located at 35.5 and 38.8°, corresponding to the (−111) and (111) planes of the monoclinic CuO, with JCPDS card no. 89-5899.

The typical SEM images of the obtained CuO NWs array on CF are shown in **Figures 3A–C**. The low-magnification SEM image in **Figure 3A** shows that CF has a well-organized 3D porous architecture. The magnified image shown in **Figure 3B** indicates the aligned CuO NWs array are 192 nm in diameter, and there are sufficient space available in CuO NWs array as indicated by the white-dashed squares, which can provide room for Ge thin film loading. Besides, the side view SEM image shown in **Figure 3C** demonstrates that all the CuO NWs array with length of ~6.1 μm are firmly rooted from Cu microfibers.

Then, a thick amorphous Ge was sputtered on the CuO NWs array using RF sputtering technique. **Figures 3D–F** show the SEM images of the CuO–Ge hybrid film. A typical image of a part of CF, as shown in **Figure 3D**, indicates that the 3D ordered nanowire architecture are well preserved after Ge coating. From **Figures 3E,F**, it is clearly observed that the average diameters and length of the nanowires are increased to 587.5 nm and 6.6 μm, respectively, due to the deposition of Ge film. There are still large space in between these nanowires after sputtering as indicated by the white-dashed squares in **Figure 3E**, which will not only benefit for accommodating the volume change but also facilitate

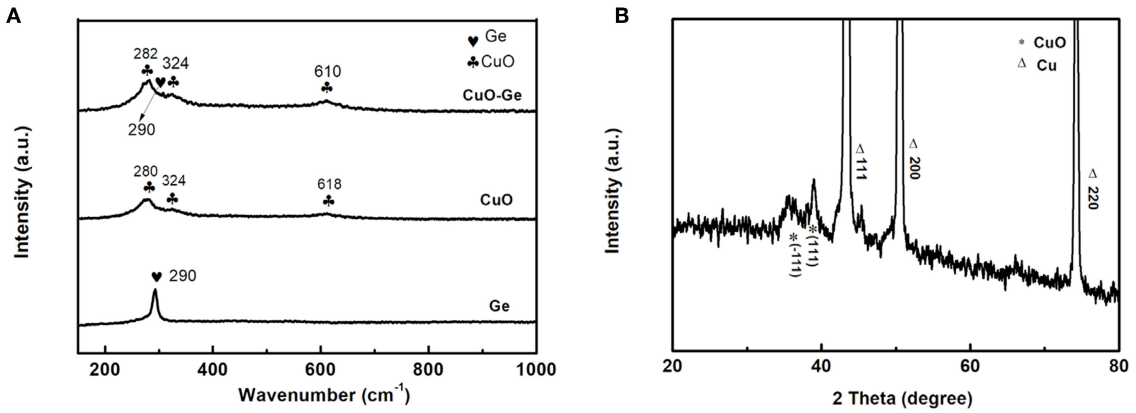

FIGURE 2 | (A) Raman spectrum of Ge, CuO NWs array, and CuO–Ge hybrid film; **(B)** X-ray diffraction (XRD) pattern of the CuO–Ge hybrid film.

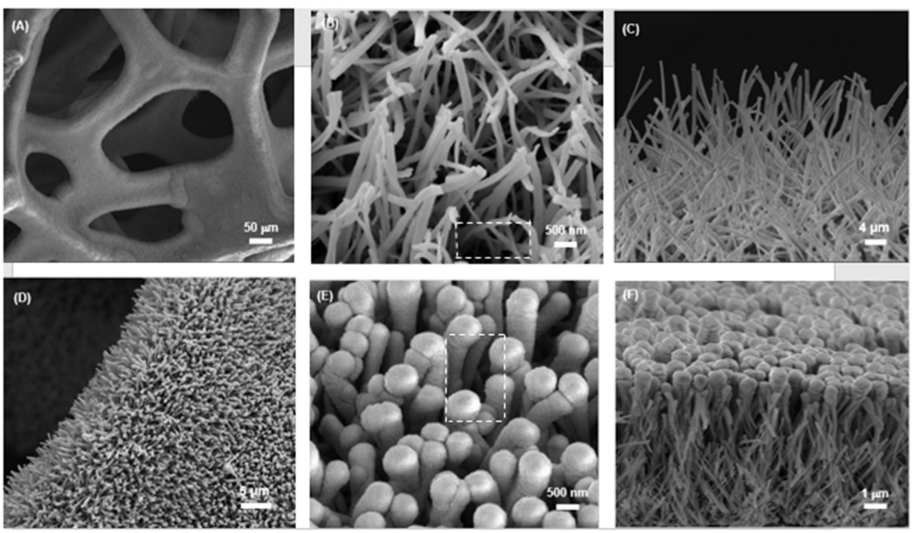

FIGURE 3 | (A,B) The top and **(C)** side view SEM images of CuO NWs array; **(D,E)** The top and **(F)** side view SEM images of the CuO–Ge hybrid film.

the diffusion of electrolyte into the electrode. From the side view SEM images shown in **Figure 3F**, it can be seen that the diameter of the synthetic nanowires is gradually decreased from the top to the bottom, which is attributed to the shadowing effect of the RF sputtering technique. It has been demonstrated that this structure is beneficial for Li storage performance (Wang et al., 2016).

We also present the TEM images of the CuO–Ge hybrid film in **Figure 4A**. The obtained distributions of Cu and Ge are shown in **Figure 4B**, the energy dispersive spectroscopy mapping profile obviously pictures that the outer sheath consists of Ge, whereas Cu is perfectly populated in the inner part of the CuO–Ge hybrid film, and the Ge films were grown uniformly and was deposited onto the whole CuO NWs.

Figure 5A shows the typical initial discharge and charge profiles of the CuO–Ge hybrid film, CuO NWs array, and Ge film with the voltage window of 0.01–3 V (Li^+/Li) at a current density of 0.8 mA cm^{-2}. The CuO–Ge hybrid film delivers an initial discharge and charge capacity of ∼5.09 and 3.81 mA h cm^{-2}, giving the initial Coulombic efficiency of 74.8%. The irreversible discharge capacity is associated with the formation of solid electrolyte interface layer and the irreversible insertion of Li^+ into CuO and Ge films, which are common for CuO and Ge based anodes (Chan et al., 2008; Chockla et al., 2012; Yuan et al., 2012; Mullane et al., 2013; Liu et al., 2018a). The low Coulombic efficiency may restrict the capacity of anode materials; however, it has been demonstrated that LIBs must undergo a few charge–discharge cycles, which is generally called the "formation process" (Chen et al., 2013). Besides the first cycle, the Coulombic efficiency of the battery was all above 99.2%, indicating excellent recyclability. In contrast, the first discharge and charge capacities are 3.34 and 2.50 mA h cm^{-2} for CuO NWs array and 0.71 and 0.59 mA h cm^{-2} for Ge film, respectively. The CuO–Ge hybrid film electrode exhibits much higher initial charging areal capacity when compared with the sum of the Ge film and CuO NWs array

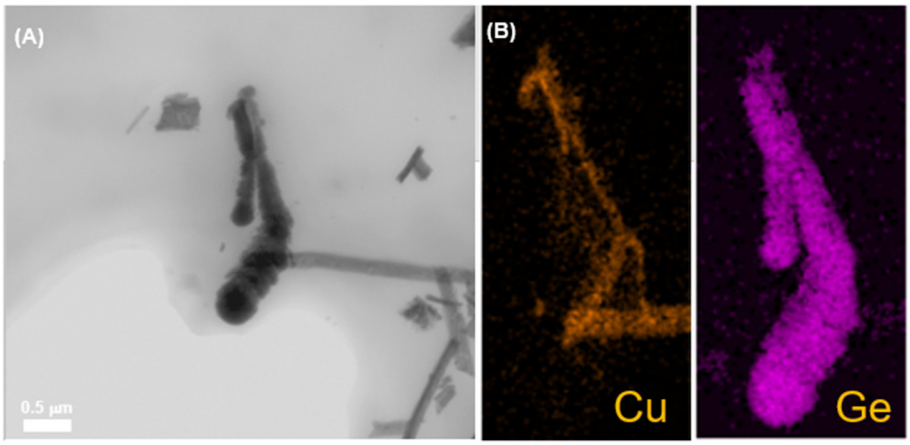

FIGURE 4 | (A) Annual dark-field TEM image of the CuO–Ge hybrid film; **(B)** elemental mapping of CuO–Ge hybrid film: the corresponding Cu, Ge EDX maps.

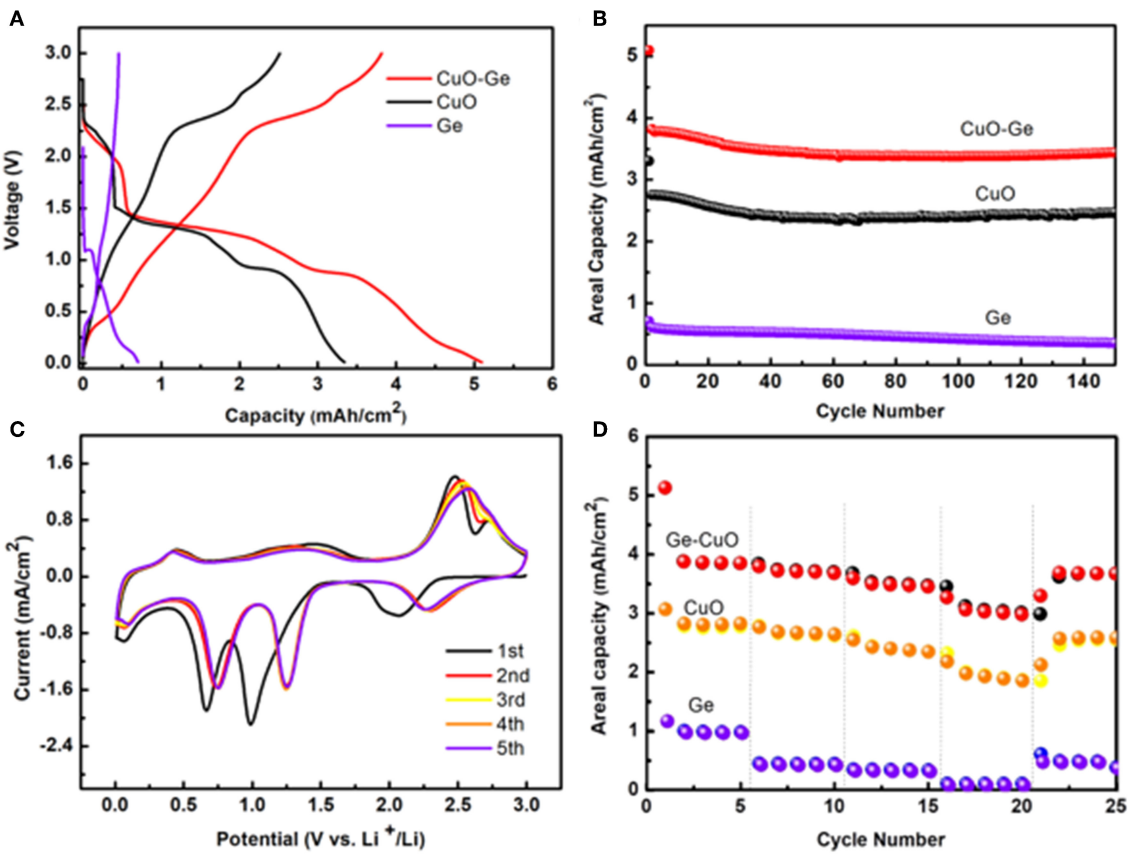

FIGURE 5 | (A) The initial voltage profiles of the CuO–Ge hybrid film, CuO NWs array, and Ge film; **(B)** the cycle performance of the CuO–Ge hybrid film, CuO NWs array, and Ge film; **(C)** the initial five cyclic voltammetry (CV) curves of the CuO–Ge hybrid film; **(D)** rate performance of CuO–Ge hybrid film, CuO NWs array, and Ge film.

electrode. This is because the mass loading of the Ge film on CuO NWs array is higher than that on CF attribute to the larger surface area of the CuO NWs array, demonstrating the structural advantages of the CuO NWs array.

Figure 5B compares the cycle performance of the CuO–Ge hybrid film, CuO NWs array and Ge film for subsequent 150 cycles at a high current density of 0.8 mA cm^{-2}. For the CuO–Ge synthesized film electrode, a reversible discharge capacity of

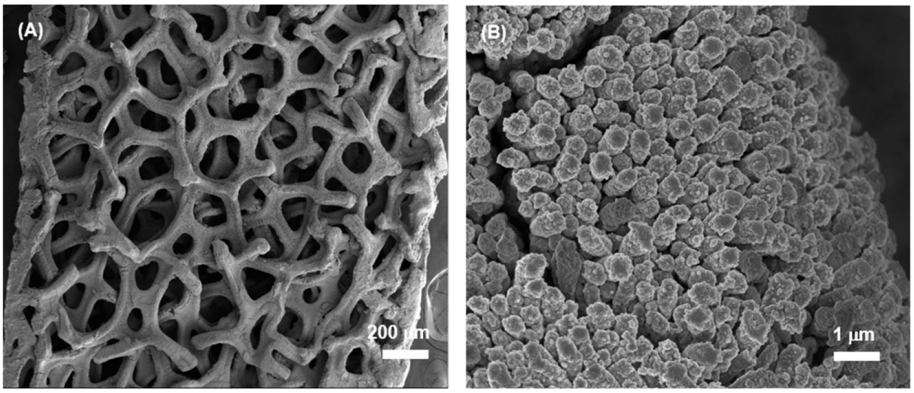

FIGURE 6 | (A,B) SEM images of the CuO–Ge hybrid film after 50 cycles.

3.81 mA h cm^{-2} was achieved at the second cycle, corresponding to a specific capacity of 883 mA h g^{-1}. The electrode could still deliver a high areal capacity of ∼3.45 mA h cm^{-2} with a capacity retention of 90.5% after 150 cycles (the corresponding specific capacity contribution from Ge was 1,462 mA h g^{-1}, and CuO was 678 mA h g^{-1}). In contrast, the CuO NWs array electrode could deliver a capacity of 2.47 mA h cm^{-2} after 150 cycles, which corresponds to the 90.0% of the original one. While Ge film can only obtain a reversible capacity of 0.2 mA h cm^{-2} after 150 cycles with a much lower capacity retention of 59.3%. The CuO–Ge hybrid film electrode exhibits a superior improvement in Li storage performance compared to the other electrodes, which may be attribute to the novel structure design using a hierarchical 3D nanostructure to combine two high theoretical capacity materials. The well-separated CuO NW arrays will not only provide large area for larger mass loading of Ge but also the large void space to overcome the large volume change during charge and discharge.

The initial few CV curves of the CuO–Ge hybrid film electrode were conducted in range of 0.01–3.0 V at a scan rate of 0.1 mV s^{-1} as displayed in **Figure 5C**. It can be indicated from these peaks that there is a multistep electrochemical reaction between Li and the hybrid electrode. A broad but moderate peak at ∼2.1 V corresponding to the initial formation of Li_xCuO in the first cathodic sweep. Then, two succession reduction peaks were observed at ∼1.0 and ∼0.66 V, corresponding to the transformation of Li_xCuO into Cu_2O and Cu; then, a moderate peak at ∼0.07 V was observed, which was associated with the formation of the Li_xGe alloy (Rudawski et al., 2013; Guo et al., 2015). These reduction peaks shifted toward slightly higher voltages in the following scans, which might associate with the drastic Li driven structural modifications during the initial discharge and charge process (Yunhua et al., 2014). A peak was found at 0.44 V during the first anodic scan, attributing to the phase transition of Li_xGe to Ge; then, two distinct peaks at ∼1.5 and ∼2.5 V and a shoulder peak at ∼2.7 V appeared, which was associated with oxidation of Cu^0 to Cu^+ and Cu^{2+} (Dong et al., 2016; Xu et al., 2016; Wang et al., 2018). These results are in agreement with the other reports of electrochemical reactions of Ge and CuO with Li (Seo et al., 2011; Ren et al., 2013; Xinghui et al., 2014; Wei et al., 2017; Lin et al., 2018; Wang et al., 2018). The CV curves were well-overlapped with each other from the second cycle afterwards, suggesting that the electrode has a good reversibility.

The rate capability is further tested for the CuO–Ge hybrid film electrode, which is of significant importance for high power energy storage. The rate performance was evaluated by charging–discharging at varied current densities varying from 0.4 to 4 mA cm^{-2}. As shown in **Figure 5D**, after the first five cycles at the current density of 0.4 mA cm^{-2}, the obtained electrode showed a high discharge areal capacity of 3.85 m A h cm^{-2}; then, it slightly reduced to 3.68 and 3.45 m A h cm^{-2} at current rates of 0.8 and 1.6 mA cm^{-2}. Even at a rate as high as 4 mA cm^{-2}, the CuO–Ge hybrid film could still deliver a reversible capacity of ∼2.98 m A h cm^{-2}, corresponding to the 77.4% capacity of the capacity at 0.4 mA cm^{-2}. After the rate returned back to the initial value of 0.4 mA cm^{-2} for five cycles, 94.5% of the initial charge capacity was regained. In the comparison, the CuO NWs exhibited a capacity of 2.83, 2.65, 2.35, and 1.86 m A h cm^{-2}, respectively, and eventually obtained a capacity of 2.59 m A h cm^{-2}. As for the Ge film, it only showed a capacity of 0.98, 0.44, 0.33, and 0.10 m A h cm^{-2}, respectively. Indicating the benefit from the favorable nanostructures as well as the synergic effect of the Ge film and CuO NWs array, the hybrid electrode hybrid film electrode has wonderful rate capability far beyond the CuO NWs and Ge film electrode.

To examine the structure stability of the CuO–Ge hybrid film electrode upon repeated discharge/charge process, the electrode was disassembled after 50 cycles. As shown in **Figure 6A**, the CuO–Ge hybrid film were uniformly remained on the CF with no detaching signs. From high magnification SEM shown in **Figure 6B**, one can see that the hierarchical CuO–Ge hybrid films maintain their original structure even after 50 cycles, indicating high structural stability of the hybrid structure, which proves that this novel structure can withstand the dramatic volume change caused during repeated discharge and charge cycles. Therefore, the excellent lithium storage performance of the CuO–Ge hybrid

film electrode is mainly due to the following aspects: (1) The well-separated CuO NW arrays can not only provide large area for higher mass loading of Ge, resulting in higher areal capacity, but also improve the cycle performance of the Ge film by providing sufficient void space to alleviate the large volume change of the Ge film. (2) The hierarchical porous feature in the hybrid film not only provides sufficient space to accommodate the drastic volume change but also facilitates the lithium diffusion into the inner electrodes. (3) The Cu in the lithiated CuO NWs will promote the electronic conductivities, enhancing the rate performance of the electrodes (Yang et al., 2014).

CONCLUSIONS

In conclusion, an efficient strategy to prepare self-supporting electrode with ultrahigh areal capacity for LIB application has been introduced. The obtained CuO–Ge hybrid film electrode exhibits excellent lithium storage performance. It can deliver a high areal capacity of 3.81 mA h cm^{-2} after 150 cycles, corresponding to 90.5% of the original one. Furthermore, the electrode could deliver high areal capacities of 2.98 mA h cm^{-2} even at ultrahigh current density of 4 mA cm^{-2}. The hierarchical CuO–Ge hybrid film grown directly on CF could be a novel substitute of graphite for LIBs, and the facial and efficiency synthesis strategy sheds light on improving the areal capacity of the self-supporting electrodes, which can be applicable for preparation of other high capacity hybrid electrode for energy storage application.

DATA AVAILABILITY STATEMENT

All datasets generated for this study are included in the article/supplementary material.

AUTHOR CONTRIBUTIONS

All authors have contributed in various degrees to the analytical methods used, to the research concept, to the experiment design, to the acquisition of data, or analysis and interpretation of data, to draft the manuscript, or to revise it critically for important intellectual content.

FUNDING

This work was supported by the National Natural Science Foundation of China (grant number 11704071), the Excellent Youth Foundation of Fujian Scientific Committee (grant number 2019J06008), the Natural Science Foundation of Fujian Province, China (grant number 2017J01503), and the Award Program for Fujian Minjiang Scholar Professorship.

REFERENCES

Cao, F., Xia, X. H., Pan, G. X., Chen, J., and Zhang, Y. J. (2015). Construction of carbon nanoflakes shell on CuO nanowires core as enhanced core/shell arrays anode of lithium ion batteries. *Electrochim. Acta* 178, 574–579. doi: 10.1016/j.electacta.2015.08.055

Chan, C. K., Zhang, X. F., and Cui, Y. (2008). High capacity Li ion battery anodes using ge nanowires. *Nano Lett.* 8, 307–309. doi: 10.1021/nl0727157

Chang, W.-C., Lu, S.-P., Chu, H.-C., and Tuan, H.-Y. (2019). Lithium-ion battery anodes of stacked nanowire laminate for ultrahigh areal capacities. *ACS Sustain. Chem. Eng.* 7, 156–164. doi: 10.1021/acssuschemeng.8b02409

Chen, L. B., Lu, N., Xu, C. M., Yu, H. C., and Wang, T. H. (2009). Electrochemical performance of polycrystalline CuO nanowires as anode material for Li ion batteries. *Electrochim. Acta* 54, 4198–4201. doi: 10.1016/j.electacta.2009.02.065

Chen, Z., Yan, Y., Xin, S., Li, W., and Song, W. G. (2013). Copper germanate nanowire/reduced graphene oxide anode materials for high energy lithium-ion batteries. *J. Mater. Chem. A* 1, 11404–11409. doi: 10.1039/c3ta12344h

Cheng, S., Shi, T., Tao, X., Yan, Z., Huang, Y., Li, J., et al. (2016). *In-situ* oxidized copper-based hybrid film on carbon cloth as flexible anode for high performance lithium-ion batteries. *Electrochim. Acta* 212, 492–499. doi: 10.1016/j.electacta.2016.07.058

Chockla, A. M., Klavetter, K. C., Mullins, C. B., and Korgel, B. A. (2012). Solution-grown germanium nanowire anodes for lithium-ion batteries. *ACS Appl. Mater. Interfaces* 4, 4658–4664. doi: 10.1021/am3010253

Cong, L., Xie, H., and Li, J. (2017). Hierarchical structures based on two-dimensional nanomaterials for rechargeable lithium batteries. *Adv. Energy Mater.* 7:1601906. doi: 10.1002/aenm.201601906

Dong, J., Hu, Z., Tong, Y., Wang, J., Zhu, M., Chen, T., et al. (2016). Facile fabrication of MOF-derived octahedral CuO wrapped 3D graphene network as binder-free anode for high performance lithium-ion batteries. *Chem. Eng. J.* 313, 1623–1632. doi: 10.1016/j.cej.2016.11.063

Guo, W., Sun, W., and Wang, Y. (2015). Multi-layer CuO@NiO hollow spheres: microwave-assisted metal-organic-framework derivation and highly reversible structure-matched stepwise lithium storage. *ACS Nano* 9, 11462–11471. doi: 10.1021/acsnano.5b05610

Huang, J. F., Zhu, Y. H., Yang, X. L., Chen, W., Zhou, Y., and Li, C. Z. (2015). Flexible 3D porous CuO nanowire arrays for enzymeless glucose sensing: *in situ* engineered versus *ex situ* piled. *Nanoscale* 7, 559–569. doi: 10.1039/C4NR05620E

Hyojin, L., Gyu, K. M., Cheol Ho, C., Yang-Kook, S., Seung, Y. C., and Jaephil, C. (2005). Surface-stabilized amorphous germanium nanoparticles for lithium-storage material. *J. Phys. Chem. B* 109, 20719–20723. doi: 10.1021/jp052620y

Kim, S.-W., Ngo, D. T., Heo, J., Park, C.-N., and Park, C.-J. (2017). Electrodeposited germanium/carbon composite as an anode material for lithium ion batteries. *Electrochim. Acta* 238, 319–329. doi: 10.1016/j.electacta.2017.04.027

Li, L., Seng, K., Feng, C., Liu, H., and Guo, Z. (2013). Synthesis of hollow GeO2 nanostructures, transformation into Ge@C, and lithium storage properties. *J. Mater. Chem. A* 1, 7666–7672. doi: 10.1039/c3ta11381g

Lin, X., Lin, J., Niu, J., Lan, J., Reddy, R.C. K., Cai, Y., et al. (2018). *In situ* synthesis of Cu2O–CuO–C supported on copper foam as a superior binder-free anode for long-cycle lithium-ion batteries. *Mater. Chem. Front.* 2, 2254–2262. doi: 10.1039/C8QM00366A

Liu, S., Feng, J., Bian, X., Qian, Y., Liu, J., and Xu, H. (2015). Nanoporous germanium as high-capacity lithium-ion battery anode. *Nano Energy* 13, 651–657. doi: 10.1016/j.nanoen.2015.03.039

Liu, X., Lin, N., Xu, K., Han, Y., Lu, Y., Zhao, Y., et al. (2018a). Cu3Ge/Ge@C nanocomposites crosslinked by the *in situ* formed carbon nanotubes for high-rate lithium storage. *Chem. Eng. J.* 352, 206–213. doi: 10.1016/j.cej.2018.07.015

Liu, X., Liu, Y.-S., Harris, M. M., Li, J., Wang, K.-X., and Chen, J.-S. (2018b). Germanium nanoparticles supported by 3D ordered macroporous nickel frameworks as high-performance free-standing anodes for Li-ion batteries. *Chem. Eng. J.* 354, 616–622. doi: 10.1016/j.cej.2018.08.056

Mi-Hee, P., Kitae, K., Jeyoung, K., and Jaephil, C. (2010). Flexible dimensional control of high-capacity Li-ion-battery anodes: from 0D hollow to 3D porous germanium nanoparticle assemblies. *Adv. Mater.* 22, 415–418. doi: 10.1002/adma.200901846

Mironovich, K. V., Evlashin, S., Bocharova, S., Yerdauletov, M., Dagesyan, S., Egorov, A., et al. (2017). Gaining cycling stability of Si- and Ge-based negative Li-ion high areal capacity electrodes by using carbon nanowall scaffolds. *J. Mater. Chem. A* 5, 18095–18100. doi: 10.1039/C7TA03509H

Mullane, E., Kennedy, T., Geaney, H., Dickinson, C., and Ryan, K. M. (2013). Synthesis of tin catalyzed silicon and germanium nanowires in a solvent–vapor system and optimization of the seed/nanowire interface for dual lithium cycling. *Chem. Mater.* 25, 1816–1822. doi: 10.1021/cm400367v

Ren, J. G., Wu, Q. H., Tang, H., Hong, G., Zhang, W. J., and Lee, S. T. (2013). Germanium-graphene composite anode for high-energy lithium batteries with long cycle life. *J. Mater. Chem. A* 1, 1821–1826. doi: 10.1039/C2TA01286C

Rudawski, N. G., Yates, B. R., Holzworth, M. R., Jones, K. S., Elliman, R. G., and Volinsky, A. A. (2013). Ion beam-mixed Ge electrodes for high capacity Li rechargeable batteries. *J. Power Sources* 223, 336–340. doi: 10.1016/j.jpowsour.2012.09.056

Seo, M. H., Park, M., Lee, K. T., Kim, K., Kim, J., and Cho, J. (2011). High performance Ge nanowire anode sheathed with carbon for lithium rechargeable batteries. *Energy Environ. Sci.* 4, 425–428. doi: 10.1039/C0EE00552E

So, J. Y., Lee, C. H., Kim, J. E., Kim, H. J., Jun, J., and Bae, W. G. (2018). Hierarchically nanostructured CuO(-)Cu current collector fabricated by hybrid methods for developed Li-ion batteries. *Materials* 11:1018. doi: 10.3390/ma11061018

Sun, N., Peng, C. L., Zheng, J. C., He, Z. J., Tong, H., Tang, L. B., et al. (2018). Self-assembled 3D network GeOx/CNTs nanocomposite as anode material for Li-ion battery. *Powder Technol.* 338, 211–219. doi: 10.1016/j.powtec.2018.07.011

Susantyoko, R. A., Wang, X., Sun, L., Pey, K. L., Fitzgerald, E., and Zhang, Q. (2014). Germanium coated vertically-aligned multiwall carbon nanotubes as lithium-ion battery anodes. *Carbon* 77, 551–559. doi: 10.1016/j.carbon.2014.05.060

Susantyoko, R. A., Wang, X., Sun, L., Sasangka, W., Fitzgerald, E., and Zhang, Q. (2015). Influences of annealing on lithium-ion storage performance of thick germanium film anodes. *Nano Energy* 12, 521–527. doi: 10.1016/j.nanoen.2015.01.024

Wang, J., Du, N., Zhang, H., Yu, J., and Yang, D. (2012). Cu–Si1–xGex core–shell nanowire arrays as three-dimensional electrodes for high-rate capability lithium-ion batteries. *J. Power Sources* 208, 434–439. doi: 10.1016/j.jpowsour.2012.02.039

Wang, X., Sun, L., Susantyoko, R. A., and Zhang, Q. (2016). A hierarchical 3D carbon nanostructure for high areal capacity and flexible lithium ion batteries. *Carbon* 98, 504–509. doi: 10.1016/j.carbon.2015.11.049

Wang, Z., Zhang, Y., Xiong, H., Qin, C., Zhao, W., and Liu, X. (2018). Yucca fern shaped CuO nanowires on Cu foam for remitting capacity fading of Li-ion battery anodes. *Sci. Rep.* 8:6530. doi: 10.1038/s41598-018-24963-2

Wei, Y., Yan, Z., Pan, B., Qiu, Z., Jian, L., Tan, Z., et al. (2017). Hierarchical MCMB/CuO/Cu anode with super-hydrophilic substrate and blind-hole structures for lithium-ion batteries. *J. Alloys Compounds* 719, 353–364. doi: 10.1016/j.jallcom.2017.05.195

Xiaojun, Z., Liutao, Y., Lingling, W., Rong, J., Guangfeng, W., and Baoyou, G. (2012). High electrochemical performance based on ultrathin porous CuO nanobelts grown on Cu substrate as integrated electrode. *Phys. Chem. Chem. Phys.* 15, 521–525. doi: 10.1039/C2CP43501B

Xinghui, W., Rahmat Agung, S., Yu, F., Leimeng, S., Qizhen, X., and Qing, Z. (2014). Vertically aligned CNT-supported thick Ge films as high-performance 3D anodes for lithium ion batteries. *Small* 10, 2826–2829. doi: 10.1002/smll.201400003

Xu, J., Liu, Y., He, L., Zhang, C., and Zhang, Y. (2016). Facile synthesis of CuO mesocrystal/MWCNT composites as anode materials for high areal capacity lithium ion batteries. *Ceram. Int.* 42, 12027–12032. doi: 10.1016/j.ceramint.2016.04.129

Xu, J. F., Ji, W., Shen, Z. X., Li, W. S., Tang, S. H., Ye, X. R., et al. (2015). Raman spectra of CuO nanocrystals. *J. Raman Spectrosc.* 30, 413–415. doi: 10.1002/(SICI)1097-4555(199905)30:5<413::AID-JRS387>3.0.CO;2-N

Xu, T., Lin, N., Cai, W., Yi, Z., Zhou, J., Han, Y., et al. (2018). Stabilizing Si/graphite composites with Cu and *in situ* synthesized carbon nanotubes for high-performance Li-ion battery anodes. *Inorgan. Chem. Front.* 5, 1463–1469. doi: 10.1039/C8QI00173A

Yan, C., Xu, T., Ma, C., Zang, J., Xu, J., Shi, Y., et al. (2019). Dendrite-free Li metal plating/stripping onto three-dimensional vertical-graphene@carbon-cloth host. *Front. Chem.* 7:714. doi: 10.3389/fchem.2019.00714

Yang, L. C., Gao, Q. S., Li, L., Tang, Y., and Wu, Y. P. (2010). Mesoporous germanium as anode material of high capacity and good cycling prepared by a mechanochemical reaction. *Electrochem. Commun.* 12, 418–421. doi: 10.1016/j.elecom.2010.01.008

Yang, Z., Bai, S., Yue, H., Li, X., Liu, D., Lin, S., et al. (2014). Germanium anode with lithiated-copper-oxide nanorods as an electronic-conductor for high-performance lithium-ion batteries. *Mater. Lett.* 136, 107–110. doi: 10.1016/j.matlet.2014.08.034

Yuan, F. W., Yang, H. J., and Tuan, H. Y. (2012). Alkanethiol-passivated ge nanowires as high-performance anode materials for lithium-ion batteries: the role of chemical surface functionalization. *ACS Nano* 6:9932. doi: 10.1021/nn303519g

Yunhua, X. U., Jian, G., Liu, Y., Zhu, Y., and ZACHARIAH, Michael, R., et al. (2014). Superior electrochemical performance and structure evolution of mesoporous Fe2O3 anodes for lithium-ion batteries. *Nano Energy* 3, 26–35. doi: 10.1016/j.nanoen.2013.10.003

Zhang, J., Yu, T., Chen, J., Liu, H., Su, D., Tang, Z., et al. (2018). Germanium-based complex derived porous GeO2 nanoparticles for building high performance Li-ion batteries. *Ceram. Int.* 44, 1127–1133. doi: 10.1016/j.ceramint.2017.10.069

Conflict of Interest: The authors declare that the research was conducted in the absence of any commercial or financial relationships that could be construed as a potential conflict of interest.

frontiers in Chemistry

ORIGINAL RESEARCH
published: 18 February 2020
doi: 10.3389/fchem.2020.00083

First-Principle Insights Into Molecular Design for High-Voltage Organic Electrode Materials for Mg Based Batteries

Johann Lüder[1]* *and Sergei Manzhos*[2]*

[1] Department of Materials and Optoelectronic Science, National Sun Yat-sen University, Kaohsiung City, Taiwan, [2] Centre Énergie Matériaux Télécommunications, Institut National de la Recherche Scientifique, Varennes, QC, Canada

Low cost, scalability, potentially high energy density, and sustainability make organic magnesium (ion) battery (OMB) technologies a promising alternative to other rechargeable metal-ion battery solutions such as secondary lithium ion batteries (LIB). However, most reported OMB cathode materials have limited performance due to, in particular, low voltages often smaller than 2 V vs. Mg^{2+}/Mg and/or low specific capacities compared to other competing battery technologies, e.g., LIB or sodium ion batteries. While the structural diversity of organic compounds and the large amount of possible chemical modifications potentially allow designing high voltage/capacity OMB electrode materials, the large search space requires efficient exploration of potential molecular-based electrode materials by rational design strategies on an atomistic scale. By means of density functional theory (DFT) calculations, we provide insights into possible strategies to increase the voltage by changes in electronic states via functionalization, by strain, and by coordination environment of Mg cations. A systematic analysis of these effects is performed on explanatory systems derived from selected prototypical building blocks: five- and six-membered rings with redox-active groups. We demonstrate that voltage increase by direct bandstructure modulation is limited, that strain on the molecular scale can in principle be used to modulate the voltage curve and that the coordination/chemical environment can play an important role to increase the voltage in OMB. We propose molecular structures that could provide voltages for Mg insertion in excess of 3 V.

Keywords: magnesium battery, ab initio modeling, organic cathode material, rational design, DFT, molecular design

OPEN ACCESS

Edited by:
Oleksandr Malyi,
University of Oslo, Norway

Reviewed by:
Dan Huang,
Guangxi University, China
Young-Kyu Han,
Dongguk University Seoul,
South Korea

***Correspondence:**
Johann Lüder
johann.lueder@mail.nsysu.edu.tw
Sergei Manzhos
sergei.manzhos@emt.inrs.ca

Specialty section:
This article was submitted to Electrochemistry, a section of the journal Frontiers in Chemistry

Received: *02 August 2019*
Accepted: *27 January 2020*
Published: *18 February 2020*

Citation:
Lüder J and Manzhos S (2020) First-Principle Insights Into Molecular Design for High-Voltage Organic Electrode Materials for Mg Based Batteries. Front. Chem. 8:83. doi: 10.3389/fchem.2020.00083

INTRODUCTION

The development of smart grids, renewable energy sources (Dunn et al., 2011) and electro-mobility (Lu et al., 2013) are just a few fields that demand improved electric energy storage technologies. New solutions, which meet the growing demands of scalability, better performance, and lower costs, should also be sustainable and non-toxic. Secondary metal ion battery technologies are at the forefront of current electrical energy storage research as they can provide high energy density, be used in mobile as well as stationary/large scale applications and could last thousands of charge-discharge

cycles (Hameer and van Niekerk, 2015). Metal ion batteries are increasingly used not only in mobile devices but also to palliate load-level balancing of solar- and wind power plants. To fully access the benefits of this type of technology, many aspects need to be improved such as slow ion diffusion kinetics limiting the rate performance or capacity and cyclability limitations as well as user and environmental safety (Goodenough, 2012).

Many open challenges are of course materials related; specifically, the active electrode material's interaction with metal-ions, e.g., lithium (Li) (Diouf and Pode, 2015), counter ions (Chen et al., 2018) or common electrolytes critically dictates the materials performance. Today, various types of active electrode materials (from here on referred to as electrode for brevity but to be distinguished from contact electrodes) are known that can be manufactured from various sources. Examples are layered structures (Kulish et al., 2014; Sun et al., 2016; Ortiz-Vitoriano et al., 2017), metal oxides (Liu et al., 2017), polymers (Nishide et al., 2004; Koshika et al., 2010; Muench et al., 2016), or metal-organic frameworks (Xue et al., 2016). Electrode materials can differ in their redox-active centers—like compounds with oxygen or sulfur atoms, or functional groups. Thus, the search for high-performance electrode materials extends over a huge search space of materials, and much effort was made and will continue to be necessary to explore it further to find new materials leading to improved battery performance (Mohtadi and Mizuno, 2014; Yabuuchi et al., 2014; Kim et al., 2015a; Wang et al., 2015; Muench et al., 2016; Mauger et al., 2017; Leisegang et al., 2019).

Organic electrode materials have gained much interest (Liang et al., 2012; Lee et al., 2018; Manzhos, 2019) as their production can be sustainable (Xu et al., 2008; Zeng et al., 2014), and non-expensive; they can be recyclable, non-toxic and have a low carbon footprint at the same time (Liang et al., 2012; Deng et al., 2013). They can rely on well-developed chemistries and industrial base. Indigo carmine is an example of a well-known organic material that can be used as an electrode (Yao et al., 2010). Moreover, organic materials are most suitable for sustainable energy storage technologies and do not defeat the purpose of renewable energy technologies (i.e., sustainability and scalability). For instance, load leveling of electric grids in which a fluctuating amount of excess energy from renewable energy sources must be stored and released. In addition, it was shown that by some measures (e.g., extremely high cycling rate) organic materials can outperform commercially available inorganic electrode materials (Koshika et al., 2009). Development of organic electrode materials for metal ion batteries has picked up momentum in recent years, both through experimental and theoretical studies (Stephan and Nahm, 2006; Bhatt and O'Dwyer, 2015; Chen and Manzhos, 2016a; Padhy et al., 2018; Tripathi et al., 2019) Moreover, many of their properties including redox activity can be tuned (Oltean et al., 2016; Chen et al., 2017) by molecular design allowing an excellent adaptability for particular technological fields. Remaining challenges to achieve better performance in e.g., capacity, voltage, power, rate capability, and cyclic stability might be solvable.

Among all secondary metal ion battery types, only Li ion batteries are widely used, for instance in commercially available lithium cobalt oxide based batteries due to their high energy density. However, lithium as a resource is very unevenly distributed and is relatively scarce, whereas many other metallic elements, which can be used for so-called post-lithium batteries, like sodium (Na), magnesium (Mg), or aluminum (Al) are abundant (Leisegang et al., 2019). Much research effort has therefore been directed to make use of alternative metal ions that could replace Li. Na ion is a suitable candidate for these batteries because Na is abundant, cheap and it has a similar valance shell structure as Li, i.e., one unpaired valence *s* electron (Ratnakumar et al., 1990; Wenzel et al., 2011; Lu et al., 2012; Slater et al., 2013). Often, sluggish kinetics, low voltage and low capacity limit the success of Na ion batteries. Moreover, the same inorganic host materials used in Li ion batteries may be unsuitable for reversible Na insertion. Well-known examples are graphite and silicon wherein lithiation but not sodiation can be achieved (Stevens and Dahn, 2001; Ge et al., 2012; Malyi et al., 2013). Nonetheless, organic and inorganic materials for Na ion electrodes were discovered that can outperform commercially available Li ion batteries in some key performance parameters (Zhao et al., 2016; Lee et al., 2018; Padhy et al., 2018).

Multivalent charge carriers like Mg^{2+} or Al^{3+} (Mohtadi and Mizuno, 2014; Leisegang et al., 2019) could theoretically double and triple the capacity per carrier of the active material compared to Li^{+} and Na^{+} as two (for Mg) or three (for Al) electrons would be transferred per active cation instead of the one electron from Li or Na. In particular, metallic Mg as anode material is interesting in this regard due to further benefits that are (i) being environmentally friendly, (ii) non-toxic, (iii) biodegradable and (iv) allowing for dendrite-free deposition (Gregory, 1990). For inorganic materials, examples for electrode materials for the storage of multivalent active cations are vanadium oxides or manganese oxide and Prussian blue analogs that work with several metal ions including Mg^{2+} (and others; Hayashi et al., 2004; Xu et al., 2015; Tojo et al., 2016; Kulish et al., 2017a,b; Koch and Manzhos, 2019). However, the larger charge on the ions leads to significant polarization and has negative effects on the kinetics/diffusion rate in inorganic solids (Kulish and Manzhos, 2017). Organic electrode materials could in principle achieve fast kinetics with multivalent cations compared to inorganic materials due to larger atomic spacing (Canepa et al., 2017) but it is still a challenging field of research. Few multivalent organic electrode materials with sufficiently high voltage for a cathode were reported, that are, e.g., quinones such as anthraquinones providing voltages of ca. 2 V as Mg ion battery cathodes (Sano et al., 2012; Zhao-Karger et al., 2013; Bitenc et al., 2015, 2016; Pan et al., 2016a,b). The low voltage is a key problem in multivalent batteries and is a direct consequence of multivalence: the average voltage V to achieve a given state of charge is

$$V = -\Delta G/ne, \tag{1}$$

where ΔG is the respective free energy change, e the electron charge and n the number of charges transferred per elementary reaction (i.e., $n = 2$ with Mg; Urban et al., 2016). That is to say, for a cathode, a very high ΔG (i.e., high Mg-host interaction energy) should be achieved while preserving stability of the electrode material and reversibility of Mg insertion. Many organic materials that are redox-active with Na or Li atoms such

as the well-studied carboxylates (Park et al., 2012; Renault et al., 2013; Sk and Manzhos, 2016) do not result in strong enough interaction that would allow using them in Mg ion batteries.

A systematic approach is required to understand and improve organic electrodes for multivalent Mg (ion) batteries. Rational design based on atomic insights from *ab initio* computations is critically important for this purpose and in particular to understand and systematically explore the connection between material properties, such as electronic structure, interlayer spacing and crystallinity, and the redox processes in materials (Miroshnikov et al., 2016; Seo et al., 2016; Araujo et al., 2017; Molaei et al., 2017). Different design approaches should be tested computationally for molecules and for solids to modulate the interaction strength with inserted metal ions and the voltage (Kulish et al., 2017a). For instance, *p*-doping, i.e., the creation of a "hole" state in the electronic structure in the vicinity of the valence band maximum (and below the lowest electronic conduction state) increases the binding strength of Li in aluminum doped silicon and of Li on boron-doped disodium terephthalate by ca. 1 and 2 eV, respectively (Legrain and Manzhos, 2015; Lüder et al., 2017a,b). Adding/replacing electron-withdrawing groups, e.g., F atoms or cyano (CN) groups, in a molecular structure can also increase the voltage by increasing the binding strength to the active cation (Chen and Manzhos, 2016c; Chen et al., 2018). Doping is only one way to affect the performance of batteries and it is particular in that it directly addresses the electronic structure of a material. Other modifications can aim to alter strain effects, the chemical surrounding, or a combination of them. In this work, we focus on materials that work by reduction, i.e., in materials in which the lowest unoccupied molecular orbital (LUMO) of the electrode determines the redox potential. For materials that work by oxidation, the HOMO (highest occupied molecular orbital) determines the voltage and effective strategies there can be different (Geniès et al., 1989; Chen and Manzhos, 2016c; Rodriguez-Pérez et al., 2016; Chen et al., 2018).

In this study, we explore conceptual solutions for high voltage organic molecule based Mg (ion) electrode materials operating by reduction using Density Functional Theory (DFT) calculations. We organize the paper as follows: firstly, we explore conceptually the limitations of the approach of increasing the voltage in organic Mg-ion batteries working by reduction only by direct electronic effects. We show that this mechanism has substantial limitations on achievable voltages and possibly leads to unwanted side reactions. With the help of small organic molecules consisting of five- and six-membered rings with redox-active carbonyl groups that we employ as model systems, we show the extent to which expected voltage can be modulated by design of electronic structure such as the use of substitutional doping (Lüder et al., 2017a,b). We study how much the electronic effects can be separated from others for these systems. Secondly, the influence of strain (linear, rotational (bending) and dihedral strain) on the expected voltage with a molecule is elucidated (Chen and Manzhos, 2016b). Because of the limitations of design by the modulation of the electronic states, strain design and the effective use of it to increase the interaction strength to metal ions can potentially further contribute to increase in voltage. Third, we discuss a new design aspect that addresses the arrangement of the coordination centers such as ring linking and fusion to design cation environments with high redox potentials.

METHODS

The Gaussian (Frisch et al., 2016) package was used to perform DFT (Hohenberg and Kohn, 1964; Kohn and Sham, 1965) calculations. The B3LYP functional (Becke, 1993) and the 6–31+G(d,p) basis set were used on all atoms. This basis set provides sufficiently accurate energies for the attachment of alkali atoms on organic molecules due to the inclusion of diffuse and polarized functions.

The formation energy per metal atom of m ($m = 1, 2, 3, \ldots$) metal atoms (e.g., Mg) and one molecular complex was computed from the total energy of m metal atoms attached to the complex at their fully relaxed geometry (E_r^{mol+M}) and the total energies of m isolated metal atoms (E^M) and the isolated and relaxed molecule (E_r^{mol}).

$$E_{ad} = \left(E_r^{mol+M} - E_r^{mol} - m\,E^M\right) / m \tag{2}$$

From the formation energy, the voltage V vs. Mg^{2+}/Mg can be estimated according to Ceder et al. (1997) and Urban et al. (2016)

$$V = -\frac{\left(E_{ad} - E_{coh}^M\right)}{en} \tag{3}$$

which relates the formation energy of the Mg-molecule complex to the cohesive energy of the metal E_{coh}^M in its bulk phase. For Mg E_{coh}^M is taken from the literature as 1.51 eV (Kaxiras, 2003; Kittel, 2005), and the charge (en) transferred in the redox process with n being the number of electron charges per cation is taken as two e^- for Mg. This method of estimating the voltage approximates the Gibb's free energy (Equation 1) by neglecting entropy contributions as well as effects from vibrations. Nonetheless, the approach based on electronic energies computed by DFT to compute voltages has been successfully used before (Urban et al., 2016). It can also be used for molecular systems with accurate reproduction of experimental voltages with models of molecular solids, while in isolated molecular models the neglect of environmental effects causes an underestimation of the absolute values of the voltage on the order of 1 V but allows reliable comparative calculations between different molecular structures (Sk and Manzhos, 2016; Chen et al., 2017; Manzhos, 2019). This is also the approach used here—we use molecular calculations to compare the effect of molecular building blocks on the strength of interaction with Mg atoms and on voltage vs. Mg^{2+}/Mg.

The binding strength of a Mg atom to the electrode material should exceed the cohesive energy of metallic Mg, or else the so-called plating will occur. When the binding energy is equal to the cohesive energy, the equivalent voltage based on Equation (3) would be 0 V. When there is no binding between the molecule and the Mg atom the theoretical voltage based on Equation (3) is

formally −0.755 V and is negative as long as the binding strength is weaker than E_{coh}^{M} of metal *M*. Negative voltage would of course not be observed experimentally but will be used in what follows for formal comparison between molecules. Also, as single-molecule models underestimate the voltage, molecular systems with formally negative voltages might be of practical interest.

The linear (achieved through elongation of bond lengths, e.g., between Mg and the redox-active parts or intramolecular bonds), rotational (caused by bending) and dihedral (i.e., through changes in dihedral angles) strain energy E_s of a molecule, that is caused by the attachment of the Mg atoms or structural deformations induced otherwise, is computed as the energy difference between the molecular structure it assumes when the metal atom is attached (but single point calculations are done without the metal atom) or the deformation is applied (E_f^{mol}) and the isolated fully relaxed molecule or the molecule before the deformation (E_r^{mol})

$$E_s = E_f^{mol} - E_r^{mol} \tag{4}$$

Linear strain is created by pulling a molecular complex apart along a chosen direction. The relaxation of the structure is performed on all but a minimal set of frozen atoms to control the strain direction. Bending strain generated by pushing a set of atoms within a molecular complex closer to each other and keeping their coordinates fixed during structural relaxation while all other atoms fully relax. Dihedral strain is set by freezing the coordinates of atoms fixed during structural relaxation that define a dihedral angle between connected rings. In this study, all deformations that lead to strain other than by Mg attachment are achieved by keeping atomic coordinates fixed during structural relaxations.

RESULTS AND DISCUSSION

Limits of Electronic Effects for Voltage Increase in Organic Mg (Ion) Electrode Materials

It was shown in several studies that the energies of the LUMO significantly correlate to the voltage achieved with materials operating by reduction as the electron from the attached alkali atom, e.g., Li, will occupy the LUMO of the molecule (Burkhardt et al., 2013; Liang et al., 2013; Kim et al., 2015b, 2016; Lüder et al., 2017a). Specifically, a stabilization of the LUMO energy of comparable systems, for instance by substitutional doping, show strong correlations to voltage increase. When one uses in this model the LUMO energy before molecular reduction, we address this model as static. However, the precise value of the voltage increase will depend on several factors due to structural and electronic relaxations during the redox reaction. For Li-ion electrode materials, the energy difference between the energy (eigenvalue) ε_{Li2s} of the 2*s* level in Li (or the Fermi level in the metallic anode if it is used as a reference) and the LUMO of the molecule will lead to a gain in total energy (and free energy) that will drive the reaction and largely determine the voltage, see Equation (1). According to this model, any change in the LUMO energy will affect the voltage, i.e., a lower LUMO will lead to a larger voltage. In our previous studies (Lüder et al., 2017a,b; Chen et al., 2019), we showed that substitutional *p*-doping can be used to lower the LUMO of a molecule. The LUMO shifts to a lower energy and therefore the energy gained in the redox reaction is increased, which was observed for different prototypical organic Li- and Na-ion electrode materials.

The same mechanism can be explored for Mg atom in which the role of the HOMO energy level of the Mg atom (ε_{Mg3s}) and the electronic structure of the tested molecules are evaluated. In **Figure 1A**, the theoretical voltage computed for the attachment of one Mg atom is plotted vs. LUMO energy for a large number of tested molecular structures. The structures are shown in the Supplementary Material in **Figures S1–S5**. One observes that there is indeed a correlation, albeit somewhat loose, between the voltage and the LUMO. We highlighted different areas in **Figure 1A**. The areas are obtained by a *k*-means cluster finding algorithm on the data. The separation in three groups is based on the assumption that the tested molecules can be separated into non-working, low voltage and high voltage electrode materials. The algorithm employed the HOMO and LUMO energies, as shown in **Figure 1B** together with the HOMO-LUMO gap (black points) as features. The three areas can be roughly distinguished as molecules with higher voltages that do correlate well to very low LUMO energies (blue area, "deep LUMO"), molecules with high LUMO energies and formally negative voltage (i.e., unsuitable as active electrode materials, green area), and molecules with moderately high LUMO energies (magenta). In **Figure 1A**, the scatter of voltage-LUMO data is not surprising as there are other factors than bandstructure energy (we will liberally use "bandstructure" as set language even when talking about molecules).

The red curve in **Figure 1A** shows the linear regression of the LUMO-voltage data. The curve shows the well-known correlation between decreasing the LUMO energy and increasing the voltage, which is frequently observed for Li- and Na-ion electrode materials (organic and inorganic). Here we see that such correlation also largely holds for Mg attachment as well. It should be noted that the LUMO energies refer to the values of the single molecule without metal atom attached. The curve shows that a LUMO energy of <-3 eV is needed for a working anode as implied in Equation (3). Furthermore, the curve also reveals that for high voltage electrodes (more than 2 V) a LUMO energy of <-8 eV would be required from this mechanism.

The simplified picture above is based on the frozen state approximation. Relaxation effects could be significant. To account for the energy level relaxation, the energy level of the molecular LUMO, which becomes occupied by the valence electrons of the metal atom, may shift to lower energies. This process was observed, for instance, for the boron-doped coronene molecule under Li and Na attachment (Lüder et al., 2017b). Here, we include the LUMO relaxation effect after reduction and assume that the shifted LUMO will not decrease to energies below the HOMO energy. Thus, the change of free energy based on the electron transfer from metal to an

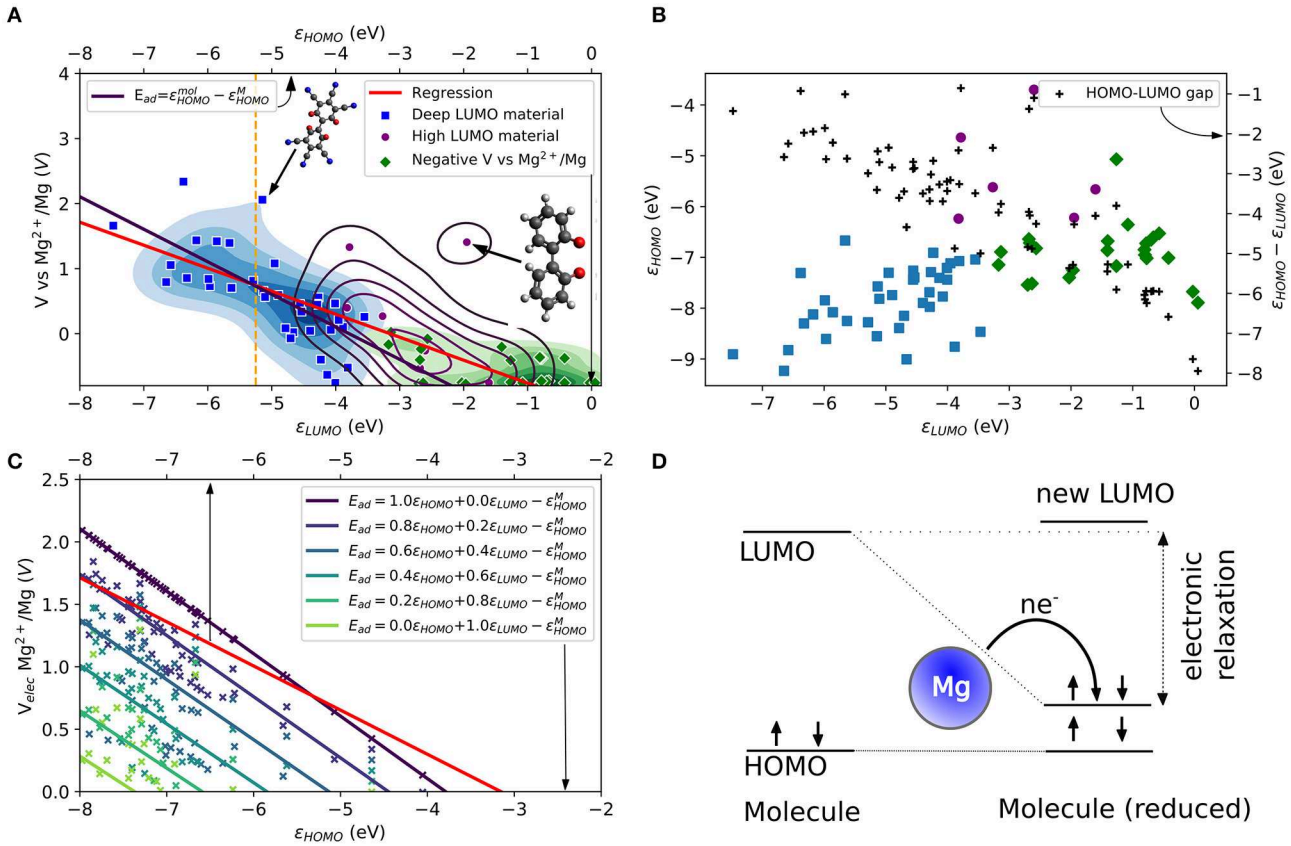

FIGURE 1 | (A) Computed LUMO eigenvalues and theoretical voltages vs. Mg^{2+}/Mg for a set of small organic molecules. The molecules are categorized into three groups (blue, purple and green areas and data points) by a k-means algorithm. A linear regression (red curve) is compared to an electronic approximation (black curve) to Equation (2). The top axis refers to a comparison based on the electronic effects assuming a LUMO relaxation reaching HOMO values. **(B)** Comparison of the relation between HOMO and LUMO eigenvalues, and HOMO-LUMO gaps for the three categories in the dataset. **(C)** Comparison of the linear regression (red curve) from (a) different LUMO relaxation values in the electronic approximation to Equation (2). **(D)** Schematic of the LUMO relaxation process during the redox reaction. For a Mg atom, two electrons are transferred (i.e., $n = 2$). Arrows indicate electrons with spin-up and spin-down. Color code is H (white), C (gray), N, (blue), O (red), F (light blue), Mg (yellow), and S (dark yellow) here and below.

organic electrode (which is the net effect, even though the electrons transfer through the external circuit) can increase by the electronic relaxation of the LUMO energy during the redox reaction. Of course, the most significant change is achieved when the LUMO energy relaxes to values close to the HOMO energy. This effect becomes less significant for the redox process with decreasing LUMO energy level as displayed in **Figure 1B** due to the decrease of the HOMO-LUMO gap (black dots, right axis) or reduced relaxation. The figure also shows the three different types of materials determined by the *k*-means classification, which are distinguishable by their HOMO and LUMO.

Figure 1C compares the regression of the computed data with the extended electronic model (i.e., including LUMO energy relaxations) illustrated in **Figure 1D** at different amounts of state relaxations. The free energy that enters the computation of the voltage [or the E_{ad} of Equation (3)] is replaced by a weighted energy difference between HOMO and LUMO energy of the molecule and the HOMO energy of the Mg atom (−5.3 eV). It reads

$$E_{ad} = a\,\varepsilon^{mol}_{HOMO} + b\,\varepsilon^{mol}_{LUMO} - \varepsilon^{Mg}_{HOMO} \tag{5}$$

in which the weight factors satisfy $a + b = 1$. The sets of data points (indicated by different coloring) correspond to different weighting factors of the computed data shown in **Figures 1A,B** and the solid lines to their resulting linear regressions. The values of HOMO and LUMO energies are regarded in this model as a key determining factor of E_{ad} and therefore give the limits of the electronic model. This model results in two extreme cases for the computed voltage that can be compared to the computed data. However, it must be noted that the calculated data (Equation 3) use the total energy changes obtained by DFT, while the estimates of the model are based on eigenvalue changes. Their sole purpose is to elucidate possibilities and limitations of voltage modulation by electronic effects. It is a measure of the gain in energy solely due to bandstructure (equivalent to a charge transfer in frozen orbitals), while the computed voltage

data include further relaxation channels (e.g., charge distribution, transfer, bond length changes) that affect the change in free energy, too. The energy of the LUMO defines one electronic limit (light green curve). The corresponding curve in **Figure 1C** is far below the linear regression of the computed data (red curve). For this case, working voltages ($V > 0$) require HOMO energies of <-7 eV because the redox process will not benefit from any LUMO relaxation in the static case. With increasing electronic relaxation, i.e., the LUMO after reduction approaching values closer the HOMO energy, the curve approaches voltages close to 2 V. The other limit (black curve) is yielded by the HOMO energy, i.e., electronic relaxation where the occupation of LUMO makes its energy approach the HOMO. The resulting curve intersects with the regression curve of the computed data at ca. −5.5 eV while it overestimates voltages below and underestimates voltages above this energy. The same curve is overlaid in **Figure 1A** as black curve and it can be regarded as the electronic limit. From the figure, it becomes clear that the LUMO must be very deep to result in a positive voltage. In this model, the LUMO must be lower than ca. −8 eV to achieve voltages larger than 2 V.

Besides the apparent 2 V limit by electronic structure design, two more observations should be mentioned: First, neither the extended electronic model nor the static model offers a solution to the intrinsic limitation of electronic structure design for Mg electrode materials. Instead, they can be understood as different mechanisms (or point of views) in the redox process governed by electronic effects. While the static model requires a low LUMO for high voltages, this can also be achieved with a high LUMO material but with sufficient relaxation effects (requiring a low energy of HOMO). Second, while the electronic limit based on the HOMO energy appears similar to the regression curve based on the computed data, the actual LUMO relaxation does not reach energies close to the HOMO of the molecule before reduction. Thus, the electronic model is compensating for other effects that appear simultaneously, as mentioned above.

As a reference of realistic and technologically relevant materials operating by reduction, we consider the LUMO energies of tetracyanoethylene (TCNE) which is known for its electron-accepting property, i.e., a very low LUMO energy in a stable molecule associated with a large absolute electron affinity (Pearson, 1986). The LUMO energy of TCNE is shown as vertical dashed orange line at −5.25 eV (Chen and Manzhos, 2016b) in **Figure 1A**. A lower LUMO would in principle results in stronger reduction activity. Besides the difficulties of designed materials with extremely low LUMO energies, such materials would be extremely unstable. Even as packing effects in a solid state are expected to result in a somewhat higher voltage than computed from a single-molecule model (Manzhos, 2019), this clearly shows the severe limitation of the strategy of LUMO design in the case of Mg ion batteries even as it served well organic material design for Li and Na ion batteries.

Electrodes in organic Mg and Mg-ion batteries often use carbonyl groups, which create the danger of parasitic MgO formation. The formation energy of MgO of 3.07 eV implies an equivalent of about 0.75 V vs. a metallic Mg anode. This estimate gives a target for the minimal voltage that a molecule should achieve to avoid loss of capacity because of redox reactions resulting in voltages above these values, the formation of MgO could be avoided.

Figure 1 contains data for several classes of small organic molecules with a ring structure, including benzene, 1,4-benzoquinone, biphenyl and biphenylene. They include the unmodified molecules, and, e.g., carbonyl, CN- and F-functionalized derivatives; details can be seen in SI. These functional substituents are known as electron-withdrawing groups. Thus, any substitution in benzene, benzene-based molecules or similar ring structures is expected to result in an electro-positive part (e.g., C atoms) and a more electro-negative part (i.e., the functional groups). Besides the redistribution of electronic charge, stabilizing effect on HOMO and / or LUMO energy and therefore changes in the interaction strength between a metal cation and the redox-active molecule can be anticipated, potentially with an increase in voltage. This was observed before, as mentioned earlier, in organic Li- and Na-ion electrode materials. However, the CN/F-functionalized benzene results cannot confirm this for organic Mg (and in principle Mg-ion) electrode as it did not significantly increase the interaction with Mg. In addition, we also investigated other halogen functionalization of benzene (e.g., Cl and Br). Our results indicate that electronic effects achieved by functionalization of materials can lead to small modulations of the voltage if a sufficient number of redox-active groups such as carbonyls are present.

On the other hand, a careful inspection of the data shown in **Figure 1A** reveals a few exceptional prototypical molecules (indicated by arrows and given molecular structures of biphenyl derived molecules). These molecules have (i) a LUMO energy higher than the one of TCNE and are therefore expected to be stable and (ii) their computed voltages are far above the regression curve and even beyond the electronic limit indicating that other processes in these molecules occur that strongly benefit the redox mechanism. Identifying the mechanism behind a higher computed voltage in these molecules and deriving molecule design strategies based on them will be discussed in the following.

Effect of Structural Modifications Leading to Strain

Reversible structural modifications can influence the total energy of a molecule as well as electronic states. HOMO, LUMO energies and the HOMO-LUMO gap can be modulated by strain. Both, changes in the total energy and that of individual electronic states can in principle lead to changes in the interaction strength between molecules and Mg atom(s). Thus, it will affect the voltage according to Equations (1–3). However, the direct application of this idea for molecular-based electrode design and practical applications in batteries is not frequently explored.

To efficiently modify voltage curves, the changes of the total energy must mainly affect the mentioned interaction between the metal atom and the molecule while the intra-molecular changes and their associated energies are small, or vice versa. When the structural modifications induce total energy changes of similar size and same direction (that means endo- or exothermic), the

resulting energy difference in the redox mechanism will cancel out according to Equation (1).

We distinguish between three principal structural changes: linear stretch, bending of the molecular plane, and dihedral rotation. For these three strain designs, we discuss prototypical systems.

Linear Strain

Here we study a system of a Mg atom coordinated to two molecules by two carbonyl groups, to account for the transfer of two electrons (one to each group). In a system of linear geometry in which two molecules with a carbonyl group surround a Mg atom, one way to introduce linear strain is by pulling either one of the molecules or both molecules simultaneously away from the Mg atom. Linear strain can also be introduced by elongating the bonds within a molecule. However, our investigation showed that for the latter case, effects on the LUMO or HOMO energy position are minor, and the binding strength to Mg atoms is barely affected. Moreover, the strong covalent bonds within organic molecule prevent a significant elongation by forces with technologically relevant magnitude. Thus, we focus on the approach of changing intermolecular geometry, i.e., the Mg-O bonds.

The chosen molecular complex that is used to investigate the effects of linear strain on voltage modulation is shown in **Figure 2**. We select a ring-fused linear molecule consisting of five six-membered rings. The molecule was laterally functionalized with two carbonyl groups with a distance between them of ca 9.8 Å, i.e., forming a pentacenedione (PAD) isomer. To systematically investigate the effect of linear strain on voltage modulation at the molecular scale and to provide technologically relevant insights, constraint geometry optimizations are required imposing constraints on and offering control of degrees of freedom. We restrict our analysis to a planar configuration of two PADs. This allows us to directly probe the correlation between atomic geometry, electronic effects, and the applied strain. **Figure 2A** shows the equilibrium structure of this (planar) configuration of the complex formed by a Mg atom and two 4,8-pentacendione molecules. We formed a series of geometries (of which three selected cases are shown in **Figure 2B**) in which the intramolecular degrees of freedom are relaxed, and the molecules are made slide in parallel to and past each other in the same plane. The initial structure in **Figure 2B** has the same Mg-O bond lengths as in the equilibrium structure. The middle figure of this panel shows the strained structure at an intermediate strain stage. The right panel of **Figure 2B** shows the most strained structure with a displacement of ca 12 Å and an O-Mg-O bond which is again similar to the one of the initial structures.

Figure 2C shows (top panel) changes in the binding strength of the configuration with the strongest binding, and changes in the total energy of the structure with and without the Mg atom (middle panel); binding distances to and Mulliken charges of the Mg atom (bottom panel); HOMO and LUMO eigenvalues of the Mg-complex and the complex without Mg atom. At the geometry with the largest strain energy shown in the middle of **Figure 2B**, there is a significant decrease in binding strength, up to 3.5 eV. The decrease in binding strength translates into a voltage reduction of 1.75 V. At this stage, one Mg-O distance increases to 6 Å, which is too long for any covalent bond, see middle panel of **Figure 2C**. Hence, the complex has lost one of the two bonds while the other Mg-O distance remains at a typical value for strong bonds of ca. 1.9 Å. In addition, the electron

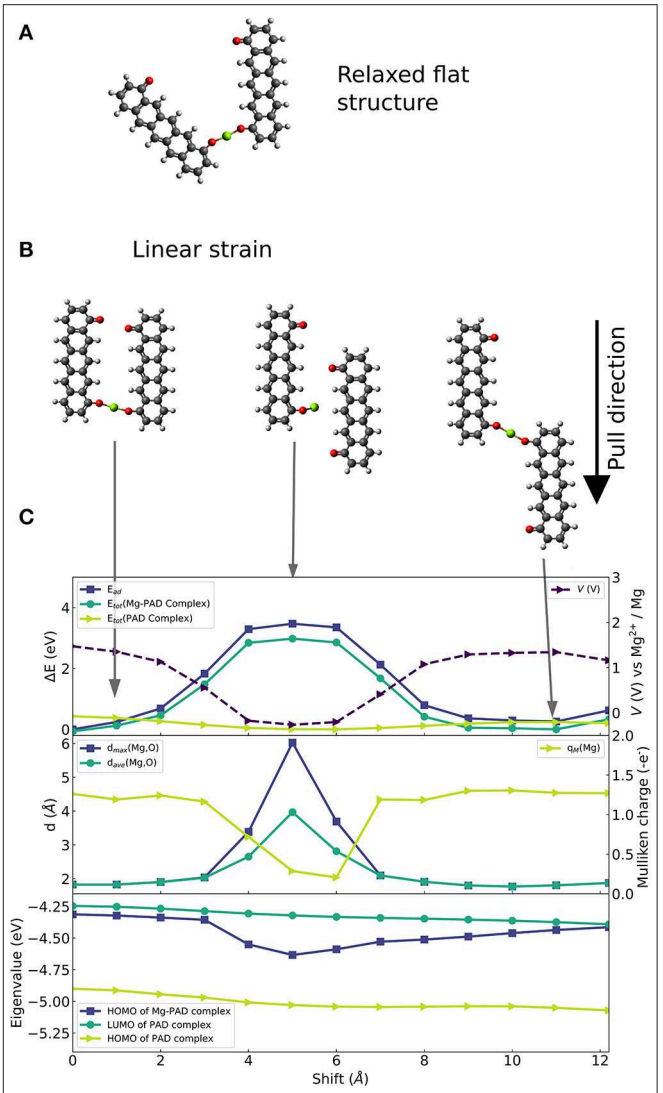

FIGURE 2 | Constrainted calculation on 6-membered ring-fused PAD structure with two carbonyl groups per molecule. **(A)** Optimized geometry of the planar system. **(B)** Selection of strained configurations in which one of the PAD molecules is parallelly shifted with respect to the other molecule: (left) Initial structure with parallel alignment of the PAD molecules shown in **(A)**, (middle) configuration with the highest strain energy equivalent, (right) configuration with final shift with a similar O-Mg-O bond as in initial structure. **(C)** Overview of electronic changes and properties during the shift: (top) Change of reaction energy (left axis) of Mg insertion (dark blue, square), change of energy of the complexes with (green, circle) and without Mg atom (light green, triangle), as well as computed voltage during parallel shift (right axis, dashed curve). (Middle) Maximal (blue, squares) and average distance (green, circles) between nearest two O atoms and the Mg atom; Mulliken charge on the Mg atom (light green curve) is given on the right axes. (Bottom) Eigenvalues of HOMO before and after Mg attachment (light green and blue, respectively) and eigenvalues of LUMO before Mg attachment (green).

charge transfer from Mg to the organic part of the molecule is reduced, which is seen in a drop of Mulliken charge on Mg to almost 0. Then, the decrease of binding strength can be explained by the loss of a Mg-O bond.

In contrast, the average and maximal distance of Mg-O are <2 Å (that is for average and max.) for maximal binding strength, and the Mulliken charge on Mg is ca. $+1.3\ |e|$ which corresponds to transfer of two electrons. Besides, the electronic structure (HOMO and LUMO) of the complex without the Mg atom (green curves in the lower panel of **Figure 2C**) is only slightly affected by strain. The LUMO relaxation effect is given by the energy difference between the LUMO energy of the molecular complex before Mg insertion (dark turquoise curve) and HOMO energy of the Mg-molecule complex (blue curve). It is very interesting that this relaxation effect shows a significant increase that correlates with the strain dependent weakening of the binding strength. This suggests that both effects, one being a charge transfer and bond release driven—the other being an electronic effect, act in the presented case in opposite directions.

At the final stage of the applied strain, the average and maximal Mg-O distance, Mulliken charge and binding strength reach values similar to the ones given at the initial stage indicating possible reversibility. Moreover, they imply that a key factor to efficiently design molecular systems, that can employ strain-based voltage modulation, is the ability to control the distance between Mg and the redox-active groups, and the number of formed Mg-O bonds. This suggests that the design of coordination of Mg to several redox-active groups is important; we will address this issue in the section Design of Coordination Environment of Mg Cations. However, the seen strain effects mainly reduce the voltage. Thus, the charging voltage of an organic electrode material can be reduced by applying linear deformation assuming the microstructure of the material supports this reversibly.

The results of the linear strain are in agreement with basic chemistry: at large distances no bonds are formed while at shorter distances the hybridization of states causes the formation of bonds (and consequent charge transfer leading to more ionic interactions). It should be noted that there is no strong correlation between the changes of the LUMO of the molecule only complex, and that changes in V are almost binary to situations when Mg binds to one and to two redox centers—preferring two redox centers. For situations in which several redox centers surround the Mg ion—such as in a solid, a large molecule or several molecules—controlling the distances and amount of redox active centers binding to Mg may provide a way to increase voltages.

Bending Strain

We analyze the effect of bending in molecular complexes in which Mg binds to two neighboring molecules. Similarly to the linear strain section, constrained geometry optimizations were performed to investigate the effects of a bent molecular structure on the binding strength between organic electrode materials and the inserted Mg atom.

We chose the 1,2-benzoquinone (BQE), 2,3-naphthalenedione (NPH) and 2,3-anthracenedione (ACD), which are molecules similar to PAD but with a reduced number of fused six-membered rings. BQE, NPH and ACD have one, two and three fused 6-membered rings, respectively. In each initial structure of the molecular complexes, two identical molecules from a linear complex with a Mg atom at its center. A planar configuration was imposed by symmetry during relaxation to simplify the evaluation of the bending effect (the NPH and ACD complexes have dihedral angles different from 0° at their lowest energy configurations). The complexes in their fully relaxed planar form are shown in **Figure 3A**. The bending was initialized by decreasing the distance d between the outer most carbon atoms (called the edge of the molecule) in steps of 1 Å until a distance of ca. 4 Å was reached. Four different bending stages of Mg-di-NPH are shown **Figure 3B** in which curved arrows indicate the bending direction. An example of a final bending configuration is shown in **Figure 3C** for the ACD Mg complex with almost parallel molecular parts.

Figure 3D shows the increase in strain energy (E_s) when the Mg complexes are forced into a bent structure. All other atoms but those at the edges are allowed to fully relax including the bonds between the Mg atom and the carbonyl groups. Thus, any effect leading to a weakening of this bond (i.e., an increase of E_s or a decrease of E_{ad}) is expected to be accurately represented. After a steep increase at the beginning, the bending curves for the three studied complexes yield similar values of 0.8 to 1.2 eV (corresponding to a voltage decrease of ca. 0.5 V vs. Mg^{2+}/Mg) when the two molecules reach almost parallel alignments (at a distance of ca. 4 Å), shown in **Figure 3D**, left panel. This indicates that the bending strain is not (strongly) depending on the size of the molecule but depends on the bond angle formed between O-Mg-O, shown in **Figure 3D**, right panel.

Dihedral Strain

The effect of changing a dihedral angle in a molecular structure on the interaction strength between Mg and an organic molecule can be tested similarly to the effect of bending. However, single fused-ring molecules like biphenylene or naphthalene exhibit strong restoring forces when the molecular structures are twisted. Neither electronic nor structural changes were found to be large enough under this deformation to result in significant voltage changes for these molecules. Thus, we focus on molecular prototypes like biphenyl-derived systems (as seen in the section Limits of Electronic Effects for Voltage Increase in Organic Mg (Ion) Electrode Materials) with a bond between ring structures that can act as a rotational axis. Although biphenyl is known for its sterically hindered full dihedral rotation of the two phenyl rings, we expect to see a rather low energy increase for a wide range of dihedral angles. The mentioned bond on which the dihedral rotation is performed is referred to as the rotation axis and the change of dihedral angle as $\Delta\gamma$.

Two carbonyl groups were introduced into the biphenyl molecule ($C_{12}H_8O_2$, referred to in the following as BipO2) shown in **Figure 4A**. The carbonyl groups are on opposite phenyl rings. For this molecule, two principal configurations of the molecule are possible—one with the two carbonyl groups close to each

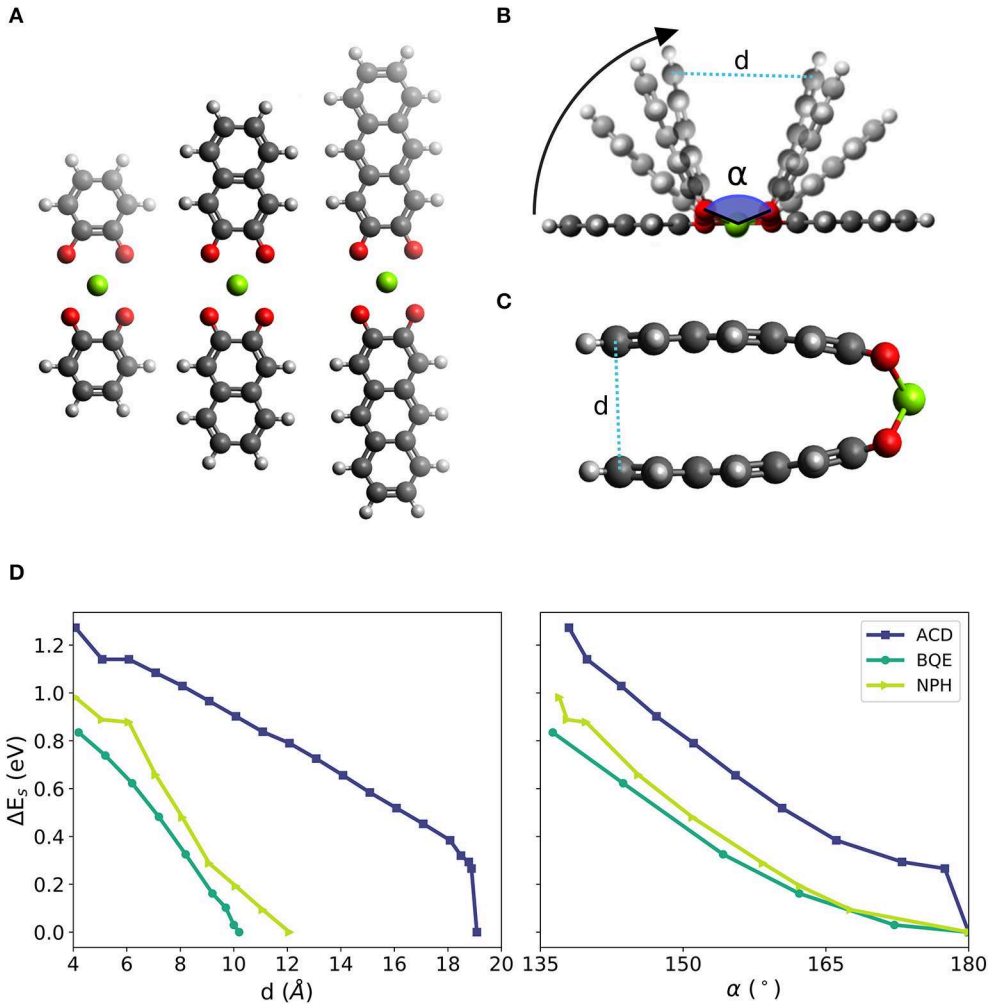

FIGURE 3 | (A) Linear configurations of two prototypical molecules of different size (from left to right: one, two and three fused benzene-like rings, i.e., complexes based 1,2-benzoquinone (BQE), 2,3-naphthalenedione (NPH) and 2,3-anthracenedione (ACD), respectively) with two neighbored carbonyl groups of each molecule surrounding one Mg atom. **(B)** Schematic of the bending simulations with bending angle α defined by the O-Mg-O bonds across the two organic molecules in the structure and distance d between the outer parts of the complex. **(C)** Example of final bending configuration of the NPH complex with almost parallel molecular planes of the two ACD molecules in the complex. **(D)** Change of strain energy during bending as function of distance d (left) and as function of the bending angle α (right).

other (as shown in the figure) and the other with them far from each other. This is obtainable by a dihedral rotation. The larger separation of the carbonyl groups is energetically preferred by 0.3 eV. Bond lengths between atoms defining the dihedral rotation are taken at the relaxed molecular geometry and are kept constant when calculating the voltages for different dihedral angles. Similarly to the linear strain case, this degree of freedom allows us to manipulate the (binding) distances between carbonyl groups and a Mg atom.

The constrained calculations were performed with two reference structures to estimate the influence of initial conditions on the computed voltage changes. One structure represents the charged and the other the discharged state of the material. The discharged state is given by BipO2 with an attached Mg atom, i.e., $Mg(C_{12}H_8O_2)$—referred to as MgBipO2. The charged state is given by BipO2, using the close-carbonyl group configuration because this is the configuration assumed by the molecule directly after the detachment of the Mg atom. The effect of Mg attachment, i.e., discharging, results in differences in the structure of the organic part of the molecule, which is most noticeable in the bond length and the dihedral angle between the phenyl-like rings. For the charged state (i.e., BipO2 without Mg) shown in **Figure 4A**, the bond length between the phenyl rings is 1.39 Å and has a dihedral angle of 30° while for the discharged system (MgBipO2) shown in **Figure 4B**, the bond length and dihedral angle increase to 1.51 Å and 71°, respectively. The impact on the computed properties with the different initial configurations in the constrained optimization is analyzed in **Figures 4C–F**. In these figures, we also compare the effect of keeping all atomic positions of the molecular structure fixed (i.e., only the position

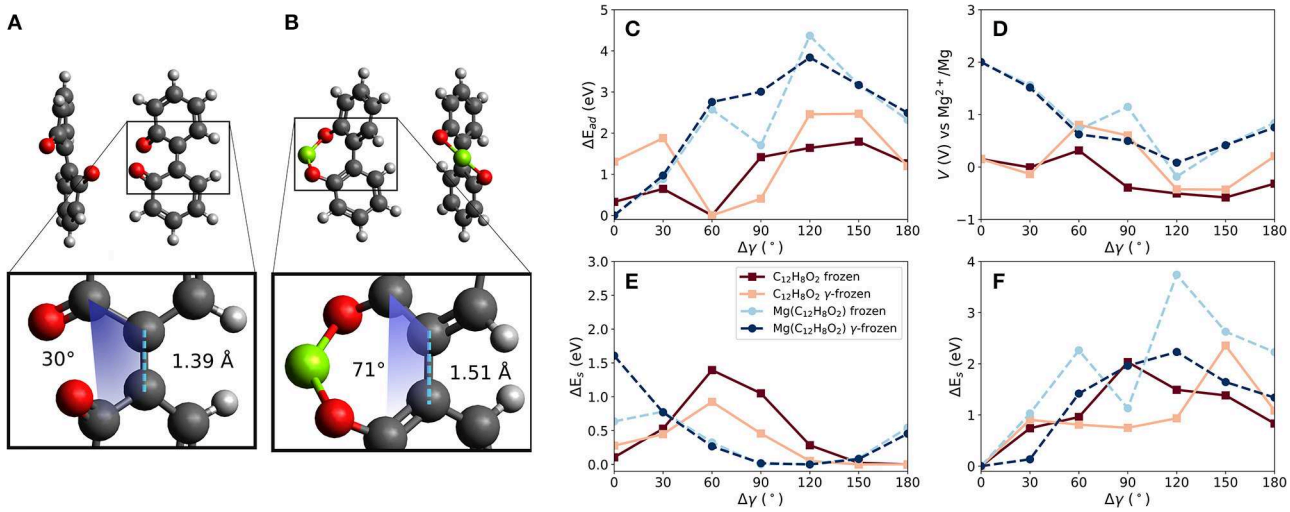

FIGURE 4 | Effects of dihedral angle change in a biphenyl-like molecule with two carbonyl groups (BipO2) at connected phenyl-like rings. Differences in bond lengths between phenyl-like rings and dihedral angle γ in **(A)** BipO2 after Mg detachment and **(B)** MgBipO2, i.e., BipO2 with one attached Mg atom. **(C)** Change of interaction strength between Mg and the molecule for frozen and partly frozen, i.e., γ-frozen, relaxations based on the optimized BipO2 structure, as shown in **(A)**, red curves, and based on MgBipO2, as shown in **(B)**, blue curves. The computed voltages are shown in **(D)**. The strain energies given in **(E)** and **(F)** are computed without and with one attached Mg atom, respectively.

of the Mg atom is optimized—labeled as "frozen") to the frozen dihedral angle calculation (i.e., all atomic positions but the ones defining the dihedral angle are allowed to relax during the structure optimization—labeled as "γ-frozen").

Figure 4C compares the change of interaction energy (E_{ad}) and **Figure 4D** shows the computed voltage vs. Mg^{2+}/Mg for both of the reference structures, i.e., BipO2 and MgBipO2. The dihedral angle change of the configuration with strongest binding differs by around 60° between the BipO2 and MgBipO2 references. This is a consequence of the dihedral angle increase under Mg attachment.

For the MgBipO2 reference system, the binding energy between the Mg atom and the BipO2 molecule is −5.5 eV when fully relaxed (i.e., $MgC_{12}H_8O_2$), corresponding to a voltage of 2.0 V vs. Mg^{+2}/Mg. Under dihedral rotation, the binding energy reduces to −1.1 and −1.7 eV (an energy decrease of 4.4 eV and 3.8 eV) for the frozen and γ-frozen optimization leading to a voltage of −0.2 and 0.1 V vs. Mg^{2+}/Mg (i.e., changes of 2.2 and 1.9 V), respectively. Both maxima are at a dihedral angle change of ca. 120°, which yields an almost flat geometry. The steric hindrance in the latter configuration is present in the molecular structure with and without the attached Mg atom. The binding energy weakening and voltage decrease is then a consequence of the removal of one of the Mg-O bonds. The loss of one bond (or reduction of bond order) also results in a reduced charge transfer. This is supported by the binding energy and voltage computed at $\Delta\gamma$ of 180°. In this configuration, the carbonyl groups have a large distance from each other, and a Mg atom can only bind to one of them. The binding weakens by ca. 3 eV and the voltage takes a value of 0.8 V—values similar to the ones seen with the bond release mechanism in linear strain applied to PAD (see above) indicating that these values are somewhat characteristic of a single Mg-O bond in these molecules and the voltage reduction is caused by the loss of a Mg-O bond.

Similar changes but of smaller magnitude are seen in the BipO2 reference calculations. The curves are shifted by around 60°, which follows the change of the dihedral angle under Mg attachment during full optimization. The strongest interaction between the Mg atom and the BipO2 reference molecule yields a binding energy of −3.3 (−2.1) eV corresponding to a voltage of 0.9 (0.2) V vs. Mg^{2+}/Mg for the γ-frozen (frozen) optimization. Dihedral rotation changes these values by 2.6 (1.8) eV setting the lower estimate of the voltage change to 1.3 (0.9) V. This is given at 60° for the frozen and γ-frozen BipO2 reference. The voltages reach their maximum because this configuration is most similar to the fully optimized structure of MgBipO2. Interestingly, the voltage curve is changing sign for both cases, frozen and γ-frozen constrained geometry calculations. In principle, this could indicate a polarity change of direct current. Then, the charging cycle could be replaced by a mechanical formation. However, the calculation misses to account for any aggregate state contribution to the voltage which is in the order of 1 V. This may shift the voltage curve above the point of polarity change. Nevertheless, the principle should be transferable to other materials. Depending on the onset of the voltage-capacity curve, the strain induced polarity change may be applicable to low-voltage electrode materials in general.

For the tested γ-frozen configurations, the LUMO shift of the molecule has a range of 0.63 eV and the HOMO shift of the MgBipO2 has a range of 0.4 eV. The frozen cases also have ranges of 0.6 eV or less. The Mulliken charges are between 0.9 and 0.5 q at 0 and 150° for MgBipO2 (frozen and γ-frozen) and 0.6 and 0.1 q for the BipO2 configuration at 30 and 150°, respectively. This means that the bond between Mg and the molecule becomes less

ionic and weakens due to a dihedral rotation. In general, this can be seen in a reduction of bond order or the loss of a bond. In the context of the calculations, it is the loss of one of the Mg-O bonds in MgBipO2. Thus, structural effects are a major factor to be considered besides the observed small changes in electronic structure for dihedral angle controlled voltage changes in this molecule and potentially similar systems.

Figures 4E,F compare the effect of strain energy E_S when the Mg atom is removed and when it is present, respectively. Without an attached Mg atom (**Figure 4E**), the strain is minimized at round 120° for BipO2 and MgBipO2, as expected by the energetically preferred structure of BipO2 in which the carbonyl groups have a large separation distance. The transition potential of the rotation of BipO2 is ca. 0.9 and 1.4 eV for the γ-frozen and frozen calculation, respectively. For the MgBipO2 reference system, the molecule stores strain energy at the optimized structure due to the dihedral rotation under Mg attachment. Without Mg atom, this is partly released when the dihedral rotation reaches values similar to the one of the relaxed BipO2. In contrast, the strain energy increases by dihedral rotation when a Mg atom is attached. The max. values increase to more than 2 eV for all cases, see **Figure 4F**, and the increase in strain energy correlates roughly with a decrease in interaction strength with Mg in the case of the MgBipO2 reference. Since the distances between the redox-active groups and the Mg atom increase with increasing change of the dihedral angle, this correlation can be understood from the elongation and eventual loss of bonds between redox-active groups and the Mg atom.

For BipO2, the voltage change by dihedral strain is estimated to be between 1.3 and 1.9 V. To further explore torsion on the molecular scale for voltage modulation, we proceed with three other molecules of a similar structure. **Figure 5A** shows a 1,1′-bi(1,4-cyclohexadiene-1-yl)-2,2′,6,6′-tetrone (BCT) molecule with a Mg atom attached in two configurations in which the dihedral angle between the 6-membered rings differ by 90°. We chose the molecules with a Mg atom attached as initial geometries. The blue arrow indicates the change of dihedral angle and the superimposed structures distinguish the atomic geometry before the rotation (faded out and with red oxygen atoms) and with 90° rotation (indicated by benzene-like ring with blue oxygen atoms). The loss of one Mg-bond and the bending of the molecular structure is visible. **Figure 5B** gives an overview of the structural changes after constrained relaxation for which the dihedral angle was changed in steps of 30° in a range from 0 to 180°. It is kept fixed during relaxation. The loss of one Mg-O bond for geometries with a dihedral rotation close to 90° is visible. **Figures 5C–F** show the investigated molecules. The systems were derived from the BipO2 molecule with a few modifications; this includes: **C**) combination of five- and six-membered ring–$C_{10}NH_7O$, **D**) and **E**) a different number of carbonyl groups on the phenyl-like rings and **F**) replacing carbonyl groups with $R_2C = S$ functional groups ($BipS_4$). **Figure 5G** shows the changes in interaction strength (ΔE_{ad}) as a function of change of dihedral angle γ for the structures shown in **Figures 5C–F**. As seen above, the change of interaction strength defines the change in voltage. However, a slight bend in the bond between the rings can cause differences in the interaction strengths at 0 and 180° due to a reduced structural symmetry.

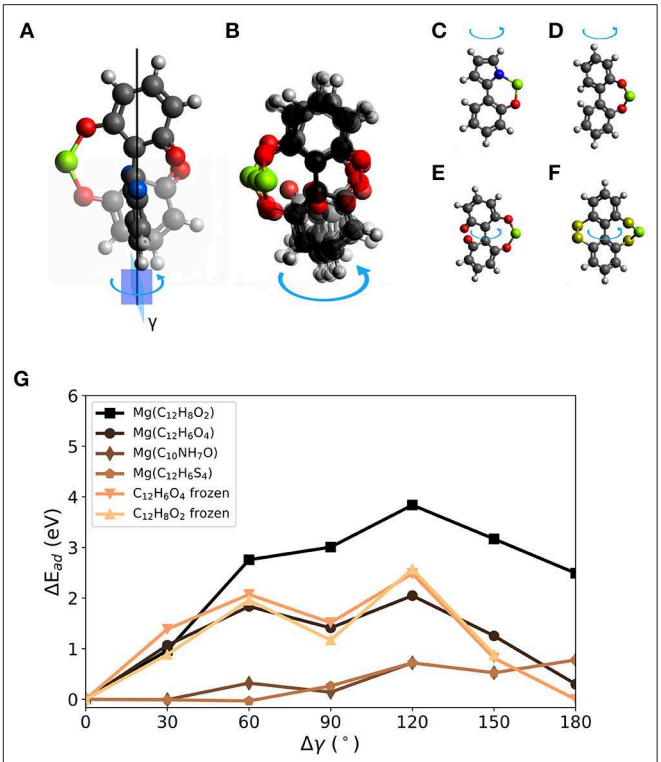

FIGURE 5 | Rotation of the dihedral angle γ in biphenyl-derived molecules with carbonyl as redox-active group. **(A)** 1,1′-Bi(1,4-cyclohexadiene-1-yl) -2,2′,6,6′-tetrone (BCT) with chosen rotational axis (black vertical line) and angle (arrow). The initial structure is given with red O atoms and the final position with a changed dihedral angle between 6-membered rings indicated by blue O atoms on the ring. **(B)** Superposition of investigated rotated structures of BCT 0° to 180° in steps of 30°. Overview of molecules investigated for dihedral strain design: **(C)** $C_{10}NH_7O$, **(D)** $C_{12}H_8O_2$ (BipO2), **(E)** BCT, and **(F)** $C_{12}H_6S_4$. **(G)** Change of interaction strength with a Mg atom for different dihedral angles γ.

In general, the tested molecules with carbonyl groups yield larger interaction strengths with Mg. Between BCT and BipO2, the differences are small. They have similar maximum voltages (e.g., 2.1 V for BCT). In contrast to BipO2, BCT and Mg interact via two carbonyl groups in each of the phenyl-like rings. At dihedral rotations of more than 90°, the distance between Mg and O atoms will increase again in BCT leading to significantly smaller ΔE_{ad} compared to BipO2. The other molecules have smaller maximum binding strengths. The interaction energies (voltages) of BipS4 and $C_{10}NH_7O$ with Mg are −1.7 eV (0.1 V) and −3.1 eV (0.8 V), respectively.

For all tested molecules, the curves reach the point of maximal change of the interaction energy at a twisted structure with a dihedral angle changed by around 90 or 180°. This can be caused by the presence of one or two redox-active groups at the rotated ring or the bend structure due to Mg attachment on one side of a molecule. All molecules but $C_{10}NH_7O$ significantly undergo a bending away from the attached Mg atom, in addition to the change of dihedral angle of the molecular structure. This can

result in additional strain during the rotation. $C_{10}NH_7O$ has a dihedral angle of 0° at full relaxation when Mg is attached. At a rotation of 180°, the distance between the redox-active groups and Mg is maximized and the interaction energy decreases by 0.8 eV. A similar decrease was observed for the $C_{12}H_6S_4$ complex. For both complexes, the absolute decrease is smaller than for the MgBipO2 case since the binding strength is weaker. Although the $C_{12}H_6S_4$ complex has two redox-active groups on each 6-membered ring, the maximal change of the interaction energy is not found at 90° but at 180° caused by a slightly bent structure and the changed interaction between S atoms. In all these cases, the strain can drastically decrease the interaction strength between molecule and Mg atom, and the interaction strength can be reduced by 80 % by torsion on the molecular scale.

Overall, the influence of the relative orientation of molecular planes and their redox-active groups, either within the same molecule or same complex but different molecules, can be a significant factor for changing the voltage-capacity curve if mechanical control on the molecular level can be achieved. In all tested cases, the interaction strength decreases between the molecules and the Mg atom leading to a lower theoretical voltage. While the molecular torsion does not increase the voltage, it could potentially be used to lower the charging voltage due to the weaker interaction strength. At certain dihedral angles, the binding strength can change by up to 2–3 eV translating to a voltage reduction of 1 to 1.5 V. Large steric hindrance can be expected that prevents a 180° rotation for practical cases.

Design of Coordination Environment of Mg Cations

Mg atoms can bond in different ways to one or more redox-active groups of the active electrode material. They may also experience interaction with other molecules present in the electrode. Already in the example of the linear strain in the organic PAD-Mg complex shown above, the interaction strength with Mg differs when one or when two molecules simultaneously attach via a carbonyl group to Mg. Previously it was reported that the chemical environment can increase the voltage for organic Li and Na ion batteries, for instance, seen in the increase by ca. 1 V due to bulk phase (Manzhos, 2019 and references therein). Thus, it is not surprising if this also applies to organic electrode materials for MIB.

We study the effect of the local environment around the Mg atom created by molecules with carbonyl groups, that is the coordination of a different number and arrangement of carbonyl groups to a central Mg atom. The effect of a different number of redox centers in the same type of geometry was investigated by comparison between the benzoquinone (tBQE) and 1,2-benzoquinone (BQE). BQE and tBQE are structural isomers ($C_6H_4O_2$) that allow us to probe the effect of the intramolecular carbonyl distance on the voltage. The effect of a different chemical character was tested by comparison between the tBQE and phenyloxidanyl molecule (C_6H_5O). Three different types of geometries were selected to test the influence of the arrangements, that are: linear, trigonal and tetragonal, displayed in **Figure 6**. It should be noted that in most cases, molecular

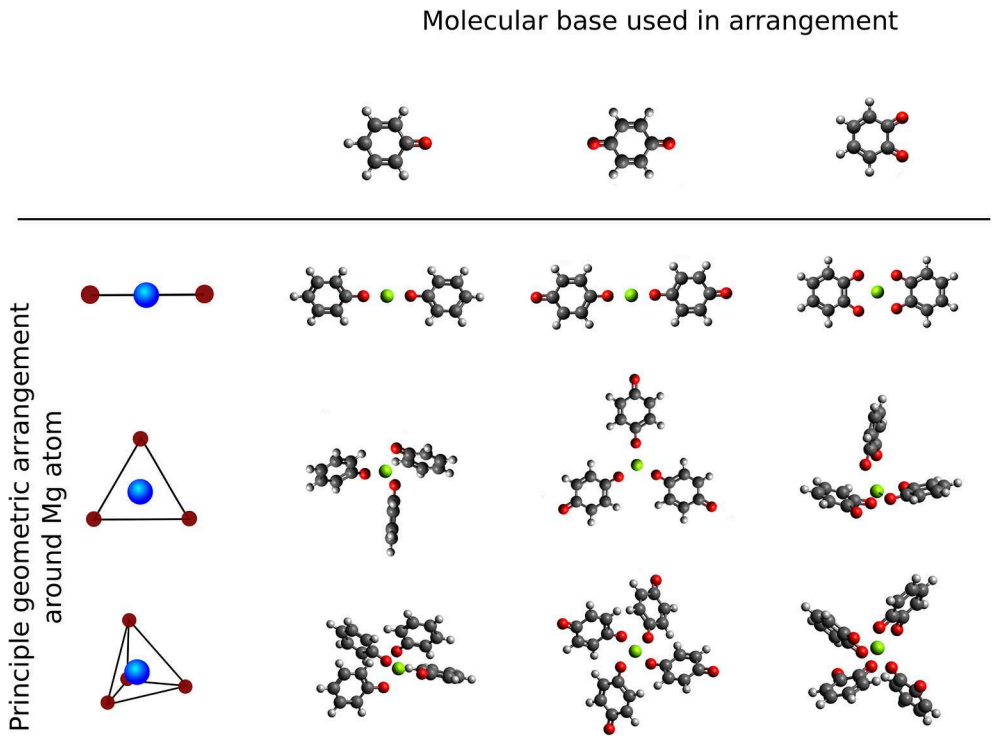

FIGURE 6 | Overview of principle high symmetry arrangements around Mg atom centers (top to bottom: single molecule, linear, trigonal and tetrahedral) with different carbonyl based 6-membered ring molecules (left to right: principle geometries, phenyloxidanyl, benzoquinone and 1,2-Benzoquinone.

TABLE 1 | Formation energies (eV) [theoretical voltages (V) vs. Mg2+/Mg] for systems shown in **Figure 6**.

	Phenyloxidanyl	Benzoquinone (tBQE)	1,2-Benzoquinone (BQE)
Single molecule + Mg	−1.72 [0.10]	−0.44 [−0.53]	−2.11 [0.30]
Linear complex	−4.88 [1.68]	−2.01 [0.24]	−5.83 [2.16]
Trigonal complex	−6.44 [2.46]	−3.92 [1.21]	−6.98 [2.73]
Tetrahedral complex	−7.04 [2.77]	−5.13 [1.81]	−7.11 [2.80]

systems without a central Mg atom show weak or no binding in our calculations, partly because we do not include van-der-Walls interactions (on purpose, as we are interested in electronic effects). Furthermore, we adapt Equation (2) by substitution E_r^{mol} with $w\ E_r^{mol}$ where w is the number of molecules in the final geometry.

The computed interaction energies and resulting theoretical voltages for the fully relaxed systems (structures shown in **Figure 6**) are presented in **Table 1**. tBQE has voltages of 0.2 to 1.8 V when more than one molecule coordinates to the Mg cation while a single BQE molecule results in a formally negative voltage of −0.5 V. Phenyloxidanyl has a voltage of ca. 1.7–2.8 V that is higher than those of tBQE in comparable configurations possibly due to its radical character. The BQE based configurations result in even higher voltages (0.3 V for one molecule and 2.2–2.8 V for linear to tetragonal configurations) than for tBQE and are of similar magnitude as for phenyloxidanyl. Although BQE does not have a radical character, the increase in voltage compared to BQE could arise through the interaction of the positive Mg cation and the two negatively charged carbonyl groups of each BQE. A possible consequence for the design of active Mg cathode material is to create a chemical environment for the Mg atom with a large number of redox-active groups. The results show that the type of coordination geometry can lead to a, e.g., max. voltage of 2.8 V for BQE that is an increase of 2.7 V compared to a single molecule. The number of redox centers that coordinate to Mg is a key factor to achieve this high voltage and it can change the voltage by more than 2 V. Interestingly, chemical locality design can change a non-working electrode, e.g., single molecule tBQE, into a working electrode, e.g., a trigonal complex of tBQE.

A Promising Molecular Design

The idea of combining structural and electronic design is applied to a complex ring system, a cycloparaphenylene molecule consisting of three fused biphenyl-like units ($C_{36}H_{24}$), shown in **Figure 7**. This molecular system combines the previously described effects of dihedral rotation, chemical environment, and it is possible to introduce electronic modifications, for example, by functionalization. We discuss possible modifications to an inner (with six H atoms, not shown) and an outer ring (with 18 H atoms). The bonds between the phenyl rings allow rather easy partial rotational changes. Up to six carbonyl groups can be in the inner ring. Then, the O atoms can take, e.g., a linear, trigonal, square-planar, tetragonal and bipyramidal-like symmetry for a central Mg ion inserted into the center of the molecule. Regarding the relative positions of the O atoms, these geometries are similar to the one shown in the section Design of Coordination Environment of Mg Cations. Of course, different combinations of sites of the carbonyl group are possible for two to four O atoms in the inner ring. The optimized geometries of the ring molecule with one to six carbonyl groups and an inserted Mg atom are shown in **Figures 7A–F**, respectively.

Figure 8 shows the voltage vs. Mg^{2+}/Mg computed for the insertion of one Mg atom in the inner ring of the $C_{36}H_{24}$ molecule and its derivatives with different numbers of O atoms. There is no strong interaction between Mg atoms and the $C_{36}H_{24}$ molecule (no O atoms), resulting in a theoretical voltage of −0.75 V, i.e., the molecule is not suitable for Mg storage. The first carbonyl group increases the interaction strength and results in a slightly positive voltage. The most significant increase in the voltage is observed when increasing the number of inner carbonyl groups from one to two. This is similar to the cases of individual molecules with their carbonyl groups around the Mg atom. Introduction of more inner ring carbonyl groups increases the voltage to a value of slightly more than 2.53 V vs. Mg^{2+}/Mg. Depending on the number of carbonyl groups, the structure of the molecule exhibits different dihedral angle rotations between six-membered rings when the Mg atom is inserted (the strain energy is estimated at 2.7 eV). In contrast, the presence of carbonyl groups without an inserted Mg atom has a minor effect on these angles.

Introducing carbonyl groups in the inner ring can serve two purposes. First, it introduces redox-active groups. Choosing O atoms is obvious since carbonyl groups are known to result in working organic electrode materials, e.g., BQE. Second, the O atoms have a larger electronegativity than H atoms, thus they have an electron-withdrawing effect and they can stabilize the LUMO energies in organic compounds. From zero to six O atoms, the LUMO decreases from −1.43 to −3.81 eV, a change of −2.38 eV. As a result, the electronic effect on the voltage increase is at most 1.19 V while the computed voltage change is 3.28 V. This indicates that also for this system, electronic effects alone cannot fully explain the voltage increase and the number and character of bonds formed between the Mg atom and the carbonyl groups must be considered.

Outer ring functionalization gives another example of the interplay between electronic and structural effects on the voltage. We explore functionalization with F and with O atoms, and the resulting effect on the voltage for the insertion of one Mg atom. In this way, the contribution from the chemical locality (inner ring structure) and electronic changes through functionalization can be combined. The former option (substitution with F atoms leading to $C_{36}F_{18}O_6$, structure is shown in **Figure 9**) can increase the theoretical voltage to 3.51 V vs. Mg^{2+}/Mg (an increase by 1 V) at full outer ring fluorination and the latter option (O atoms–$C_{36}O_{24}$) results in a maximal voltage of 3.17 V (an increase by 0.64 V). An overview of voltages and voltage changes between the F-functionalized and the non-functionalized ring structure

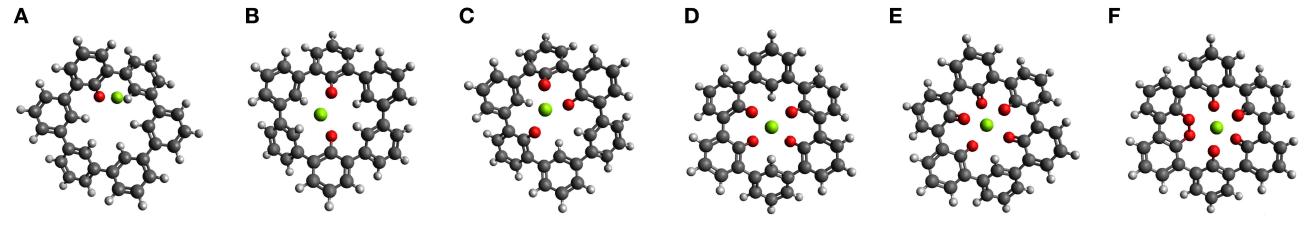

FIGURE 7 | Optimized structures of $MgC_{36}O_nH_{24-n}$ $n = \{1,2,3\ldots6\}$ where $n = 1$ **(A)** increases to $n = 6$ **(F)**.

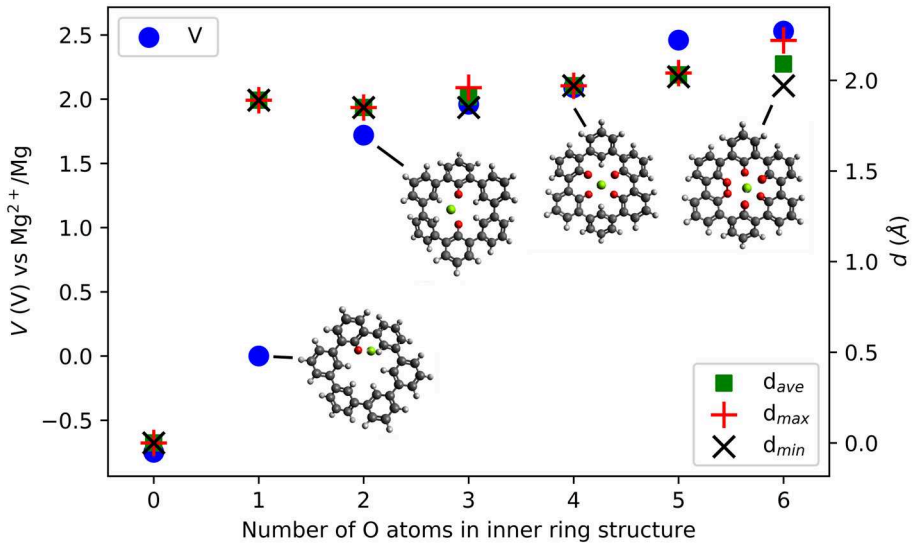

FIGURE 8 | Computed voltage (V) vs. Mg^{2+}/Mg (left axis) and Mg-O distances d {average, maximal, minimal} (Å) (right axis) in triple-biphenyl ring structures as a function of the number of O atoms in the inner ring of the molecule.

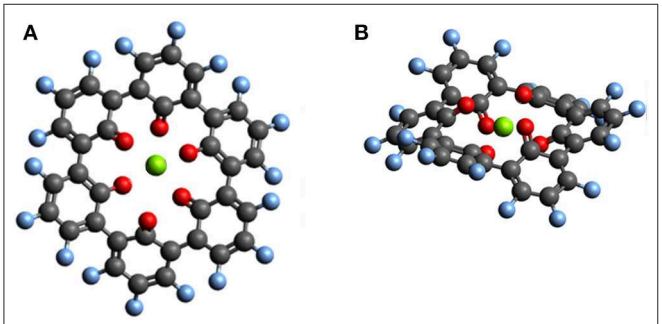

FIGURE 9 | Top view **(A)** and side view **(B)** of the optimized structure of hypothetical $C_{36}F_{18}MgO_6$ molecule for which a voltage of 3.51 V vs. Mg^{2+}/Mg was computed.

is shown in **Figure 10**, top and bottom panel, respectively. The right panel of **Figure 10** shows the voltage changes depending on the number of carbonyl groups in the inner-ring. The LUMO of the F functionalized molecule is stabilized by 1.46 eV and the O functionalized one is stabilized by 2.9 eV. The counter-intuitive relation between an increase in voltage and LUMO stabilization requires to extend a model that is only based on LUMO energy changes to understand the atomistic reasons behind the observed effects.

While the change of LUMO energy can often explain any voltage increase by electronic effects, we introduce a contribution accounting for the chemical environment to extend the LUMO based empirical model. Since F atoms have a larger electronegativity than O and H atoms, a charge redistribution can take place when the molecule is functionalized with F atoms. To consider this in a simple approach, we measure the charge redistribution on the redox-active atoms (here the O atoms in the inner ring). Since we are only interested in changes due to functionalization of the outer ring, the charge redistribution can be estimated by the Mulliken charges.

We provide a simple model based on the LUMO energy changes and the changes in the Mulliken charges of the redox-active atoms (nearest neighbor to inserted Mg atom) to estimate a voltage increase for Mg batteries. The model is based on the assumption that the energy level of the LUMO and the Coulombic charges estimated as point charges surrounding a central Mg ion will contribute to the interaction strength. Furthermore, we assume that the change of the voltage is

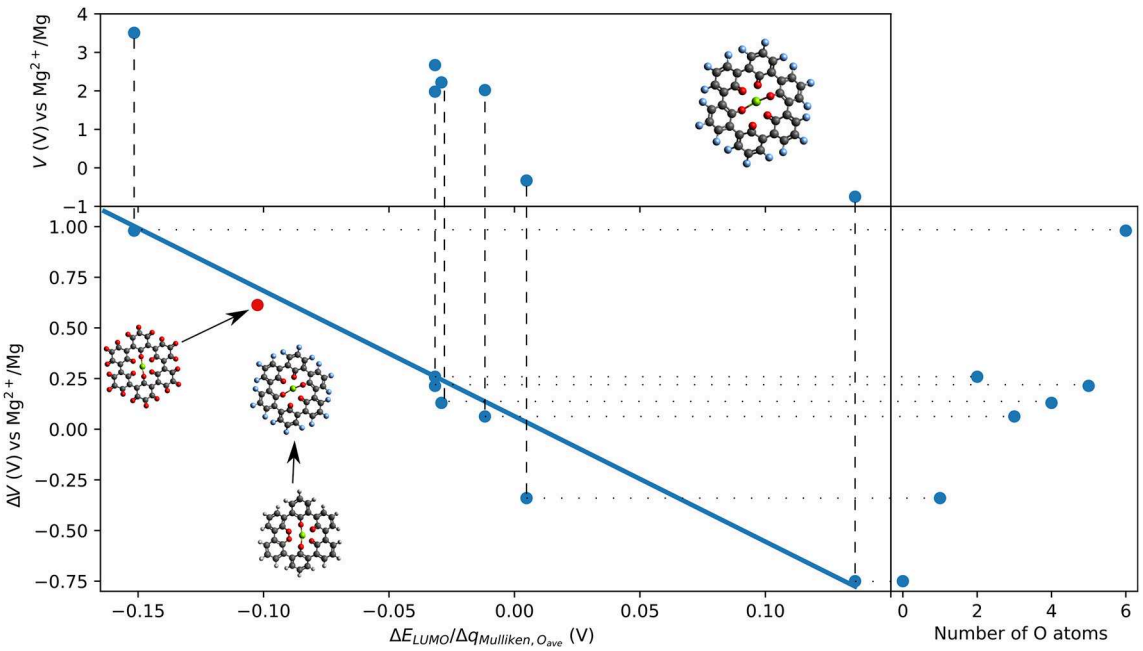

FIGURE 10 | F-functionalization induced changes in voltage vs. Mg^{2+}/Mg as a function of the ration of change of LUMO energy and Mulliken charges on O atoms in the inner ring of triple-biphenylene molecule. The insert shows a linear regression (solid blue line). One data point (red dot) shows the result of $C_{36}O_{24}$.

proportional to the change of LUMO energy, and that it is indirectly proportional to the averaged change of charge on the redox-active centers due to functionalization.

The linear regression (shown as solid blue line in the bottom panel of **Figure 10**) for organic Mg electrode materials operating by reduction confirms a relatively linear trend over the ratio of change in LUMO eigenvalue and change in Mulliken charges on the redox-active groups that are involved in the redox process. The suggested model can also explain our previous observation that electronic modification in the coronene molecule does not result in increased voltages for Mg batteries while it affects the interaction with Li and Na ions (Lüder et al., 2017b). Furthermore, the model was confirmed with the result of the O-functionated ring structure that is indicated as red dot in **Figure 10** and it may find application in other systems, too.

Among all investigated structures, the $C_{36}O_{24}$ molecule might be the most promising one for further investigation aiming to optimize its potential vs. Mg^{2+}/Mg. It has a conceptual similarity to oxocarbon salts (Zhao et al., 2016) which showed promise for monovalent batteries. For this system, we computed multiple Mg atom attachments since the O functionalization introduced more carbonyl groups that can be used to store more Mg atoms. The capacity corresponding to the attachment of up to 5 Mg atoms results still in voltages of ca. 2 V or more vs. Mg^{2+}/Mg. As the attachment takes place at the outer ring carbonyl groups, these voltages are a lower estimate and chemical locality of bulk materials constituted by neighboring molecules could further increase the voltage at higher capacities.

CONCLUSIONS

Organic Mg ion batteries are still in their early stages of development. Specifically, it is challenging to design insertion type active high-voltage electrode materials; many types of molecules that show good performance in monovalent batteries do not work for Mg ion batteries and do not bind Mg. Even for molecular materials with appreciable interaction energy with Mg, bivalency means very low voltages. In this work, we have explored computationally design strategies that could be used to increase voltages, applying them to several prototypical molecular systems. We considered electronic structure design, structural changes/functionalizations, strain design as well as the design of Mg coordination environment.

We find that it is possible to increase the voltage of organic electrodes for Mg batteries by several volts by a combination of electronic and structural design. Electronic structure design based on LUMO stabilization, however, shows severe limitations to voltages of not more than 2 V for most materials. In particular, we demonstrate that an increase of voltage by 4.3 V to a maximal voltage of 3.5 V vs. Mg^{2+}/Mg can be achieved when electronic effects are combined with engineering of the local chemical environment. Designing coordination environment for Mg atoms can change the voltage by 2.0 to 2.5 V already for small molecules and appears to be a promising strategy.

Three types of strain that are linear strain, bending and dihedral strain can influence the interaction strength to Mg; here, we found they lead to lower interaction

energies/voltages. Strain design may find potential application in lowering the charging potential if mechanical control at the molecular level is achievable. A reduction of 0.5 V for bending and 1–2 V for linear and dihedral strain may be achievable.

Based on the results obtained with the ring structures that combine electronic effects with effects of the chemical locality, we provide an empirical model based on two computable molecular properties, LUMO energy change and changes of Mulliken charges, to estimate the voltage change due to structural modifications such as fluorination.

In this paper, we explored what would be theoretical limits of voltage increase by modifications of molecular and electronic structure. Some of these modifications could be achieved in a way which is intrinsic to a single molecule (e.g., doping, use of functional groups causing steric hindrance to induce strain, or coordination to several redox-active centers of the same molecule) and is expected to be stable under battery cycling. Other modifications that we explored (e.g., linear or dihedral strain or coordination to redox-active centers of several molecules) would require development of practical design strategies to stabilize these environments (e.g., anchoring (Chen and Manzhos, 2015) to approach the theoretical limits delimited here.

DATA AVAILABILITY STATEMENT

All datasets generated for this study are included in the article/**Supplementary Material**.

AUTHOR CONTRIBUTIONS

JL: calculations, data analysis, and text. SM: conceptualization, data analysis, and text.

FUNDING

JL acknowledges funding through the Ministry of Science and Technology (MOST) Taiwan under grant MOST108-2112-M-110-001-MY2 and was grateful to the National Center for High-performance Computing for computer time and facilities.

ACKNOWLEDGMENTS

We thank Dr. Yingqian Chen for performing some test calculations and for discussions.

SUPPLEMENTARY MATERIAL

The Supplementary Material for this article can be found online at: https://www.frontiersin.org/articles/10.3389/fchem.2020.00083/full#supplementary-material

REFERENCES

Araujo, R. B., Banerjee, A., Panigrahi, P., Yang, L., Strømme, M., Sjödin, M., et al. (2017). Designing strategies to tune reduction potential of organic molecules for sustainable high capacity battery application. *J. Mater. Chem. A* 5, 4430–4454. doi: 10.1039/C6TA09760J

Becke, A. D. (1993). A new mixing of Hartree–Fock and local density-functional theories. *J. Chem. Phys*. 98, 1372–1377. doi: 10.1063/1.464304

Bhatt, M. D., and O'Dwyer, C. (2015). Recent progress in theoretical and computational investigations of Li-ion battery materials and electrolytes. *Phys. Chem. Chem. Phys*. 17, 4799–4844. doi: 10.1039/C4CP05552G

Bitenc, J., Pirnat, K., Bančič, T., Gaberšček, M., Genorio, B., Randon-Vitanova, A., et al. (2015). Anthraquinone-based polymer as cathode in rechargeable magnesium batteries. *ChemSusChem* 8, 4128–4132. doi: 10.1002/cssc.201500910

Bitenc, J., Pirnat, K., Bančič, T., Gaberšček, M., Genorio, B., Randon-Vitanova, A., et al. (2016). Poly(hydroquinoyl-benzoquinonyl sulfide) as an active material in Mg and Li organic batteries. *Electrochem. Commun*. 69, 1–5. doi: 10.1016/j.elecom.2016.05.009

Burkhardt, S. E., Bois, J., Tarascon, J.-M., Henning, R. G., and Abruna, H. D. (2013). Li-carboxylate anode structure-property relationships from molecular modeling. *Chem. Mater*. 25, 132–141. doi: 10.1021/cm302839z

Canepa, P., Sai Gautam, G., Hannah, D. C., Malik, R., Liu, M., Gallagher, K. G., et al. (2017). Odyssey of multivalent cathode materials: open questions and future challenges. *Chem. Rev*. 117, 4287–4341. doi: 10.1021/acs.chemrev.6b00614

Ceder, G., Aydinol, M. K., and Kohan, A. F. (1997). Application of first-principles calculations to the design of rechargeable Li-batteries. *Comput. Mater. Sci*. 8, 161–169. doi: 10.1016/S0927-0256(97)00029-3

Chen, Y., Cho, C.-R., and Manzhos, S. (2019). Lithium attachment to C60 and nitrogen- and boron-doped C60: a mechanistic study. *Materials* 12:2136. doi: 10.3390/ma12132136

Chen, Y., Lüder, J., and Manzhos, S. (2017). Disodium pyridine dicarboxylate vs. disodium terephthalate as anode materials for organic Na ion batteries: effect of molecular structure on voltage from the molecular modeling perspective. *MRS Adv*. 2, 3231–3235. doi: 10.1557/adv.2017.323

Chen, Y., Lüder, J., Ng, M.-F., Sullivan, M., and Manzhos, S. (2018). Polyaniline and CN-functionalized polyaniline as organic cathodes for lithium and sodium ion batteries: a combined molecular dynamics and density functional tight binding study in solid state. *Phys. Chem. Chem. Phys*. 20, 232–237. doi: 10.1039/C7CP06279F

Chen, Y., and Manzhos, S. (2015). Lithium and sodium storage on tetracyanoethylene (TCNE) and TCNE-(doped)-graphene complexes: a computational study, *Mater. Chem. Phys*. 156, 180–187. doi: 10.1016/j.matchemphys.2015.02.045

Chen, Y., and Manzhos, S. (2016a). A comparative computational study of lithium and sodium insertion in van der Waals and covalent tetracyanoethylene (TCNE) -based crystals as promising materials for organic lithium and sodium ion batteries, *Phys. Chem. Chem. Phys*. 18, 8874–8880. doi: 10.1039/C5CP07474F

Chen, Y., and Manzhos, S. (2016b). A computational study of lithium interaction with tetracyanoethylene (TCNE) and tetracyaniquinodimethane (TCNQ) molecules. *Phys. Chem. Chem. Phys*. 18, 1470–1477. doi: 10.1039/C5CP06140G

Chen, Y., and Manzhos, S. (2016c). Voltage and capacity control of polyaniline based organic cathodes: an ab initio study. *J. Power Sources* 336, 126–131. doi: 10.1016/j.jpowsour.2016.10.066

Deng, W., Liang, X., Wu, X., Qian, J., Cao, Y., Ai, X., et al. (2013). A low cost, all-organic Na-ion battery based on polymeric cathode and anode. *Sci. Rep*. 3:2671. doi: 10.1038/srep02671

Diouf, B., and Pode, R. (2015). Potential of lithium-ion batteries in renewable energy. *Renew. Energy* 76, 375–380. doi: 10.1016/j.renene.2014.11.058

Dunn, B., Kamath, H., and Tarascon, J.-M. (2011). Protein methyltransferases: a distinct, diverse, and dynamic family of enzymes. *Science* 334, 928–935. doi: 10.1126/science.1212741

Frisch, M. J., Trucks, G. W., Schlegel, H. B., Scuseria, G. E., Robb, M. A., Cheeseman, J. R., et al. (2016). *Gaussian 09, Revision, E.01*. Wallingford, CT: Gaussian, Inc.

Ge, M., Rong, J., Fang, X., and Zhou, C. (2012). Porous doped silicon nanowires for lithium Ion battery anode with long cycle life. *Nano Lett*. 12, 2318–2323. doi: 10.1021/nl300206e

Geniès, E., Hany, P., and Santier, C. (1989). Secondary organic batteries made with thick free standing films of electrochemically prepared polyaniline. *Synth. Met*. 28, 647–654. doi: 10.1016/0379-6779(89)90585-7

Goodenough, J. B. (2012). Rechargeable batteries: challenges old and new. *J. Solid State Electrochem*. 16, 2019–2029. doi: 10.1007/s10008-012-1751-2

Gregory, T. D. (1990). Non-aqueous electrochemistry of magnesium. *J. Electrochem. Soc*. 137, 775–780. doi: 10.1149/1.2086553

Hameer, S., and van Niekerk, J., (2015). A review of large-scale electrical energy storage. *Int. J. Energy Res*. 39, 1179–1195. doi: 10.1002/er.3294

Hayashi, M., Arai, H., Ohtsuka, H., and Sakurai, Y. (2004). Electrochemical insertion/extraction of calcium ions using crystalline vanadium oxide. *Electrochem. Solid-State Lett*. 7, A119–A122. doi: 10.1149/1.1675951

Hohenberg, P., and Kohn, W. (1964). Inhomogeneous electron gas. *Phys. Rev*. 136, B864–B871. doi: 10.1103/PhysRev.136.B864

Kaxiras, E. (2003). *Atomic and Electronic Structure of Solids*. Cambridge: Cambridge University Press. doi: 10.1017/CBO9780511755545

Kim, H., Kwon, J. E., Lee, B., Hong, J., Lee, M., Park, S. Y., et al. (2015a). High energy organic cathode for sodium rechargeable batteries. *Chem. Mater*. 27, 7258–7264. doi: 10.1021/acs.chemmater.5b02569

Kim, J. G., Son, B., Mukerjee, S., Schuppert, N., Bates, A., Kwon, O., et al. (2015b). A review of lithium and non-lithium based solid state batteries. *J. Power Sources* 282, 299–322. doi: 10.1016/j.jpowsour.2015.02.054

Kim, K. C., Liu, T., Lee, S. W., and Jang, S. S. (2016). First-principles density functional theory modeling of Li binding: thermodynamics and redox properties of quinone derivatives for lithium-ion batteries. *J. Am. Chem. Soc*. 138, 2374–2382. doi: 10.1021/jacs.5b13279

Kittel, C. (2005). *Introduction to Solid State Physics, 8th Edn*. Hoboken, NJ: John Wiley & Sons, Inc.

Koch, D., and Manzhos, S. (2019). A comparative first-principles study of lithium, sodium and magnesium insertion energetics in brookite titanium dioxide. *MRS Adv*. 4, 837–842. doi: 10.1557/adv.2018.631

Kohn, W., and Sham, L. J. (1965). Self-consistent equations including exchange and correlation effects. *Phys. Rev*. 140, A1133–A1138. doi: 10.1103/PhysRev.140.A1133

Koshika, K., Chikushi, N., Sano, N., Oyaizu, K., and Nishide, H. (2010). A TEMPO-substituted polyacrylamide as a new cathode material: an organic rechargeable device composed of polymer electrodes and aqueous electrolyte. *Green Chem*. 12, 1573–1575. doi: 10.1039/b926296b

Koshika, K., Sano, N., Oyaizu, K., and Nishide, H. (2009). An aqueous, electrolyte-type, rechargeable device utilizing a hydrophilic radical polymer-cathode. *Macromol. Chem. Phys*. 210, 1989–1995. doi: 10.1002/macp.200900257

Kulish, V. V., Koch, D., and Manzhos, S. (2017a). Ab initio study of Li, Mg, and Al insertion into rutile VO_2: fast diffusion and enhanced voltages for multivalent batteries, *Phys. Chem. Chem. Phys*. 19, 22538–22545. doi: 10.1039/C7CP04360K

Kulish, V. V., Koch, D., and Manzhos, S. (2017b). Insertion of mono- vs. bi- vs. trivalent atoms in prospective active electrode materials for electrochemical batteries: an ab initio perspective. *Energies* 10:2061. doi: 10.3390/en10122061

Kulish, V. V., Malyi, O. I., Ng, M. F., Chen, Z., Manzhos, S., and Wu, P. (2014). Controlling Na diffusion by rational design of Si-based layered architectures. *Phys. Chem. Chem. Phys*. 16, 4260–4267. doi: 10.1039/c3cp54320j

Kulish, V. V., and Manzhos, S. (2017). Comparison of Li, Na, Mg, and Al-ion insertion in vanadium pentoxides and vanadium dioxides. *RSC Adv*. 7, 18643–18649. doi: 10.1039/C7RA02474F

Lee, S., Kwon, G., Ku, K., Yoon, K., Jung, S-K., Lim, H-D, et al. (2018). Recent progress in organic electrodes for Li and Na rechargeable batteries. *Adv. Mater*. 2018, 1704682. doi: 10.1002/adma.201704682

Legrain, F., and Manzhos, S. (2015). Aluminum doping improves the energetics of lithium, sodium, and magnesium storage in silicon: a first-principles study. *J. Power Sources* 274, 65–70. doi: 10.1016/j.jpowsour.2014.10.037

Leisegang, T., Meutzner, F., Zschornak, M., Münchgesang, W., Schmid, R., Nestler, T., et al. (2019). The aluminum-ion battery: a sustainable and seminal concept? *Front. Chem*. 7:268. doi: 10.3389/fchem.2019.00268

Liang, Y., Tao, Z., and Chen, J. (2012). Organic electrode materials for rechargeable lithium batteries. *Adv. Energy Mater*. 2, 742–769. doi: 10.1002/aenm.201100795

Liang, Y., Zhang, P., and Chen, J. (2013). Function-oriented design of conjugated carbonyl compound electrodes for high energy lithium batteries. *Chem. Sci*. 4, 1330–1337. doi: 10.1039/c3sc22093a

Liu, X., Huang, J.-Q., Zhang, Q., and Mai, L. (2017). Nanostructured metal oxides and sulfides for lithium–sulfur batteries. *Adv. Mater*. 29:1601759. doi: 10.1002/adma.201601759

Lu, L., Han, X., Li, J., Hua, J., and Ouyang, M. (2013). A review on the key issues for lithium-ion battery management in electric vehicles. *J. Power Sources* 226, 272–288. doi: 10.1016/j.jpowsour.2012.10.060

Lu, Y., Wang, L., Cheng, J., and Goodenough, J. B. (2012). Prussian blue: a new framework of electrode materials for sodium batteries. *Chem. Commun*. 48, 6544–6546. doi: 10.1039/c2cc31777j

Lüder, J., Cheow, M. H., and Manzhos, S. (2017a). Understanding doping strategies in the design of organic electrode materials for Li and Na ion batteries: an electronic structure perspective. *Phys. Chem. Chem. Phys*. 19, 13195–13209. doi: 10.1039/C7CP01554B

Lüder, J., Legrain, F., Chen, Y., and Manzhos, S. (2017b). Doping of active electrode materials for electrochemical batteries: an electronic structure perspective. *MRS Commun*. 7, 523–540. doi: 10.1557/mrc.2017.69

Malyi, O. I., Tan, T. L., and Manzhos, S. (2013). A comparative computational study of structures, diffusion, and dopant interactions between Li and Na insertion into Si. *Appl. Phys. Express* 6, 027301. doi: 10.7567/APEX.6.027301

Manzhos, S. (2019). Organic electrode materials for lithium and post-lithium batteries: an ab initio perspective on design. *Curr. Opin. Green Sustain. Chem*. 17, 8–14. doi: 10.1016/j.cogsc.2018.12.005

Mauger, A., Armand, M., Julien, C. M., and Zaghib, K. (2017). Challenges and issues facing lithium metal for solid-state rechargeable batteries. *J. Power Sources* 353, 333–342. doi: 10.1016/j.jpowsour.2017.04.018

Miroshnikov, M., Divya, K., Babu, G., Meiyazhagan, A., Arava, L. M. R., Ajayan, P. M., et al. (2016). Power from nature: designing green battery materials from electroactive quinone derivatives and organic polymers. *J. Mater. Chem. A* 4, 12370–12386. doi: 10.1039/C6TA03166H

Mohtadi, R., and Mizuno, F. (2014). Magnesium batteries: current state of the art, issues and future perspectives. *Beilstein J. Nanotechnol*. 5, 1291–1311. doi: 10.3762/bjnano.5.143

Molaei, M., Mousavi-Khoshdel, S. M., and Targholi, E. (2017). First-principles investigation of the complex of 2, 5-furandicarbonitrile-Al-doped graphene as a possible electrode material for Na-ion batteries. *Curr. Appl. Phys*. 17, 272–278. doi: 10.1016/j.cap.2016.12.005

Muench, S., Wild, A., Friebe, A., Haupler, B., Janoschka, T., and Schubert, U. S. (2016). Polymer-based organic batteries. *Chem. Rev*. 116, 9438–9484. doi: 10.1021/acs.chemrev.6b00070

Nishide, H., Iwasa, S., Pu, Y.-J., Suga, T., Nakahara, K., and Satoh, M. (2004). Organic radical battery: nitroxide polymers as a cathode-active material. *Electrochim. Acta* 50, 827–831. doi: 10.1016/j.electacta.2004.02.052

Oltean, V.-A., Renault, S., Valvo, M., and Brandell, D. (2016). Sustainable materials for sustainable energy storage: organic Na electrodes. *Materials* 9:142. doi: 10.3390/ma9030142

Ortiz-Vitoriano, N., Drewett, N. E., Gonzalo, E., and Rojo, T. (2017). High performance manganese-based layered oxide cathodes: overcoming the challenges of sodium ion batteries. *Energy Environ. Sci*. 10, 1051–1074. doi: 10.1039/C7EE00566K

Padhy, H., Chen, Y., Lüder, J., Gajella, S. R., Manzhos, S., and Balaya, P. (2018). Charge and discharge processes and sodium storage in disodium pyridine-2,5-dicarboxylate anode-insights from experiments and theory. *Adv. Energy Mater*. 8:1701572. doi: 10.1002/aenm.201701572

Pan, B., Huang, J., Feng, Z., Zeng, L., He, M., Zhang, L., et al. (2016b). Polyanthraquinone-based organic cathode for high-performance rechargeable magnesium-ion batteries. *Adv. Energy Mater*. 6:1600140. doi: 10.1002/aenm.201600140

Pan, B., Zhou, D., Huang, J., Zhang, L., Burrell, A. K., Vaugey, J. T., et al. (2016a). 2,5-Dimethoxy-1,4-Benzoquinone (DMBQ) as organic cathode for rechargeable magnesium-ion batteries. *J. Electrochem. Soc*. 163, A580–A583. doi: 10.1149/2.0021605jes

Park, Y., Shin, D-S., Woo, S. H., Choi, N. S., Shin, K. H., Oh, S. M., et al. (2012). Sodium terephthalate as an organic anode material for

sodium ion batteries. *Adv. Mater.* 24, 3562–3567. doi: 10.1002/adma.201201205

Pearson, R. G. (1986). Absolute electronegativity and hardness correlated with molecular orbital theory. *Proc. Natl. Acad. Sci. U. S. A.* 83, 8440–8441. doi: 10.1073/pnas.83.22.8440

Ratnakumar, B. V., Di Stefano, S., Williams, R. M., Nagasubramanian, G., and Bankston, C. P. (1990). Organic cathode materials in sodium batteries. *J. Appl. Electrochem.* 20, 357–364. doi: 10.1007/BF01076041

Renault, S., Brandell, D., Gustafsson, T., and Edstrom, K. (2013). Improving the electrochemical performance of organic Li-ion battery electrodes. *Chem. Commun.* 49, 1945–1947. doi: 10.1039/c3cc39065a

Rodriguez-Pérez, I. A., Jian, Z., Waldenmaier, P. K., Palmisano, J. W., Chandrabose, R. S., Wang, X., et al. (2016). A hydrocarbon cathode for dual-ion batteries. *ACS Energy Lett.* 1, 719–723. doi: 10.1021/acsenergylett.6b00300

Sano, H., Senoh, H., Yao, M., Sakaebe, H., and Kiyobayashi, T. (2012). Mg^{2+} storage in organic positive-electrode active material based on 2,5-dimethoxy-1,4-enzoquinone. *Chem. Lett.* 41, 1594–1596. doi: 10.1246/cl.2012.1594

Seo, D.-H., Lee, J., Urban, A., Malik, R., Kang, S., and Ceder, G. (2016). The structural and chemical origin of the oxygen redox activity in layered and cation-disordered Li-excess cathode materials. *Nat. Chem.* 8, 692–697. doi: 10.1038/nchem.2524

Sk, M. A., and Manzhos, S. (2016). Exploring the sodium storage mechanism in disodium terephthalate as anode for organic battery using density-functional theory calculations. *J. Power Sources* 324, 572–581. doi: 10.1016/j.jpowsour.2016.05.101

Slater, M. D., Kim, D., Lee, E., and Johnson, C. S. (2013). Sodium-ion batteries. *Adv. Funct. Mater.* 23, 947–958. doi: 10.1002/adfm.201200691

Stephan, A. M., and Nahm, K. S. (2006). Review on composite polymer electrolytes for lithium batteries. *Polymer* 47, 5952–5964. doi: 10.1016/j.polymer.2006.05.069

Stevens, D. A., and Dahn, J. R. (2001). The mechanisms of lithium and sodium insertion in carbon materials. *J. Electrochem. Soc.* 148, A803–A811. doi: 10.1149/1.1379565

Sun, X., Bonnick, P., and Nazar, L. F. (2016). Layered TiS_2 positive electrode for Mg batteries. *ACS Energy Lett.* 1, 297–301. doi: 10.1021/acsenergylett.6b00145

Tojo, T., Sugiura, Y., Inada, R., and Sakurai, Y. (2016). Reversible calcium ion batteries using a dehydrated prussian blue analogue cathode. *Electrochim. Acta* 207, 22–27. doi: 10.1016/j.electacta.2016.04.159

Tripathi, A., Chen, Y., Padhy, H., Manzhos, S., and Balaya, P. (2019). Experimental and theoretical studies of trisodium-1,3,5- benzene tricarboxylate as a low voltage anode material for sodium ion batteries. *Energy Technol.* 7:1801030. doi: 10.1002/ente.201801030

Urban, A., Seo, D.-H., and Ceder, G. (2016). Computational understanding of Li-ion batteries. *NPJ Comput. Mater.* 2:16002. doi: 10.1038/npjcompumats.2016.2

Wang, Y., Liu, B., Li, Q., Cartmell, S., Ferrara, S., Deng, Z. D., et al. (2015). Lithium and lithium ion batteries for applications in microelectronic devices: a review. *J. Power Sources* 286, 330–345. doi: 10.1016/j.jpowsour.2015.03.164

Wenzel, S., Hara, T., Janek, J., and Adelhelm, P. (2011). Room-temperature sodium-ion batteries: improving the rate capability of carbon anode materials by templating strategies. *Energy Environ. Sci.* 4, 3342–3345. doi: 10.1039/c1ee01744f

Xu, C., Chen, Y., Shi, S., Li, J., Kang, F., and Su, D. (2015). Secondary batteries with multivalent ions for energy storage. *Sci. Rep.* 5, 1–8. doi: 10.1038/srep14120

Xu, J., Thomas, H. R., Francis, R. W., Lum, K. R., Wang, J., and Liang, B. (2008). A review of processes and technologies for the recycling of lithium-ion secondary batteries. *J. Power Sources* 177, 512–527. doi: 10.1016/j.jpowsour.2007.11.074

Xue, J., Fan, C., Deng, Q., Zhao, M., Wang, L., Zhou, A., et al. (2016). Silver terephthalate ($Ag_2C_8H_4O_4$) offering *in-situ* formed metal/organic nanocomposite as the highly efficient organic anode in Li-ion and Na-ion batteries. *Electrochim. Acta* 219, 418–424. doi: 10.1016/j.electacta.2016.10.017

Yabuuchi, N., Kubota, K., Dahbi, M., and Komaba, S. (2014). Research development on sodium-ion batteries. *Chem. Rev.* 114, 11636–11682. doi: 10.1021/cr500192f

Yao, M., Araki, M., Senoh, H., Yamazaki, S., Sakai, T., and Yasuda, K. (2010). Indigo dye as a positive-electrode material for rechargeable lithium batteries. *Chem. Lett.* 39, 950–952. doi: 10.1246/cl.2010.950

Zeng, X., Li, J., and Singh, N. (2014). Recycling of spent lithium-ion battery: a critical review. *Crit. Rev. Environ. Sci. Technol.* 44, 1129–1165. doi: 10.1080/10643389.2013.763578

Zhao, Q., Wang, J., Lu, Y., Li, Y., Liang, G., and Chen, J. (2016). Oxocarbon salts for fast rechargeable batteries. *Angew. Chem.* 128, 12716–12720. doi: 10.1002/ange.201607194

Zhao-Karger, Z., Zhao, X., Fuhr, O., and Fichtner, M. (2013). Bisamide based non-nucleophilic electrolytes for rechargeable magnesium batteries. *RSC Adv.* 3, 16330–16335. doi: 10.1039/c3ra43206h

Conflict of Interest: The authors declare that the research was conducted in the absence of any commercial or financial relationships that could be construed as a potential conflict of interest.

frontiers in Chemistry

PERSPECTIVE
published: 28 February 2020
doi: 10.3389/fchem.2020.00152

Building High Power Density of Sodium-Ion Batteries: Importance of Multidimensional Diffusion Pathways in Cathode Materials

*Mingzhe Chen, Yanyan Zhang, Guichuan Xing and Yuxin Tang**

Institute of Applied Physics and Materials Engineering, University of Macau, Macau, China

Emerging sodium-ion batteries (SIBs) devices hold the promise to leapfrog over existing lithium-ion batteries technologies with respect to desirable power/energy densities and the abundant sodium sources on the earth. To this end, the discoveries on novel cathode materials with outstanding rate capabilities are being given high priority in the quest to achieve high power density SIBs devices, and the multi-dimensional Na^+ migration pathways with low diffusion energy barriers are crucial. In light of this, the recent development of Prussian blue analogs and sodium superionic conductor (NASICON)-type materials with 3D Na^+ diffusion pathways for building high power density NIBs are provided in this perspective. Ultimately, the future research directions to realize them for real applications are also discussed.

Keywords: high power density, multidimensional diffusion pathways, cathode materials, sodium-ion batteries devices, materials design

OPEN ACCESS

Edited by:
Cheng Zhong,
Tianjin University, China

Reviewed by:
Xifei Li,
Xi'an University of Technology, China
Shiyou Zheng,
University of Shanghai for Science and Technology, China

****Correspondence:***
Yuxin Tang
yxtang@um.edu.mo

Specialty section:
This article was submitted to Electrochemistry, a section of the journal Frontiers in Chemistry

Received: *12 December 2019*
Accepted: *18 February 2020*
Published: *28 February 2020*

Citation:
Chen M, Zhang Y, Xing G and Tang Y (2020) Building High Power Density of Sodium-Ion Batteries: Importance of Multidimensional Diffusion Pathways in Cathode Materials. Front. Chem. 8:152. doi: 10.3389/fchem.2020.00152

INTRODUCTION

Although Li-ion batteries have received tremendous success in electronic and portable devices, the high price of lithium due to its limited and unequally distributed resources (**Figure 1A**) may hinder its further application in novel large-scale electrochemical energy storages systems (EESs) (Choi and Aurbach, 2016; Hwang et al., 2017; Vaalma et al., 2018). The rapid development of renewable energy sources such as wind energy, solar energy, and tide energy requires more cost-efficient and highly reliable large-scale EESs. SIBs have been widely considered as promising candidates for next-generation low-cost energy storage devices due to the almost unlimited resources of sodium (Li et al., 2017; Chen et al., 2019b,c). Due to the large atomic radius of Na (0.97 Å for Na^+ and only 0.68 Å for Li^+), however, hurdles that hinder the further applications of SIBs are mainly found in their sluggish sodium diffusion kinetics and large volume expansion, which are both critical parameters for revolutionary power density performance that can meet the real needs of power grids and large-scale EESs (Dai et al., 2017; Chen et al., 2019a). Therefore, it is important to explore novel cathode materials for SIBs with improved Na kinetics. From the solid-state diffusion perspective, the dimensions of diffusion pathways are the extremely important factors determining the diffusion coefficient of Na^+ as well as the diffusion energy barriers. For facile and rapid ionic transportation, the cathode materials that possess three-dimensional (3D) Na^+ migration pathways accompanied by low diffusion energy barriers are promising for building the high-power density SIBs (You et al., 2016; Chen S. et al., 2017). To this end, two emerging groups of Prussian blue analogs (PBAs) and sodium superionic conductor (NASICON)-type materials are recently

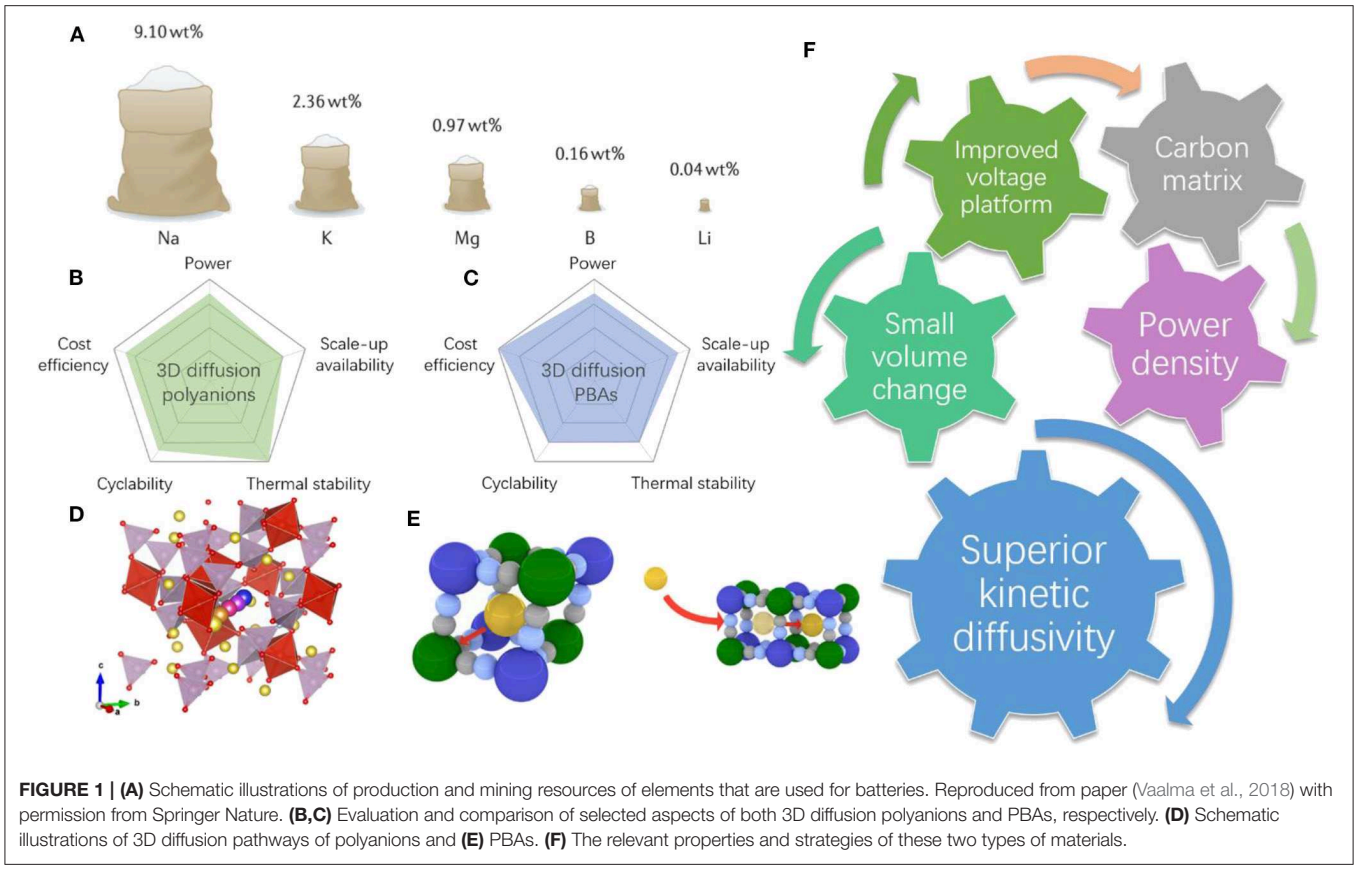

FIGURE 1 | (A) Schematic illustrations of production and mining resources of elements that are used for batteries. Reproduced from paper (Vaalma et al., 2018) with permission from Springer Nature. **(B,C)** Evaluation and comparison of selected aspects of both 3D diffusion polyanions and PBAs, respectively. **(D)** Schematic illustrations of 3D diffusion pathways of polyanions and **(E)** PBAs. **(F)** The relevant properties and strategies of these two types of materials.

developed. They both possess open 3D stable frameworks, exceptionally high ionic conductivities, and 3D sodium diffusion pathways. More importantly, these two types of materials usually undergo minimal volume changes during cycling, and their structures are highly tunable with different electrochemical properties (Lee et al., 2014; Wang B. et al., 2018). We compared the five important aspects for the real applications of these two types of materials in **Figures 1B–E**. We have witnessed an outstanding increase in publications regarding cathode materials with 3D diffusion pathways (Kim et al., 2012; You et al., 2016; Fedotov et al., 2018; Hurlbutt et al., 2018). Specifically, strategies such us nanosizing particles, introducing a uniform carbon coating/carbon matrix, and heteroatom doping are heavily used for better electrochemical properties (**Figure 1F**). These strategies have been developed to regulate the microstructures and surface atomic configurations to accelerate the charge transfer and kinetic properties as the same time.

In this perspective, we highlight (i) the specific key issues that are hindering the wider applications of these 3D Na^+ diffusion pathway materials, (ii) the recent novel and potential strategies to achieve high-performance SIBs, and (iii) the approaches to achieve higher energy/power densities and long-term cycling stability, and (iv) the new emerging SIB devices. Our perspective sharps the future development of cathode materials for the high-power density of SIBs and provides effective methodologies for other related next-generation energy storage devices.

PBAs WITH 3D Na^+ DIFFUSION PATHWAYS

Low-cost Na-hosting Prussian blue analogs usually possess the general structural formula of $Na_xM_2[M_1(CN)_6]_y{\cdot}nH_2O$ ($0 \leq x \leq 2$, $0 \leq y \leq 1$), where M_1 and M_2 are transition metal such us Mn, Fe, Co, etc. (Li et al., 2015). Within this structure, PBAs allow various modifications of their chemical compositions without changing the overall crystalline structure. Normally, most of the studied PBAs occurs as cubic phases with 6-fold coordination of $Fe^{II,III}$-O_6 octahedra participating in the redox reactions (Xiao et al., 2015). Theoretically, PBAs allow a maximum number of two Na^+ ions per formula unit if both the M_1 and the M_2 transition metal elements are electrochemically active, which can lead to a potential capacity over 170 mAh g^{-1}, completely comparable with all other kinds of cathode material for SIBs (Wu et al., 2017). Such high capacity is not easy to achieve, however, since the defects, vacancies, and water molecules will greatly influence the crystal structures of PBAs. Their zeolitic water molecules tend to occupy the interstitial sites that are essential for the sodium ion diffusion. The ideal situation is that all the zeolitic water can be completely removed, while the coordination water can be retained to render structural stability. In addition, the poor intrinsic electronic conductivity of PBAs also remains a great challenge for better C-rate performance, although they possess 3D diffusion pathways. From the previous density function theory (DFT) calculations, the intercalation of Na^+ with a larger ionic radius will incur the cost of increased insertion

potential, since the steric interactions have a close correlation with the hydration energy. Both sodium and potassium possess sufficiently high redox potentials that an appropriate energy density can be secured. The role of water in ionic conductivity is still an open question for all researchers. A paddlewheel mechanism was previously proposed, in which the alkali metal ions move through channels and vacancies (Wessells et al., 2011). Coordinated water is beneficial to facilitate ion migration, while zeolitic water has a negative influence, obstructing improvement of ionic conductivity. Both computational and experimental insights into the effects of the presence of water in PBAs are urgently needed.

One promising approach is to synthesize and optimize the Na-rich phase, Prussian white. When M_2 is Mn and M_1 is Fe in $Na_xM_2[M_1(CN)_6]_y{\cdot}nH_2O$ ($0 \leq x \leq 2$, $0 \leq y \leq 1$), a higher content of Na can be achieved. The valence of Fe is +2, however, and it is vulnerable to being oxidized to +3, so an inert atmosphere is required during both fabrication and centrifugal separation processes. By facile sodium citrate added precipitation method, Na-rich monoclinic phase $Na_xMnFe(CN)_6$ was successfully synthesized by Shen et al. (2018). Uniform microsize cuboid particles were obtained, and all the involved elements were uniformly distributed (**Figures 2A–C**). The high reversible capacity of 133.1 mAh g^{-1} was obtained, and satisfactory rate performance was achieved from 0.1 C to 10 C (1 C = 150 mA g^{-1}), as shown in **Figures 2D,E**. The uniform cuboid particle morphology provides extra convenience for fast ion diffusion apart from the original 3D pathways. In recent years, rhombohedral PBAs have been receiving more and more attention, since the concentration of coordinated water can be reduced due to the rhombohedral lattice symmetry, which is particularly favorable for the Na-rich phases. A zero-strain nickel hexacyanoferrate (NiHCF) was introduced by Ji et al. (2016) using a simple coprecipitation method. It delivered a high operation voltage, good cycling performance, and superior C-rate capability. They found that the unexpected high operation voltage was mainly attributable to the asymmetric residence of Na^+ ions along with the low charge density around Fe^{2+}. Different charge density analyses indicated that the Na^+ ions in cubic-structured NiHCF (c-NiHCF) tend to stay exactly in the center of interstitial channels (**Figure 2F**), while for rhombohedral-structured NiHCF (r-NiHCF), the Na^+ ions prefer to asymmetrically stay at N-coordinated corners (**Figure 2G**). Also the Na-N distance in r-NiHCF is shorter than that in c-NiHCF. Dramatic electron polarization round N atoms occurs, leading to a charge redistribution between adjacent Ni^{2+} and Fe^{2+} ions.

Therefore, the operation voltage of r-NiHCF is slightly higher than that of c-NiHCF. This phenomenon also facilitates fast sodium diffusion with excellent C-rate performances. In addition, the open-channel 3D diffusion pathways can guarantee satisfactory low-temperature performance. You et al. synthesized the $Na_2FeFe(CN)_6$ materials with carbon nanotubes (CNT) to achieve potential low-temperature properties (You et al., 2016). The well-decorated CNT network provides excellent electrical contact with the current collector. In addition, they performed a DFT study and found that the evenly distributed enriched 24*d* sites can provide uniform 3D Na^+ diffusion and feasible diffusion pathways, as shown in **Figures 2H,I**. There, PBAs are ideal candidates for low-temperature SIBs (Song et al., 2015; Peng et al., 2018). Further exploration should be focused on the inherent relationship between the crystal structure and the vacancies and water, and how these factors influence the sodium diffusion under various circumstances also needs to be urgently understood in detail.

POLYANIONIC COMPOUNDS WITH 3D Na^+ DIFFUSION PATHWAYS

The polyanionic-type cathode materials are one of the important branches among all the kinds of available electrodes for SIBs. Their merits are obvious and distinctive, such as outstanding cycling stability, high safety, and suitable operating voltages (Lu et al., 2017; Chen et al., 2020). Most of the polyanionic compounds consist of the corner- or edge-sharing MO_6 (*M* = transition metal) octahedra with connected XO_4 (*X* = P, S, Si, etc.) tetrahedra. This unique structure can provide sufficient stability and ionicity around the MO_6 octahedra, and, in turn, the ionic conductivity can be sustained within its 3D framework (Guo et al., 2017). Their sturdy framework can also render only small or even tiny volume shrinkage during cycling, since the topotactic reaction mechanism is dominant. Most of the polyanionic compounds are thermally stable due to their non-flammable nature (Ni et al., 2017). Also, polyanionic compounds normally possess high initial cycle Coulombic efficiency (ICE), which is an important parameter when making full cells. Nevertheless, most of the polyanionic compounds suffer from inherent low electronic conductivity, and therefore a well-decorated carbon coating and network are essential for their C-rate performance. According to the previous report, the majority of polyanionic composites possess one- or two-dimensional (1D or 2D) sodium diffusion pathways (Kim et al., 2013, 2015; Chen M. et al., 2017; Panigrahi et al., 2017; Chen et al., 2018; Fang et al., 2018; Zhu et al., 2019). The low-dimensional sodium diffusion pathways cannot guarantee satisfactory C-rate capabilities, especially in low temperature environments. Therefore, it is necessary to highlight those polyanionic compounds that possess unique 3D sodium diffusion pathways that are conducive toward real applications of SIBs and relevant energy storage devices. One class of these polyanionic composites comprises the sodium superionic conductor (NASICON)-type materials. Due to their high ionic conductivities, the NASICON-type materials also have been investigated as solid-state electrolytes (Li et al., 2018; Lu et al., 2018). Numerous papers have reported various NASICON-type materials, including both cathodes and anodes for SIB devices (Bui et al., 2015; Wang et al., 2017; Gao et al., 2018; Hu et al., 2018; Wang E. et al., 2018). Recently, we have introduced a new Fe-based polyanionic compound, $Na_4Fe_3(PO_4)_2(P_2O_7)$, which can be classified as a new NASICON-type material (Chen et al., 2019a). With the help of ethylenediaminetetraacetic acid (EDTA) as the complexing agent in a sol-gel approach, the

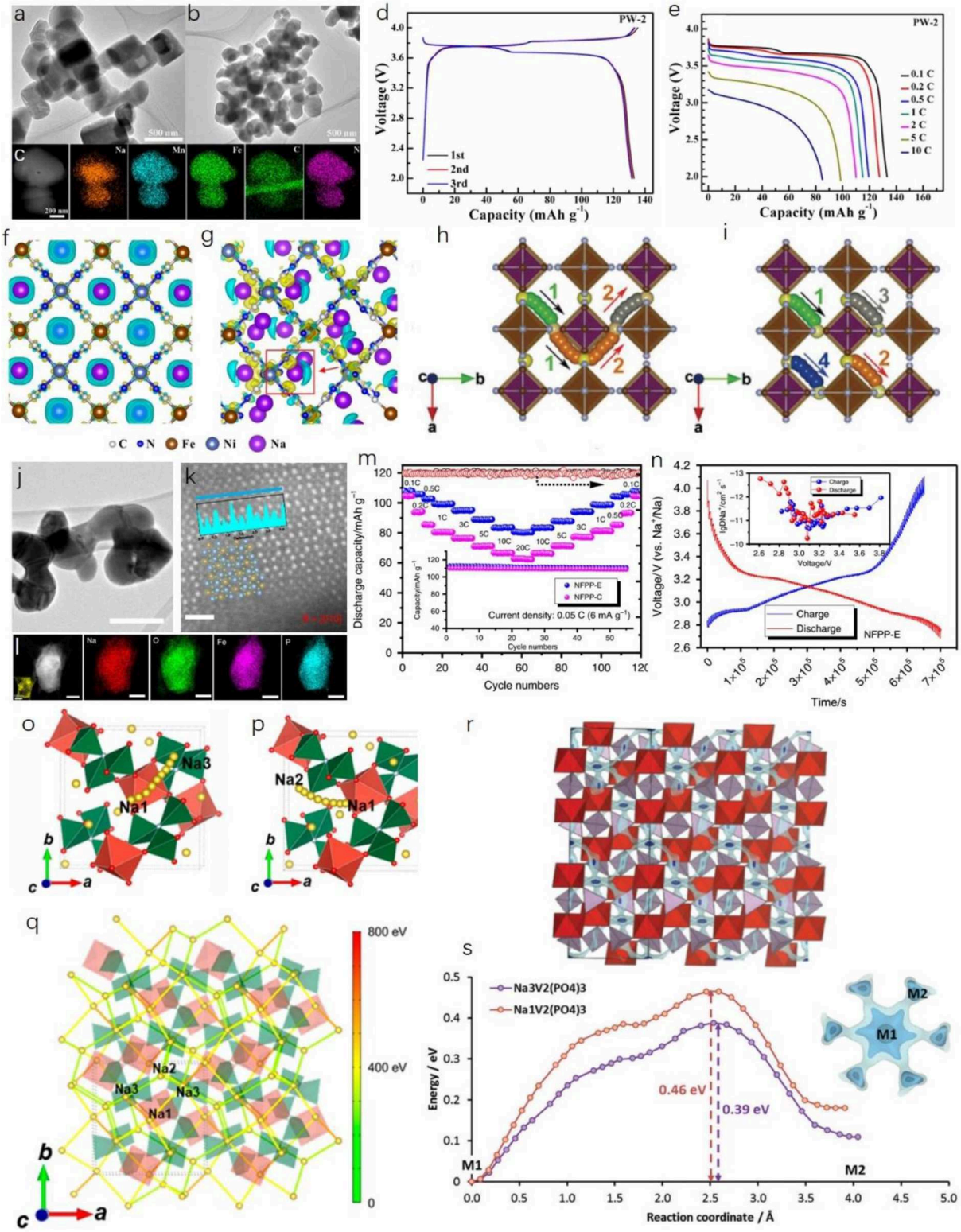

FIGURE 2 | (A,B) Transmission electron microscope (TEM) images of Na-rich monoclinic phase $Na_xMnFe(CN)_6$. **(C)** Scanning TEM-energy dispersive spectroscopy (STEM-EDS) element mapping results for $Na_xMnFe(CN)_6$. **(D)** Charge-discharge profile and **(E)** C-rate performance of the as-obtained sample. Reproduced from paper (Shen et al., 2018) with permission from the American Chemical Society. Charge density analyses of **(F)** cubic-structured NiHCF and **(G)** rhombohedral-structured NiHCF. Reproduced from paper (Ji et al., 2016) with permission from the American Chemical Society. **(H,I)** Front view of possible 3D Na^+ pathways between adjacent equivalent 24*d* sites. Reproduced from paper (You et al., 2016) with permission from WILEY-VCH. **(J)** Bright field (BF) image,

(Continued)

FIGURE 2 | (K) High-angle annular dark-field (HAADF) image with line profile in the inset, and **(L)** STEM-EDS mapping of as-obtained $Na_4Fe_3(PO_4)_2(P_2O_7)$ (NFPP) nanoplate. **(M)** C-rate performance and cycling stability (inset) of NFPP-E nanoplate. **(N)** Galvanostatic intermittent titration technique (GITT) curve of NFPP-E electrode and corresponding calculated diffusion coefficient of Na^+ ions. Reproduced from paper (Chen et al., 2019a) with permission from the Nature Publishing group. **(O,P)** Two typical 3D sodium diffusion pathways in $Na_3V(PO_3)_3N$ material and the **(Q)** corresponding activation barriers. Reproduced from paper (Kim et al., 2017) with permission from the American Chemical Society. **(R)** NASICON-type $Na_3V_2(PO_4)_3$ material with energy isosurface, showing interweaving of 3D Na^+ pathways and **(S)** migration pathways of Na^+ in the open 3D framework involving M1-M2-M1 hopping. Reproduced from paper (Wong et al., 2017) with permission from the Royal Society of Chemistry.

$Na_4Fe_3(PO_4)_2(P_2O_7)$ nanoplates (denoted as NPFF-E) can be well-obtained with a high degree of crystallinity, as shown in **Figures 2J,K**. All the detected elements are uniformly distributed in one NPFF-E particle (**Figure 2L**). Outstanding C-rate performance can be obtained, and satisfactory cycling stability can be achieved as well (**Figure 2M**). In addition, we also determined the sodium diffusion coefficient through a galvanostatic intermittent titration technique (GITT) study. From **Figure 2N**, the sodium diffusion coefficients range from 10^{-13} to 10^{-10} cm^2 s^{-1}, which is highly competitive with other recognized NASICON-type materials. These high diffusion coefficients are critical for low-temperature performance.

Another newly recognized family of NASICON-type cathode materials with 3D sodium diffusion pathways comprises the V-based N-substituted polyanionic materials. Kang et al. recently reported a new member of the 4 V-class of zero-strain cathode materials, $Na_3V(PO_3)_3N$, with unique 3D diffusion pathways for Na^+ ions (Kim et al., 2017). One PO_3N tetrahedron is connected to three VO_6 octahedra, leading to a strong inductive effect which, in turn, influences the operation voltage during charge/discharge. The relevant sodium ion diffusion pathways and diffusion energy barriers were calculated via a DFT study, and illustrations are presented in **Figures 2O–Q**. This exciting discovery has opened up new interest in the high-voltage N-substituted cathode materials with unique unexpected 3D sodium diffusion pathways. As for the well-recognized NASICON-type $Na_3V_2(PO_4)_3$ material, great attention has been extensively paid to it due to its outstanding merits (high operation voltage, acceptable specific capacity, and excellent cyclability). Its 3D sodium diffusion properties have been well-investigated, with the 3D network involving M1-M2-M1 hops and low energy barriers. Each Na in an M1 site is actively connected to six M2 sites. The corresponding illustrations are shown in **Figures 2R,S**. In addition, we would like to see more polyanionic compounds discovered with 3D Na^+ diffusion pathways in the search for advanced SIB storage devices with high power densities. It is suggested that further exploration should be concentrated on improving the reaction kinetics based on a more comprehensive understanding. Nevertheless, due to the intrinsic low electron conductivity of polyanionic material, how to maintain the well-designed carbon matrix or network and large-scale synthesis is still very challenging.

DISCUSSION AND PERSPECTIVES

The ultimate goal for advanced sodium ion battery devices has never changed, that they should be thoroughly competitive with the lithium ion battery in energy density, power density, and lower overall manufacturing cost (Tang et al., 2017, 2018; Zhang et al., 2017, 2019; Guo et al., 2020). For full-cell sodium ion battery devices, the emphasis always falls on the cathode parts, since they possess key parameters such as high enough operation voltages, large theoretical capacity, and most of all, acceptable high-rate capability. Materials with 3D sodium diffusion pathways are a promising branch among all the reported ones, and their distinctive physical and chemical properties deserve more integrated investigations and a deeper and more comprehensive understanding. Both the PBAs and the polyanionic compounds with 3D sodium diffusion pathways have shown outstanding fast kinetics, leading to superior C-rate performance at various current densities. Further investigations are suggested to be focused on the improvements of their intrinsic kinetic properties as well as mass-production issues. Specifically, for PBAs, as mentioned above, the structure-kinetics-performance relationship is subject to the influence of each crystallographic component: binary carbon- and nitrogen-coordinated transition metal ions, the density distribution of electronic states at each sodium site, and the vacancies created by either zeolitic water or coordinated water. When dealing with the specific concerns about the actual Na^+ diffusion channels and ionic conductivity, the bond length between carbon and carbon-coordinated transition metal elements is one of the key parameters for channel size, which, in turn, affects the ionic conductivity. The content of vacancies also has a strong influence on the Na^+ diffusion channels and ionic conductivity. The appropriate amount of vacancies will provide extra channels for Na^+ diffusion without cracking the local crystal structure. Nevertheless, how these parameters quantitatively influence the ionic conductivity as well as the crystal stability is still poorly understood. Another important issue that should not be neglected is the electronic conductivity. Up until now, only a few papers have focused on improving electronic conductivity directly by using the generalized gradient approximation with the Hubbard correction (GGA + U) method. Experimentally speaking, the electronic conductivity is strongly correlated with all the factors mentioned above and needs to be determined in an equational relationship. In the case of polyanionic compounds, the electronic conductivity is the most troublesome problem, and a well-designed carbon coating and carbon network are necessary even when the materials have high ionic conductivities. Therefore, how to maintain the delicate carbon network in a large-scale manufacturing procedure is a critical issue for the real application of polyanionic composites. Unlike the PBAs, only some of the reported materials possess 3D sodium diffusion pathways, although almost

all the polyanionic compounds have open 3D frameworks. Compared to the PBAs, the activation energy barriers of these polyanionic compounds are slightly higher. Heteroatom doping can be considered as an effective approach to alter the pristine electron state density distributions around both MO_6 octahedra and XO_4 tetrahedra, which, in turn, may lower the charge barriers around each sodium site. The transition metal migration is also poorly understood to date [such as for $Na_4M_3(PO_4)_2(P_2O_7)$ (M = Fe, Mn, etc.)], and how the phenomenon affects the related ion diffusion pathways and ionic conductivity should be determined in the future. It is also important to continuously discover more novel polyanionic cathode materials with 3D sodium diffusion pathways that have higher capacity and operation voltages. Besides, another important research direction is that how to combine both the PBAs and polyanions with the solid-state electrolyte properly so that their unique 3D diffusion properties can be more significantly magnified.

In **Table S1**, we summarize some of the reported cathodes for SIB devices with unique 3D diffusion pathways and their corresponding diffusion coefficients and activation barriers. These types of cathodes are especially important for high-power SIB devices for real applications. We can reasonably anticipate more technical breakthroughs, such as precise control of the water content in PBAs, ways to maintain a well-decorated carbon network at the industrial level, efficient organic/solid state electrolytes to fully achieve their theoretical capacities, and, in turn, the advanced SIB devices can be further designed and developed from a more technology based point of view.

DATA AVAILABILITY STATEMENT

The datasets generated for this study are available on request to the corresponding author.

AUTHOR CONTRIBUTIONS

MC, YZ, and GX prepared the manuscript. YT supervised the project.

FUNDING

This work was funded by The Science and Technology Development Fund, Macau SAR (Grant Nos. 0057/2019/A1 and 0092/2018/A2).

ACKNOWLEDGMENTS

The authors thank Dr. Tania Silver for critical reading of the manuscript.

SUPPLEMENTARY MATERIAL

The Supplementary Material for this article can be found online at: https://www.frontiersin.org/articles/10.3389/fchem.2020.00152/full#supplementary-material

REFERENCES

Bui, K. M., Dinh, V. A., Okada, S., and Ohno, T. (2015). Hybrid functional study of the NASICON-type $Na_3V_2(PO_4)_3$: crystal and electronic structures, and polaron-Na vacancy complex diffusion. *Phys. Chem. Chem. Phys.* 17, 30433–30439. doi: 10.1039/C5CP05323D

Chen, M., Chen, L., Hu, Z., Liu, Q., Zhang, B., Hu, Y., et al. (2017). Carbon-Coated $Na_{3.32}Fe_{2.34}(P_2O_7)_2$ cathode material for high-rate and long-life sodium-ion batteries. *Adv. Mater.* 29:1605535. doi: 10.1002/adma.201605535

Chen, M., Cortie, D., Hu, Z., Jin, H., Wang, S., Gu, Q., et al. (2018). A novel graphene oxide wrapped $Na_2Fe_2(SO_4)_3$/C cathode composite for long life and high energy density sodium-ion batteries. *Adv. Energy Mater.* 8:1800944. doi: 10.1002/aenm.201800944

Chen, M., Hua, W., Xiao, J., Cortie, D., Chen, W., Wang, E., et al. (2019a). NASICON-type air-stable and all-climate cathode for sodium-ion batteries with low cost and high-power density. *Nat. Commun.* 10:1480. doi: 10.1038/s41467-019-09170-5

Chen, M., Liu, Q., Wang, S.-W., Wang, E., Guo, X., and Chou, S.-L. (2019b). High-abundance and low-cost metal-based cathode materials for sodium-ion batteries: problems, progress, and key technologies. *Adv. Energy Mater.* 9:1803609. doi: 10.1002/aenm.201803609

Chen, M., Liu, Q., Zhang, Y., Xing, G., Chou, S. and Tang, Y. (2020). Emerging polyanionic and organic compounds for high energy density, non-aqueous potassium-ion batteries. *J Mater. Chem. A.* doi: 10.1039/C9TA11221A

Chen, M., Wang, E., Liu, Q., Guo, X., Chen, W., Chou, S.-L., et al. (2019c). Recent progress on iron- and manganese-based anodes for sodium-ion and potassium-ion batteries. *Energy Storage Mater.* 19, 163–178. doi: 10.1016/j.ensm.2019.03.030

Chen, S., Wu, C., Shen, L., Zhu, C., Huang, Y., Xi, K., et al. (2017). Challenges and perspectives for NASICON-type electrode materials for advanced sodium-ion batteries. *Adv. Mater.* 29:1700431. doi: 10.1002/adma.201700431

Choi, J. W., and Aurbach, D. (2016). Promise and reality of post-lithium-ion batteries with high energy densities. *Nat. Rev. Mater.* 1:16013. doi: 10.1038/natrevmats.2016.13

Dai, Z., Mani, U., Tan, H. T., and Yan, Q. (2017). Advanced cathode materials for sodium-ion batteries: what determines our choices? *Small Methods* 1:1700098. doi: 10.1002/smtd.201700098

Fang, Y., Liu, Q., Xiao, L., Rong, Y., Liu, Y., Chen, Z., et al. (2018). A fully sodiated $NaVOPO_4$ with layered structure for high-voltage and long-lifespan sodium-ion batteries. *Chem* 4, 1167–1180. doi: 10.1016/j.chempr.2018.03.006

Fedotov, S. S., Kabanova, N. A., Kabanov, A. A., Blatov, V. A., Khasanova, N. R., and Antipov, E. V. (2018). Crystallochemical tools in the search for cathode materials of rechargeable Na-ion batteries and analysis of their transport properties. *Solid State Ion.* 314, 129–140. doi: 10.1016/j.ssi.2017.11.008

Gao, H., Seymour, I. D., Xin, S., Xue, L., Henkelman, G., and Goodenough, J. B. (2018). $Na_3MnZr(PO_4)_3$: a high-voltage cathode for sodium batteries. *J. Am. Chem. Soc.* 140, 18192–18199. doi: 10.1021/jacs.8b11388

Guo, Q., Mao, J., Huang, J., Wang, Z., Zhang, Y., Hu, J., Dong, J., Sathasivam, S., Zhao, Y., Xing, G., et al. (2020). Reducing oxygen evolution reaction overpotential in cobalt-based electrocatalysts via optimizing the "microparticles-in-spider web" electrode configurations. *Small* 16:e1907029. doi: 10.1002/smll.201907029

Guo, S.-P., Li, J.-C., Xu, Q.-T., Ma, Z., and Xue, H.-G. (2017). Recent achievements on polyanion-type compounds for sodium-ion batteries: syntheses, crystal chemistry and electrochemical performance. *J. Power Sources* 361, 285–299. doi: 10.1016/j.jpowsour.2017.07.002

Hu, Q., Yu, M., Liao, J., Wen, Z., and Chen, C. (2018). Porous carbon-coated $NaTi_2(PO_4)_3$ with superior rate and low-temperature properties. *J Mater. Chem. A.* 6, 2365–2370. doi: 10.1039/C7TA10207K

Hurlbutt, K., Wheeler, S., Capone, I., and Pasta, M. (2018). Prussian blue analogs as battery materials. *Joule* 2, 1950–1960. doi: 10.1016/j.joule.2018.07.017

Hwang, J. Y., Myung, S. T., and Sun, Y. K. (2017). Sodium-ion batteries: present and future. *Chem. Soc. Rev.* 46, 3529–3614. doi: 10.1039/C6CS00776G

Ji, Z., Han, B., Liang, H., Zhou, C., Gao, Q., Xia, K., et al. (2016). On the mechanism of the improved operation voltage of rhombohedral nickel hexacyanoferrate as cathodes for sodium-ion batteries. *ACS Appl. Mater. Interfaces* 8, 33619–33625. doi: 10.1021/acsami.6b11070

Kim, H., Park, I., Seo, D. H., Lee, S., Kim, S. W., Kwon, W. J., et al. (2012). New iron-based mixed-polyanion cathodes for lithium and sodium rechargeable batteries: combined first principles calculations and experimental study. *J. Am. Chem. Soc.* 134, 10369–10372. doi: 10.1021/ja3038646

Kim, H., Shakoor, R. A., Park, C., Lim, S. Y., Kim, J.-S., Jo, Y. N., et al. (2013). $Na_2FeP_2O_7$as a promising iron-based pyrophosphate cathode for sodium rechargeable batteries: a combined experimental and theoretical study. *Adv. Funct. Mater* 23, 1147–1155. doi: 10.1002/adfm.201201589

Kim, H., Yoon, G., Park, I., Park, K.-Y., Lee, B., Kim, J., et al. (2015). Anomalous Jahn–Teller behavior in a manganese-based mixed-phosphate cathode for sodium ion batteries. *Energy Environ. Sci.* 8, 3325–3335. doi: 10.1039/C5EE01876E

Kim, J., Yoon, G., Lee, M. H., Kim, H., Lee, S., and Kang, K. (2017). New 4V-Class and zero-strain cathode material for Na-ion batteries. *Chem. Mater.* 29, 7826–7832. doi: 10.1021/acs.chemmater.7b02477

Lee, H.-W., Wang, R. Y., Pasta, M., Lee, S. W., Liu, N., and Cui, Y. (2014). Manganese hexacyanomanganate open framework as a high-capacity positive electrode material for sodium-ion batteries. *Nat. Commun.* 5, 5280. doi: 10.1038/ncomms6280

Li, W.-J., Chou, S.-L., Wang, J.-Z., Kang, Y.-M., Wang, J.-L., Liu, Y., et al. (2015). Facile method to synthesize Na-enriched $Na_{1+x}FeFe(CN)_6$ frameworks as cathode with superior electrochemical performance for sodium-ion batteries. *Chem. Mater.* 27, 1997–2003. doi: 10.1021/cm504091z

Li, X., Huang, Y., Wang, J., Miao, L., Li, Y., Liu, Y., et al. (2018). High valence Mo-doped $Na_3V_2(PO_4)_3$/C as a high rate and stable cycle-life cathode for sodium battery. *J. Mater. Chem. A.* 6, 1390–1396. doi: 10.1039/C7TA08970H

Li, Y., Lu, Y., Zhao, C., Hu, Y.-S., Titirici, M.-M., Li, H., et al. (2017). Recent advances of electrode materials for low-cost sodium-ion batteries toward practical application for grid energy storage. *Energy Storage Mater.* 7, 130–151. doi: 10.1016/j.ensm.2017.01.002

Lu, J., Nishimura, S.-,i., and Yamada, A. (2017). Polyanionic solid-solution cathodes for rechargeable batteries. *Chem. Mater.* 29, 3597–3602. doi: 10.1021/acs.chemmater.7b00226

Lu, Y., Li, L., Zhang, Q., Niu, Z., and Chen, J. (2018). Electrolyte and interface engineering for solid-state sodium batteries. *Joule* 2, 1747–1770. doi: 10.1016/j.joule.2018.07.028

Ni, Q., Bai, Y., Wu, F., and Wu, C. (2017). Polyanion-Type electrode materials for sodium-ion batteries. *Adv. Sci.* 4, 1600275. doi: 10.1002/advs.201600275

Panigrahi, A., Nishimura, S.-,I., Shimada, T., Watanabe, E., Zhao, W., Oyama, G., et al. (2017). Sodium Iron(II) Pyrosilicate $Na_2Fe_2Si_2O_7$: a potential cathode material in the Na_2O-FeO-SiO_2 system. *Chem. Mater.* 29, 4361–4366. doi: 10.1021/acs.chemmater.7b00764

Peng, J., Wang, J., Yi, H., Hu, W., Yu, Y., Yin, J., et al. (2018). A Dual-Insertion type sodium-ion full cell based on high-quality ternary-metal prussian blue analogs. *Adv. Energy Mater.* 8:1702856. doi: 10.1002/aenm.201702856

Shen, Z., Guo, S., Liu, C., Sun, Y., Chen, Z., Tu, J., et al. (2018). Na-rich prussian white cathodes for long-life sodium-ion batteries. *ACS Sustain. Chem. Eng.* 6, 16121–16129. doi: 10.1021/acssuschemeng.8b02758

Song, J., Wang, L., Lu, Y., Liu, J., Guo, B., Xiao, P., et al. (2015). Removal of interstitial H_2O in hexacyanometallates for a superior cathode of a sodium-ion battery. *J Am. Chem. Soc.* 137, 2658–2664. doi: 10.1021/ja512383b

Tang, Y., Deng, J., Li, W., Malyi, O. I., Zhang, Y., Zhou, X., et al. (2017). Water-soluble sericin protein enabling stable solid-electrolyte interphase for fast charging high voltage battery electrode. *Adv. Mater* 29:1701828. doi: 10.1002/adma.201701828

Tang, Y., Zhang, Y., Malyi, O. I., Bucher, N., Xia, H., Xi, S., et al. (2018). Identifying the origin and contribution of surface storage in tio2(b) nanotube electrode by *in situ* dynamic valence state monitoring. *Adv. Mater* 30, 1802200. doi: 10.1002/adma.201802200

Vaalma, C., Buchholz, D., Weil, M., and Passerini, S. (2018). A cost and resource analysis of sodium-ion batteries. *Nat. Rev. Mater.* 3:18013. doi: 10.1038/natrevmats.2018.13

Wang, B., Han, Y., Wang, X., Bahlawane, N., Pan, H., Yan, M., et al. (2018). Prussian blue analogs for rechargeable batteries. *Science* 3, 110–133. doi: 10.1016/j.isci.2018.04.008

Wang, E., Chen, M., Liu, X., Liu, Y., Guo, H., Wu, Z., et al. (2018). Organic cross-linker enabling a 3D porous skeleton-supported $Na_3V_2(PO_4)_3$/carbon composite for high power sodium-ion battery cathode. *Small Methods* 3:1800169. doi: 10.1002/smtd.201800169

Wang, E., Xiang, W., Rajagopalan, R., Wu, Z., Yang, J., Chen, M., et al. (2017). Construction of 3D pomegranate-like $Na_3V_2(PO_4)_3$/conducting carbon composites for high-power sodium-ion batteries. *J Mater. Chem. A* 5, 9833–9841. doi: 10.1039/C7TA00153C

Wessells, C. D., Peddada, S. V., McDowell, M. T., Huggins, R. A., and Cui, Y. (2011). The effect of insertion species on nanostructured open framework hexacyanoferrate battery electrodes. *J. Electrochem. Soc.* 159, A98–103. doi: 10.1149/2.060202jes

Wong, L. L., Chen, H., and Adams, S. (2017). Design of fast ion conducting cathode materials for grid-scale sodium-ion batteries. *Phys. Chem. Chem. Phys.* 19, 7506–7523. doi: 10.1039/C7CP00037E

Wu, J., Song, J., Dai, K., Zhuo, Z., Wray, L. A., Liu, G., et al. (2017). Modification of transition-metal redox by interstitial water in hexacyanometalate electrodes for sodium-ion batteries. *J. Am. Chem. Soc.* 139, 18358–18364. doi: 10.1021/jacs.7b10460

Xiao, P., Song, J., Wang, L., Goodenough, J. B., and Henkelman, G. (2015). Theoretical study of the structural evolution of a $Na_2FeMn(CN)_6$ cathode upon Na intercalation. *Chem. Mater.* 27, 3763–3768. doi: 10.1021/acs.chemmater.5b01132

You, Y., Yao, H. R., Xin, S., Yin, Y. X., Zuo, T. T., Yang, C. P., et al. (2016). Subzero-temperature cathode for a sodium-ion battery. *Adv. Mater.* 28, 7243–7248. doi: 10.1002/adma.201600846

Zhang, Y., Malyi, O. I., Tang, Y., Wei, J., Zhu, Z., Xia, H., et al. (2017). Reducing the charge carrier transport barrier in functionally layer-graded electrodes. *Angew. Chem. Int. Ed.* 56, 14847–14852. doi: 10.1002/anie.201707883

Zhang, Y., Tang, Y., Deng, J., Leow, W. R., Xia, H., Zhu, Z., et al. (2019). Correlating the Peukert's constant with phase composition of electrode materials in fast lithiation processes. *ACS Mater. Lett.* 1, 519–525. doi: 10.1021/acsmaterialslett.9b00320

Zhu, T., Hu, P., Wang, X., Liu, Z., Luo, W., Owusu, K. A., et al. (2019). Realizing three-electron redox reactions in NASICON-structured $Na_3MnTi(PO_4)_3$ for sodium-ion batteries. *Adv. Energy Mater.* 9:1803436. doi: 10.1002/aenm.201803436

Conflict of Interest: The authors declare that the research was conducted in the absence of any commercial or financial relationships that could be construed as a potential conflict of interest.

Advantages of publishing in Frontiers

OPEN ACCESS
Articles are free to read for greatest visibility and readership

FAST PUBLICATION
Around 90 days from submission to decision

HIGH QUALITY PEER-REVIEW
Rigorous, collaborative, and constructive peer-review

TRANSPARENT PEER-REVIEW
Editors and reviewers acknowledged by name on published articles

Frontiers
Avenue du Tribunal-Fédéral 34
1005 Lausanne | Switzerland

Visit us: www.frontiersin.org
Contact us: info@frontiersin.org | +41 21 510 17 00

REPRODUCIBILITY OF RESEARCH
Support open data and methods to enhance research reproducibility

DIGITAL PUBLISHING
Articles designed for optimal readership across devices

FOLLOW US
@frontiersin

IMPACT METRICS
Advanced article metrics track visibility across digital media

EXTENSIVE PROMOTION
Marketing and promotion of impactful research

LOOP RESEARCH NETWORK
Our network increases your article's readership